



STRONG MICROWAVES IN PLASMAS

2003

Volume 2

*Institute of Applied Physics
Nizhny Novgorod*

RUSSIAN ACADEMY OF SCIENCES
INSTITUTE OF APPLIED PHYSICS

STRONG MICROWAVES IN PLASMAS

PROCEEDINGS
OF THE INTERNATIONAL WORKSHOP

*Nizhny Novgorod,
1 – 9 August 2002*

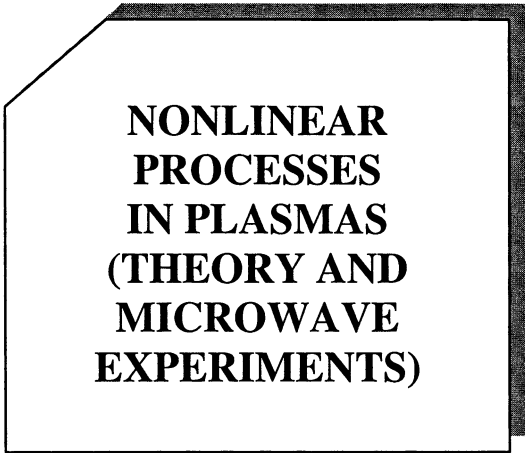
Edited by
A.G. Litvak

In two volumes
Volume 2

Nizhny Novgorod – 2003

© Institute of Applied Physics
Russian Academy of Sciences, 2003

ISBN 5-8048-0039-X



**NONLINEAR
PROCESSES
IN PLASMAS
(THEORY AND
MICROWAVE
EXPERIMENTS)**

COLLISIONAL EFFECTS IN ULTRA-HIGH ILLUMINATED PLASMAS: FROM THE THEORY TO THE EXPERIMENT

A. A. Balakin and G. M. Fraiman

Institute of Applied Physics RAS, Nizhny Novgorod, Russia

The electron-ion collisions in plasmas with strong laser fields is analyzed. It is shown that the concept of "strong fields" in the collision problem in plasmas is determined by the single parameter, namely, the ratio of the oscillatory electron radius to the distance from the ion, at which Coulomb ion field equals the laser field amplitude. It is found that the phase space structure is strongly modified as the value of this parameter increases: stochastic attractor appears, predecessors' analytical approaches become unjustified. By numerical and analytical analysis, the boundary of attraction region is found, energy exchange processes are studied, expressions for effective frequencies and cross-sections are obtained. It is shown from theory and experiment that the efficiencies of all main energy exchange channels caused by collisions (such as Joule heating, harmonics generation, bremsstrahlung radiation, fast electron generation) increase independently from the field polarization as the laser field intensity grows.

1. Introduction

Interest to the problem of the pair electron-ion collisions in strong electromagnetic fields having been observed already during the last 40 years [1–5], that witnesses by itself about its importance and fundamental nature. This problem becomes especially actual in latter years in connection with the development of lasers of high power with densities of energy till 10^{18-21} W/cm², corresponding to ultra-relativistic oscillatory energies of electrons. Physical phenomenons, discovered at investigation of such fields interaction with usual and cluster plasma, and possible applications (from laser controlled fusion till transformation of the optical radiation to radiation of Roentgen wave lengths range) lead to that the problem of pair collisions in plasma transformed itself from the pure academic to important applied problem. It is the narration of the modern state of the problem of pair electron-ion collisions in plasma at the presence of strong fields of electromagnetic radiation, that is the main object of this lecture.

Traditionally investigation of electron-ion collisions in strong electromagnetic fields is fulfilled on the basis of third models. All this models are grounding on the approximation of pair collisions, i.e. it is supposed that the probability of the simultaneous collision of third and more particles in one point of space is negligible. This leads to that all characteristics of collisions integral for one-particle distribution function may be found from the solution of the problem of scattering of the beam of non-interacting (test) electrons on the only ion [6].

One should note, that the narration in many secondary works has complicated itself sufficiently in comparison with original works. At the same time,

such complication leads only to merely illusory strictness and does not add any new ideas compared with originals. Therefore we are citing, in general, only those publications, where a certain progress in understanding has been reached or review works.

The model of "small-angles" scattering [5–8] is the most popular. Here the linear trajectory is considered in capacity of unperturbed electron drift trajectory and all effects are estimated in frames of the theory of perturbation along this trajectory.

It is obvious, that in frames of this approximation electron-ion collisions occur in different moments "non-correlated" between themselves. That is, it is proposed, that in case of the beam with homogeneous initial particles distribution, including the distribution on the field phases, moments of collisions¹ will also be distributed homogeneously on the field period. More over, in frames of this approximation the possibility of attraction of an electron to the ion during the scattering is not considered. In other words, in frames of linear trajectories approximation it is supposed, that electron can not bend it's trajectory substantially equally as during the whole process of scattering as till the moment of the last blow. Actually, this is the same approximation, that has been used in [6].

Another model (the low frequency approximation, [8, 9]) describes collisions including the scattering on large angels. It is proposed though, that sufficiently strong outer field accelerates electrons before and after the collision (Coulomb field of the ion on this stages is supposed negligible) and only the static field of the nearest ion is important during the process of scattering. Also like in the model of linear trajectories it is proposed, that collisions occur at accidental moments of time. Since in such formulation of the problem the contribution from the scattering on large angles is small, then the result coincides with small-angles approximation results with logarithmic accuracy.

The quantum model (Born approximation on the Coulomb potential [10]) leads to the same results that both previously approximations in force of the account of effects of only the first order in quasi-classic expansion. So, in all approximations enumerated above results differing only by logarithmic factors have been gotten. It seems, that general for all propositions about non-correlated character of collisions moments and the impossibility for electron to bend it's drift trajectory (to attracts itself to the ion) during repeated oscillations near the ion were the main cause of mentioned coincidence. Especially clearly this is demonstrated in recent works [7], where author directly from the kinetic equation with the collisions integral in Landau form² derived, again with logarithmic accuracy,

¹ Further under the moment of collision we mean the moment of the nearest approaching of an electron to the ion during the scattering. This collision itself we shall name like the last collision or the last blow.

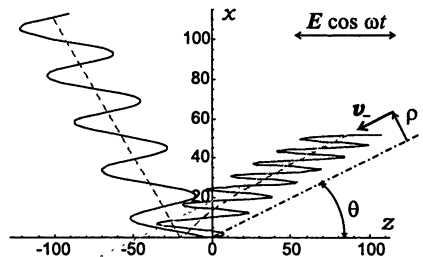
² We shall remind [6], that the derivation of the Landau collisions integral is basing on supposition about the homogeneous distribution of collisions moments and determining contribution of the distant (merely rectilinear) scattering.

the same results (for effective frequency of collisions, efficiency of harmonics generation etc.) that in works cited above. Seemingly, the coincidence of results given by three different, to the first sight, approximations become the cause of the extinction of the interest to this themes for more than thirty years.

2. Particles dynamics in strong fields

That effects have been omitted in traditional models? Let us consider, how the collision is described traditionally. We shall remind, that in absence of the Coulomb field of the ion the particle movement is the superposition of oscillations in EM wave field with oscillatory velocity $\mathbf{v}_{osc} = e\mathbf{E}/m\omega_0$ (ω_0 and \mathbf{E} are frequency and amplitude of EM wave) and the drift with constant drift velocity \mathbf{v} . In all mentioned models it is supposed, that the drift occurs along the direct line and fulfills only the "delivery" of particles in interaction region and then the collision with the ion proper occurs. Different models are describing this collision with different degree of accuracy (with or without account of near collisions, when the scattering occurs on large angles; with quantum mechanics apparatus or in frames of classic mechanics). Since particles are considered like homogeneously distributed in space before the collision, then the contribution of particles scattering on large angles is small. Indeed, it is known from the Reserford problem, that from all particles with initial velocity \mathbf{v} only those particles are scattering on large angles, which approach to the ion on a distance lesser than the Reserford radius $b_v = e^2Z/mv^2$. Since in strong fields it is counted, that the scattering occurs with oscillatory velocity $v_{osc} \gg v$ and corresponding Reserford radius $b_{osc} = e^2Z/mv_{osc}^2$ is small, then the contribution of the scattering on large angles is negligible. The particle is supposed to leave the scattering region after the blow.

Fig. 1. The typical electron trajectory (full line), drift trajectory (dashed line) and parameters of the electron being scattered (\mathbf{v} is the velocity, ρ is the impact parameter, θ is the angle between velocity and field \mathbf{E}). Dotted line represents the drift trajectory in "rectilinear" approximation.



The numerical simulation shows another dynamics of the scattering of particle. Figure 1 with the drift electron trajectory demonstrates this. In strong fields due to the large oscillations radius $r_{osc} = eE/m\omega_0^2 \gg b_{osc}$ the particle returns repeatedly to the ion and experiences many distant (sometimes they are named

"soft") collisions during the process of scattering. The drift energy of the particle at this is merely constant but the sufficient bending of *the drift trajectory*¹ occurs. As a result, before the last "hard" blow (that is he, practically, who changes the particle energy) electrons happen to be more close to the ion, than at the rectilinear drift movement. As a consequence of this, energy variation of particles at first being far from the ion increases sufficiently at the scattering and many other new effects arises. It is to the analysis of these effects at electron-ion collisions in strong EM fields with accounting of the bending of particles drift trajectories, that this work is devoted to.

In present lecture, generally, collisions processes in non-relativistic fields are considered. Such limitation is justified by the sufficient simplification in analytical consideration. The exception is those paragraphs connected with discussion concerning experimental result (p. 7), where relativistic intensities are realized. More over, we limit ourselves with the classic description. The short analysis of quantum corrections is mentioned in the conclusion part.

3. Pair collision approximation

In this paragraph we shall discuss, how one may reduce the problem concerning the search of the electron-ion collisions integral in strong fields in equation for one-particle distribution function in rare plasma to the problem of the scattering of the beam of test electrons on the ion. Since this result seems to be quite obvious, we shall adduce only short derivation to demonstrate, that the so called pair collisions approximation is by no means equivalent to the small-angles approximation.

The simplest mode to derive the equation for one-particle distribution function is the method of Bogolubov's "chain" [6]. As it is known, the idea of the method consists in continues transition from many-particles distribution function for all plasma particles to one-particle function, two-particle one and so on. At this in rare plasma it is enough to limit oneself with two-particle distribution function, i.e. to tear the chain off already on the second step. This procedure is well known and described in details in many text-books. Our remark consists in that the analogous unlinking of correlations may be done also for plasma in strong field of EM wave. It is most easy to fulfill this procedure in drift coordinates. Their convenience consists in that at the transition to drift coordinates the left part of the kinetic equation becomes not dependent on the outer field and, accordingly, on the time. All information about the strong outer field is in collision integral, which becomes evidently depending on time:

$$S_t[f] = \frac{\partial}{\partial p_i} \int \frac{\partial U}{\partial r_i} G(\mathbf{r}, \mathbf{p}, t; \mathbf{r}', \mathbf{p}', t') \frac{\partial U}{\partial r_j'} \frac{\partial f}{\partial p_j'} d^3 r' d^3 p' dt' d^3 r. \quad (1)$$

¹ We shall name the difference after the subtraction of the particle oscillations from it's trajectory in laboratory coordinate system like the drift trajectory.

Here $U(\mathbf{r}, t) = e^2 Z / |\mathbf{r} - \mathbf{r}_{osc}(t)|$ is the oscillating Coulomb potential of the ion.

An ordinary conditions have been used at the derivation of this expression. Namely, as in the scattering problem without fields, it is proposed that the influence of other ions on the scattering process is negligible, i.e. plasma is rare enough. In other words, there should be small particles in interaction volume V_{int} :

$$nV_{int} \ll 1. \quad (2)$$

In plasma with weak fields this condition reduces itself to the condition of the presence of many particles in Debye sphere.

Physical sense of collisions integral (1) is usual. It provides the change of drift impulses and kinetic energy of electrons at the scattering on ions in the field of EM wave. This field itself is supposed to be smooth in space on the scale of collision and is slowly varying in time. This is usually true always, since just quasi-monochromatic fields are under consideration here. It should be also noted, that in the same way like in Boltzman collisions integral, the function $G(\dots)$ standing in kernel is nothing but the Green function of the problem of scattering of the beam of electrons with initial drift impulse fixed on infinity on the only ion. More detailed we shall consider this problem further. Here we shall just note, that predecessors results may be classified most easy in terms of this Green function. Particularly, the rectilinear trajectories approximation (sometimes being not too accurate called like the small-angles one) corresponds to that the initial and final impulses in Green function are supposed to be equal and the drift trajectory is considered like rectilinear. Correspondingly, in momentary blow approximation [9] at the account of the average for the period of the change of energy with wave field it is also proposed, that particles are moving homogeneously and rectilinear before the blow. The difference consists only in more accurate account of data of scattering for small impact parameters. So far as in these models distant collisions (mind, that in both models impact parameter at the scattering does not change itself) give the basic contribution into the change of energy, then contribution of near collisions with small impact parameters is negligible and results of both models coincide.

It is clear now, what may give rise to new results. As long as electrons oscillate in the vicinity of the ion for many periods, attraction and, as a consequence, the change of the density of test electrons near the ion may prove to be essential. The second less obvious result consists in that collisions phases themselves cease to be equiprobable. That is, the attraction process is accompanied with electrons bunching.

4. The strong field

Now let us discuss at which fields intensities mentioned effects are significant. Or what the term "strong" field means?

To answer these questions we should analyze the Green function G being determined by test particles trajectories in (1). The latter are described by Newton equation (non-relativistic case):

$$\ddot{\mathbf{r}} = -\frac{\partial}{\partial \mathbf{r}} \frac{1}{|\mathbf{r} - \mathbf{r}_{osc}|}, \quad \mathbf{r}_{osc} = -\frac{1}{\Omega^2} \cos \Omega t. \quad (3)$$

This equation is written in dimensionless form after the introduction of characteristic scales

$$r_E = \sqrt{\frac{eZ}{E}}, \quad \omega_E = \sqrt[4]{\frac{eE^3}{m^2Z}}, \quad v_E = \sqrt[4]{\frac{Ze^3E}{m^2}}. \quad (4)$$

A dimensionless frequency

$$\Omega = \frac{\omega_0}{\omega_E} = \left(\frac{\omega_0^4 m^2 Z}{eE^3} \right)^{1/4} \quad (5)$$

is the only dimensionless parameter¹, entering the equation (3) and characterizing the pumping field. An amplitude E and frequency ω_0 enter into parameter Ω in combination ω_0^4/E^3 . This means, that collisions in strong high-frequency fields (e.g. of the laser diapason) are similar to collisions in more weak low-frequency fields (e.g. of microwaves diapason)². This means also, that the phase space structure is determined itself by only this parameter and is different in principle in regions of high-frequency (weak) $\Omega \gg 1$ and low-frequency (strong) $\Omega \ll 1$ field. How this structure changes at the parameter variation?

At large Ω values (weak fields) essential changes in phase space structure will be only in small vicinity of separatrix, detaching spacing hyperbolic trajectories from periodical. With growth of the field (decrease of the parameter Ω) the stochastic layer volume increases and at $\Omega \ll 1$ it becomes about $1/\Omega \gg 1$. In dimensional variables of stochastic region this corresponds to the oscillatory radius in coordinate space and oscillatory impulse in impulse space. This evolution is depicted qualitatively on Fig. 2.

From the point of view of the problem of scattering this means, that the particles dynamics is regular and the change of energy with field may be counted on Landau model in weak fields ($\Omega \gg 1$) or until the drift (thermal) electron velocity is large in comparison with oscillatory one. On the contrary, the region of irregular dynamics in phase space of the system becomes determining in case of the strong field ($\Omega \ll 1$), when oscillatory velocity is larger than drift one significantly.

¹ This is true, certainly, only in frames of equation (3) suitability, i. e. for non-relativistic case.

² Obviously, that other plasma parameters (temperature and concentration) should be recounted in proper way.

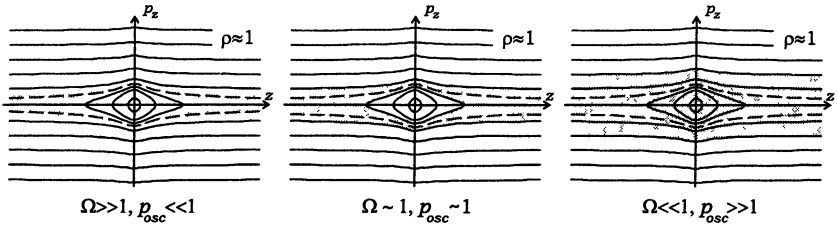


Fig. 2. The change of the region of stochasticity (qualitatively) in phase space at the parameter Ω variation. Dashed line depicts separatrix curve.

Already this simple consideration show, that in early works of 60–70 years these effects could not be taken into account adequately, since the term "stochasticity" itself just having been conceived. More over, this problem was too difficult also for numerical simulation.

5. Numerical results

What numerical results provide? On Fig. 3 there are electrons drift trajectories for longitudinal (Fig. 3, a, initial velocity is along the field) and transverse scattering (Fig. 3, b). It is seen, that these trajectories depend essentially on the

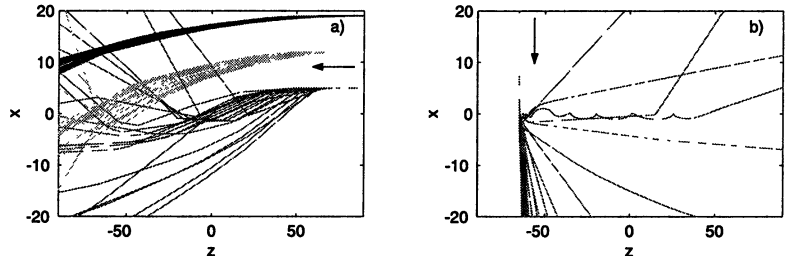


Fig. 3. Drift trajectories of particles at the same initial impact parameters but at different field phases for $\Omega = 0.125$ and $v = 0.1 v_{osc}$. An arrow points the initial particles velocity direction. Trajectories with different impact parameters correspond to different gradations of the gray. It is seen the appearance of the complicated (stochastic) dynamics at small impact parameters.

spacing phase (a phase at the start moment). This dependence is especially evident for small impact parameters. So, providing distant particles are moving merely along the only line and may be properly described in frames of small-angles approximation (Fig. 3, a), the strong dispersion of trajectories is observed already on the boundary of the attraction region (the region of initial coordinates from which particles get into small vicinity of the ion $\propto b_{osc}$). Trajectories behaviour themselves is stochastic like inside the attraction region.

It is seen from the Fig. 3, that alongside with "frontal" collisions (particles flying exactly along the axis Oz on distances of the order $b_{osc} = \Omega^2$) particles with the impact parameter far exceeding b_{osc} experience also the change of energy of the same order. In traditional models we would see the essential scattering only at frontal collisions. From Fig. 3 it is seen also the second consequence of the attraction: the dependence of the change of energy on impact parameters is not the one-to-one function. In strong fields at $v < v_{osc}$ a situation is realized, when particles from substantially different impact parameters go to the same point of the space (in particular, into the region b_{osc} near the ion). That is, multifluxity being absent in weak fields is realizing itself. Alongside with this stochastics arises, i.e. small variation of initial parameters lead to essential divergence of trajectories and to the difference of final velocities of particles.

Note, that the boundary of the attraction region is simultaneously the boundary of strong particles energy variations also (Fig. 4) [12]. Indeed, to change greatly it's energy particle need to approach to the ion, but particles outside the attraction region can not fly close to ion, consequently, they can not change strongly their energy. A variation of the test particles distribution function depending on coordinates is the micro-characteristics of the attraction influence. We shall mention, that this function is supposed to be constant in traditional models. In calculations this function becomes proportional to $\propto 1/\rho$ (ρ is transverse coordinate before the hard collision). This is the integrable singular dependence, leading to reinforcement of the role of near collisions and, as a consequence, to the increase of all energetic processes (Joule heating, radiation harmonics generation and appearance of fast particles).

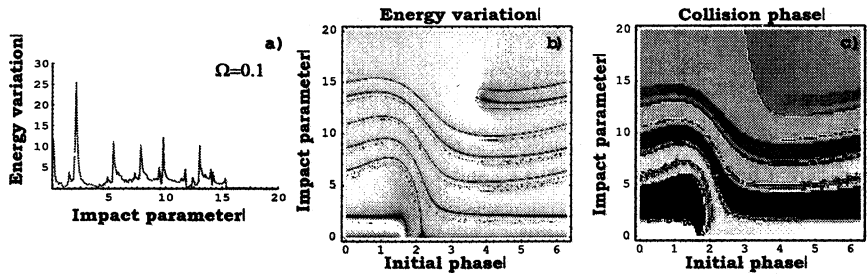


Fig. 4. Dependence of the energy variation from the impact parameter, averaged on the spacing phases (a); energy variation (b) and phase of the hard (last) collision (c) in dependence on the impact parameter and initial phase for longitudinal propagation. More dark gradations of the gray depict higher value of quantity.

Fig. 4, c has more information interesting for us. The question is the dependence of phase of hard (the last) collision on the phase of spacing and impact pa-

parameter. Quite unexpected results consist in that the attraction process is accompanied by evident electrons bunching [15]. For quantitative estimation of this effect we found the field phase at the moment, when electron is mostly close to ion during the whole process of scattering (the hard collision phase). Remarkable result consists in that all electrons experiencing appreciable change of energy (compare with Fig. 4, *b*) have close phases of the hard blow. More attentive analysis of these phases leads to conclusion, that they correspond to maximums of oscillatory velocity.

In conclusion of this paragraph, we shall accentuate, that even for $\Omega = 0.1$ calculation of the whole problem of scattering (for all angles between the field and a beam) is very difficult and takes a lot of time and utmost resources of modern personal computers. At the same time, let us say for fluxes 10^{18} W/cm² at the wave length 1 mk the small parameter interesting for us is $\Omega = 0.01$. Therefore analytical results gain special value.

6. Analytics

Let us consider, that may be done in this direction. First of all note, that the problem of scattering (3) is described by Hamiltonian equations with potential periodical on time. This means, that one may pass on to point mappings for drift coordinates and impulses of the particle in period. Consequently, in force of the Hamiltonian nature the problem reduces itself to finding of the only scalar function – generating function of the mapping. It is well-known from theoretical mechanics, that to find generating function it is enough to calculate operation on one period and to express it as a function of, for example, initial coordinates and final impulses $S = S(\mathbf{r}_{ini}, \mathbf{p}_{out})$. At this the remaining pair of canonical coordinates is, correspondingly, equal:

$$\mathbf{p}_{ini} = \frac{\partial S}{\partial \mathbf{r}_{ini}}, \quad \mathbf{r}_{out} = \frac{\partial S}{\partial \mathbf{p}_{out}}. \quad (6)$$

It should be noted, that we can use different approximations during the one period.

A number of important features of mapping (6) one may discover in important particular case of quasi-longitudinal distribution in neglect of particle displacement across the electric field because of the drift velocity $v_{\perp} \ll 2\pi/\rho v_{osc}$ ¹. Here the mapping is dividing on displacement part for longitudinal coordinate and impulse and on mapping for transverse coordinate $\rho = \sqrt{x^2 + y^2}$:

$$\bar{\rho} = |\rho - 2\pi/\rho|. \quad (7)$$

¹ At the drift velocity sufficiently small all qualitative effects being under discussion in this paragraph will take place also for circular polarization.

The mapping (7) is represented graphically on Fig. 5.

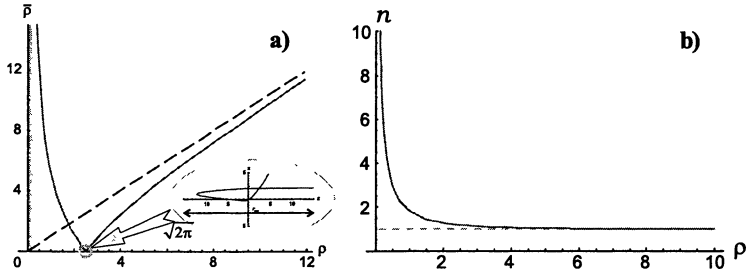


Fig. 5. The dependence of the impact parameter $\bar{\rho}$ in iteration of mapping (7) on impact parameter ρ is depicted on right picture (a). The region of losses of particles at the scattering on large angles is hatched. The point, from which particles get exactly to the ion in one iteration of mapping, is marked out specially. On left picture (b) there is a dependence of particles concentration on the impact parameter ρ for: unperturbed distribution (dotted line) and the utmost value in infinite number of iterations (full line), which is the invariant measure of mapping (7).

Mapping (7) does not describe the scattering of particles on large angles and their departure from the region of scattering. For the account of such particles one may introduce the region of losses with the width of the order $b_{osc} = \Omega^2 \xrightarrow{\Omega \rightarrow 0} 0$ (the hatched region on Fig. 5), at getting in which particles are supposed to leave the region of scattering.

Let us consider features of mapping (7). In the first place, it is necessary to notice the arising of multifluxity, when particles having started from different impact parameters come simultaneously into the same point of the space because of attraction. The simplest example is the fact, that alongside with particles with small initial parameters $\rho_{ini} \leq b_{osc}$ particles passing the ion one time, being scattered on the small angle and having hit the ion at return (Fig. 5) get into the same vicinity. Impact parameter ρ_1 corresponding to these particles may be found easy: $\rho_1 = \sqrt{2\alpha\pi}$. Analogous, there are particles, having accomplished two, three etc. oscillations with impact parameters ρ_1, ρ_2, \dots . There will be $N \approx r_{osc} / vT \propto v_{osc} / v$ of such groups of particles in all. In this case all particles with $\rho < \rho_N$ in the long run prove to be in region $\bar{\rho} \leq \rho_1$.

The appearance of singularity in correlation function is the second important feature of mapping (7). As mentioned above, all particles with impact parameters $\rho \leq \rho_{att}$ are shrinking during the scattering to the region $\rho \leq \rho_1$. It is interesting, what the particles distribution before "the last" (i.e. in diapason $[0, \rho_1]$) collision is. To answer this question let us find the change of concentration (or, that is the

same, the spatial density of the correlation function) in iteration of mapping (7) from the law of conservation of number of particles:

$$\bar{n}\rho d\bar{\rho}d\bar{z} = n\rho d\rho dz.$$

After conveying the old coordinate ρ through the new one $\bar{\rho}$ from mapping (7) and using inequality $\rho > \rho_1$ (particles having not hit yet into the region $[0, \rho_1]$ are considered) one can find:

$$\bar{n} = n(\rho) \frac{\rho^3}{\bar{\rho}(\rho^2 + 2\alpha\pi)}, \quad \rho(\bar{\rho}) = \frac{1}{2} \left(\bar{\rho} + \sqrt{\bar{\rho}^2 + 8\alpha\pi} \right). \quad (8)$$

In particular, as one should expect, the concentration is practically stable at large impact parameters $\bar{\rho} \gg \sqrt{8\alpha\pi} = 2\rho_1$. Though there is a singularity in concentration (compare with Fig. 4):

$$\bar{n} \approx n \frac{\rho_1}{2\bar{\rho}} \quad (\text{at } \bar{\rho} \ll \rho_1) \quad (9)$$

at small impact parameters.

The account of $N \gg 1$ particles spacings leads to the concentration distribution before the last blow like:

$$n \approx n_0 (1 + a/\rho), \quad (10)$$

where the coefficient $a \approx b_v$ should be separated from the full mapping (including for transverse beam fall).

The third feature of mapping (7) is the arising of stochastic dynamics. It was already noted in previous point, that the dynamics of the scattering of particles proves to be very difficult and stochastic in strong pumping field. Mapping (7) demonstrates the same fact. Indeed, from one side, it is globally attracting¹. From the other side, the central part of the mapping is locally instable. As a result, intermixing of particles occurs. This is exactly one from stochastic dynamics criteria. Coulomb center here is playing the role of "the organizer" of the compound stochastic attractor.

An unusual feature of Coulomb attractor consists in permanent loss of particles due to the scattering on large angles. Particles having hit (due to the attraction to the ion at repeating oscillations at regular dynamics or due to Arnold diffusion (stochastic "wandering" of particle at stochastic dynamics)) in small vicinity of the ion experience the large-angles scattering and gather velocity comparable with oscillatory one. As a result, they, from one side, leave the attractor area, but, from other side, give contribution to collisional current and, accord-

¹ It is necessary to mention, that the hitting of the particle into the region $\rho \leq \sqrt{r_{osc} r_E}$ is accompanied with strong change of it's velocity and possible departure from the scattering area, so that mapping (7) is no longer suitable.

ingly, to coherent radiation. Since at the scattering on large angels particles gain velocity being directed contrary to the instantaneous oscillations velocity direction, one should expect the intense generation of the collisional current and, respectively, coherent radiation, increasing with the growth of the stochastic area, i.e. with the increase of the pumping field intensity.

7. Experimental consequences

Let us discuss results of some experiments. It will be shown further, that in regime of the strong field intensities of all plasma processes – Joule heating, harmonics generation, formation of "tails" of fast particles – do not decrease and depend weakly on the field polarization. We shall demonstrate results of known experiments on interaction of the intense laser radiation with plasma, which may be simply explained by the theory developed above.

Let us begin from the analysis of the efficiency of Joule heating and fast electrons generation at collisions. In recent experiments with petawatt laser in USA [16] with energy of a pulse till 50 J at duration 0.5–10 pc and radiation intensity 10^{18-21} W/cm² at interaction with prepared beforehand plasma with concentration 10^{17-19} cm⁻³ it was discovered, in particular, that at such intensities the heating of the bulk of electrons depends weakly on the field and, is determined, in general, by only duration of the pulse of radiation. More over, it was observed, that the interaction process is accompanied with generation of a comparatively large number of fast electrons with the summary energy till tens percent of the laser pulse energy. That is, it was found, that radiation is well absorbed and the energy of fast particles is comparable with the thermal energy of the bulk. It is on this fact, practically, on which all further results of this group and, seemingly, also results of Japanese explorers [11] on observation of fast protons and neutrons at such interactions are based.

From where fast electrons appear and why the absorption is so noticeable? Authors either pronounce general words about strong turbulence or say cautiously about the incomprehensibility of these effects. Let us consider, that our theory will predict. On Fig. 6 experimental results of several works [11, 16] are depicted. Here the full

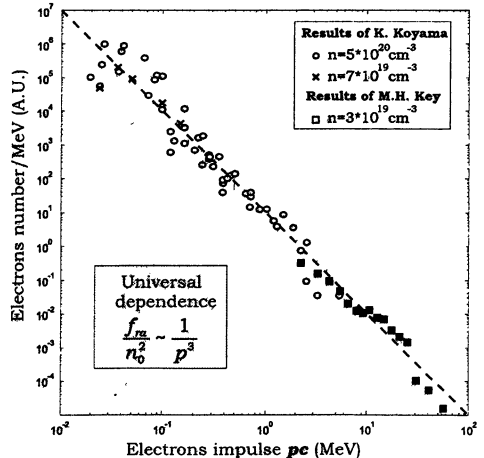


Fig. 6. The comparison of experimental [11, 16] and theoretical (dotted line) dependencies of hot electrons distribution on impulse.

line represents the result of our estimations for the number of fast electrons, normalized on the square of concentration, in dependence on normalized electron impulse pc . We see good coincidence in the range of energies of energies of fast particles from tens keV till 30 MeV.

It should be noted, that authors [11] in their works say about the dependence on the electrons energy. But we built the dependence on the product of impulse and velocity of light. This one and the same for relativistic range of energy (at intensities larger than 10^{18} W/cm²) but it is different in principle at small energies. Therefore, including of results [11] in graphics is a certain arbitrariness from our side. We have done it, since, in the first place, only in this work one can observe the dependence on plasma concentration. Besides, a simple erratum is not eliminated.

The point is that authors use the scheme with multi-channel scintillator, in which photons number in every channel at converting to visible radiation is indeed determined by the energy of every electron. But the number of having hit to the channel fast electrons itself is determined by only their longitudinal impulse (both in relativistic and non-relativistic cases). The point is that for hitting of electron to the channel authors use the small-angles deviation of electrons in interspace with magnetic field. But the small angle of deviation (the number of the channel) in this case depends on longitudinal impulse only.

It is not difficult to estimate the Joule heating efficiency. With account of attraction effect the Joule heating, caused by the electrons-ion collisions, increases monotonously with the field growth and in strong fields is determined by the simple relation:

$$Q \approx 4\pi n^2 m v_{osc}^2 \left(2v_{osc} b_{osc}^2 \ln(r_a / b_{osc}) + v b_v b_{osc} \right). \quad (11)$$

That is, in strong fields it is really merely not dependent on the intensity (the latter one only determines the size of the area, occupied by the strong field, and ionization degree) and, consequently, the temperature is determined by the pulse duration only (Fig. 7, a). In particular, we get the temperature of the order of several hundreds of eV indeed for experimental conditions [16].

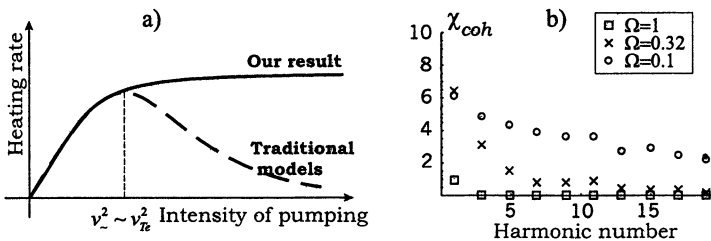


Fig. 7. Qualitative dependence of the heating rate on the pumping intensity (a); the dependence of the coherent radiation cross-section χ_{coh} on radiated harmonic number (b) for different frequencies of the pumping field Ω .

One more group of experiments consists in observation of high harmonics in rare plasma with strong laser field (see review [3]). Authors observe incomprehensibly high intensities of radiation on harmonics (till 11–13) of the basic frequency at intensities of the order 10^{18} W/cm². Though in the beginning they pronounced words about the strong turbulence, but for the last time one suppose, that radiation is caused with harmonics in movement of separate electrons in strong fields (the so called nonlinear emission of free electrons, the nonlinear Thompson scattering). It seems to us, that this point of view is not justified.

Let us dwell in this question circumstantially. Indeed, in such strong fields magnetic wave field becomes significant and every electron in the field of linearly polarized electromagnetic wave moves alongside the so called figure eight curve [13]. That is, relativism is substantial and harmonics in movement of the only electron are large. Nevertheless, in plasma, when on the wave lengths λ there are many electrons (in conditions of experiments $n = 10^{19}$ cm³ and $\lambda^3 \approx 10^{-6}$ cm⁻³) at finding of the current density this effect is suppressed due to modulation of electrons density (relativistic converting of scales). This effect is known [13], but, seemingly, is forgotten for the present time. It is most easily to illustrate it for our case of cold plasma in frames of relativistic hydrodynamics. Really, supposing that the density of drift centers n_0 of oscillating electrons is constant, one has for the density of transverse current in the wave field:

$$j_{\perp} = env_{\perp} . \tag{12}$$

Here $v_{\perp} = e/c A \exp i(\omega t - kx) \cdot (1 - v_x/c)$. It is seen, that because of relativism the spectrum of velocity enriches itself strongly. And what about the current spectrum? From the equation of continuity

$$\frac{\partial n}{\partial t} + \text{div} \mathbf{j} = 0 \tag{13}$$

we have $n = n_0 / (1 - v_x/c)$. That is, the concentration proves to be modulated also. Finally, one has for the density of current

$$j_{\perp} = (e/c) n_0 A \cdot \exp i(\omega t - kx) ! \tag{14}$$

So, harmonics may appear only in orders n/n_{cr} . That is, the intensity of free electrons emission on harmonics is very small.

And what collisions gives? For understanding not only the attraction effect but also the bunching effect (p. 5) are very important. Since we convinced ourselves, that electrons not only attract themselves to the ion but also are bunching on the field phase, it is clear, that they can radiate noticeably on harmonics. On Fig. 7, *b* the dependence of the coherent radiation cross-section χ_{coh} , characterizing the coherent radiation intensity (for more details see [15]), on the harmonic number is represented. This cross-section is the basic characteristics of the coherent component of collisional current.

Note, that in case of isotropic drift distribution function of electrons only odd harmonics are observed. From Fig. 7 one can see, that the coherent radiation should vanish in weak fields ($\Omega \ll 1$) and at high temperatures ($v_{osc} < v$). The most interesting fact is that the radiation should be observed with the same intensity like at the circular polarization of the pumping field.

Conclusions

So, in strong fields in plasma basic energetic processes (Joule heating, fast electrons generation, coherent radiation on harmonics of pumping) become more intense. The basic parameter, determining the term strong field, is

$$1/\Omega = \sqrt[4]{\frac{eE^3}{m^2 Z \omega^4}} \approx 10 \frac{(P/10^{16})^{3/8}}{Z^{1/4}} (\lambda) \gg 1.$$

Here in dimensional estimation power is measured in W/cm^2 and wave length in microns. It is seen, that if in laser range the field for terrawatt lasers is strong only like minimum, than in microwave range the power may be substantially lower.

Important conditions of suitability of the model of pair collisions in strong fields are conditions on pulse duration and plasma concentration. The condition on pulse duration is obtained from the demand, that electron manage to oscillate near the ion proper number of times. So far as only electrons with drift velocities directed perpendicular to the pumping wave field give the basic contribution in all integral characteristics, then it is enough the pulse to be of several periods. Analogous, the condition on plasma density (more exactly the condition on how much plasma is rare) consists in that the interaction volume at collisions to be small in comparison with inter-particles volume ($nV_{int} \ll 1$). Taking into account, that the basic contribution in collisions the transverse scattering gives, and, consequently, $V_{int} \approx b_v^2 \cdot r_{osc}$, for concentration one has the next estimation: $n < 10^{19} T^2 \omega^2 / Z^2 \sqrt{P}$. Here, as everywhere in estimations, the temperature is in eV, frequency is in 10^{15} rad/s, P in 10^{16} W/cm^2 . It is seen, that in microwave range this condition is sufficiently difficult to satisfy. More weak evaluation is obtained for the boundary of correlations effects realization ($r_E \ll r_{de}$). For this it is enough $n_e \ll 9 \cdot 10^{22} T \sqrt{P} / Z^2 \text{ cm}^{-3}$.

One more important question, which we are going to discuss, is why in strong fields one may use the classic description? The matter is [14] that in force of exceptionality of the Coulomb problem of scattering, where differential cross-section both in quantum and classic problems are coincides fully, for suitability of the classic description it is enough, that Debroyl wave length of electron, estimated on oscillatory velocity, to be small in comparison with r_E -dimensional area, from which the scattering occurs. It is easy to see, that with the increase of field this condition becomes more weak: $P \gg 2 \cdot 10^{-6} \omega^4 / Z^2$.

In conclusion we shall notice, that because of the absent of room we have discussed just initial consequences of collisions effects in strong fields. First of all, very important questions about electrodynamic phenomenons in plasma in strong collisions remain beyond the frame. The matter is that plasma in strong field itself is essentially non-equilibrium media and the presence of coherent collisional effects should (and it did exactly) lead to specific dissipative instabilities in such media.

The work has been done due to support of Russian Foundation of Basic Research (grants 01-02-16575, 02-02-06005).

References

1. *Marcuse D.*, Bell. Syst. Tech. J., **41**, 1557 (1962).
2. *Corcum P. B., Burnett M. H., Ivanov M. Y.*, Opt. Lett., **19**, 1 (1994).
3. *Chen S.-Y., Maksimchuk A., Umstadter D.*, Phys. Rev. Lett., **84**, 5528 (2000).
4. *Yudin G. L., Ivanov M. Y.*, Phys. Rev. A, **63**, 033404 (2001).
5. *Dawson J., Oberman G.*, Phys. Fluids, **5**, 517 (1962); *Silin V. P.*, Zh. Eksp. Teor. Fiz., **47**, 2254 (1964) [Sov. Phys. JETP, **20**, 1510 (1965)]; *Shvets G., Fisch N. J.*, Phys. Plasmas, **4**, 428 (1997).
6. *Lifshitz E. M., Pitaevski L. P.*, Physical Kinetics (Pergamon, Oxford, 1981).
7. *Silin V. P.*, Zh. Eksp. Teor. Fiz., **114**, 864 (1998).
8. *Mittleman M. H.* Introduction to the Theory of Laser-Atom Interactions (Plenum Press, New York and London, 1993).
9. *Kroll N. M., Watson K. M.*, Phys. Rev. A, **8**, 804 (1973).
10. *Bunkin F. V., Kazakov A. E., Fedorov M. V.*, Sov. Phys. Uspekhi, **107**, 559 (1973); *Pert G. J.*, Phys. Rev. E, **51**, 4778 (1995).
11. *Koyama K., Saito N., Tanimoto M.* In ICPP 2000, Quebec, Canada, ICPP 4051, page MP1.067 (2000).
12. *Fraiman G. M., Mironov V. A., Balakin A. A.*, Phys. Rev. Lett., **82**, 319 (1999); *Fraiman G. M., Mironov V. A., Balakin A. A.*, Zh. Eksp. Teor. Fiz., **115**, 463 (1999); *Fraiman G. M., Mironov V. A., Balakin A. A.*, Phys. of plasma, **8**, 2502 (2001).
13. *Landau L. D., Lifshitz E. M.* Theory of the field (Nauka, Moscow, 1988).
14. *Landau L. D., Lifshitz E. M.* Quantum mechanics (Nauka, Moscow, 1988).
15. *Fraiman G. M., Mironov V. A., Balakin A. A.*, Zh. Exp. Teor. Fiz., **120**, 797 (2001).
16. *Key M. H., Cable M. D.* et al., Phys. Plasmas, **5**, 1966 (1998); *Hatchet S. P., Brown C. G.* et al., Phys. Plasmas, **7**, 2076 (2000).

CYCLOTRON MASERS IN SPACE

V. Yu. Trakhtengerts, A. G. Demekhov, M. J. Rycroft¹

Institute of Applied Physics, Nizhny Novgorod, Russia

¹CAESAR Consultancy, Cambridge, UK

We review briefly the quasilinear and non-linear physics of cyclotron interactions between whistler mode waves and energetic electrons in space magnetic traps such as geomagnetic flux tubes or solar coronal loops. These interactions can lead to the generation of noise-like emissions or phase-coherent discrete signals in the frequency-time domain. Recent results on improvements in the theoretical understanding of such processes and on new observations of energetic electrons and whistler-mode waves in space are presented.

1. Introduction

It is customary today to call a generator or amplifier of electromagnetic waves a maser (*Microwave Amplification by the Stimulated Emission of Radiation*) if its operation is based on the stimulated emission of distributed oscillators. Electrons and ions, rotating around an ambient magnetic field, are the oscillators in so-called cyclotron masers (CMs).

There are two types of CMs in space, which differ considerably from each other. In the Earth's magnetosphere the first type operates on open field lines in the auroral region at heights between 10^3 and 10^4 km, in plasma cavities where the plasma density is so low that the electron plasma frequency is much smaller than the electron cyclotron frequency. Here auroral kilometric radiation (AKR) is generated by energetic electrons in such a maser system (Fig. 1).

The specific feature of a space gyrotron where AKR is generated is the presence of cold electrons whose number density is comparable with the number density of energetic electrons. A very important aspect of space gyrotrons is the inhomogeneity of both the magnetic field strength and the plasma parameters, the detailed investigation of which is an active field of research today.

The eigenmodes of these auroral CMs are electromagnetic waves with frequencies close to the electron cyclotron frequency; the wave vector \mathbf{k} is almost perpendicular to the geomagnetic field \mathbf{B} . These auroral CMs are rather similar to a family of laboratory devices, termed gyrotrons. The operation of these devices is based on the cyclotron interaction of electrons, moving along a homogeneous

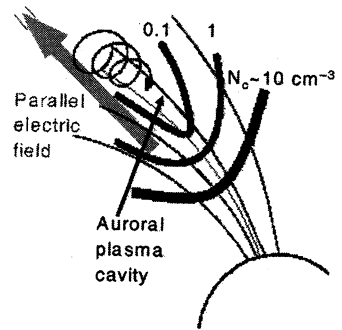


Fig. 1. Generation region of auroral kilometric radiation.

magnetic field through an evacuated region inside a geometrical cavity resonator. A specific feature of a laboratory CM is the cyclotron interaction of a well-organized beam of electrons rotating around a homogeneous magnetic field with a monochromatic electromagnetic wave having a spatially fixed field structure. As a rule, such an electron beam has a very narrow spread in particle energies and pitch-angles. The investigation of such devices has a rich history, beginning with the pioneering paper of Twiss [1] on the cyclotron instability. Very important contributions both to the theoretical development of the subject and to the design and construction of such devices have been made by the Gorky (now Nizhny Novgorod) group of scientists under the leadership of A. V. Gaponov-Grekhov [2]. These generators now find a wide range of applications in the fields of plasma experiments, controlled thermonuclear fusion, radar transmitters and plasma and chemical technology.

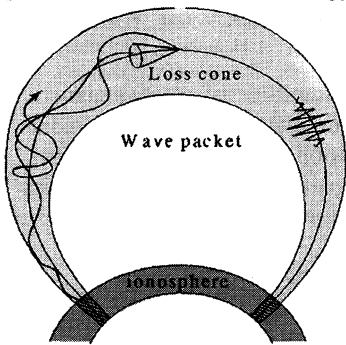


Fig. 2. Whistler and ion-cyclotron masers.

The second type of CMs in space, either electron or ion masers, operate along closed magnetic flux tubes (Fig. 2) filled by a dense cold plasma. For such CMs the electron plasma frequency is greater than the electron gyrofrequency. In the Earth's magnetosphere these CMs function within the plasmasphere and in filaments of dense cold plasma outside (and sometime attached to) the plasmasphere.

Both types of CMs occur widely in natural plasmas – they exist in the magnetospheres of planets, in the solar corona and in the plasma envelopes of active stars. Typical parameters of space CMs are summarized in Table 1.

Table 1. Parameters of space cyclotron masers

	B , Gs	N_c , cm^{-3}	T_c , eV	ω_B , s^{-1}	ω_p , s^{-1}	v_{ei} , s^{-1}	W_h , keV	N_h/N_c	l_{cl} , m	L , m
Earth's magne- tosphere	$5 \cdot 10^{-3}$	10^2	1	$8 \cdot 10^4$	$6 \cdot 10^5$	0	40	10^{-4} – 10^{-5}	10^6	10^7
AKR	0.1	1	1–10	$2 \cdot 10^6$	$6 \cdot 10^4$	0	1–10	0.1–1	10^4	10^4
Solar CM	20	$3 \cdot 10^{10}$	6	$3 \cdot 10^9$	10^{10}	10^5	50	10^{-3}	10^3	10^8

The main focus of this review is on CMs of the second type. They are large scale features of the planetary magnetospheres. Via single or multi-hop wave propagation and amplification along geomagnetic flux tubes, they determine the population (energy spectrum and pitch-angle distribution) of energetic charged

particles distributed in space around the Earth. In other cosmic plasmas with closed (dipole like) magnetic field lines, they can crucially influence the properties of energetic charged particles there too.

In many laboratory experiments, magnetic mirrors are produced by additional magnetic fields due to current-carrying coils at the ends of the device. In a planetary magnetosphere or for a magnetic loop reaching into the solar corona, the trap is caused by the dipole like geometry of the magnetic field. Such a magnetic trap, containing dense plasma, serves as a CM cavity, the high-energy fraction of which is the active substance for the CM. The ends of the magnetic flux tube, immersed in the planetary ionosphere, serve as mirrors for the electromagnetic waves. The eigenmodes in space CMs are whistler or Alfvén waves, which possess one very important property; they are guided by the magnetic field. The situation is similar to that in fiber optics when light is guided by dielectric filaments. Cyclotron resonance occurs when the electric field of a circularly polarized wave propagating through the plasma exactly matches the Doppler-shifted cyclotron motion of a charged particle. It takes place when the Doppler-shifted wave frequency coincides with the particle gyrofrequency, and can occur either for whistler mode waves and energetic electrons, or for Alfvén (hydrodynamic) waves and energetic ions.

CM operation is based on the cyclotron instability (CI), which is due to the transverse anisotropy of the charge particle distribution function; this exists when the effective temperature transverse to the magnetic field direction, T_{\perp} , exceeds the longitudinal temperature, T_{\parallel} (the anisotropy factor $\alpha = T_{\perp} / T_{\parallel}$ is greater than unity). It is important to recognize that this anisotropy, with $\alpha > 1$, is a natural feature of adiabatic traps, because of the existence of the loss cone. This is the region in pitch-angle space with values near zero, where the energetic charged particles are lost through the ends of the magnetic trap by collision with atoms or molecules of the upper atmosphere. There are many other causes of the transverse anisotropy of energetic charged particles in space, such as magnetic compression, charge particle transport within planetary magnetospheres, acceleration by global electric fields, stochastic acceleration mechanisms, and so on. Most sources supply energetic particles with a wide spread of energies and pitch-angles. In space, as we shall see, the inhomogeneous magnetic field and broad range of energies and pitch-angles radically change the wave-particle interaction process from the laboratory case with its well-organized beam and monochromatic wave.

The theory of such space CMs, operating via a magnetic trap, was developed in relation to two geophysical phenomena, namely natural ELF (from 0.3 to 3 kHz) and VLF (from 3 to 30 kHz) electromagnetic emissions [3] and the Earth's radiation belts [4]. Early estimates showed that the intensity of ELF/VLF emissions was very much higher than the intensity of thermal equilibrium emission from the Van Allen radiation belt electrons. The idea of quantitatively connecting these audio frequency radio emissions with the cyclotron instability (CI)

of radiation belt electrons first appeared in 1963 (see below). The subject has been actively developed in the succeeding four decades.

ELF/VLF emissions observed on the ground and in space alike include both broadband noise-like electromagnetic emissions, such as hiss and quasi-periodic noise bursts, and narrowband, or discrete, emissions having a quasi-monochromatic structure. Among these are natural signals, such as successions of rising frequency tones named chorus, and whistlers generated by lightning discharges, as well as man-made signals from VLF transmitters propagating in the whistler mode, and triggered VLF emissions from both natural and man-made signals.

The CM theory to explain such observations developed in two practically independent directions. The first of these is based on a quasi-linear (QL) theory of gyroresonant wave-particle interactions, which is valid for noise-like emissions, when the electromagnetic field can be considered to be the sum of independent wave packets with stochastic phases and a broad frequency spectrum. This radiation interacts with the energetic particles as it does with particles in many energy level systems. In such a situation the mathematical description of CM operation is very similar to the balance approach applied to quantum generators [5]. In particular, as with quantum generators, the fundamental generation regime in CMs is a relaxation oscillation, when both the wave intensity and particle flux are modulated with a period depending on the properties of both the particle source and the wave and particle sinks. The bandwidth of the oscillation, and hence the quality factor, also depend on these source and sink properties. This is the basis of many other wave generation regimes of CMs (e.g., periodic, spike-like and stochastic). It leads to explanation of the different modulation phenomena in natural electromagnetic emissions and energetic charged particle dynamics.

The first fundamental papers in the QL direction were published by Trakhtengerts [6], Brice [7, 8], Andronov and Trakhtengerts [9], and Kennel and Petschek [10]. These studies were based on the classical plasma physics of Sagdeev and Shafranov [11], Zheleznyakov [12], Drummond and Pines [13], Vedenov, Velikhov and Sagdeev [14]. Important contributions to the development of this theory in the Earth's magnetosphere were carried out by Trakhtengerts [15, 16], Kennel [17], Gendrin [18], Tverskoi [19], Cornwall, Coroniti and Thorne [20], Coroniti and Kennel [21], Roux and Solomon [22], Lyons, Thorne and Kennel [23], Schulz and Lanzerotti [24]. The monograph by Bespalov and Trakhtengerts [25] partly summarizes the state of QL theory.

The second direction develops a nonlinear theory of monochromatic wave particle interactions, generalizing for the case of an inhomogeneous magnetic field. Here the first paper specifically considering space (magnetospheric) plasmas was that of Dungey [26]. New experimental results from the VLF transmitters at Russia and at Siple station, Antarctica, stimulating development of the nonlinear theory, were published over a period of more than 25 years from 1967; for a review, see Molchanov [27], and Helliwell [28]. The key idea about second-

order cyclotron resonance as a generation mechanism for discrete VLF emissions in the magnetosphere was first formulated by Helliwell [29]. Important and original contributions to quantitative developments of this nonlinear theory were made by Dysthe [30], Nunn [31, 32], Sudan and Ott [33], Budko et al. [34], Helliwell and Crystal [35], Karpman et al. [36], Matsumoto et al. [37], Roux and Pellat [38], Sagdeev et al. [39] and others. These theories are somewhat similar to those of laboratory CMs in the case of a homogeneous magnetic field, but have very important novel features when the magnetic field is inhomogeneous.

Both directions – quasilinear theory and nonlinear theory for monochromatic waves – lead to explanations of certain phenomena, noise-like emissions in the first case and triggered emissions in the second. Natural electromagnetic phenomena, produced by CM operation and observed on the ground or in space, reveal the very interesting phenomenon that noise-like emissions may sometime become quasimonochromatic signals, or vice versa. Thus, in some sense, disorder produces order. The modern theory of a CM enables such a change to be understood. This transition can be due to the appearance of a step deformation on the distribution function at a certain velocity, when energetic particles interact with noise-like emission. So, starting from noise-like emissions, we come to the situation when it is necessary to use the theory of monochromatic wave interaction with a specific particle distribution, taking phase effects into account. The very interesting backward wave oscillator (BWO) generation regime can then be realized; wave reflection and positive feedback are organized in a BWO generation regime via a particle beam whose specific properties are prepared by the noise-like emission.

Below we present a more detailed description of the theoretical models for space CM operation and discuss some results and perspectives of their laboratory modeling.

2. The basis of cyclotron wave-particle interactions

The cyclotron resonance condition forms the basis of cyclotron wave-particle interactions:

$$\omega - \omega_B = kv_{\parallel}, \quad (1)$$

where ω and \mathbf{k} are the frequency and wave vector of the whistler waves, $k = |\mathbf{k}|$, ω_B is the electron gyrofrequency, and v_{\parallel} is the field-aligned component of the electron velocity. Further, the case of ducted whistler propagation is considered, when $\mathbf{k} \parallel \mathbf{B}$, \mathbf{B} being the vector geomagnetic field. In an inhomogeneous magnetic field, ω_B , v_{\parallel} and k are functions of the coordinate z along the magnetic field \mathbf{B} . In accordance with (1) the electrons with different v_{\parallel} interact with a given wave (ω , k) at different points along the magnetic field line. Electrons with parallel velocities

$$|v_{\parallel}| < v_{\min} \equiv (\omega_{BL} - \omega_{\max}) / k_{\max}, \quad (2)$$

do not interact with whistler mode waves; here $\omega_{BL} = \omega_B(z=0)$ is the gyrofrequency at the equatorial crossing of the magnetic flux tube whose McIlwain parameter is L , ω_{\max} is the maximum frequency in the spectrum of whistler waves, $k_{\max} = k_L(\omega_{\max}, z=0)$. For the whistler cyclotron instability the spectrum of unstable waves goes up to a maximum value

$$\omega_{\max} = (1 - \alpha^{-1}) \omega_{BL}, \quad (3)$$

where $\alpha = T_{\perp}/T_{\parallel}$ is the transverse anisotropy of the electron distribution function, T_{\perp} and T_{\parallel} are the mean energies of energetic electrons across (T_{\perp}) and along (T_{\parallel}) the magnetic field line. The cyclotron instability ($\gamma > 0$) takes place at the frequencies $\omega < \omega_{\max}$ (3). The growth rate reaches a maximum value at ω_{opt} and after that decreases toward low frequencies due to the decrease of the number of resonant electrons. In the case of a Maxwell distribution function with a temperature anisotropy, this number is proportional to $\exp[-mv_{RL}^2/(2T_{\parallel})]$, where m is the mass of the electron, and the resonance velocity $v_{RL} = (\omega - \omega_{BL})/k_L$. In a sufficiently dense cold plasma the maximum value of γ is reached at the equator, and equals [40]

$$\gamma_{\max} = 0.2(\alpha - 1) \frac{n_{HL}}{n_{cL}} \omega_{BL}. \quad (4)$$

The corresponding optimum frequency for growth, ω_{opt} , does not depend on the anisotropy coefficient α and is actually determined from the relation $[mv_{RL}^2/(2T_{\parallel})]_{\text{opt}} \sim 1$. That gives

$$\omega_{\text{opt}} \approx \omega_{BL} / \beta_*, \quad \beta_* = \frac{16\pi n_{cL} T_{\parallel}}{H_L^2} \quad (\text{in C.G.S. units}), \quad (5)$$

where n_{HL} and n_{cL} are the densities of the hot and cold plasma components in the equatorial cross-section of the magnetic flux tube, specified by L . In the dense cold plasma, $\beta_* \gg 1$, and pitch-angle diffusion prevails. In the case $\beta_* < 1$, the interval (2) actually includes all energetic electrons, and the cyclotron instability becomes ineffective. In the Earth's magnetosphere the condition $\beta_* > 1$ is fulfilled inside the plasmasphere and in detached cold plasma regions.

Let us consider a quantitative example. For that we choose the L -value $L = 4$, and the typical anisotropy $\alpha = 3/2$. For a dipole geomagnetic field we find $B_L \equiv 500 \gamma$ ($1 \gamma = 1 \text{ nT} = 10^{-5} \text{ Gs}$) and $\omega_{HL}/2\pi \approx 12.5 \text{ kHz}$. Putting $T_{\parallel} = 20 \text{ keV}$, and $n_{cL} = 2 \cdot 10^2 \text{ cm}^{-3}$ one obtains $\beta_* \approx 7.7$ and $f_{\text{opt}} = \omega_{\text{opt}}/2\pi \approx 1.7 \text{ kHz}$. This is a typical frequency for VLF/ELF hiss on this L -shell [3, 44]. For moderate magnetic activity we take the flux density of trapped electrons $S_L \approx 2 \cdot 10^7 \text{ cm}^{-2} \text{ s}^{-1}$ [57], which corresponds to $n_{HL} \approx 3 \cdot 10^{-3} \text{ cm}^{-3}$. The growth rate (4) under these parameters is $\gamma_{\max} \approx 0.1 \text{ s}^{-1}$. The important characteristic of the cyclotron instabil-

ity is the one-hop amplification $\Gamma \approx 2\gamma l/V_{gL}$, where V_{gL} is the group velocity of whistler mode waves. In our example $\Gamma \approx 0.12$.

The quantitative description of cyclotron electron-whistler interactions, including nonlinear effects, is based on the self-consistent system of equations for the wave field and for the distribution function of energetic electrons. The equation for the slowly varying magnetic field complex amplitude b with frequency ω and wave vector $\mathbf{k} \parallel \mathbf{H}$ can be written as

$$\left(\frac{\partial}{\partial t} + V_g \frac{\partial}{\partial z} \right) b = \frac{2\pi V_g}{c} J_R, \quad (6)$$

where V_g is the wave group velocity, J_R is the current of resonant electrons, obeying (1), which has the form:

$$J_R = -e \int_0^\infty \int_{-\infty}^\infty \int_0^{2\pi} u_\perp^2 F e^{i(\varphi - \psi)} d\varphi dv_\parallel du_\perp, \quad (7)$$

where $v_\perp = u_\perp e^{i\varphi}$ and v_\parallel are velocity components across and along the magnetic field \mathbf{B} , ψ is the contribution to the whistler phase, which is related to the current of cold plasma, $\partial\psi/\partial t = -\omega$, $\partial\psi/\partial z = \mathbf{k}$; ω and \mathbf{k} are connected by the well-known dispersion relation: $k = (\omega_p/c)\omega^{1/2}(\omega_B - \omega)^{-1/2}$, where ω_p is the electron plasma frequency.

The distribution function in (7) should be found from the collisionless kinetic equation; this is equivalent to solving the nonlinear equation of motion for an energetic electron. Sometimes (for an analysis of the linear stage of the cyclotron instability and for a quasilinear approach) it is convenient to present the distribution function F in the form of a Taylor series:

$$F = \bar{F} + \frac{\partial F}{\partial v^2} \Delta v^2 + \frac{\partial F}{\partial \mu} \Delta \mu + \dots, \quad (8)$$

where \bar{F} is the slowly varying part of F , Δv^2 and $\Delta \mu$ are given by the solution of the charged particle's equation of motion, v is the modulus of the velocity, $\mu = \sin^2\vartheta B(z)/B_L$, and ϑ is the pitch-angle (the angle between velocity \mathbf{v} and magnetic field \mathbf{B}). Further, we shall use equations (6)–(8) for a description of the different cases of cyclotron whistler-electron interactions.

3. Quasilinear approach

We shall start from the quasilinear description of whistler-electron interactions, which is valid for noise-like electromagnetic emissions and a smooth velocity dependence of the averaged-over-a-wave-period distribution function \bar{F} . ELF/VLF noise-like emissions, so called hiss, are actually observed in the magnetosphere and they are the subject of our considerations in this section.

In the case of a smooth distribution function \bar{F} we can use the presentation of a full distribution function F in the form (8). In the quasilinear approach the iteration procedure uses (8) and averages over the phases of waves to give the diffusion equation for \bar{F} , which takes wave-particle interactions into account [40, 41]. The substitution of (8) into the field equation (6) permits us to obtain the wave energy transfer equation in a standard form with the growth rate γ , which depends on \bar{F} (see below, (10)).

This system of quasilinear equations is rather complicated, especially if we take into account the magnetic field inhomogeneity in the real system. We use some simplifications, which are based on the following considerations. First, it is possible to average the initial equations for the electron distribution function \bar{F} and the spectral energy density ϵ_ω of whistler waves over the period of the oscillations of particles and waves between reflection points, taking into account a small change of \bar{F} and ϵ_ω on these time scales (see the quantitative example, given in Section 2). Secondly, we consider the case of a sufficiently dense cold plasma, when $\omega_{\text{opt}} \ll \omega_{BL}$, and only pitch-angle diffusion has to be taken into account. Details of the calculations can be found in [40, 41]. The resulting system of quasilinear equations takes the form (omitting the bar over the \bar{F}):

$$\frac{\partial F}{\partial t} + \mathbf{V}_{DL} \frac{\partial F}{\partial \mathbf{r}} = \frac{1}{T_b} \frac{\partial}{\partial \mu} \mu D \frac{\partial F}{\partial \mu} + I - \delta F, \quad (9)$$

$$\frac{\partial \epsilon_\omega}{\partial t} + \mathbf{V}_{g\perp} \frac{\partial \epsilon_\omega}{\partial \mathbf{r}} = (\gamma - \nu) \epsilon_\omega, \quad (10)$$

where F is the distribution function of energetic electrons averaged over the period of the electron oscillations between magnetic mirror points $T_b = \oint dz/v_{\parallel}$, ϵ_ω is the spectral energy density averaged over the period of wave packet oscillations between ionospheric mirrors $T_g = \oint dz/v_g$, \mathbf{r} is the radius vector of the equatorial cross-section of the particular flux tube in the magnetosphere, \mathbf{V}_{DL} and $\mathbf{V}_{g\perp}$ are the drift and group velocity components in this cross-section, respectively, I is the energetic particle source, and the term δF describes the electron losses through the loss cone:

$$\delta = \begin{cases} \nu/l & 0 \leq \mu \leq \mu_c, \\ 0 & \mu > \mu_c, \end{cases} \quad (11)$$

where $\mu_c = B_l/B_0$ specifies the loss-cone boundary, B_0 is the magnetic field at the foot of the flux tube on the Earth's surface, and ν characterizes the wave losses in the ionosphere:

$$\nu = |\ln R|/T_g, \quad (12)$$

where R is the reflection coefficient of a downcoming whistler mode wave.

The self-consistent character of this system of equations is determined by the dependence of the diffusion coefficient on ϵ_ω and the growth rate γ on F ; these are:

$$D = \int K(\mu, \nu, \omega) \epsilon_\omega d\omega, \quad (13)$$

$$\gamma = \int G(\mu, \nu, \omega) \left(\frac{\partial F}{\partial \mu} - \frac{\omega}{\omega_{BL}} F \right) \nu^3 d\nu d\mu, \quad (14)$$

where K and G are known functions of the arguments, and the integration limits depend (in the general case) on μ and ν for D and on ω for γ [40]. In the case of a sufficiently dense cold plasma, these dependencies can be neglected.

On the basis of the system of equations (9)–(10), the formation of the electron precipitation pattern can be considered during the main phase of a magnetic storm. This phase is accompanied by the injection of energetic particles on the night side of the magnetosphere and their drift to the morning (electrons) and evening (proton) sides. At the same time erosion of the plasmasphere takes place, with the formation of an extended tongue of dense cold plasma, as shown in Fig. 3. Precipitation occurs where the energetic particles come into contact with the plasmapause or detached plasma region. In the case of electrons there are two such zones: one is on the morning side, and the other in the afternoon. This process of cyclotron whistler-electron interactions, when energetic particles come into a region with enhanced cold plasma density during their magnetic drift in longitude, can be described quantitatively on the basis of the stationary system ($\partial/\partial t = 0$) in (9)–(10). Such a solution was obtained in [42, 43], which permitted the authors to explain quantitatively many peculiarities of the electron precipitation pattern during the main phase of a magnetic storm.

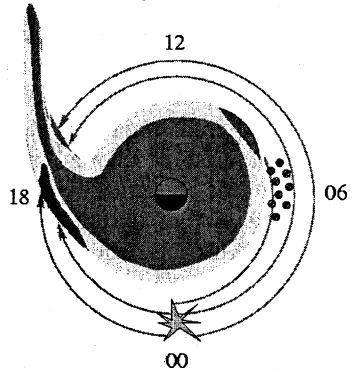


Fig. 3. Precipitation zones of energetic particles in the Earth magnetosphere. Ions and electrons drift westward and eastward, respectively.

4. Generation of discrete emissions

There are two major groups of discrete ELF/VLF emissions – triggered emissions and chorus. As a rule, triggered VLF emissions have a definite source, which is a quasimonochromatic whistler packet, generated either by a ground-based VLF transmitter or a lightning discharge. Triggered signals are classified by their spectral forms and can be risers, fallers or hooks. Chorus are perhaps the

most mysterious ELF/VLF emissions in the magnetosphere [45], with no obvious source and consisting of a succession of rising tones. The period here can be much less than the bounce period of energetic electrons between magnetic mirror points or the period equal to the group delay of the whistler signal between conjugate ionospheres. The characteristics of these signals – a narrow dynamic spectrum, a very large growth rate, and a succession of similar signals – cannot be explained in the frame of quasilinear theory, which has been used in the previous section in relation to hiss emissions. It is clear that discrete emissions must be generated by well-organized beams of electrons. In the case of triggered VLF emissions, such beams appear as a consequence of electron acceleration in the field of a quasimonochromatic whistler wave. In this case a well-organized, bunched electron beam with a delta-function distribution over the field-aligned velocity component v_{\parallel} appears at the back edge of a whistler wave packet. Moving in the inhomogeneous magnetic field this beam generates the secondary whistler wavelet, and the task of theory is to explain the intensity and the frequency spectrum of this wavelet.

In the case of chorus emission the situation is more complicated: visible causes for the appearance of well-organized electron beams and for the formation of a succession of separate elements are absent. The frequently close connection of chorus with hiss, which serves as a lower-frequency background for the chorus elements, indicates that hiss plays an important role in chorus generation. Indeed, the calculations in [46] showed that a singularity in the form of the step on the distribution function of energetic electrons is formed during the process of cyclotron instability development. This step serves as a boundary in velocity space between resonant and nonresonant electrons. When the nonresonant region is small, as is so in a sufficiently dense cold plasma, this singularity can be neglected and we deal with hiss generation. In the opposite case the steepening of a step leads to a major change of the cyclotron instability, which moves into a hydrodynamic stage, when phase effects are very important. Qualitatively the sharp step behaves as a delta-function: a discrete emission is generated and a new, so-called backward wave oscillator (BWO) generation regime [47] is realized, which can explain the succession of chorus elements (see below).

A quantitative approach to these problems is based on the same system of equations (6)–(7), but in this case phase effects leading to a bunching of the electrons must be taken into account; the quasilinear approach, based on phase mixing, is clearly not valid. In the general case the system of equations (6)–(7) is very complicated. Under certain assumptions they are used in computer simulations. Further, we shall review some general analytical results, which follow from an analysis of the system of equations (6)–(7). They include two principal aspects. The first is the second order cyclotron resonance condition, which determines the frequency spectrum of the discrete emission, generated by the electron beam in the inhomogeneous magnetic field. The second is the transition of the cyclotron instability to the BWO generation regime, which corresponds to the

absolute instability development (without mirrors for waves) and which is very important for chorus generation.

5. Second order cyclotron resonance effects and the generation of triggered VLF emissions

We start from the linear problem of whistler wavelet generation in an inhomogeneous magnetic field by an electron beam whose velocity component along the magnetic field $V_*(z, t)$ is a known function of z and t (z is the coordinate along the magnetic field and t is time). By a wavelet we mean that the whistler frequency is changing with time and position coordinate. Such a formulation corresponds, for example, to the generation of a triggered emission by a well organized electron beam, ejected from the back edge of a pump whistler packet, in the case when the secondary emission does not really influence the beam velocity. Further we take the initial distribution function of beam particles over v_{\parallel} in the form of a step. The calculations show [52] that in the case of a δ -function the results are similar. We discuss the difference between the δ -function and step-function later in this section.

Substitution of the step-function instead of $F(W, I, t)$ into equations (6)–(7) gives us the following system of equations for the wave magnetic field complex amplitude b and the resonant current [53]:

$$\left(\frac{\partial b}{\partial t} - V_g \frac{\partial b}{\partial z} \right) = \alpha_1 (j + j_0), \quad (15)$$

$$\left(\frac{\partial j}{\partial t} + V_*(z, t) \frac{\partial j}{\partial z} \right) = \alpha_2 b + i\Delta \cdot j, \quad (16)$$

where $j = JB^{-3/2}$, $J_0 = B^{3/2}j_0$ is the current of phase-bunched electrons, produced by the initial wave, $\Delta = \omega + kV_* - \omega_B$, V_* is the velocity of the step, $\alpha_1 = (2\pi V_g/c)B^{3/2}$, and the coefficient α_2 is given in [53]. For a wavelet of relatively small amplitude it is possible to write the solution of equations (15)–(16) in integral form:

$$b(\xi, \eta) = \alpha_1 \int_{\eta}^{\xi} j_0(\xi', \eta) \exp[\Gamma(\xi', \xi, \eta)] d\xi', \quad (17)$$

where

$$\text{Re}\Gamma(\xi', \xi, \eta) = \alpha_1 \alpha_2 \int_{\xi' \eta_0(\xi')}^{\xi} \int_{\eta}^{\eta} \cos \left(\int_{\eta'}^{\eta} \Phi(\eta'', \xi') d\eta'' \right) d\eta' d\xi', \quad (18)$$

is the amplification, $\Phi = (V_g/(V_g + V_*)) \Delta$, and the variables ξ and η are connected with z and t by the relations:

$$\eta = t + \int_{z_0}^z \frac{dz'}{V_g(z')}, \quad \xi = \int_{z_0}^z \frac{dz'}{V_*(z')} - t. \quad (19)$$

In the solution of (17) the frequency of the wavelet generated is a function of η and defined from the condition of the maximum value of $|b(\xi, \eta)|$. The integration in (17) can be performed with the help of the stationary phase method (see [53]), and the evaluation of $\max|b|$ actually gives us the second order cyclotron resonance condition, which can be written as:

$$\frac{\partial}{\partial \xi} [\omega(\eta) + k(\xi, \eta)V_*(\xi) - \omega_B(\xi, \eta)] = 0. \quad (20)$$

This condition must be fulfilled together with the first order cyclotron resonance condition (1). The relations (1) and (20) therefore determine the dynamic spectrum $\omega(z, t)$ of the discrete emission. Calculations show that the second order cyclotron resonance condition (20) is the same in both cases of a step-function and a δ -function, but the maximum values of $|b|$ are different. In the paper [53] some examples of fallers and risers obtained on the basis of (19)–(20) are given. These signals can be generated by electron beams, which are produced by long and short whistler pulses respectively.

In the above estimations of the spectral form of the secondary whistler wavelets we did not take into account the nonlinear change of the beam velocity under the influence of the emitted waves. In the frame of our approach this could be taken into consideration by adding the energy conservation law to equations (19)–(20) in order to describe the slow change of the beam velocity under the action of the waves.

In another limiting case, when a nonlinear change of the beam velocity prevails, it is possible to derive the second order cyclotron resonance condition from the nonlinear equations, describing the motion of a single electron in the inhomogeneous magnetic field in the presence of a whistler wavelet, as was done in [32, 54, 55, 56]. The maximum energy exchange between the wavelet and the electrons takes place under the condition [55]

$$|S| = \frac{1}{2\Omega_{ir}^2} \left| \left(3V_R - \frac{kV_{\perp}^2}{\omega_B} \right) \frac{\partial \omega_B}{\partial z} - \frac{2\omega + \omega_B}{\omega} \frac{d\omega_B}{dt} \right| \sim 0.2 - 0.8, \quad (21)$$

where $V_R = (\omega - \omega_B)/k$ is the cyclotron resonance velocity from (1), and Ω_{ir} is related to the magnetic wave amplitude b by

$$\Omega_{ir} = \left(kV_{\perp} \frac{eb}{mc} \right)^{1/2}. \quad (22)$$

When the initial beam velocity is constant (i.e. it does not depend on z and t) the condition (21) corresponds to the maximum value of the nonlinear wavelet amplification; it determines the dependence of ω on z and t (together with (1)). Ac-

tually, the relation (21) corresponds to the second order resonant condition in the other limit, when the nonlinear change of the beam velocity prevails.

6. Generation of chorus emissions

As was noted above, in the case of chorus we have no obvious source of a well-organized electron beam, which is necessary for the generation of discrete emissions.

The solution of this problem seems to lie in some features of the quasilinear relaxation of the cyclotron instability, which lead to the appearance of singularities on the electron distribution function, in particular, a step-like deformation. Figure 4 shows the results of a computer simulation of the nonstationary system of equations (9)–(10), when $\partial/\partial \mathbf{r} = 0$. The formation of a step on the distribution function F during the development of the cyclotron instability is clearly seen, together with a sharp increase of the growth rate and the wave intensity.

On the morning side of the magnetosphere, the cold plasma gradient at the plasmapause is generally rather smooth or the plasmasphere may be somewhat irregular in structure. In this case the number of nonresonant electrons is not small and the role of the step-like deformation of the distribution function can be very important. It leads to a crucial change of the character of the cyclotron instability and to the appearance of a new generation regime with discrete emissions.

Some quantitative results on chorus generation by the electron beam with a step-like distribution function can be obtained from the system of equations (15)–(16). In the case of chorus generation, the external current j_0 is absent (an initial whistler wave of large amplitude is absent) and secondary whistler waves grow from spontaneous noise. In comparison with the previous case of a triggered emission, we consider now the more common case when the beam density can be large and, generally speaking, the solution (17) is not valid.

The solution of the system of equations (15)–(16) in the case when Δ depends on z is rather complicated. Following [47] we shall consider the simplified homogeneous length-

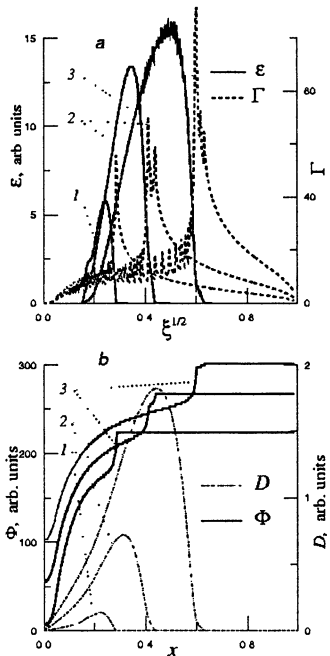


Fig. 4. The dependences of the gain Γ and the whistler energy density ϵ on the sine x of the equatorial pitch angle at different times (from [46]).

limited model. The length l of this system is determined from the phase mismatching condition:

$$\int_{-l/2}^{l/2} \frac{|\Delta|}{V_{\max}} dz \equiv \int_{-l/2}^{l/2} \frac{|\omega_B - \omega - kV_m|}{V_{\max}} dz \leq \frac{\pi}{2}, \quad (23)$$

where V_m is the velocity of the step and $\omega_B - \omega - kV_m = 0$ at the equator, $z = 0$. In the case of a dipole magnetic field we obtain from (22) (see [29, 47]):

$$l = (R_0^2 L^2 / k)^{1/3}, \quad (24)$$

where R_0 is the Earth radius, and L is the parameter of a geomagnetic shell. In such a formulation we are actually dealing with a Backward Wave Oscillator (BWO) of length l , in which the phase (and group) velocity of the whistler waves is directed against the beam (step) velocity. The difference between a classical

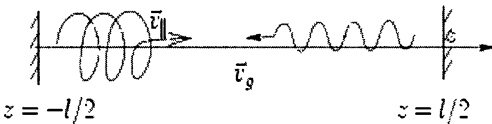


Fig. 5. Scheme of backward wave oscillator

laboratory BWO device and the magnetospheric BWO generator is in the different distributions of energetic electrons over velocity – a δ -function in laboratory devices and a step-function in the magnetospheric BWO.

The linear stage of the BWO generation regime in the case of a step-function is described by the system of equations (15)–(16), where in our approximation $j_0 = 0$, $\Delta = \text{constant}$, and the interaction region is $\Delta z \leq l$ (Fig. 5). So we have:

$$\frac{\partial b}{\partial t} + V_g \frac{\partial b}{\partial z} = \alpha_1 j, \quad (25)$$

$$\frac{\partial j}{\partial t} - V_{\max} \frac{\partial j}{\partial z} - i\Delta \cdot j = \alpha_2 b. \quad (26)$$

The system of equations (25)–(26) should be solved with the following boundary conditions:

$$\begin{aligned} z = l/2: & \quad b = b_{ext}, \quad j = 0, \quad R = 0; \\ z = -l/2: & \quad b = b_{ent}, \quad R = 0, \end{aligned} \quad (27)$$

where $b_{ent(ext)}$ is the wave amplitude at the entrance (or exit) of the interaction region, and R is the wave reflection coefficient in the ionosphere. The BWO generation regime corresponds to the transition in the system (25)–(27) to the absolute instability, when the amplification coefficient $\Gamma = b_{ext}/b_{ent}$ goes to infinity. Actually, the equation $\Gamma^{-1} = 0$ determines the transition to the BWO generation.

Putting $b, j \sim \exp(-i\Omega t)$, it is easy to find the threshold and the growth rate γ_{BWO} of the absolute instability, corresponding to BWO generation. In the optimal conditions, $\Delta = 0$, and we have from the condition $\Gamma^{-1} = 0$:

$$\gamma_{\text{BWO}} = \frac{ql}{4} (V_g^{-1} + V_{\text{max}}^{-1})^{-1} (1 - q_{\text{thr}}/q), \quad (28)$$

where $q = p\omega_{BL}/(V_g V_{\text{max}})\gamma_0$, p is the step height, $q_{\text{thr}}^{1/2} = \pi/2l$, and γ_0 is the growth rate (4) for the smooth distribution function. In conditions when $(q_{\text{thr}}/q)^{1/2} \cong 0.5$ and $1 - q_{\text{thr}}/q \cong 0.25$, the ratio

$$\frac{\gamma_{\text{BWO}}}{\gamma_0} \sim \frac{3p\omega_{BL}l}{16(V_{\text{max}} + V_g)}. \quad (29)$$

We now make some quantitative estimates. We take the same parameters as in Section 2: $L = 4$, $n_{cL} = 2 \cdot 10^2 \text{ cm}^{-3}$, and $\beta_* \cong 7.7$. In this case $k \cong 1 \text{ km}^{-1}$ and the interaction region length $l \cong 10^3 \text{ km}$. In the case $\omega \ll \omega_{BL}$ we have $V_g \cong 2\omega/k$, $V_{\text{max}} \cong \omega_{BL}/k$ and $q \cong (pk^2/\omega)\gamma_0$. Putting $p = 0.3$, $\omega = 10^4 \text{ s}^{-1}$ and $\gamma_0 = 0.1$ we find $q \cong 3 \cdot 10^{-6} \text{ km}^{-2}$ and $q^{-1/2} \cong 1.7 \cdot 10^{-3} \text{ km}^{-1}$. On the other hand $q_{\text{thr}}^{1/2} = \pi/2l \cong 1.57 \cdot 10^{-3} \text{ km}^{-1}$, that is the BWO threshold is achieved for $\gamma_0 \cong 0.1$, which corresponds to the electron flux density $S_L \sim 2 \cdot 10^7 \text{ cm}^{-2} \text{ s}^{-1}$. If we take $(q_{\text{thr}}/q)^{1/2} \cong 2$, we find from (28)–(29) that $\gamma_{\text{BWO}} \sim 40 \text{ s}^{-1}$ and $\gamma_{\text{BWO}}/\gamma_0 \sim 10^2$. Thus the transition to the BWO generation regime is quite possible.

We shall now consider some qualitative effects which follow from the similarity of the physical process in laboratory BWO devices and in the magnetospheric BWO generator. According to [58] the generation regime in a laboratory BWO device becomes periodic when the parameter q reaches some bifurcation value: $q_p^{1/2} \approx 2q_{\text{thr}}^{1/2}$. We can expect a similar bifurcation in our magnetospheric case. The periodic regime means that the generation of waves takes place in the form of a succession of separate pulses, with the succession period being equal to [58, 59]:

$$T_M \approx 1.5l (V_g^{-1} + V_{\text{max}}^{-1}), \quad (30)$$

where l is determined by the relation (24). The magnetic field b of the waves can be estimated from (22), if we use the relation, which follows from the analysis of the absolute instability [60],

$$\frac{\Omega_{\text{tr}}}{\gamma_{\text{BWO}}} \approx \frac{32}{3\pi}. \quad (31)$$

Here γ_{BWO} is determined from (28) under the condition that $(q_{\text{thr}}/q)^{1/2} = 2$, which corresponds to the threshold for the periodic BWO regime.

Now it is possible to summarize this theoretical model of chorus generation as follows. Energetic electrons drift into the generation region (a detached cold

plasma region or the plasmopause) in the process of their magnetic drift in longitude. After that the cyclotron instability switches on and quasilinear relaxation begins, which prepares the transition to the BWO generation regime. According to [59] the duration of this stage is $\tau_{QL} \sim 3$ to 10 s. That is in accordance with the supermodulation period of chorus intensity, which is seen in experimental observations [45]. After the formation of a step-like deformation on the distribution function the fast stage of chorus generation occurs, with a total duration on the local magnetic flux tube $\Delta t > T_b$. The period between successive chorus elements is determined by (30) and, for our example ($L = 4$, $V_g = 2 \cdot 10^4$ cm/s), is equal to $T_M \sim 0.1$ s. The chorus magnetic field amplitude b can be estimated from (31) and (28). In the case $\omega/\omega_{BL} = 0.3$, $(q_{thr}/q)^{1/2} = 2$ (the threshold for the periodic regime), $\gamma_{BWO} \sim 50$ s $^{-1}$ and $b \sim 2$ m γ . All these values for T_M , b , and γ_{BWO} are in satisfactory agreement with experiment. More detailed comparison with experimental data can be found in the paper [59].

7. CM in the solar corona

An important specific feature of the solar corona is the presence of magnetic field-aligned filaments, called prominences, with a very dense and cold background plasma. The processes related to solar activity lead to filling these filaments with energetic charged particles. The most popular mechanism of charged particle acceleration in the solar chromosphere and corona is the magnetic reconnection and magnetic compression, which, under the conditions in the solar corona, can be accompanied with further cooling of background plasma [62]. Such dense and cold plasma determines high threshold of CI in solar magnetic loops due to the damping of whistler waves related to electron-ion collisions. This threshold can be written as [61]

$$\gamma_{CI} \approx 0.2(\alpha - 1) \frac{n_{hL}}{n_{cL}} \omega_{BL} \geq \frac{\omega}{\omega_{BL}} \nu_{ei}. \quad (32)$$

Here γ_{CI} is the CI growth rate (4), the collision frequency ν_{ei} is equal to

$$\nu_{ei} \approx 50 n_{cL} T_e^{-3/2}, \quad (33)$$

where n_{cL} and T_e should be measured in cm $^{-3}$ and degrees K, respectively.

It is clear that the high threshold (32) makes it possible to accumulate in the compressed magnetic flux tube large energy in the form of energetic particles (electrons). After the CI threshold is achieved, the instability develops explosively due to the heating of the background plasma by the whistler waves, i.e., increase in T_e in (33). The CI starts in the central ("equatorial") cross-section of the magnetic flux tube, where the threshold (32) is minimum. Therefore, the region heated by the waves is very strongly localized. As a result, two important

processes develop: precipitation of energetic electrons in the dense solar atmosphere, similar to the energetic electron precipitation in the Earth's radiation belt, and formation of a thermal shock propagating from the "equator" in both directions along the magnetic field line. These processes are shown in Fig. 6.

The quantitative theory of these eruptive processes was developed by Trakhtengerts [61]. It was shown that, under certain conditions, the kinetic energy density of plasma in the heating region can exceed the magnetic energy density. In this case, solar mass ejections to the interplanetary space can occur.

Quantitative estimations made in [61] demonstrate the possibility to relate certain class of eruptive phenomena in the solar corona to the CI of the solar radiation belts, briefly described above.

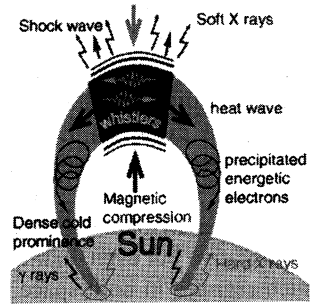


Fig. 6. CM in solar corona

8. Laboratory modeling of space CM

Studies of CI in application to space and laboratory plasmas developed independently. In 1965–1990, CI development has been observed in several laboratory experiments with magnetic mirror traps [64–68]. The process was characterized by spike-like precipitation of energetic electrons through the mirror plugs, accompanied with bursts of electromagnetic emission at frequencies below the electron gyrofrequency. The authors of these experiments were able to relate the observations to the CI, but they did not attempt to explain temporal characteristics of the spike-like CI development. Self-consistent models allowing one to do that were most actively developed for space CMs (see the previous sections).

On the basis of these approaches it was suggested in [69] to design a CM with background plasma that uses one of the nonlinear mechanisms of spike-like wave generation in plasma magnetic traps. It was noticed in [69] that for laboratory plasma experiments, besides the growth rate increase due to the modification of the distribution function and the decrease in damping rate due to the heating of background plasma by the generated waves, there exists one more mechanism of positive feedback leading to spike-like generation. This mechanism is related to the conditions of wave reflection from the trap ends, which are absent in a laboratory device with smooth distribution of cold plasma along the external magnetic field if $\omega < \omega_p$. Since $\omega < \omega_B$ for the parallel-propagating waves, they can be effectively reflected by the device walls only if $\omega_p < \omega < \omega_B$. This condition can be met in the process of plasma decay, and further decrease in ω_p and, hence, increase in the reflection coefficient, can be accelerated by enhanced losses of energetic electrons due to the interaction with the generated waves.

Following [69], an attempt to interpret all above-mentioned laboratory experiments using a unified approach was undertaken in [70]. It was shown that, indeed, the nonlinear mechanisms discussed above can be successfully applied to the laboratory experiments.

Space cyclotron masers have many similarities with laboratory magnetic traps, since their regimes are determined by the same set of basic linear and nonlinear mechanisms. On the other hand, space and laboratory plasmas have very different parameters and, hence, the maser regimes can exhibit not only quantitative but even qualitative differences. Therefore, comprehensive studies of such regimes in both space and laboratory experiments and cross-comparison of the results will allow us to achieve deeper understanding of plasma dynamics in a wide range of parameters. Table 2 summarizes the parameters of laboratory experiments which could help in modeling different aspects of space CMs.

Table 2. Parameters of laboratory experiments for modeling space cyclotron masers. Two upper rows show parameters of facilities actually used for this purpose at IAP [71, 72], while two lower rows represent desired setups

	B , Gs	N_e , cm^{-3}	T_e , eV	ω_B , s^{-1}	ω_p , s^{-1}	v_{ei} , s^{-1}	W_{hs} , keV	N_h/N_c	l_{Cl} , m	L_{exp} , m
WCM (magnetosphere)	10^4	10^{14}	300	$2 \cdot 10^{11}$	$5 \cdot 10^{11}$	10^6	10	10^{-4}	2	0.2
	100	10^{12}	5	$2 \cdot 10^9$	$5 \cdot 10^{10}$	$5 \cdot 10^6$	< 0.1	10^{-2}	0.2	1
Gyrotron (AKR)	10^4	10^{10}	–	$2 \cdot 10^{11}$	$4 \cdot 10^{10}$	–	10	0.1–1	0.1	0.1
SCM (Solar corona)	10^4	$3 \cdot 10^{14}$	1	$2 \cdot 10^{11}$	10^{12}	10^{10}	> 1	$3 \cdot 10^{-2}$	0.02	0.2

The first row in this table represents the experiment recently started at IAP and specifically aimed at detailed study of nonlinear dynamics in plasma CM. Some preliminary results of this study are summarized in [72]. The hot-electron population (~ 10 keV) with anisotropic velocity distribution is produced in the trap by the electron-cyclotron resonance discharge. Quasi-periodic spikes of precipitated energetic electrons are detected by the current pulses produced by these electrons hitting pin-diode detectors at the ends of the trap. Associated with these spikes is the electromagnetic emission propagating quasi-parallel to the magnetic field. The emission spectrum is bounded from above by the frequency which is below the electron gyrofrequency in the central cross-section of the trap. The electron precipitation mechanism was identified as the turbulent diffusion at whistler-mode waves generated by the cyclotron instability of the energetic elec-

trons. The spikelike regimes observed in experiment can be consistently explained in terms of electron cyclotron maser theory. More detailed description of these results and further studies will be the subject of future papers.

9. Conclusions

The theory of cyclotron masers in space has united successfully many achievements of the modern physics of plasmas and electronics. It turns out well to explain on this basis many features of wave-particle interaction in the planetary magnetospheres and in the solar corona. At the same time CMs in space have emphasized many new problems, which demand new approaches both in theory and experiment.

Among these problems are the role of background plasma in formation of CM eigenmodes, the energy exchange between the hot and cold plasma components, influence of the magnetic field and plasma inhomogeneity on the spectrum and dynamics of wave generation. To our mind, the most important problem is transition from noise-like to discrete emission, which testifies formation of phase-bunched clusters in the phase space.

The solution of these problems is in the further development of experimental and theoretical investigations. The theoretical models should include the sophisticated computer simulations to be closed to the real situation. The laboratory modeling seems to be very important and fruitful. But it is borne in mind that the modern problems of CMs in space demand for its solution extremely high time, space, and phase-space resolutions in particle and wave measurements.

Some problems can be solved now only in natural experiments. This is true for the measurements of the phase-space fine structure as well as investigations of ion CMs with their tremendous scales. The special space project "Resonance", aimed at solution of these and other problems of CMs in the Earth's magnetosphere, is now under joint development. This project is funded by RASA and performed by the Space Research Institute (IKI), Institute of Applied Physics, Lavochkin Association, and several other Russian institutes. The international cooperation for the first phase (A) of this project has been supported by INTAS. Within the framework of this project, it is planned to launch a satellite on a special so-called magneto-synchronous orbit. Moving along this orbit, the satellite can provide the long-term measurements in a fixed magnetic flux tube, which are crucially important for studies of ion CMs. Moreover, the satellite will be equipped with precise charged-particle detectors for the measurements of phase-space fine structures.

We believe that the further joint space and laboratory experiments bring essential progress in investigation of CMs in space.

Acknowledgements. The work of VT and AD was supported by the Russian Foundation for Basic Research (grants 02–02–17109 and 02–02–17092) and by the Division of General Physics and Astronomy of the Russian Academy of Sciences. The authors also wish to acknowledge support from INTAS, grant 99–0502.

References

1. *Twiss R. Q.* Austral. J. Phys., 1958, **11**, 567.
2. *Gaponov-Grekhov A. V., Petelin M. I.*, in Science and Mankind (Znanie, Moscow, 1981), 283 p.
3. *Helliwell R. A.* Whistlers and Related Ionospheric Phenomena (Stanford Univ. Press, Palo Alto, Calif., 1965).
4. *Van Allen J. A., Ludwig G. H., Ray E. C., McIlwain C. E.* Jet Propulsion, 1958, **28**, 588.
5. *Khanin Y. I.*, Dynamics of quantum generators (Sov. Radio, Moscow, 1975).
6. *Trakhtengerts V. Y.* Geomagn. Aeron., 1963, **3**, 442.
7. *Brice N. M. J.* Geophys. Res., 1963, **68**, 4626.
8. *Brice N. M. J.* Geophys. Res., 1964, **69**, 4515.
9. *Andronov A. A., Trakhtengerts V. Y.* Geomagn. Aeron., 1964, **4**, 233.
10. *Kennel C. F., Petschek H. E. J.* Geophys. Res., 1966, **71**, 1.
11. *Sagdeev R. Z., Shafranov V. D.* Zhurn. Eksp. Teor. Fiz., 1960, **39**, 181.
12. *Zheleznyakov V. V.* Izv. Vyssh. Uchebn. Zaved. Radiofiz., 1960, **3**, 57.
13. *Drummond W. E., Pines D.* Nucl. Fusion Suppl., 1962, **2** (part 3), 1049.
14. *Vedenov A. A., Velikhov E. P., Sagdeev R. Z.* Nucl. Fusion Suppl., 1962, **2**, 465.
15. *Trakhtengerts V. Y.* Geomagn. Aeron., 1966, **6**, 827.
16. *Trakhtengerts V. Y.* Geomagn. Aeron., 1967, **7**, 339.
17. *Kennel C. F.* Rev. Geophys., 1969, **7**, 339.
18. *Gendrin R. J.* Atm. Terr. Phys., 1968, **30**, 1513.
19. *Tverskoi B. A.* Dynamics of the Earth's radiation belts (Nauka, Moscow, 1968; in Russian).
20. *Cornwall J. M., Coronity F. V., Thorne R. M. J.* Geophys. Res., 1970, **75**, 4699.
21. *Coronity F. V., Kennel C. F. J.* Geophys. Res., 1970, **75**, 1279.
22. *Roux A., Solomon J. J.* Atmos. Terr. Phys., 1971, **33**, 1457.
23. *Lyons L. R., Thorne R. M., Kennel C. F. J.* Geophys. Res., 1972, **77**, 3455.
24. *Schulz M., Lanzerotti L. J.* Particle diffusion in radiation belts (Springer-Verlag, New York, 1974).
25. *Bespalov P. A., Trakhtengerts V. Y.* Alfvén Masers (Inst. of Appl. Phys., Gorky, 1986; in Russian).
26. *Dungey J. W. J.* Fluid Mech., 1963, **74**, 15.
27. *Molchanov O. A.* Low Frequency Waves and Induced Emissions in Near-Space Plasma (Nauka, Moscow, 1985; in Russian).
28. *Helliwell R. A.* Mod. Radio Sci., 1993, 189.
29. *Helliwell R. A. J.* Geophys. Res., 1967, **72**, 4773.
30. *Dysthe K. B. J.* Geophys. Res., 1971, **76**, 6915.
31. *Nunn D.* Planet. Space Sci., 1971, **19**, 1141.
32. *Nunn D.* Planet. Space Sci., 1974, **22**, 349.
33. *Sudan R. N., Ott E. J.* Geophys. Res., 1971, **76**, 4463.
34. *Bud'ko N. I., Karpman V. I., Pokhotelov O. A.* Cosmic Electrodynamics, 1972, **3**, 147.
35. *Helliwell R. A., Crystal T. L. J.* Geophys. Res., 1973, **78**, 7357.
36. *Karpman V. I., Istomin Y. N., Shklyar D. R.* Plasma Phys., 1974, **16**, 685.
37. *Matsumoto H., Yasuda Y.* Phys. Fluids, 1976, **19**, 1513.
38. *Roux A., Pellat R. J.* Geophys. Res., 1978, **83**, 1433.
39. *Sagdeev R. Z., Shapiro V. D., Shevchenko V. I.* Sov. Phys. JETP, 1987, **62**, 12.
40. *Bespalov P. A., Trakhtengerts V. Y.*, in Reviews of Plasma Physics, ed. Leontovich M. A. (Plenum, New York, 1986), vol. 10, 155.

41. *Stix T. H. Waves in Plasmas*, (AIP, New York, 1992).
42. *Pasmanik D. L. et al.*, *Ann. Geophys.*, 1998, **16**, 322.
43. *Pasmanik D. L., Trakhtengerts V. Y.* *Ann. Geophys.*, 1999, **17**, 351.
44. *Hayakawa M., Sazhin S. S.* *Planet. Space Sci.*, 1992, **40**, 1325.
45. *Sazhin S. S., Hayakawa M.* *Planet. Space Sci.*, 1992, **40**, 681.
46. *Trakhtengerts V. Y., Rycroft M. J., Demekhov A. G. J.* *Geophys. Res.* 1996, **101**, 13293.
47. *Trakhtengerts V. Y. J. Geophys. Res.*, 1995, **100**, 17205.
48. *Nunn D.* *Comput. Phys. Commun.* 1990, **60**, 1.
49. *Nunn D., Smith A. J. J. Geophys. Res.*, 1996, **101**, 5261.
50. *Nunn D. et al.*, *J. Geophys. Res.*, 1997, **102**, 27083.
51. *Smith A. J., Nunn D. J. Geophys. Res.*, 1998, **103**, 6771.
52. *Demekhov A. G. et al.*, *Phys. Plasmas*, 2000, **7**, 5153.
53. *Trakhtengerts V. Y. et al.*, *Phys. Plasmas*, 1999, **6**, 692.
54. *Vomvoridis J. L., Crystal T. L., Denavit J.*, *J. Geophys. Res.*, 1982, **87**, 1473.
55. *Omura Y. et al.*, *J. Atm. Terr. Phys.*, 1991, **53**, 351.
56. *Molvig K. et al.*, *J. Geophys. Res.*, 1988, **93**, 5665.
57. *Lyons L. R., Williams D. J.* *Quantitative aspects of magnetospheric physics.* (D. Reidel Publ. Co., Dordrecht, Holland, 1984).
58. *Ginzburg N. S., Kuznetsov S. P.*, in *Relativistic HF Electronics* (Inst. of Appl. Phys., Gorky, USSR, 1981; in Russian), 101 p.
59. *Trakhtengerts V. Y.* *Ann. Geophys.*, 1999, **17**, 95.
60. *Trakhtengerts V. Y.*, in *Handbook of Plasma Physics*, ed. by Galeev A. A., Sudan R. N., El-sevier N. Y., vol. 2, *Basic Plasma Physics II*, 1984, 519 p.
61. *Trakhtengerts V. Y.* *Izv. Vyssh. Uchebn. Zaved. Radiofiz.*, 1996, **39**, 699.
62. *Trakhtengerts V. Y., Shalashov A. G.* *Astron. Rep.*, 1999, **43**, 540.
63. *Ard W. B., Dandl R. A., Stetson R. F.* *Phys. Fluids*, 1966, **9**, 1498.
64. *Perkins W. A., Barr W. L.* *Proc. Int. Conf. Plasma Phys. and Controlled Nucl. Fusion Res.*, 1966, **2**, 115.
65. *Alikaev V. V., Glagolev V. M., Morosov S. A.*, *Plasma Phys.*, 1968, **10**, 753.
66. *Ikegami H. et al.*, *Phys. Fluids*, 1968, **11**, 1061.
67. *Jacquinot J. et al.*, in *Proc. Int. Conf. Plasma Phys. and Contr. Nucl. Fusion Res. (2. IAEA, Vienna, 1969)*, 347 p.
68. *Garner R. C. et al.*, *Phys. Rev. Lett.*, 1987, **59**, 1821.
69. *Gaponov-Grekhov A. V., Glagolev V. M., Trakhtengerts V. Yu.* *Zhurn. Eksp. Teor. Fiz.*, 1981, **80**, 2198.
70. *Demekhov A. G., Trakhtengerts V. Y.* *Radiophys. Quantum Electron.*, 1986, **29**, 848.
71. *Kostrov A. V., Strikovskiy A. V., Shashurin A. V.* *Fiz. Plazmy*, 2001, **27**, 149.
72. *Vodopyanov A. V. et al.*, in *Proc. 12th Joint Workshop on Electron Cyclotron Emission and Electron Cyclotron Resonance Heating*, 2002, 383 p.

CLASSICAL PLASMA ANALOGS OF THE ELECTROMAGNETICALLY INDUCED TRANSPARENCY AND LASING WITHOUT INVERSION

M. D. Tokman, A. G. Litvak, M. A. Erukhimova, A. Yu. Kryachko

IAP RAS, Nizhny Novgorod, Russia

The parametric effects of Electromagnetic Induced Transparency (EIT) and Lasing Without Inversion (LWI) have been recently very popular in the quantum electronics. In this review construction of classical models of these phenomena is described. On the basis of these models some EIT and LWI analogies for electromagnetic waves at the frequencies of electron-cyclotron resonance in plasma and electron beams are considered. The possibilities of application of these effects in plasma physics and classical electronics are discussed.

Introduction

The investigation of the interaction of electromagnetic waves with multi-levels quantum systems placed in so called coherent states has been paid considerable attention during last few years. The most popular examples of such effects are Lasing Without Inversion (LWI) [1] and Electromagnetically Induced Transparency (EIT) [2], as well as tightly connected with EIT “deceleration” [3] and “stopping” of the light [4, 5]. The interest to these effects was caused not only by their possible applications (see [1, 2, 6]), but also by their association with fundamental aspects of the physics of radiation-medium interaction. In these processes the dissipative and dispersive properties of resonant medium are cardinally modified during the interaction with radiation that does not substantially change the distribution of populations among quantum levels. So the reason why the realization of LWI and EIT is possible is that the properties of the interaction between non-monochromatic radiation and resonant quantum transitions are not always unambiguously defined by the population distribution. There is certain similarity of radiation processes in ensembles of quantum and classical electron-oscillators [7, 8, 9]. It drives us to the assumption that the system of classical particles with negative-going energy spectrum in the resonant region can be prepared in such conditions that the stimulated emission or propagation of electromagnetic waves without absorption becomes possible. This particular aspect of electrodynamics of plasmas and electron beams is the main object of this review, although we shall make further a brief mention of the corresponding peculiarities of quantum prototypes of the classical systems considered here.

Basic theoretical model in investigations of these effects is so-called Λ -scheme (see Fig. 1).

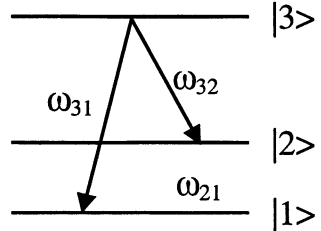


Fig. 1. Three-level Λ -scheme

The Λ -scheme consists of two high-frequency (HF) electromagnetic waves with frequencies close to the resonant frequencies of transitions $|3\rangle-|1\rangle$ and $|3\rangle-|2\rangle$, parametrically coupled by means of oscillations (quantum coherence) at the low-frequency (LF) transition $|2\rangle-|1\rangle$. The LF coherence can either be created by the external resonant LF driving field or be caused by two HF waves. In the second case the situation considered usually is a kind of resonant scattering (for more detail see [1]), when one of HF waves is the driving field, the other one is the probe field. In the LWI regime the bichromatic radiation or HF probe wave (in case of resonant scattering) can be amplified in the absence of inversion at any transition of Λ -scheme. In this process the electrons' energy is transmitted to the energy of electromagnetic field. Strictly speaking the effect of EIT is the threshold of LWI, but the resonant scattering regime of EIT is especially interesting due to the specific characteristics of the probe wave propagation (see [2–6]).

For the first time the classical analogs of quantum coherent mediums were proposed in papers [10, 11] (the systems like the optical klystron) and in [12] (parametrical interaction of waves in the isotropic plasma). These works were further developed in [13] (LWI) and [14] (EIT). But the systems proposed in these papers can be considered as classical analogs of corresponding effects in three-level systems only with great reserve because there are neither typical for quantum systems parametrical coupling of electromagnetic waves of different frequencies nor equally typical resonant interaction between electromagnetic waves and medium.

The system found as a direct classical analog (or system completely equivalent to the initial quantum systems with relation to the electromagnetic field behavior) is the parametric interaction of waves in ensemble of electrons that are in cyclotron motion in magnetic field. The classical analog of the simplest case of LWI (Λ -scheme with LF coherence prepared beforehand) found in [15] is the cyclotron parametric instability of two harmonics of gyro-frequency, coupled by the preliminary modulation on gyro-rotation phases at the beat harmonic of electrons distribution function. (The three-level block equivalent to the Λ -scheme turns out to be a part of the Landau levels system that describes the motion of a quantum electron in a magnetic field). The peculiarities of wave propagation corresponding to the EIT effect were theoretically found in [16, 17] for electron-cyclotron wave in cold plasma, coupled parametrically with electrostatic wave by means of electromagnetic driving wave. These investigations were developed in papers [18–20] (LWI) and [21, 22] (EIT).

In the first part of this review the main traits of LWI effect in classical systems are considered by the example of the “inversionless” cyclotron maser. In the second part the hydrodynamic theory of EIT effect for the electron-cyclotron waves in high-temperature plasma is presented.

1. “Inversionless” generation of cyclotron radiation

1.1. Phenomenological treatment of the LWI effect

The effect of “inversionless” amplification in the simplest quantum LWI systems (which are constructed on the basis of Λ -scheme with LF coherence prepared beforehand) as well as in their classical analogs is per se the process of parametric interaction of coherent HF modes in the modulated electron medium. Such interaction under certain conditions leads not to the transfer of energy from one mode to another, but rather to the amplification of both waves. The electron ensemble at the same time is “inversionless” in the sense that it is stable with respect to the generation of each wave separately (if for example the propagation of the other wave is forbidden by external electromagnetic conditions).

The parametric interaction of two HF waves in a medium with modulated electrodynamic characteristics can be described in the simplest case by the following truncated equations [23]:

$$\begin{cases} \beta_1 \dot{E}_1 + \gamma_1 E_1 = \delta\epsilon E_2, \\ \beta_2 \dot{E}_2 + \gamma_2 E_2 = -\delta\epsilon^* E_1, \end{cases} \quad (1)$$

where $E_{1,2}$ are the complex amplitudes of waves with frequencies and wave vectors $\omega_{1,2}$ and $k_{1,2}$, $\delta\epsilon$ is the complex amplitude of the perturbation of electrodynamic parameter of the medium with frequency $\Omega = \omega_1 - \omega_2$ and wave vector $\kappa = k_1 - k_2$, the constants β_1, β_2 are determined by the linear dispersion of the waves, and the quantities $\gamma_{1,2}$ describe the linear dissipation. Simultaneous amplification of two HF modes in the system (1) is possible only if the coefficients β_1 and β_2 have different signs. This well-known case corresponds to waves whose energies have different signs. For positive-energy waves simultaneous amplification of HF modes occurs with a sign change on the right-hand side of one of the equations (1) or with the pre-multiplication of the right-hand sides of (1) by i (the substitution $\delta\epsilon \rightarrow i\delta\epsilon$ reduces both variants into one another). It was revealed in paper [15], that the mechanism of “inversionless” amplification in the quantum Λ -scheme corresponds to the parametric interaction of the modes in the medium with modulated conductivity. Such parametric coupling is described just by equations of a desired type. At the same time the averaged (unmodulated) component of the conductivity can be positive. This provides the absorption of the modes in the absence of their parametric coupling – this system is thereupon “inversionless”.

This general interpretation of the mechanism of “inversionless” amplification enabled to formulate conditions for realization of this effect in ensemble of classical electrons. The active response to the external HF field is connected with the particles synchronized with the wave. So it is necessary to modulate the electrons distribution function in the region of the momentum space where the resonant Doppler condition [8] is fulfilled for both HF waves (but not only for their beat-

ing as in standard scattering [24]). Then this mechanism of stimulated bichromatic generation can be realized. It is important that the energy spectrum averaged over LF modulation period can be stable, i.e. “inversionless”.

The investigation of this effect in different schemes has shown [18, 19] that in classical systems (in contrast with all known quantum schemes) the realization of “inversionless” amplification is possible also in the absence of particles resonant to the waves. In this case the type of the parametric coupling required for the amplification is produced not by the modulation of the medium conductivity. The desired parametric coupling is prepared by means of “antiphase” modulation of the partial susceptibilities of the electron ensemble for two different modes. Note that in this case the electron ensemble without modulation is “purely reactive” (i.e. not dissipative) medium, but in the medium with spatial or temporal dispersion the modulation of any parameter causes the complex response to the monochromatic field [25].

In this part of the paper we shall consider one of the schemes of “inversionless” cyclotron stimulated emission. All peculiarities of different regimes of “inversionless” amplification in classical system will be demonstrated by this example.

1.2. The basic equations

Let us consider two plane waves, propagating at an angle with respect to a constant magnetic field $\mathbf{B} = B\mathbf{z}_0$ (see Fig. 2.), with the equal transverse wave numbers and different frequencies and longitudinal wave numbers:

$$\mathbf{E} = \mathbf{y}_0 \sum_{j=1}^2 \text{Re } E_j \exp(ik_{\perp}x + ik_{\parallel j}z - i\omega_j t).$$

Let the condition of Doppler resonance at the first harmonic of gyro-frequency with both waves be fulfilled for the electrons with momentum components $p_{\parallel R} = mc\rho_{\parallel R}$ and $p_{\perp R} = mc\rho_{\perp R}$:

$$\omega_j = \omega_B / \gamma_R + ck_{\parallel j} \beta_{\parallel R},$$

where $\omega_B = eB/mc$, m is the electron rest mass, c is the light velocity, $\gamma_R = (1 + \rho_{\parallel R}^2 + \rho_{\perp R}^2)^{1/2}$ and $\beta_{\parallel R}$ are respectively the relativistic gamma factor and the longitudinal velocity of resonance particles scaled to the velocity of light. Let us consider the interaction of this field with an ensemble of electrons whose momenta are close to the resonant value. This ensemble can be described by the distribution function over “slow” variables $f(r, \chi, \theta, z, X, t)$, where $r = \rho_{\parallel} / \rho_{\parallel R}$, $\chi = \rho_{\perp}^2 / 2 - \rho_{\perp R}^2 / 2$, θ is the cyclotron rotation phase, X is the transverse coordinate of the center of a “Larmor circle”. The following form

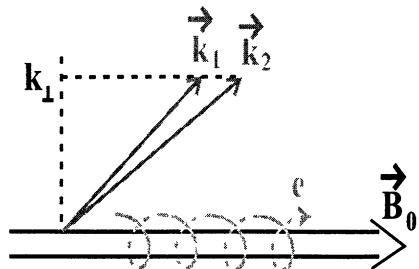


Fig. 2. “Inversionless” cyclotron maser on the first harmonic of gyrofrequency.

of the Liouville equation can be used for the distribution function [15, 18]:

$$\left(\frac{\partial}{\partial t} + \omega_H \frac{\partial}{\partial \theta} + c\beta_{\parallel} \frac{\partial}{\partial z} \right) f + \sum_{j=1}^2 F_j \left(\frac{\omega_B}{\omega_j} \frac{\partial}{\partial \chi} + n_{\parallel j} \frac{\partial}{\partial r} \right) f = 0, \quad (2)$$

where:

$$\omega_H = \omega_B \left(1 - \chi/\gamma_R^2 - \beta_{\parallel R} r/\gamma_R \right) / \gamma_R, \quad \beta_{\parallel} = \beta_{\parallel R} + r \left(1 - \beta_{\parallel R}^2 \right) / \gamma_R - \beta_{\parallel R} r / \gamma_R^2,$$

$$F_j = G \operatorname{Re} \alpha_j \exp(i\theta + ik_{\perp} X + ik_{\parallel j} z - i\omega_j t), \quad G = (\rho_{\perp R} / \gamma_R) J_1'(k_{\perp} r_H),$$

$n_{\parallel j} = ck_{\parallel j} / \omega_j$, $r = c\rho_{\perp R} / \omega_B$, J_1' is the derivative of the Bessel function, $\alpha_j = eE_j/mc$ is the normalized amplitude of the wave. We shall also use the truncated equations for the wave amplitudes:

$$\partial \alpha_j / \partial t = -(2\pi e/mc) I_j. \quad (3)$$

Let us consider the “initial-value” problem (the “boundary-value” problem was discussed in [18]). The amplitudes of the resonant harmonics of the current in (3) can be expressed in terms of the distribution function as follows [15, 18, 26]:

$$I_j = ecG \left\langle \int d\chi dr d\theta f(\chi, r, \theta, z, X, t) \exp(-i\theta - ik_{\perp} X - ik_{\parallel j} z + i\omega_j t) \right\rangle_{X, z, t}. \quad (4)$$

Parametric coupling of the waves is provided by the “preliminary” modulation of the distribution function, which can be set at the initial moment in the following way:

$$f_{in}(t=0) = f_0(\chi, r) + f_M(\chi, r) \cos(\kappa z + \varphi_M), \quad (5)$$

where $\kappa = k_{\parallel 1} - k_{\parallel 2}$. The unperturbed distribution function at the subsequent time moments differs from (5) by the phase of modulation, which takes the form $\varphi_M + \kappa z - c\kappa\beta_{\parallel} t = \varphi_M + \kappa z - \Omega t + \Delta_M t$, where $\Omega = \omega_1 - \omega_2$,

$$\Delta_M = \Omega - c\kappa\beta_{\parallel} = \Omega\chi/\gamma_R^2 - c\kappa r \left(1 - \beta_{\parallel R}^2 \right) / \gamma_R \quad (6)$$

Δ_M is the detuning of the particle synchronism with the beating wave. The partial synchronism detunings with HF waves are determined by the expressions:

$$\Delta_j = \omega_j - \omega_H - c\kappa_{\parallel j} \beta_{\parallel} = \left(\omega_j / \gamma_R \right) \left(\chi / \gamma_R + r \left(\beta_{\parallel R} - n_{\parallel j} \right) \right) = \Delta_{\chi} + \Delta_{rj}. \quad (7)$$

Let us solve the kinetic equation (2) in the linear approximation in the wave field and consider the asymptotic solution corresponding to Landau’s “pole rule”, which is valid under condition:

$$\langle \delta\Delta_j \rangle t \gg 1. \quad (8)$$

(Here $\langle \delta\Delta_j \rangle$ is the characteristic diversity of the synchronism detunings in the electron beam, determined by the distribution function.) Besides we neglect the “ballistic relaxation” of the modulated part of distribution function, so that another “time” condition must be fulfilled:

$$\Delta_M t \ll 1. \quad (9)$$

The conditions of simultaneous fulfillment of inequalities (8) и (9) can be found in [18]. As a result we obtain (taking into account (3) and (4)) the following equation of parametric coupling of the modes with close frequencies ($\omega_1 \approx \omega_2 \approx \omega$):

$$\begin{cases} \dot{\alpha}_1 + (\Gamma^0 + iD^0)\alpha_1 = -\exp(i\Phi_M t) \left((\Gamma^s + iD^s) + (\Gamma^a + iD^a) \right) \alpha_2, \\ \dot{\alpha}_2 + (\Gamma^0 + iD^0)\alpha_2 = -\exp(-i\Phi_M t) \left((\Gamma^s + iD^s) - (\Gamma^a + iD^a) \right) \alpha_1. \end{cases} \quad (10)$$

In the left-hand side the standard coefficients are presented, which define the linear susceptibility of the electron ensemble. Here Γ^0 is the linear decrement:

$$\Gamma^0 = (2\pi^2 e^2 G^2 \omega / m \gamma_R) (1 - n_{\parallel}^2) \int d\chi d r f_0(\chi, r) \partial \delta(\Delta_\chi) / \partial \Delta_\chi.$$

The right-hand terms of the equations define the parametric coupling of the modes caused by the modulation. The coefficients with index ‘s’ are determined by the symmetrical part of the function $f_M(r) = f_M^s(r) + f_M^a(r)$ (i.e. satisfying the condition $f_M^s(\chi, r) = f_M^s(\chi, -r)$):

$$\Gamma^s = \pi^2 e^2 G^2 \omega / m \gamma_R (1 - n_{\parallel} n_{\parallel 2}) \int d\chi d r f_M^s(\chi, r) \partial \delta(\Delta_\chi) / \partial \Delta_\chi,$$

$$D^s = (\pi e^2 G^2 \omega / m \gamma_R) (1 - n_{\parallel} n_{\parallel 2}) \int d\chi d r f_M^s(\chi, r) \varphi / \Delta_\chi^2,$$

while the coefficients with index ‘a’ are determined by the asymmetrical part of the modulated component of the distribution function, meeting the condition $f_M^a(\chi, r) = -f_M^a(\chi, -r)$:

$$\Gamma^a = (\pi e^2 G^2 \omega / m \gamma_R^2) (1 - n_{\parallel} n_{\parallel 2}) \times$$

$$\times \int d\chi d r f_M^a(\chi, r) r \left\{ -c\kappa (1 - \beta_{\parallel R}) t \varphi / \Delta_\chi^2 + \pi \left[\partial^2 \delta(\Delta_\chi) / \partial \Delta_\chi^2 \right] \omega (n_{\parallel} - \beta_{\parallel R}) \right\},$$

$$D^a = (\pi e^2 G^2 \omega / m \gamma_R^2) (1 - n_{\parallel} n_{\parallel 2}) \times$$

$$\times \int d\chi d r f_M^a(\chi, r) r \left\{ -c\kappa (1 - \beta_{\parallel R}) t \pi \left[\partial \delta(\Delta_\chi) / \partial \Delta_\chi \right] + (2\varphi / \Delta_\chi^3) \omega (n_{\parallel} - \beta_{\parallel R}) \right\}.$$

1.3. Different regimes of the “inversionless” parametric generation

a) The distribution function is modulated at *the transverse momentum* (we reckon that $f_M^a(r) = 0$, while the asymmetrical part of function $f_M(\chi)$ is not equal to zero). Essentially that such modulation corresponds to that the synchronism detunings (7) Δ_1 and Δ_2 oscillate in phase. Due to this fact the similar responses to both HF waves are developed in the modulated medium. We obtain that in this system one of two bichromatic exponential modes $\alpha_j \propto \exp(i\mu t)$ is amplified under condition:

$$|\Gamma^s| > \Gamma^0.$$

This is just a regime of “inversionless” amplification due to modulation of distribution function of resonant particles; meanwhile averaged part of distribution function is “not inverted”, so that $\Gamma^0 > 0$. The amplification of two modes is

achieved in this case due to the modulation of conductivity, which is optimally synchronized with the beating of HF waves. It is the direct classical analog of “inversionless” amplification in the quantum Λ -scheme.

b) The distribution function is modulated at *longitudinal momentum* (we reckon that $f_M^s(r) = 0$). Such modulation corresponds to “antiphase” oscillations of the detunings Δ_1 and Δ_2 (7), because for waveguide modes parameters $\beta_{\parallel R} - n_{\parallel}$ have different sign. Due to this fact the responses to the first and the second HF waves are also modulated with phase difference equal to π . As a result, the bichromatic exponential mode $\alpha_j \propto \exp(\mu t)$ is amplified in this system under condition:

$$|D^a| > \Gamma^0.$$

This condition can be fulfilled in the absence of particles, resonant to HF waves (when $\Gamma^0 = 0$). This is just a regime of amplification in “reactive” medium. It is realized thanks to the specific dependence of the synchronism detunings on the electron momentum components. Such dependence takes into account both relativistic gyro-frequency detuning and Doppler shift. The energy exchange mechanism between bichromatic HF field and modulated medium of nonresonant particles is analyzed in paper [27].

1.4. About saturation of the “inversionless” instability

One of the mechanisms of the stabilization of the “inversionless” instability, already investigated (see [19]), is the “ballistic restructuring” of the modulated fraction of the electrons. It develops at time $\langle \delta \Delta_M \rangle t \geq 1$, where $\langle \delta \Delta_M \rangle$ is the characteristic spread of parametric synchronism detuning (6) in the electron ensemble.

The “quasilinear” mechanism of saturation of “inversionless” instability was investigated in the paper [20]. It is necessary to note that a decrease in the energy of the electron ensemble during “inversionless” parametric generation is accompanied by the formation of a distribution function with a steeper slope along the energy axis in comparison with the slope of the initial distribution function.

Besides saturation mechanisms pointed above other processes are of importance, such as trapping of particles by the strong field of a finite-amplitude bichromatic wave and nonlinear frequency shift. But these mechanisms as applied to “inversionless” stimulated emission have not been investigated yet.

1.5. About the energetic efficiency of “inversionless” generation

In the process of “inversionless” generation like in the case of usual stimulated emission the energy is transmitted from nonequilibrium medium to the electromagnetic field. The main difference lies in the nature of nonequilibrium state. Comparing with the standard stimulated emission where the inverted energy spectrum is necessary, for the “inversionless” regime the spatial-temporal modu-

lation of distribution function is required. This circumstance determines the possibility of application of LWI as a converter of monochromatic LF radiation into non-monochromatic HF radiation. The key point in estimation of efficiency of possible “inversionless” electronic devices is the comparison of energy contributed by electrons to the amplified HF field with energy input to the preparation of the initial modulation of electrons beam. It is shown in [18], that for quasi-monoenergetic beams with wide pitch-angle spread (typical for usual magneto-injector guns) the LWI effect is realized in frame of “linear” regime of LF modulation. In such regime the energy of electron ensemble increases only in second-order in the amplitude of modulating field. In principal, the situation can be analogous for the beams with finite (but small) energy spread of electrons [15]. In these cases the energy contribution of electrons to HF waves can exceed the energy input to modulation. The situation is essentially different in case of a monotonic electron energy spectrum. LF modulation in a nonlinear particle trapping regime is required in order to reach the threshold of inversionless generation. Modulation in this case is inevitably accompanied by an essential distortion of the averaged component of the distribution function (see [15]). For this regime the following conclusion can be made on the basis of results of quasi-linear theory developed in [20]: the energy input of LF field in the modulating section turns out to be several times larger than energy input of electrons to the HF field.

In respect of the experimental applications it is interesting to realize the mechanisms of “inversionless” parametric generation in free electrons lasers, operating on the basis of undulator mechanism of particles-HF field interaction.

2. Electromagnetically induced transparency for the electron-cyclotron waves in plasma

2.1. The simplest model of EIT

The development of the simplest model of EIT relies essentially on the fact, that, generally, system of equations for the density matrix of quantum scheme corresponds to equations describing the excitation of a system of classical coupled oscillators by an external resonance force (see [16, 17]). From the viewpoint of realization of the EIT regime, a very important feature of density matrix equations is the fact that the external sources in this system (i.e. fields) not only excite the “oscillators” directly, but also provide parametric coupling between them. Therefore the adequate classical model (see Fig. 2) represents two LC circuits, which are coupled via mutual variable inductance (Fig. 3). In this case the harmonic coupling between the circuits acts as a pumping wave in the quantum system and external EMF acts as a signal wave.

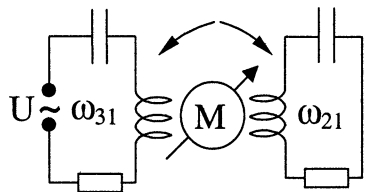


Fig. 3. The equivalent oscillatory system with lumped parameters.

It is not difficult to verify [16, 17] that the frequency dependence of the impedance for the left circuit depicted in Fig. 3 is completely equivalent to the formula for susceptibility of the quantum system relative to the signal field in the EIT regime. When the conditions of the resonant excitation of the oscillator with frequency ω_{21} are fulfilled, oscillations of the left circuit can be suppressed.

2.2. EIT for the cyclotron waves in plasma

There is a possibility of damping of resonant interaction between waves and particles in plasma due to parametric excitation of the collective degrees of freedom, e.g. electrostatic oscillations. As an example, we consider the hydrodynamical theory of EIT for the electron-cyclotron resonance in warm magnetized plasma. Our statement of the problem is the same as that in [21]. Let two circularly polarized waves with the electric field rotating in the line of the electron cyclotron motion (extraordinary waves) propagate in magnetized plasma along a constant external magnetic field $\mathbf{B} = B\mathbf{z}_0$

$$\mathbf{E}_\perp(z, t) = \text{Re}\left\{\mathbf{e}_+ \left[E_1 \exp(-i\omega_1 t + ik_1 z) + E_2 \exp(-i\omega_2 t + ik_2 z) \right]\right\}, \quad (11)$$

where $\mathbf{e}_+ = 2^{-1/2}(\mathbf{x}_0 + iy_0)$ is the wave polarization vector; and $\mathbf{x}_0, \mathbf{y}_0, \mathbf{z}_0$ are the unit vectors of the Cartesian axes.

The oscillations of the transverse and longitudinal (relative to the constant magnetic field) electron velocities are described by the Euler equations including the Lorentz force from the wave fields:

$$\begin{cases} \frac{\partial \mathbf{V}_\perp}{\partial t} + \omega_B [\mathbf{V}_\perp, \mathbf{z}_0] + \gamma \mathbf{V}_\perp + V_\parallel \frac{\partial \mathbf{V}_\perp}{\partial z} = -\frac{e}{m} \left(\mathbf{E}_\perp + V_\parallel \frac{\partial}{\partial z} \int_{-\infty}^t \mathbf{E}_\perp dt \right), \\ \frac{\partial V_\parallel}{\partial t} + \gamma V_\parallel + V_\parallel \frac{\partial V_\parallel}{\partial z} = -\frac{1}{mN_e} \frac{\partial p}{\partial z} - \frac{e}{m} E_p + \frac{e}{m} V_\perp \frac{\partial}{\partial z} \int_{-\infty}^t \mathbf{E}_\perp dt. \end{cases} \quad (12)$$

Here, γ is the effective collision frequency, E_p is the plasma-wave electric field, p is the gas-kinetic pressure, and N_e is the electron density. System (12) must be supplemented with the continuity equation

$$\frac{\partial N_e}{\partial t} + \frac{\partial (N_e V_\parallel)}{\partial z} = 0 \quad (13)$$

and with the equation that describes the excitation of an electrostatic field in the plasma wave:

$$\frac{\partial E_p}{\partial t} = -4\pi j_z = 4\pi e N_e V_\parallel. \quad (14)$$

Here, j_z is the longitudinal electron current component. Assuming the constancy of the ion density N_i and quasi-neutrality,

$$N_i = N_0 = \text{const}, \quad |N_e - N_i| \ll N_e, N_i, \quad (15)$$

we can derive a system of equations that describes the excitation of longitudinal collective oscillations by the ponderomotive force from the high-frequency fields (for definiteness, consider an adiabatic process) from Eqs. (12)–(14):

$$\begin{cases} \frac{\partial^2 n}{\partial t^2} + \gamma \frac{\partial n}{\partial t} + \omega_p^2 n - 3V_T^2 \frac{\partial^2 n}{\partial z^2} = -\frac{eN_0}{m} \frac{\partial}{\partial z} V_{\perp} \frac{\partial}{\partial z} \int_{-\infty}^t \mathbf{E}_{\perp} dt, \\ V_{\parallel} = -N_0^{-1} \int_{-\infty}^z (\partial n / \partial t) dz. \end{cases} \quad (16)$$

Here, $n = N_e - N_0$ is the perturbation of electron density, $\omega_p = (4\pi e N_0 / m)^{1/2}$ is the electron plasma frequency and $V_T = (T/m)^{1/2}$ and T are the thermal electron velocity and temperature, respectively. The excitation of plasma oscillations leads finally to the suppression of oscillations of electron velocity at the frequency of the signal wave. The EIT effect in plasma consists just in this process.

Considering the weak thermal dispersion ($k_{1,2,L} V_T \ll \omega_{1,2,L}$) we shall also assume, that the following synchronism conditions are satisfied:

$$(a) \quad |\omega_1 - \omega_B|, \quad \gamma \ll \omega_1, \omega_B, \quad (b) \quad |\omega_L - \omega_p|, \quad \gamma \ll \omega_L, \omega_p. \quad (17)$$

Here, $\omega_L = \omega_1 - \omega_2$ and $k_L = k_1 - k_2$ are the frequency and wave vector of the beats between the signal and pump waves, respectively.

Given the synchronism conditions (17a) and (17b), only the terms with the “resonance” frequencies can be retained in Eqs. (12)–(14); i.e., the method of reduced equations can be used. Note, that to derive this system of equations it is necessary to consider the nonlinear component of transversal velocity with polarization, corresponding to the ordinary wave (with the electric field rotating opposite to the direction of the electron cyclotron rotation). Due to the excitation of collective degrees of freedom the resonant components of the velocity are suppressed and the consideration of this component provides significant (but not fundamental) corrections.

From the obtained system of reduced equations we can derive an expression for the effective refractive index of the signal wave [21]:

$$N^2 = 1 - \frac{\omega_p^2 Z_p + \xi_{EC} \omega_L \omega_2 (2k_1/k_2 - 1 - \omega_1/2\omega_2)}{\omega_1 (\omega_1 - \omega_B + i\gamma) Z_p - \omega_L^2 \omega_1 \xi_{EC}}. \quad (18)$$

Here, $\xi_{EC} = |eE_2/2m(\omega_2 - \omega_B + i\gamma)|^2 (k_2/\omega_2)^2 = |V_2|^2 / (2V_{ph})^2$ is the dimensionless nonlinearly parameter, the ratio of the squares of the oscillatory and phase velocities for the pump field and $Z_p = \omega_L^2 - \omega_p^2 - 3k_L^2 V_T^2 + i\gamma \omega_L$, $Z_p = 0$ is the standard “hydrodynamic” dispersion relation for plasma waves. Expression (18) differs from that derived in [16, 17, 22] by the corrections $3k_L^2 V_T^2$, because we took into account thermal motion.

Let us now discuss the dispersion law of the signal wave under EIT conditions for warm plasma. To this end, we represent Eq. (18) as

$$Z_p (N^2 - N_0^2) = \frac{-\xi_{EC} \omega_2 \omega_L^2}{\omega_1 - \omega_B + i\gamma} \left(1 - N^2 + \frac{\omega_p^2}{\omega_1 \omega_L} \left(\frac{2k_1}{k_2} - 1 - \frac{\omega_1}{2\omega_2} \right) \right). \quad (19)$$

Here, $N_0^2 = 1 - \omega_p^2 / [\omega_1(\omega_1 - \omega_B + i\gamma)]$ is the “linear” refractive index of the signal wave in cold magnetoactive plasma (see, e. g., [7]). The quantity ξ_{EC} is a small parameter of the problem: for reasonable pump intensities (of the order of 10–100 kW/cm²), ξ_{EC} is 10^{-6} – 10^{-5} . Therefore, the signal-wave dispersion curves defined by Eq. (18) pass either near the linear signal-wave dispersion curve defined by the relation $N^2 = N_0^2$ or near the plasma-wave dispersion curve $Z_p = 0$ (shifted by the pump frequency ω_2 and wave vector k_2). This behavior of the dispersion curves is violated only near the points of intersection of the $N^2 = N_0^2$ and $Z_p = 0$ curves, where the signal-wave dispersion curves pass from one curve to the other (see Fig. 4).

Therefore, the behavior of the dispersion curves in the EIT region is actually determined by the dispersion law of plasma waves. In particular, the dispersion curves contain segments that correspond to a high group deceleration of the signal wave (which is typical for a three-level quantum system) down to a zero group velocity (which is not possible in a three-level quantum system).

Figure 5 shows the absorption-line profile for the signal wave under EIT conditions. We see that there is a frequency range where the resonant wave absorption is suppressed, with the absorption minimum roughly corresponding to the point on the dispersion curve with a zero group velocity.

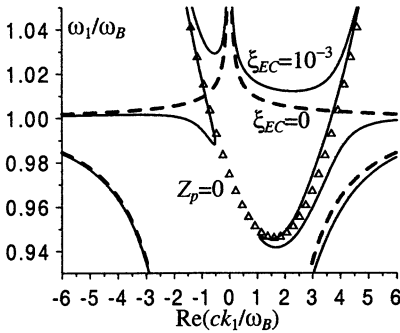


Fig. 4. The dispersion law for an EC wave under EIT conditions. $\omega_p/\omega_B = 0.75$, $\omega_2/\omega_B = 0.2$, $\gamma/\omega_B = 2.5 \cdot 10^{-3}$, $V_T/c = 7.5 \cdot 10^{-2}$.

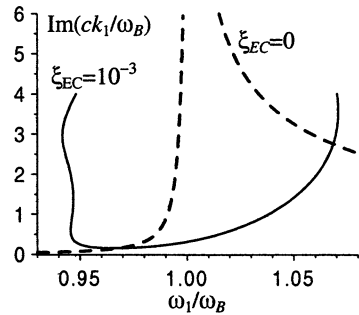


Fig. 5. The formation of a transparency window ($\text{Re}(k_1) > 0$). All parameters are the same as those in Fig. 4.

Note, that for the observation of EIT the pumping intensity should exceed the threshold value ξ_{EC}^* , determined by the dissipative effects (see also [16, 17]): $\xi_{EC}^* = (\gamma^2/\omega_p\omega_B)$.

2.3. On the possibility of the observation of EIT effect in plasma

In the hydrodynamic theory for warm plasma, it follows from (18) that the characteristic width of the signal-wave transparency band $\Delta\omega$ under EIT condi-

tions is given by the relation $|(\omega_1 - \omega_B) \text{Re} Z_p| \approx \omega_p^2 \omega_B \xi_{EC}$, which leads to the expression

$$\Delta\omega \sim \max \left\{ \left(\omega_p \omega_B \xi_{EC} \right)^{1/2}, k_L^2 V_T^2 / \omega_p \right\}. \quad (20)$$

In particular, it follows from this relation that the transparency band width in warm plasma can be significantly larger than that in cold plasma if the plasma temperature is high enough:

$$T / (mc^2) > \omega_p^2 (ck_L)^{-2} \left(\omega_B \xi_{EC} / \omega_p \right)^{1/2}. \quad (21)$$

It is important to note, that the transparency band width can cease to depend on ξ_{EC} . Thus, for example, for a pump intensity of 100 kW/cm² the plasma temperature must exceed 150 eV.

The above estimates of basic parameters for the EIT window allows us to formulate the most pessimistic requirements for the conditions for this effect to take place in plasma. The constraints on the admissible nonuniformity of the magnetic field B and density N_0 are given by Eq. (20):

$$\delta B, \delta N_0 \sim \max \left\{ \left(\omega_B \xi_{EC} / \omega_p \right)^{1/2}, k_L^2 V_T^2 / \omega_p^2 \right\}. \quad (22)$$

Here, δB and δN_0 are the relative detunings of B and N_0 respectively. For pump intensity of the order of 10 kW/sm² and for temperatures of the order of 1 and 10 keV, δB and δN_0 must be no larger than 1% and 5%, respectively. In this case, the characteristic size of the working region must be of the order of one meter (see [21]). However, it may appear that a more detailed EIT theory for an inhomogeneous layer will yield more relaxed constraints.

It is necessary to note, that all important peculiarities of dispersion curves and absorption-line profiles for the signal wave and also the estimations for the transparency band width and admissible nonuniformity of the plasma are preserved in a more careful investigation of this effect in terms of the kinetic theory (see [21]).

Conclusions

In summary let us discuss the possible applications of systems considered above. The LWI effect in ensemble of classical electrons can be used, in principal, as a method for converting microwave monochromatic radiation to HF non-monochromatic cyclotron or undulator radiation. Depending on the properties of electron beam the energy input of electron ensemble to the HF radiation can be less than energy of LF field absorbed by electrons as well as larger than it. In any case the "inversionless" nature of this effect suggests that this method of conversion must not be very sensitive to the quality of electron beam.

As for the application of EIT effect in plasma physics, it can be used in spectroscopy firstly. But in order to develop concrete schemes the theory of EIT taking into account the inhomogeneities of typical plasma objects must be developed.

Secondly the EIT-regime was suggested in [22] for use in compact plasma accelerators. The strong group deceleration typical for EIT can be used in these schemes for compression of electromagnetic pulses. It was proposed to use the magnetic undulator instead of HF pumping wave. In this scheme the efficiency of energy input of signal wave to electrostatic oscillations can be increased, although the range of allowable plasma parameters is sufficiently bounded (the closeness of cyclotron and plasma frequencies must be provided).

This work was supported by RFBR grants № 01-02-17388, № 01-02-17779.

References

1. *Kocharovskaya O.*, Phys. Rep., 1992, 219, 175–190.
2. *Harris S. E.*, Phys. Today, 1997, 50, 36–42.
3. *Marangos J.*, Nature, 1999, 397, 559–560.
4. *Liu C., Dutton Z., Behroozl C. H., Hau L. V.*, Nature, 2001, 409, 490–493.
5. *Phillips D. F., Fizischhauer A., Mair A.*, et al., Phys. Rev. Lett., 2001, 86, 783–786.
6. *Harris S. E.*, Phys. Rev. Lett., 1999, 82, 4611–4614.
7. *Ginzburg V. L.*, The Propagation of Electromagnetic Waves in Plasmas (Nauka, Moscow, 1967; Pergamon, Oxford, 1970).
8. *Zheleznyakov V. V.*, Radiation in Astrophysical Plasmas, Kluwer Academic Publishers Dordrecht/Boston/London, 1996.
9. *Gaponov A. V., Petelin M. I., and Yulpatov V. K.*, Radiophys. Quantum Electron., 1967, 10, 794–833.
10. *Sherman B., Kurizki G., Nikonov D. E., Scully M. O.*, Phys. Rev. Lett., 1995, 75, 4602–4605.
11. *Nikonov D. E., Sherman B., Kurizki G., Scully M. O.*, Opt. Commun., 1996, 123, 363–371.
12. *Harris S. E.*, Phys. Rev. Lett., 1996, 77, 5357–5360.
13. *Artemiev A. I., Fedorov M. V., Rostovtsev Y. V.* et al., Phys. Rev. Lett., 2000, 85, 4510–4513.
14. *Gordon D. F., Mori W. B., Joshi C.*, Phys. of Plasmas, 2000, 7, 3145–3166.
15. *Gaponov-Grekhov A. V. and Tokman M. D.*, JETP, 1997, 85, 640.
16. *Litvak A. G., Tokman M. D.*, Phys. Rev. Lett., 2002, 88, 095003.
17. *Litvak A. G. and Tokman M. D.*, Radioph. Quantum Electronics, 2001, 44, 375–385.
18. *Erukhimova M. A., Tokman M. D.*, JETP, 2000, 91, 255–264.
19. *Erukhimova M. A., Tokman M. D.*, Radioph. and Quantum Electronics, 2001, 44, 176–183.
20. *Erukhimova M. A., Tokman M. D.*, Plasma Physics Reports, 2001, 27, 868–874.
21. *Kryachko A. Yu., Litvak A. G., Tokman M. D.*, JETP, 2002, 95, 697.
22. *Shvets G., Wurtele J. S.*, Phys. Rev. Lett., 2002, 89, 115003.
23. *Bloembergen N.*, Nonlinear Optics (Benjamin, New York, 1965; Mir, Moscow, 1966)
24. *Litvak A. G.*, Reviews of Plasma Physics, ed. by acad. M. A. Leontovich, Consultants bureau, New York – London, 10, 294–424.
25. *Landau L. D. and Lifshitz E. M.*, Course of Theoretical Physics, V. 8, Electrodynamics of Continuous Media (Nauka, Moscow, 1982; Pergamon, New York, 1984).
26. *Bratman V. L., Ginzburg N. S., Nusinovich G. S.*, et al., Relativistic High-Frequency Electronics [in Russian], A. V. Gaponov-Grekhov (Ed.), Inst. Appl. Phys. Press, Gorky (1979), p. 157.
27. *Erukhimova M. A., Tokman M. D.*, Proceedings of the 29th EPS Conference on Plasma Phys. and Contr. Fusion (Montreux, 17–21 June 2002) ECA, 2002, 26B, 4.001.

TERAHERTZ RANGE SOURCES FROM THE ULTRA-SHORT LASER AND PLASMA INTERACTION

*D. Dorrnian, M. Starodubtsev, N. Yugami, T. Higashiguchi,
H. Kawakami, H. Ito and Y. Nishida*

Department of Energy and Environmental Science, Graduate School of Engineering,
Utsunomiya University, 7-1-2 Yoto, Utsunomiya, Tochigi 321-8585, Japan

Brief history of the plasma based high-energy particle acceleration including the $V_p \times B$ acceleration; wakefield acceleration and beatwave acceleration are reviewed. As an application of the $V_p \times B$ acceleration schema, the terahertz range radiation source is presented. The radiation in the Sub-Terahertz range is observed, which is known as $V_p \times B$ radiation, excited by the interaction of ultrashort and high intensity laser pulse with perpendicularly magnetized plasma. The frequency of the emitted radiation with the pulse width of 200 ps (detection limitation) is in the millimeter wave range (up to 0.2 THz). According to radiation theory, EM radiation is linearly polarized, vertically to the DC magnetic field vector. Polarization experimental data are in good agreement with the theory. The spatial distribution of the emitted radiation is also observed. The radiation propagates mainly in the forward direction as expected from the theory. The emergence of this field is due to the dependence of radiation characteristics on plasma parameters, which enable the radiation to be tunable in frequency and pulse duration.

1. Introduction

The present topics are strongly related to the plasma based high-energy particle accelerators driven by ultra-short terawatt laser. Therefore it is convenient to review at first the high energy particle accelerators and then we wish to go into the main topics of terahertz range radiation source.

It has been about 50 years since Fainberg proposed the concept of using electron beam to excite plasma waves and about 20 years since Tajima and Dawson proposed using laser beam instead of electrons. After that, due to advances in technology, especially the development of compact terawatt laser systems, there has been tremendous progress in theory and experiment in recent years. There have been many different kinds of experiments on the use of intense laser pulse or electron beam to excite large amplitude (up to 100 GeV/m) plasma wakes [1–2]. The energy of these wakes can be used for different purposes such as particle acceleration or radiation.

Large acceleration gradients of different kinds of plasma-based accelerators are the great interest. Accelerating electrons in a very small distance compare to huge radio frequency linear accelerators (RF linacs) with respect to the fact that electric field is at least 1000 times greater in the former one is really exciting. Known mechanisms of plasma-based accelerators are the plasma wakefield accelerators (PWFA) [3–6], the plasma beat-wave accelerators (PBWA) [7–10],

Laser wakefield accelerators (LWFA) [11–14], including the self-modulate regime and $\mathbf{V}_p \times \mathbf{B}$ accelerators (Surftron) [15–17].

In the PWFA, a relativistic electron beam can excite plasma wakefields, provided that the electron beam terminates in a time shorter than the plasma period. Fainberg apparently first proposed the concept of using electron beam driven plasma waves to accelerate charge particles in 1956 [6 and references therein] and in linear regime Chen and Dawson analyzed this mechanism in 1985 [5]. Experiment on this mechanism of acceleration was done first by Ruth *et al.* [18]. They showed that the transformer ratio (ratio of energy gain to the drive beam energy) is limited to 2 for a symmetric driving beam in the linear regime, but after him Chen *et al.* [19] showed that the transformer ratio can be increased by using asymmetric drive beam and Rosenzweig *et al.* [20] showed that in the nonlinear regime, a long symmetric drive beam could produce the bigger transformer ratio.

Next two mechanisms of accelerating electrons strongly depend on developments of the laser technology. In Fig. 1, it can be seen that how chirped pulse amplified (CPA) lasers in 1988 changed the rate of growth in accelerated electrons energy.

Before 1988 the only process to accelerate electrons by laser plasma wakes was the plasma beat wave acceleration, in which two long pulse laser beams of frequency ω_1 and ω_2 are used to resonantly excite a plasma wave. In this case laser frequency and plasma density should satisfy the condition $(\omega_1 - \omega_2) \sim \omega_p$. This idea proposed by Tajima and Dawson in 1979 [7] as an alternative to LWFA, since the technology of ultra-short high intensity lasers was not available at that time. Although the beatwave mechanism was experimentally proved before LWFA, but theoretically that was proposed after it. Plasma wave generation due to this mechanism was observed first by Clayton *et al.* [21] and the acceleration of background plasma electrons was first observed by Kitagawa *et al.* [8]. Both experiments were done by CO₂ laser.

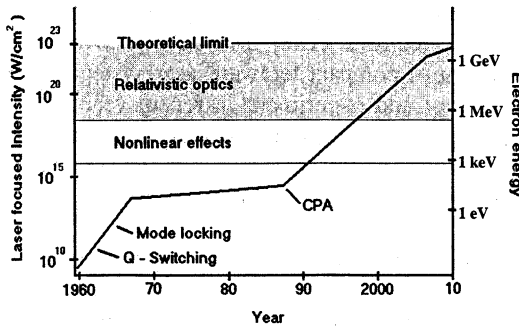


Fig. 1. The evolution of laser intensity and electron energy to the present and beyond [29].

Considering the third case, laser wakefield accelerators (LWFA), in which a single short ultrahigh intensity laser pulse drives a plasma wave. The wakefield is driven more efficiently when the laser pulse length in space is approximately equal to the plasma wavelength. The LWFA was first proposed by Tajima and Dawson in 1979 [7], but before 1988 when

the first terawatt laser system based on chirped-pulse amplification was demonstrated, doing experiment on LWFA was impossible. The first electron acceleration by this mechanism is reported by Nakajima *et al.* in 1995 [22]. At higher densities, in which the laser pulse length is long compare to the plasma wavelength, using the high power (more than critical power) laser pulse will lead to the modulation of laser pulse by plasma waves. The plasma waves can modulate the laser pulse to self-modulated LWFA. After that many other people have worked on, to increase the acceleration energy gain.

Finally $\mathbf{V}_p \times \mathbf{B}$ or surfatron mechanism to accelerate electrons is considered. Nishia *et al.* first proposed the idea in 1984 [15]. The first experiment also was done by them at the same time. Because the topic of this paper is strongly depends on this mechanism, it is necessary to go more carefully through it. Within all these acceleration mechanisms mentioned above, the surfatron is the only one which has static magnetic field, where $\omega_p \gg \omega_c$. In the presence of the magnetic field the mode-converted electrostatic plasma waves travels across the magnetic field lines and accelerates electrons very efficiently by the $\mathbf{V}_p \times \mathbf{B}$ mechanism, where \mathbf{V}_p is the phase velocity of the electron plasma wave and \mathbf{B} is the steady magnetic field intensity. Appearing a DC electric field in the wave frame accelerates trapped particles. Applying the external magnetic field can also cause another important effects in the nature of the plasma waves. In unmagnetized plasma, the wakefields are completely electrostatic. By applying a modest perpendicular DC magnetic field \mathbf{B} , the wakes find an electromagnetic component with non-zero group velocity at the frequency close to ω_p , in the direction perpendicular to the direction of laser pulse propagation and also magnetic field vector, so the electromagnetic component of wakes are enabled to propagate through plasma into the vacuum. The initial motion of plasma electrons due to the laser ponderomotive force, make them to rotate around the magnetic field lines and generate the electromagnetic part of the wake. Since the radiation frequency is very close to the plasma frequency, it is tunable with plasma density.

Theories and experiments have shown that plasma is a capable medium to convert different initial energies to coherent radiation, i. e., Raman scattering, harmonics generation, and photon acceleration. This possibility comes from the multi-mode nature of the plasma. More than these there are also two known mechanisms of plasma radiation. First one is the 'inverse mode conversion' mechanism [23]. An electrostatic plasma oscillator near the plasma frequency can radiate an electromagnetic wave at the same frequency ω_p , due to this mechanism. In this case the plasma waves, are like a dipole antenna, which oscillate in the direction of \mathbf{k} of the wave. The electromagnetic radiation primarily will be in a plane perpendicular to this direction. Another mechanism is radiation due to 'charge separation' mechanism [24]. The ponderomotive force generates a large density difference between ionic and electronic charges and this charge separation results in a powerful electromagnetic transient. The spatial distribution of this radiation depends on the spot size of laser beam. A smaller beam leads to a

shift of the maximum emission in the direction perpendicular to the laser propagation. But the $\mathbf{V}_p \times \mathbf{B}$ radiation is essentially different from both these two mechanisms, i. e. that is the inverse process of $\mathbf{V}_p \times \mathbf{B}$ acceleration mechanism. In this sense, the $\mathbf{V}_p \times \mathbf{B}$ radiation decreases the acceleration efficiency, but this is negligibly small compared with acceleration efficiency, and no serious losses take place. More details about the radiation are presented in the next section.

The emergence of this field is due to the dependence of radiation characteristics on plasma parameters, which enable the radiation to be tunable in frequency and pulse duration. These radiation sources could have applications in a wide region of topics including spectroscopy, medical imaging, astrophysics and plasma diagnostics.

The theory of the radiation generation from the wakes excited by laser pulse in the magnetized plasma have been introduced by Yoshii *et al.* [25] and the characteristics of the radiation have been observed by Yugami *et al.* [26] both under the name of radiation from Cherenkov wakes. In this paper, the first experiments of the emitted radiation in millimeter wave range from gas jet plasma wakes excited by ultrashort intense laser pulse is presented. A basic theory is described in Sec. 2. Sec. 3 describes the experimental setup. Results are presented and discussed in Sec. 4 and finally a brief conclusion is presented in Sec. 5.

2. Radiation theory

Magnetized wake equations. The geometry of the radiation scheme is shown in Fig. 2. A short laser pulse propagates in the plasma of density N at nearly the speed of light in the $+z$ direction. A DC magnetic field \mathbf{B}_0 exists in the $+y$ direction. For simplicity we take this field to be uniform in space and constant in time. From Maxwell's equations in one-dimensional case, under the present geometry, the following forms are given:

$$-\frac{\partial E_x}{\partial z} = \frac{1}{c} \frac{\partial B_y}{\partial t}, \tag{1a}$$

$$-\frac{\partial B_y}{\partial z} = \frac{1}{c} \frac{\partial E_x}{\partial t} - \frac{4\pi}{c} eNV_x, \tag{1b}$$

$$\frac{1}{c} \frac{\partial E_z}{\partial t} - \frac{4\pi}{c} eNV_z = 0. \tag{1c}$$

In Eq. (1) V_x and V_z are the components of electron velocity which satisfy the equation of motion:

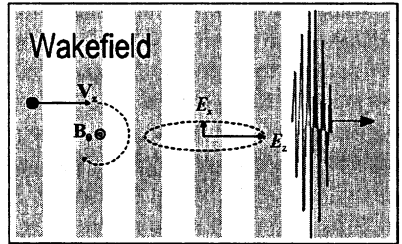


Fig. 2. The schematic view of the magnetized wakes

$$m \frac{\partial V_x}{\partial t} = -eE_x + \frac{e}{c} B_0 V_z, \quad (2a)$$

$$m \frac{\partial V_z}{\partial t} = -eE_z - e \frac{\partial \phi}{\partial z} - \frac{e}{c} B_0 V_x \quad (2b)$$

with ϕ the averaged ponderomotive potential defined by the laser pulse envelope. Here the potential ϕ and, therefore, the fields and electron velocity in the wake are functions of only $\xi = t - z/V_0$; this implies that pump depletion and laser instabilities are neglected. In terms of new variable: $\partial/\partial t \rightarrow \partial/\partial \xi$ and $\partial/\partial z \rightarrow (1/V_0)\partial/\partial \xi$, the system of equations (1) and (2) becomes:

$$\frac{\partial E_x}{\partial \xi} = \beta \frac{\partial B_y}{\partial \xi}, \quad (3a)$$

$$\frac{\partial B_y}{\partial \xi} = \beta \frac{\partial E_x}{\partial \xi} - 4\pi e \beta N V_x, \quad (3b)$$

$$\frac{\partial E_z}{\partial \xi} = 4\pi e N V_z, \quad (3c)$$

$$\frac{\partial V_x}{\partial \xi} = -\frac{e}{m} E_x + \omega_c V_z, \quad (3d)$$

$$\frac{\partial V_z}{\partial \xi} = -\frac{e}{m} E_z + \frac{e}{mc\beta} \frac{\partial \phi}{\partial \xi} - \omega_c V_x, \quad (3e)$$

in which $\beta = V_0/c$ and ω_c is the electron cyclotron frequency. Applying Laplace transformation respect to ξ is a way to solve the system of equations:

$$\tilde{E}_x = \beta \tilde{B}_y, \quad (4a)$$

$$s \tilde{B}_y = s \beta \tilde{E}_x - 4\pi e \beta N \tilde{V}_x, \quad (4b)$$

$$s \tilde{E}_z = 4\pi e N \tilde{V}_z, \quad (4c)$$

$$s \tilde{V}_x = -\frac{e}{m} \tilde{E}_x + \omega_c \tilde{V}_z, \quad (4d)$$

$$s \tilde{V}_z = -\frac{e}{m} \tilde{E}_z + \frac{e}{mc\beta} s \phi - \omega_c \tilde{V}_x. \quad (4e)$$

The mark \sim refers to Laplace transforms of the components and correspondingly ϕ is the Laplace transform of the ponderomotive potential. s is the Laplace variable. Answers are:

$$\tilde{B}_y(s) = \frac{\omega_c \omega_p^2}{cD(s)} \phi, \quad (5a)$$

$$\tilde{E}_z(s) = \frac{\omega_p^2 \beta^2 - s^2 (1 - \beta^2)}{s \omega_c \beta} \tilde{B}_y(s), \quad (5b)$$

where $D(s) = [\epsilon\beta^2\omega_p^2 - (1 - \beta^2)(s^2 + \omega_p^2 + \omega_c^2)]$, in which $\epsilon = 1 + \omega_p^2/s^2$ and as usual $\omega_p^2 = 4\pi e^2 N/m$ is a plasma frequency.

The inverse Laplace transformation of the above equations gives the components of excited magnetized wakes behind the laser pulse. They describe by the residue of the Eq. (5a) relation at the pole where $D(s) = 0$. The dispersion equation $D(i\omega) = 0$ defines the frequency ω of the wake field. The amplitude of the electric field is given at the pole $s = i\omega$ and takes the following form:

$$B_y = \frac{i\omega^3 \omega_c \omega_p^2}{2c[\omega_p^4 \beta^2 + (1 - \beta^2)\omega^4]} \varphi(i\omega). \quad (6)$$

For a laser pulse of the duration τ the ponderomotive potential form is:

$$\phi = \frac{eE_L^2}{4m\omega_L^2} \quad (7)$$

with E_L the amplitude of the electric field and ω_L the frequency of the laser pulse. In this case $\varphi(i\omega)$ for substituting in Eq. (6) is:

$$\varphi(i\omega) = \frac{eE_L^2}{2mi\omega\omega_L^2}. \quad (8)$$

Longitudinal component of the magnetized wake electric field may be expressed via the relation:

$$E_z = \frac{\omega_p^2 \beta^2 + (1 - \beta^2)\omega^2}{i\omega\omega_c \beta} B_y. \quad (9)$$

By taking also into account the contribution from another pole $s = -i\omega$, the final relation for the longitudinal component of the magnetized wakes can be obtained as:

$$E_z = \frac{eE_L^2}{2mV_0} \frac{\omega\omega_p^2}{\omega_L^2} \frac{\omega_p^2 \beta^2 + (1 - \beta^2)\omega^2}{\omega_p^4 \beta^2 + (1 - \beta^2)\omega^4} \sin \omega\xi. \quad (10)$$

Dispersion relation and boundary condition. Applying the external magnetic field in the y direction, perpendicular to the laser beam path and so $\mathbf{k} \perp \mathbf{B}_0$ and also the wave electric field $\mathbf{E} \perp \mathbf{B}_0$, radiation occurs in the extra ordinary mode (XO) and the dispersion relation is given by:

$$\frac{c^2 k^2}{\omega^2} = 1 - \frac{\omega_p^2}{\omega^2} \frac{\omega^2 - \omega_p^2}{\omega^2 - \omega_H^2}, \quad (11)$$

in which $\omega_H^2 = \omega_p^2 + \omega_c^2$ is the upper hybrid frequency. It should be noticed that the radiation can occur when $\epsilon \geq 1$, where ϵ is the dielectric constant of the medium [27]. In Fig. 3 it is shown that for the extra ordinary mode radiation, this condition is satisfied when $\omega_p \leq \omega < \omega_H$.

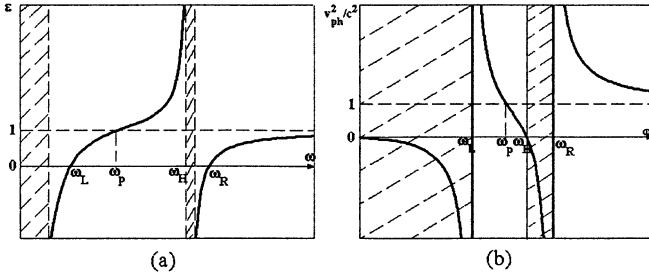


Fig. 3. Magnetized plasma dielectric changes versus ω .
The dashed regions are evanescent regions

In Fig. 4 the dispersion relation is plotted. The eigenmodes in the plasma are the left (L) and right (R) branches of the XO mode and have cutoff frequencies at $\omega_{R,L} = [\pm\omega_c + (\omega_c^2 + 4\omega_p^2)]^{1/2}$ respectively. These two branches have two components to their electric field; an electromagnetic component $E = E_x$ and an electrostatic component $E = E_z$. Waves with $\omega < \omega_L$ and $\omega_H < \omega < \omega_R$ are evanescent in the plasma. Intersection point of the wave dispersion relation Eq. (11) and the laser pulse line ($\omega = kv_{gL}$ with $v_{gL} = (1 - \omega_L^2/\omega_p^2)^{1/2}$ is the laser pulse group velocity in plasma) will introduce the radiation frequency. The laser pulse line intersects with the L branch of XO mode of the plasma. In unmagnetized plasma we also have this intersection, but although the phase velocity of the plasma waves is c their group velocity is zero. The energy deposited by the laser pulse in unmagnetized plasma does not propagate outside of the plasma and is finally dissipated in the form of plasma heating. It is noticeable that the laser pulse line never intersects with the electromagnetic eigenmode of the plasma ($\omega^2 = \omega_p^2 + k^2c^2$). In a magnetized plasma unlike the unmagnetized case the group velocity of an excited mode is not zero. Fig. 4 shows that the laser pulse can couple to a radiation mode where the velocity of the pulse $v_{gL} \sim c$ is larger than the phase velocity of the radiation. As it can be seen in Fig. 4 continuous change of the boundary will make problem for the emitted pulse, such as the plasma density decreases gradually in the boundary. Decreasing the density will make the evanescent layer wider to the downward in the figure, which will cover the radiation frequency. Tunneling through that layer will damage the radiation intensity noticeably.

In the case of sharp plasma boundary on the other hand according to the continuity of the tangen-

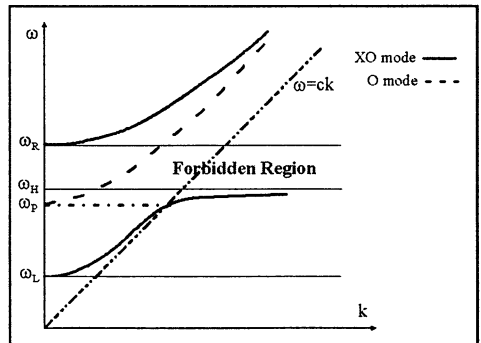


Fig. 4. Plasma dispersion relation

tial components of E , the reflected and the transmitted waves at the boundary, the transmission coefficient for E_x tends to one. Using gas jet plasma configuration with a suitable nozzle is a way to make the sharp boundary plasma.

3. Experimental setup

The experimental setup and measuring system are shown in Fig. 5. A mode locked Ti:sapphire laser beam operating at $\lambda_L = 800$ nm wavelength, with the pulse width of $\tau_L = 100$ fs (FWHM), and maximum energy of 100 mJ per pulse with 10 Hz repetition rate is used to excite wakefields. The laser pulse irradiates into the vacuum chamber through a 5 mm thickness CaF_2 window and then is focused by a lens of $f/5$ at about 0.5 mm upper than the top of the gas jet nozzle. Gas jet open time is triggered by the signal from laser pulse operation system through a pulse generator with duration of 250 μs and repetition frequency of 10 Hz similar to laser pulse repetition frequency. Different nozzles are used in the experiment in order to change the gas density and also boundaries configuration. Interaction region is laying between the DC permanent magnets poles. The strength of the applied magnetic field is up to 8 kG. As the region of this field along the $+z$ direction is about 2.5 cm, longer than x_R , the Rayleigh length, it is expected to be uniform in the interaction region. The experiment is done in the Nitrogen and Helium gases at the initial base pressure of below 5 mTorr and maximum gas jet back pressure of 8 Atm. The measurement system consists of a crystal detector, horn antenna, waveguide and oscilloscope with limitation of maximum frequency measurable at 200 ps and covering 10 Giga sample per second. Antenna and waveguide are in U-band with cut-off frequency at 31.4 GHz for TE_{10} mode to observe the temporal waveform of the radiation.

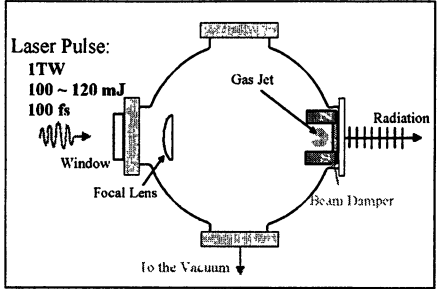


Fig. 5. Experimental setup

Interaction region is laying between the DC permanent magnets poles. The strength of the applied magnetic field is up to 8 kG. As the region of this field along the $+z$ direction is about 2.5 cm, longer than x_R , the Rayleigh length, it is expected to be uniform in the interaction region. The experiment is done in the Nitrogen and Helium gases at the initial base pressure of below 5 mTorr and maximum gas jet back pressure of 8 Atm. The measurement system consists of a crystal detector, horn antenna, waveguide and oscilloscope with limitation of maximum frequency measurable at 200 ps and covering 10 Giga sample per second. Antenna and waveguide are in U-band with cut-off frequency at 31.4 GHz for TE_{10} mode to observe the temporal waveform of the radiation.

4. Results and discussion

In Fig. 6 a typical radiation sample is shown at $B_0 = 7.8$ kG corresponds to $\omega_c = 1.4 \cdot 10^{11}$ rad/s. This satisfies the condition $\omega_p \gg \omega_c$, and the " $\mathbf{V}_p \times \mathbf{B}$ acceleration condition" exactly. The duration of the pulse is 200 ps FWHM, which is the pulse width limitation of the oscilloscope. From Nitrogen plasma also the similar result is obtained. The wake duration in the plasma can be obtained from $\tau_p \approx L_p / v_g$, where L_p is the plasma length of the order of Rayleigh length and v_g is the group velocity wakes in plasma. In this experiment with laser spot size of 20 μm

L_p is about 1.55 mm. From the stagnation theory of supersonic gas jets according to nozzle size, the electron density is calculated to be 10^{17} cm^{-3} so τ_p should be about 1 ns. Instrument limitations and the dispersion in the waveguides allow us to conclude only that the measured value is an upper limit of the pulse duration.

Figure 7 shows the intensity change of the radiation electric field when the horn antenna is rotated around "z" axis in order to find the radiation polarization. Radiation is expected to be polarized in the x direction normal to the magnetic field lines and also laser pulse propagation directions. 0 degree shows the angle of the horn antenna when the electric field is in the x direction and 90 degree refers to the electric field in the y direction.

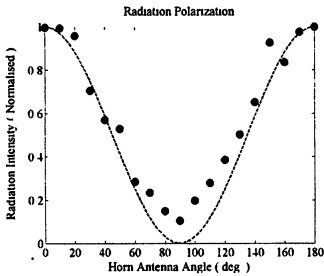


Fig. 7. Normalized intensity of the radiation versus horn antenna rotation angle.

0 degree corresponds to the direction of laser pulse propagation ($x = y = 0$). The radiation is mainly in a ± 5 degree angle respect to z axis in y - z plane in forward direction.

In order to find some information about the dependence of radiation intensity to different plasma densities, three kind of nozzles are machined. One is a simple cylindrical nozzle at 0.5 mm throat diameter (c). Another two are supersonic nozzles at 0.5 mm throat diameter and divergence angle of 12 degree. For smaller one the exit hole diameter is 1 mm (b) and for bigger one it is 1.3 mm (a). Density of the neutral flow for cylindrical nozzle is obtained by the fringe shifts of a Mach-Zhender interferometer

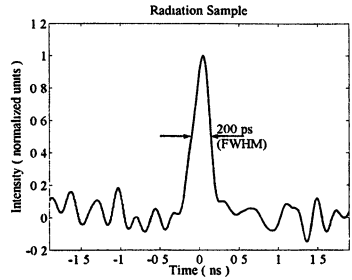


Fig. 6. A typical type of radiation

The function $\cos^2\theta$, which is theoretically expected behavior of the polarized electric field of a dipole antenna in the x direction, is also plotted in dash form in Fig. 7. Data are from Nitrogen plasma at the same density and magnetic field normalized to the maximum radiation intensity at 0 degree. Although intensity of He plasma radiation is not the same with Nitrogen but polarization direction is at the same direction.

In Fig. 8, the radiation intensity can be found in different angles refer to z axis in y - z plane.

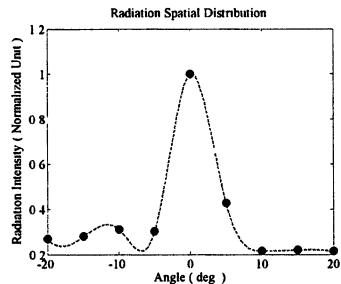


Fig. 8. Radiation spatial distribution

and for supersonic nozzles it is calculated by the stagnation theory of nozzles. Results are shown in Fig. 9. Circles, squares and diamonds refer to cylindrical, 1 mm and 1.3 mm exit supersonic nozzles respectively. All of them are measured at 0.5 mm height from nozzle tip at which laser beam is focused. In Fig. 10 three sample of the radiation pulse from nozzles are comparable. Data are radiation from He plasma at 0.15 mTorr base pressure of the interaction chamber and 1 Atm back pressure of gas jet with open time at 250 μ s. Because the detection system is not calibrated the data are just the relative intensity of the radiation detected on the oscilloscope. In Fig. 11 the intensity of radiation in different gas jet back pressures from both He and N₂ plasma is shown. In this part also the base pressure of the interaction chamber is 0.15 mTorr and gas jet open time is 250 μ s.

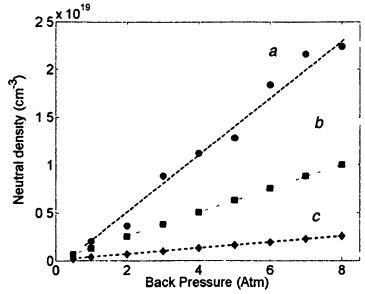


Fig. 9. Neutral density of different gas jet nozzles.

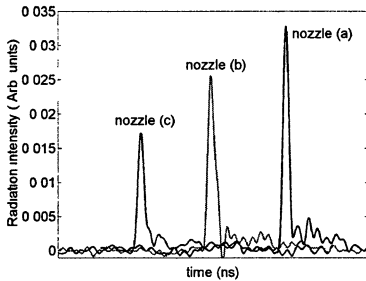


Fig. 10. Radiation intensity of three different nozzles.

$1.5 \cdot 10^{17} \text{ cm}^{-3}$, $6.5 \cdot 10^{17} \text{ cm}^{-3}$, $2 \cdot 10^{18} \text{ cm}^{-3}$, and plasma electron densities are five times bigger for N₂ and two times bigger for He. All of them are larger than the optimum magnitudes. Bigger nozzles to decrease the density damage the sharpness of boundaries, which will result in damping the radiation intensity. In Figs. 10 and 11 it is clear that increasing the plasma density in both cases of different nozzle dimensions as well as increasing the gas back pressure, decrease the plasma wakefield amplitude as is expected from theory.

In this part also the base pressure of the interaction chamber is 0.15 mTorr and gas jet open time is 250 μ s.

According to laser-plasma interaction theory, maximum wakes amplitude is created when $c\tau_L = \lambda_p$. In the present experiments, the maximum of wakefield amplitude is expected at 5 THz plasma frequency, corresponds to electron density $3.1 \cdot 10^{17}$. Increasing the density from this optimum magnitude decreases the wakes amplitude sharply [28]. The lowest neutral densities of nozzle (a), (b) and (c) are

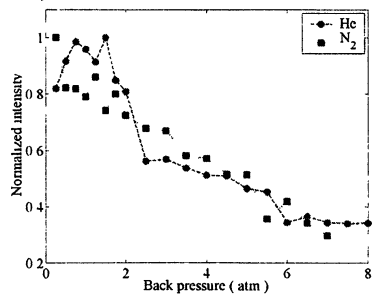


Fig. 11. Radiation intensity versus back pressure for both N₂ and He gases.

5. Conclusions

$V_p \times B$ radiation from the interaction of short intense laser pulse and magnetized gas jet plasma is investigated as a new source of coherent radiation in tunable frequency, ranging from GHz to THz. Different characteristics of radiation have also been studied.

We would like to acknowledge Professor Michael I. Bakunov at Department of Radiophysics, University of Nizhny Novgorod for his very useful discussions.

References

1. Marques J. R., Geindre J. P., Amiranoff F., Audebert P., Gauthier J. C., Antonetti A. and Grillon G., *Phys. Rev. Lett.*, **76**, 3566 (1996).
2. Modena A., Najmudin Z., Dangor A. E., Clayton C. E., Marsh K. A., Joshi C., Malka V., Darrow C. B., Danson C., Neely D. and Walsh F. N., *Nature*, **337**, 606 (1995).
3. Rosenzweig J. B., Cline D. B., Cole B., Figueroa H., Gai W., Konecny R., Norem J., Schoessow P. and Simpson J., *Phys. Rev. Lett.*, **61**, 98 (1988).
4. Nakajima K., Enomoto A., Kobayashi H., Nakanishi H., Nishida Y., Ogata A., Shoji T. and Urano T., *Nucl. Instrum. Methods*, **292**, 12 (1990).
5. Chen P., Dawson J. M., Huff R. W. and Katsouleas T., *Phys. Rev. Lett.*, **54**, 693 (1985).
6. Fainberg Y. B., Balakirev V. A., Onishchendo I. N., Sidelnikov G. L. and Sotnikov G. V., *Plasma Phys. Rep.*, **20**, 606 (1994).
7. Tajima T. and Dawson J. M., *Phys. Rev. Lett.*, **43**, 267 (1979).
8. Kitagawa Y., Matsumoto T., Minamihata T., Sawai K., Matsuo K., Mima K., Nishihara K., Azechi H., Tanaka K. A., Takabe T. and Nakai S., *Phys. Rev. Lett.*, **68**, 48 (1992).
9. Tang C. M., Sprangle P. and Sudan R., *Appl. Phys. Lett.*, **45**, 375 (1984).
10. Esarey E., Ting A. and Sprangle P., *Appl. Phys. Lett.*, **53**, 1266 (1988).
11. Sprangle P., Esarey E., Ting A. and Joyce G., *Appl. Phys. Lett.*, **53**, 2146 (1988).
12. Kaw P. K., Sen A. and Katsouleas T., *Phys. Rev. Lett.*, **68**, 3172 (1992).
13. Bereziani V. I. and Murusidze I. G., *Phys. Lett. A*, **148**, 338 (1990).
14. Chiou T.C., Katsouleas T., Decker C., Mori W.B., Wurtele J.S., Su J.J., *Phys. Plasmas*, **2**, 310 (1995).
15. Nishida Y., Yoshizumi M. and Sugihara R., *Phys. Lett.*, **105**, 300 (1984).
16. Nishida Y., Yoshizumi M. and Sugihara R., *Phys. Fluids*, **28**, 1574 (1985).
17. Nishida Y. and Shinozaki T., *Phys. Rev. Lett.*, **65**, 2386 (1990).
18. Ruth R. D., Chao A. W., Morton P. L. and Wilson P. B., *Particle Accelerators*, **17**, 171 (1985).
19. Chen P., Su J. J., Dawson J. M., Bane K. L. F. and Wilson P. B., *Phys. Rev. Lett.*, **56**, 1252 (1986).
20. Rozenzweig J. B., Breizman B., Katsouleas T. and Su J. J., *Phys. Rev. A*, **44**, 6189 (1991).
21. Clayton C. E., Joshi C., Darrow C. and Umstadter D., *Phys. Rev. Lett.*, **54**, 2343 (1985).
22. Nakajima K., Kawakubo T., Nakanishi H., Ogata A., Kitagawa Y., Kodama R., Mima K., Shiraga H., Suzuki K., Yamakawa K., Zhang T., Kato Y., Fisher D., Downer M., Tajima T., Sakawa Y., Shoji T., Yugami N. and Nishida Y., *Proc. AIP Conf.*, **335**, 145 (1995).
23. Ginzburg V. L., *The Propagation of Electromagnetic Waves in Plasmas* (Pergamon Press, New York, 1970).
24. Hamster H., Sullivan A., Gordon S., White W. and Falcone R. W., *Phys. Rev. Lett.*, **71**, 2725 (1993).
25. Yoshii J., Lai C. H., Katsouleas T., Joshi C. and Mori W. B., *Phys. Rev. Lett.*, **79**, 4194 (1997).
26. Yugami N., Higashiguchi T., Gao H., Sakai S., Takahashi K., Ito H., Nishida Y. and Katsouleas T., *Phys. Rev. Lett.*, **89**, 065003-1 (2002).
27. Ginzburg V. L., *Physics-Uspekhi*, **39**, 973 (1996).
28. Marques J. R., Dorchiev F., Amiranoff F., Audebert P., Gauthier J. C. and Geindre J. P., *Physics of Plasmas*, **5**, 1162 (1998).
29. Yamanaka C., *Inertial Fusion Sciences and Applications* (Elsevier press, 2001), Chapter 1, 30.

FORMATION AND EVOLUTION OF DUST ION-ACOUSTIC NONLINEAR STRUCTURES IN COMPLEX PLASMAS

S. I. Popel

Institute for Dynamics of Geospheres RAS, Moscow, Russia

A review on dust ion-acoustic nonlinear structures is presented

1. At present a major portion of the investigations of plasmas is devoted to multicomponent plasmas containing electrons, ions, charged microspheres or dust grains, and neutral particles. The term "complex plasmas" is finding increasing use for such plasmas. Complex (dusty) plasma systems cannot usually survive in the absence of either external sources of electrons and ions or plasma particle fluxes from the regions where there is no dust. The fluxes of electrons and ions are absorbed by dust particles, that results in variable charges of the latter. The dust particle charging process is a basis for the strong dissipativity of the complex plasma system. The strong dissipativity results in a new physics of nonlinear wave structures in complex plasmas. First, anomalous dissipation originating from dust grain charging appears. Second, new kinds of nonlinearities take place. The anomalous dissipation leads to preferential importance of shock waves in complex plasmas, which have specific features that distinguish them from ordinary collisional and collisionless shock waves. These shock waves are collisionless in the sense that they are insignificantly affected by electron-ion collisions. However, in contrast to classical collisionless shock waves, the anomalous dissipation due to dust charging involves interaction of the electrons and ions with dust grains in the form of microscopic electron and ion currents to the grain surfaces. That dust ion-acoustic shock waves associated with anomalous dissipation can actually exist was proved analytically in [1]. Dust ion-acoustic shock waves were observed for the first time in laboratory experiments at the University of Iowa (USA) [2] and at the Institute of Space and Astronautical Science (Japan) [3]. Not only shocks can propagate in complex plasmas. The possibility of the existence of the dust ion-acoustic solitons has been shown [4]. The purpose of this brief review is to present the most important results on dust ion-acoustic nonlinear structures. In Section 2 we present a theoretical description of dust ion-acoustic shock waves and compare theoretical conclusions with the experimental data. Section 3 is devoted to the description of the dust ion-acoustic solitons. In Section 4 we discuss some possibilities of observation of the dust ion-acoustic nonlinear structures and some applications. In Section 5 the main conclusions are stated.

2. Let us formulate the main experimental results on shocks in complex plasmas. The experiments [2] showed that:

- (i) Dust ion-acoustic shocks are generated at sufficiently high dust densities (under the experimental conditions of [2], at dust densities such that $\epsilon Z_{d0} \equiv n_{d0} Z_{d0} / n_{i0} \geq 0.75$, where $q_d = -Z_{de}$ is the dust grain charge, $-e$ is the electron charge, $n_{d(i)}$ is the dust (ion) density, and the subscript 0 stands for the unperturbed plasma parameters). In [2], the conclusion about the formation of a shock wave was drawn from the fact that the perturbation front steepens as time elapses. At sufficiently low dust densities, the perturbation front does not steepen but instead widens.
- (ii) When the shock wave structure has formed, the shock front width $\Delta \xi \sim M c_s / \nu_q$ is described by the theoretical estimate, which is based on the model developed in [1], where $M c_s$ is the shock-wave structure speed, M is the Mach number, c_s is the ion-acoustic speed, ν_q is the grain charging rate.
- (iii) The velocity of the dust ion-acoustic waves increases considerably with increasing ϵZ_{d0} .

In experiments [3], Nakamura *et al.* revealed that the most important feature of dust ion-acoustic shocks in complex plasmas is the following.

- (iv) In the absence of dust, the effect of the electron and ion charge separation gives rise to oscillations in the shock wave profile in the vicinity of the shock front, while the presence of dust suppresses these oscillations.

In this context, the requirement to the theoretical model is the adequate description of the relevant experiments. We use the so-called ionization source model developed in [5, 6]. We note that under the experimental conditions of [2, 3], the ionization source term in the evolutionary equation for the ion density should be independent on the electron density [6]. Theoretical investigations have been carried out for the following values of the plasma parameters, which correspond to the experimental those: the electron and ion temperatures were equal to one another, $T_e = T_i = 0.2$ eV; the background ion density $n_{i0} = 1.024 \cdot 10^7$ cm⁻³ was the same for all series of simulations; the grain radius was $a = 0.1$ μm; the width of the rectangular initial perturbation was 25 cm; and the excess initial perturbed ion density above the background ion density in the remaining unperturbed plasma was $\Delta n_i / n_{i0} = 2$ (see Fig. 2 in [2]). The calculations were carried out for different values of the parameter ϵZ_{d0} .

In Fig. 1 (which is analogous to Fig. 2 from [2]), we illustrate the time evolution of the ion density at

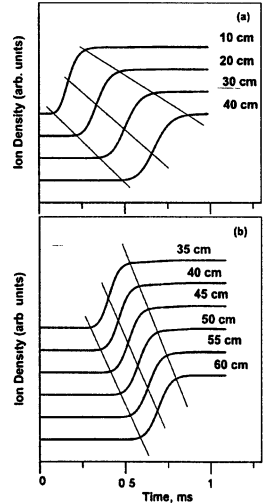


Fig. 1

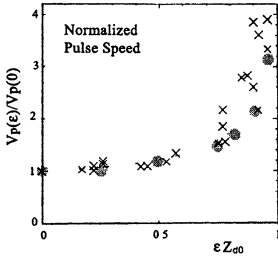


Fig. 2

Fig. 2, *b* in [2]) and also to the estimate obtained using the theoretical model of [1].

The initial perturbation evolves in such a way that its front velocity V_p becomes nearly constant about 1 ms after it starts propagating through the background plasma. Figure 2 shows the dependence of the perturbation front velocity (normalized to its value in the absence of dust, $\epsilon = 0$) on the parameter ϵZ_{d0} . For comparison, we also plot the experimental points (crosses) taken from Fig. 5 in [2]. The calculated results are represented by closed circles. The agreement between theory and experiment is quite good.

Now, we test our theoretical model against the experimental result (iv), which was obtained in [3]. The experiments described in that paper were carried out with a double plasma device, which was modified so that the dust component was present in the plasma. The parameters of the dusty plasma were as follows: $T_e \approx 1\text{--}1.5$ eV, $T_i < 0.1$ eV, $n_{e0} \sim 10^8\text{--}10^9$ cm $^{-3}$, and the dust grain radius $a \approx 4.4$ μm . The unperturbed dust density n_{d0} was varied from 0 to about $\sim 10^5$ cm $^{-3}$. Dust ion-acoustic shock waves were excited by applying a triangular voltage pulse with a peak amplitude of 2.0 V and a rise time of about 10 μs to the driver anode. The calculations were carried out for different dust densities and for the following parameter values: $T_e = T_i = 1.5$ eV, $n_{i0} = 2.3 \cdot 10^8$ cm $^{-3}$ (the ion background density was the same for all series of simulations), and the dust grain radius $a = 4.4$ μm . The width of the perturbation ($\Delta x \approx 20$ cm) and its shape were determined self-consistently, in accordance with the method for exciting a shock wave. It should be noted that Nakamura and Bailung [7] compared the theoretical and experimental potential differences between the grains and the plasma under essentially the same conditions as those prevailing in the experiments of [3]. They found that, although the ion temperature in those experiments was significantly lower than the electron temperature ($T_i \ll T_e$), the experimental results were best fitted by the curve calculated for $T_i = T_e$. They attributed this circumstance to the possible ion acceleration to energies comparable to the electron energy. That is why, in our calculations, the values of the electron and ion temperatures were taken to be the same.

In Fig. 3 (which is analogous to Fig. 3 from [3]), we illustrate the time evolution of the ion density at different distances from the grid. The time evolutions were calculated for (*a*) $n_{d0} = 0$ (the electron density being $n_{e0} = 2.3 \cdot 10^8$ cm $^{-3}$) and

different distances from the grid. The time evolutions (heavy curves) were calculated for $\epsilon Z_{d0} = 0$ (*a*) and $\epsilon Z_{d0} = 0.75$ (*b*). The light curves show the widening of the wave front (at $\epsilon Z_{d0} = 0$) and its steepening (at $\epsilon Z_{d0} = 0.75$). This agrees with the experimental data from [2]. The extent to which the shock front widens was calculated to be $\Delta \xi \sim Mc_s / v_q \sim 0.3$ ms (see Fig. 1, *b*), which corresponds to that observed experimentally (see

(b) $n_{d0} = 1.46 \cdot 10^4 \text{ cm}^{-3}$ (the electron density being $n_{e0} = 4.6 \cdot 10^8 \text{ cm}^{-3}$). We can see that the electron and ion charge separation gives rise to oscillations in the shock wave profile and that the dust suppresses these oscillations, as is the case in the experiments of [3]. The theoretically calculated rise time of the shock front is about $5 \mu\text{s}$, which corresponds to the experimental data.

Hence, the theoretical ionization source model makes it possible to describe all the main experimental results on dust ion-acoustic shock waves.

3. Let us discuss the possibility of the existence of the dust ion-acoustic solitons in complex plasmas. The anomalous dissipation caused by the charging processes means that the existence of completely steady-state nonlinear structures is impossible. In reality, this note is truth for any real system. However, in complex plasmas it leads to qualitatively new results [4]. The usual consideration of a soliton assumes that the electrons are not trapped by the potential well formed by the soliton. However, this assumption is violated when the inequality $\tau \gg L/v_{Te}$ is valid, where τ is the characteristic time of the variation of the soliton field, L is the characteristic spatial scale of the soliton, and v_{Te} is the electron thermal velocity. In complex plasmas the characteristic time τ of soliton damping is determined by the relationship $\tau^{-1} \sim \nu_q$ and the inequality $\tau \gg L/v_{Te}$ is fulfilled for for the most of dusty plasmas. Thus in the dusty plasmas it is necessary to take into account the effect of adiabatically trapped electrons.

We have performed the following investigations.

- (1) We have studied the steady-state compressed solitons, which propagate with a constant speed (Mach number) M , with taking into account the influence of adiabatically trapped electrons. Here we neglect the dissipation processes related to the dust particle charging (below we use the notion "steady-state soliton" for the solitons satisfying equations which do not take into account these dissipation processes).
- (2) We have considered the evolution of the initial steady-state soliton (from the previous item) in complex plasmas with taking into account the dissipation processes related to the dust particle charging and absorption of plasma particles on dust.
- (3) We have studied the interaction of two different compressive dust ion-acoustic solitons with the trapped electrons taking into account their damping due to the anomalous dissipation.

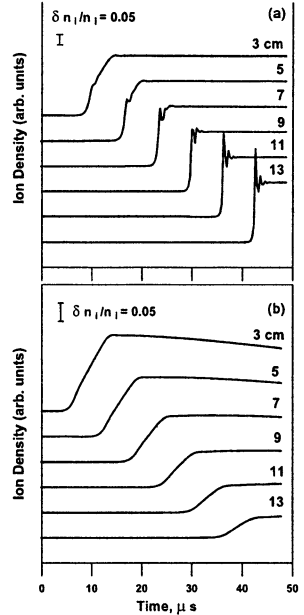


Fig. 3

The main results of the investigation are the following.

1) The properties of the compressive solitons with the trapped electrons are very different from those with not trapped those (Boltzmann electrons). In particular, the maximum possible amplitude of the soliton with the trapped electrons is much larger than that of the "Boltzmann" soliton, while the region of allowable Mach numbers for the former is much wider than for the latter. This can be seen from Fig. 4, which represents the dependencies of the maximum value of Mach number M_{\max} (a) and the maximum soliton amplitude φ_0 on $Z_{d0}d \equiv Z_{d0}n_{d0}/n_{e0}$ for the compressive soliton with the trapped electrons (thin lines) and that with Boltzmann electrons (bold lines). This shows the principal possibility to study experimentally the role of trapped electrons in the soliton formation.

2) The evolution of the initial perturbation in the form of the steady-state compressive soliton with the trapped electrons occurs in the following manner. The soliton is damped due to the dissipation originating from the dust particle charging processes. The speed of the perturbation decreases. However, at any time the form of the evolving perturbation is similar to that of the steady-state compressive soliton with the trapped electrons corresponding to the Mach number at this moment of time. This fact is related to small variations in the dust particles charges (less than several per cent from the equilibrium value).

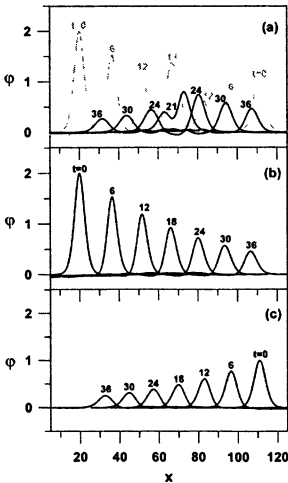


Fig. 5

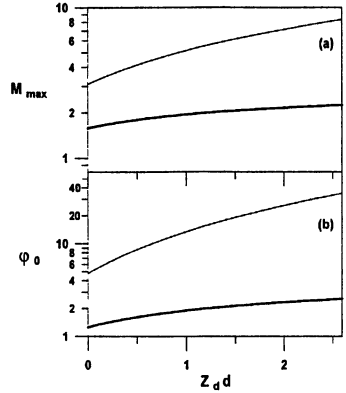


Fig. 4

3) After the interaction of two damped solitons, each perturbation has the form, which is close to that of the same soliton perturbation propagating individually from the beginning (not subjected to the interaction). This property is the property inherent in solitons. In Fig. 5 the interaction (a) of two individual compressive solitons (b) and (c) with the trapped electrons is presented. Grey and black lines correspond to the soliton profiles before and after the interaction at different moments of time t . At $t = 0$ all the perturbations have the form of the steady-state solitons.

Thus there is a possibility of the existence of the dust ion-acoustic compressive solitons which are damped and slowed down, but their form corresponds to the soliton one for the running value of their speed. After their interaction they conserve

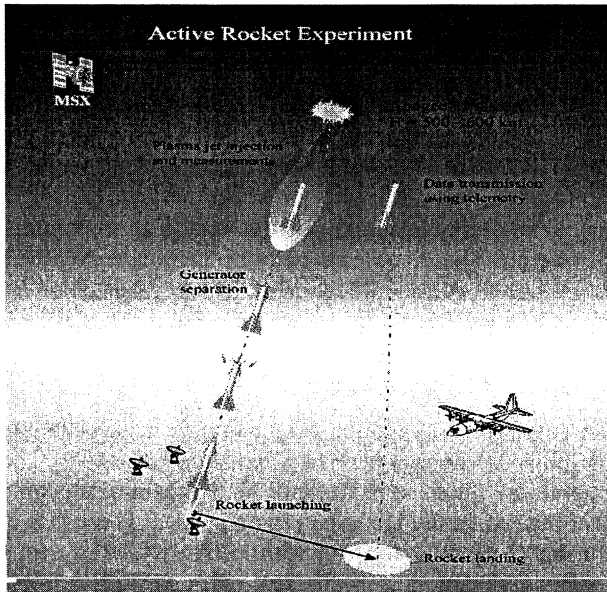


Fig. 6

the soliton form. The role of trapped electrons in such solitons is significant. These solitons can be called as "dissipative solitons".

4. Here we present some possibilities of observation of the dust ion-acoustic nonlinear structures and some applications where their physics can be important.

(1) The idea of the formation of shocks related to dust charging in active rocket experiments, which involve the release of some gaseous substance in near-Earth space, was forwarded in [8]. The source for the charged particle release in the ionosphere in these experiments is the generator of high-speed plasma jets. The shock wave front is associated with the fore (border)-part of the jet propagating in the plasma of the ionosphere. Macro (dust) particles appear as a result of condensation. Drops are charged due to their interaction with the ambient plasma and the photoelectric effect. The optimum speeds of the jet are 10 km/s. The optimum altitudes for such experiments are 500–600 km. The scheme of the active experiment is given in Fig. 6.

(2) The presence of dust in cometary coma can modify shock wave formed as a result of Solar wind interaction with a comet [9]. The outer shock wave (bow shock) can be considered as the dust ion-acoustic shock wave, because it is formed as a result of the interaction of cometary ions with Solar wind protons. For dust densities $n_d > 10^6 \text{ cm}^{-3}$ near the comet nucleus, charged dust particles influence drastically the structure of the bow shock front. Its width is in accordance with the theory of shocks related to dust particle charging.

(3) The fact that the dissipative solitons have the properties very different from those of the Boltzmann solitons can be helpful from the viewpoint of space plasma observations and diagnostics.

Among the applications to industry the hypersonic aerodynamics should be noted. The main problems of hypersonic flight in an atmosphere are associated with generation of shocks resulting in high mechanical and thermal load on elements of an aircraft construction, sharp growth of drag force, and reduction of ramjet efficiency. The desirable solution is the modification of properties of air surrounding the aircraft. There is a possibility of the weakening the negative effects, which is related to the modification in shock propagation when plasma methods (local heating and ionization of air surrounding the aircraft) are used. However, dust (aerosol particles), which is formed as a result of condensation of air surrounding the aircraft modify also the shock behaviour.

5. Thus, an anomalous dissipation originating from the charging processes results in a possibility of the existence of a new kind of shocks. The theoretical ionization source model allows us to describe all the main results on the dust ion-acoustic shocks obtained in the laboratory experiments. There is a possibility of the existence of the dissipative dust ion-acoustic solitons. The dust ion-acoustic nonlinear structures are important in different real and artificial objects of geophysical and space plasmas. Their physics should be taken into account in the problems of hypersonic aerodynamics.

This work was supported by INTAS (grant № 2001-0391).

References

1. *Popel S. I., Yu M. Y., and Tsyтовich V. N.* Phys. Plasmas, 1996, **3**, 4313.
2. *Luo Q.-Z., D'Angelo N., and Merlino R. L.* Phys. Plasmas, 1999, **6**, 3455.
3. *Nakamura Y., Bailing H., and Shukla P. K.* Phys. Rev. Lett., 1999, **83**, 1602.
4. *Popel S. I., Golub' A. P., Losseva T. V. et al.*, 29th EPS Conf. Plasma Phys. Contr. Fusion, 2002, **26B**, O-5.32.
5. *Popel S. I., Golub' A. P., Losseva T. V., and Bingham R.* JETP Letters, 2001, **73**, 223; *Popel S. I., Golub' A. P., Losseva T. V. et al.*, Phys. Plasmas, 2001, **8**, 1497.
6. *Popel S. I., Golub' A. P., and Losseva T. V.*, JETP Letters, 2001, **74**, 362.
7. *Nakamura Y. and Bailing H.*, Rev. Sci. Instrum., 1999, **70**, 2345.
8. *Popel S. I. and Tsyтовich V. N.* Astrophys. Space Sci., 1999, **264**, 219.
9. *Gisko A. A., Popel S. I., Losseva T. V., and Vladimirov S. V.*, in preparation.

SELF-CONSISTENT ELECTROMAGNETICALLY DRIVEN LANGMUIR TURBULENCE IN OVERDENSE PLASMA

A. V. Kochetov, V. A. Mironov, G. I. Terina¹, M. V. Shaleev

Institute of Applied Physics, RAS, Nizhny Novgorod, 603950, Russia

¹Radiophysical Research Institute, Nizhny Novgorod, 603950, Russia

Instability of steady-state reflection of an incident electromagnetic wave from the overdense plasma slab due to the excitation of strong Langmuir turbulence is observed by means of computer simulations. Amplitude thresholds of dynamic regimes are specified and structures of penetrating waves in stratified plasma are studied. It is obtained that the penetration speed is determined by the growth rate of modulation instability and skin-layer scale. Landau damping of Langmuir waves is found to be considerably large and it limits the depth of penetration up to a few skin-layer scales.

Introduction

It is known that processes of modulation instability plays an essential role in the formation of Langmuir solitons and the corresponding inhomogeneities of plasma density (cavitons), which can modify strongly the real and imaginary parts of electromagnetic wave effective dielectric constant [1–3]. This modification, for example, leads to the penetration of incident electromagnetic wave through the bounded layer of overdense plasma, what had been discussed in the frameworks of steady state models with given induction approach [4, 5] for plasma bleaching interpretation, while for fixed averaged electric field [2, 3] strong collisionless damping of electromagnetic energy in perturbed plasma was revealed. The study of self-consistent penetration dynamics due to excitation of strong Langmuir turbulence in overdense plasma layer emitted by the strong electromagnetic wave with prescribed amplitude is specific features of presented paper.

Problem formulation, basic equations

We assume that the half-space $0 < z < L$ is filled by the plasma with unperturbed density $n_0(z) > N_c$, where $N_c = m\omega^2/4\pi e^2$, ω is the wave frequency, m, e are the electron mass and charge respectively. The plasma layer is irradiated by the normally incident electromagnetic wave with given amplitude $E_0(t)$. Electromagnetic field in vacuum $z \leq 0$ combines of the incident and reflected wave with amplitude E_r , $z \geq 0$ – transmitted wave E_t . Density of plasma is modified in the field by Miller's force $\mathbf{F} = -T \nabla |u|^2$, $u = E/E_p$ is the complex amplitude of the wave, normalized to plasma field, $E_p^2 = 16\pi N_c T$, T is the temperature of electrons (we seek the solution of the electric field in the layer in the form $E(x, t) = E(x, t) \exp(-i\omega t)$).

For the description of the field evolution in plasma the modified nonlinear Schrödinger equation (NSE) is used

$$i \frac{\partial u}{\partial t} + \frac{\partial^2 u}{\partial x^2} + \frac{\partial^2 u}{\partial z^2} + (\epsilon_0 - n)u = 0. \quad (1)$$

It is written in dimensionless variables with units $t = 2/\omega$, $x = \sqrt{3r_d}$, $z = 1/k_0 = c/\omega$, c is the light velocity, $n = N_c$, $u = E_p$. We consider structures being the periodic in the x direction with the period much smaller than their scale in the z direction. In such case we can neglect by the longitudinal (z) component of the field appearing due to density stratification along x axe. In the z direction the standard boundary conditions of the continuation of the tangential components of electric and magnetic field require in dimensionless variables that

$$e_z = -ie + 2ie_0(t) \Big|_{z=0}, \quad (2)$$

$$e_z = ie \Big|_{z=l}, \quad (3)$$

where $e = \bar{u}$ is the averaged electromagnetic field ($\bar{}$ means the averaging over period in the x direction) in the difference of total u , including both the electromagnetic and plasma fields, l is a normalized width of the layer.

We perform the analysis of (1)–(3) simulating the nonlinearity like for steady state ponderomotive density perturbations [2] with additional term

$$n = \overline{|u|^2} - |u|^2, \quad (4)$$

keeping $\bar{n} = 0$, because plasma density modification along x axes is considered to be short scaled and so rapid comparing to field evolution.

The typical laws of the smooth turning on (at $t = 0$) and turning off (at $t = t_1$) amplitude of incident wave are fixed by the next formulas:

$$e_0(t) = e_0(1 - \exp(-t^2/T_0^2)), \quad e_0(t) = e_0 \exp(-(t-t_1)^2/T_1^2), \quad T_0, T_1 \gg 1. \quad (5)$$

We assume that the initial field distribution ($u(x, z, t) = 0$) to be uniform in the x direction and to be linear skin-layer structure ($n = 0$) in the z direction exciting of incident wave with amplitude e_0 .

After averaging (1) we get the equation for the electromagnetic component $e(z)$

$$i \frac{\partial e}{\partial t} + \frac{\partial^2 e}{\partial z^2} + \epsilon_{eff} e = 0, \quad \epsilon_{eff} = \epsilon_0 + \frac{\overline{|u|^2} u}{u} - \overline{|u|^2}, \quad \epsilon_0 = 1 - n. \quad (6)$$

To close the system (1)–(3), (6) we suppose $u(x, z) - e(x, z)$ is a smooth function of z so (1) transforms to

$$i \frac{\partial u}{\partial t} + \frac{\partial^2 u}{\partial x^2} + (\epsilon_0 - n)u = -\frac{\partial^2 e}{\partial z^2}. \quad (7)$$

The set of equations (1)–(7) is solved numerically using the combination of spatial mesh approximation and spectral methods. During simulations (7) we take into account a spectral dependent damping of Langmuir waves as according well known Landau formula, as modeling damping $\Gamma(k) = \beta^2 k^2$.

Numerical results

The calculations show that there are two thresholds for the steady state instability depending on the incident wave amplitude: the first one for the development of modulation instability in the skin-layer of an incident wave; the second one for the wave penetration. For half bounded plasma layer (that is the same for the layer with the width much more than the skin-layer scale) the first one corresponds to the threshold for modulation instability of the electromagnetic field in uniform overdense plasma $e_0 = E_{th} = (\epsilon_0 | / 2)^{1/2}$. The second one is a bit (less than 10%) larger than the threshold from analytical estimation of [4].

In Fig. 1 the typical profiles of electromagnetic field amplitude along z coordinate (on the left) and of the total field along x coordinate (on the right) at section $x = 0$ at developed stage of penetration are demonstrated.

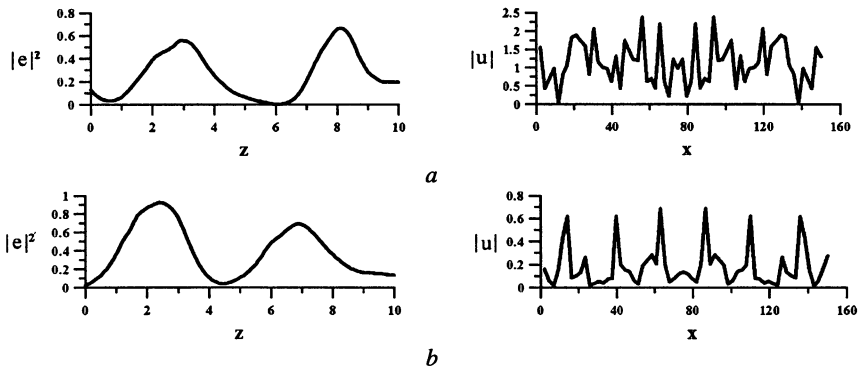


Fig. 1. a) $t = 200$, b) $t = 250$; $\epsilon_0 = -0.025$, $e_0 = 0.2$

The corresponding dynamics of real and imaginary parts of ϵ_{ef} profiles is shown in the Fig. 2. The dynamics of the penetration into the more dense plasma is presented in Fig. 3, 4. Depending on the plasma density and damping parameter β , which controls the spectral dependent Langmuir waves absorption, the evolution of the coordinate of the right boundary of stratified plasma region is shown in Fig. 5. The collisionless absorption of Langmuir waves really can limit the

depth of penetration up to a few skin-layer scales because the imaginary part of effective dielectric constant is of the same order as the real one. Nevertheless the time dependent transmission index, for example, for thick layer as Fig. 6, goes beyond 10%.

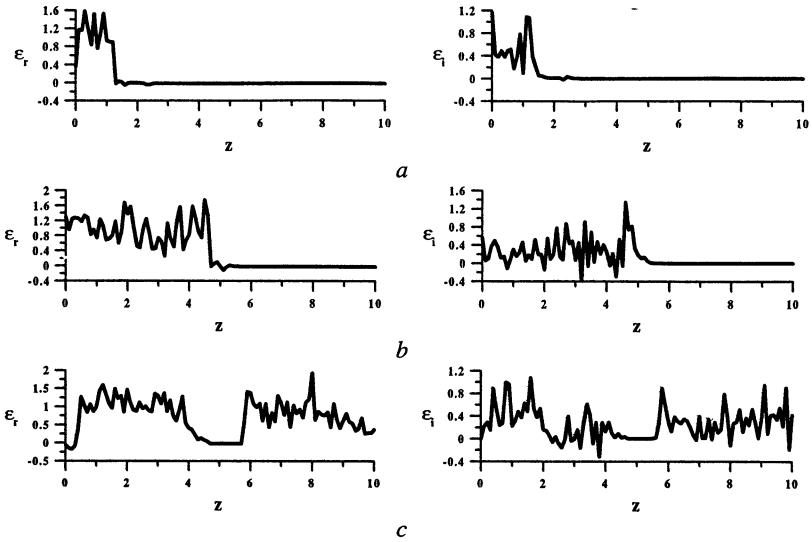


Fig. 2. Real part ϵ_r (on the left) and imaginary ϵ_i (on the right) of effective dielectric constant at the moments: *a*) $t = 100$; *b*) $t = 150$; *c*) $t = 250$ for $\epsilon_0 = -0.025$, $e_0 = 0.2$.

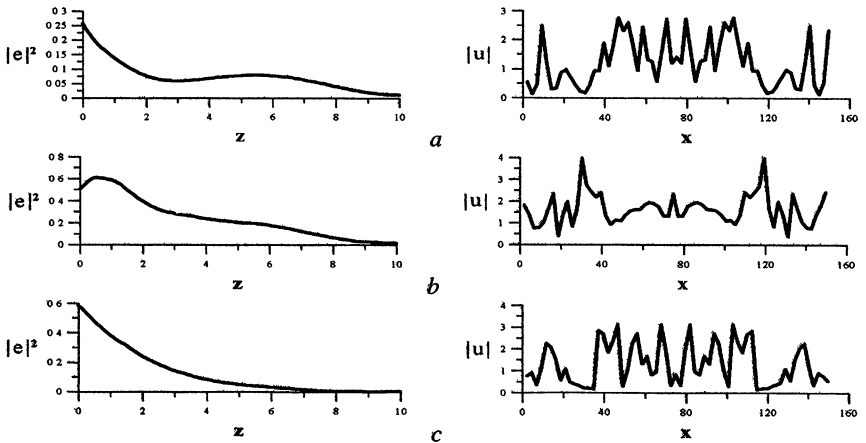


Fig. 3. *a*) $t = 50$; *b*) $t = 100$; *c*) $t = 200$ for $\epsilon_0 = -0.1$, $e_0 = 0.38$, $\beta = 1.5$

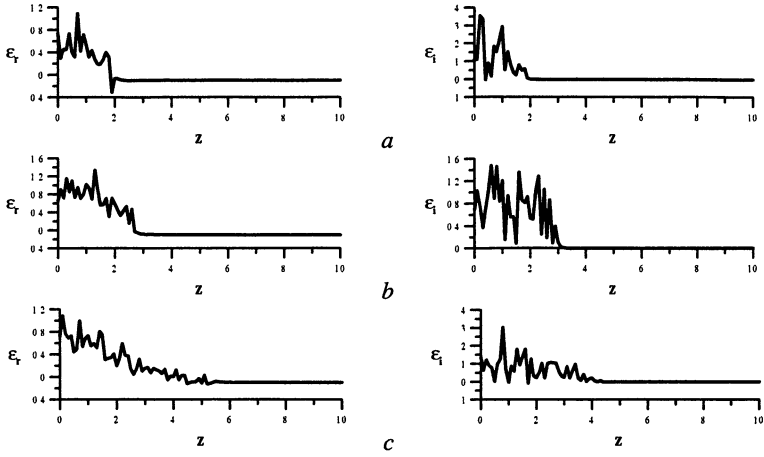


Fig. 4. Real part ε_r (on the left) and imaginary ε_i (on the right) of effective dielectric constant at the same moments as in Fig. 3.

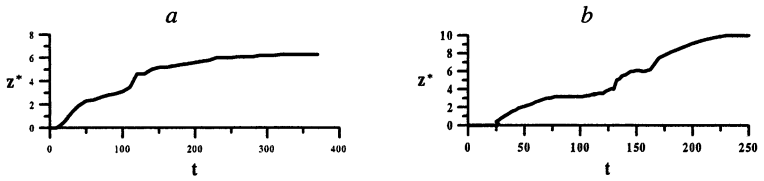


Fig. 5. Expansion of the perturbation region depending on time for a) $\varepsilon_0 = -0.1$, $\varepsilon_0 = 0.38$, $\beta = 1.5$, b) $\varepsilon_0 = -0.025$, $\varepsilon_0 = 0.2$, $\beta = 1.25$.

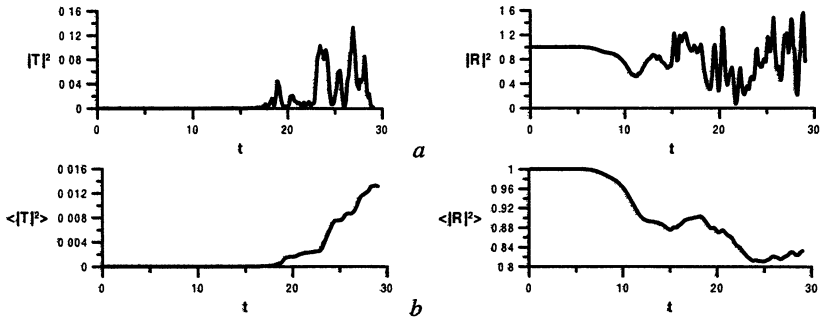


Fig. 6. Transmission $|T|^2$ (a), reflection $|R|^2$ (b) indexes and their averaged over time values $l = 10$, $\varepsilon_0 = -0.25$, $\varepsilon_0 = 0.65$.

Conclusions

The modification of electrodynamics characteristics of stratified plasma due to self-consistent electromagnetically driven excitation of strong Langmuir turbulence leads to the penetration of electromagnetic wave, incident onto the boundary of overdense plasma layer, deep into the plasma. The speed of density modification is determined by the growth rate of modulation instability and skin-layer scale. Landau damping of excited plasma waves is found to be sufficiently important and limits the depth of the penetration in order of a few skin-layer scales. The obtained results must be important, for example, for adequate theoretical interpretation of experimental results for plasma bleaching [6] or artificial ionosphere modification by powerful radiowaves [7, 8].

Acknowledgements. The authors acknowledge the support of this work in part by RFBR grant № 02-02-17277.

References

1. *Shapiro D. V., Shevchenko V. I.*, Handbook of Plasma Physics 2 (Elsevier, Amsterdam, 1984).
2. *Litvak A. G.* Reviews of Plasma Physics (Consultants Bureau, N. Y., 1986).
3. *Kochetov A. V., Mjoelhus E.*, Proc. Intern. Workshop "Strong microwaves in plasmas" (SMP99), Ed. A. G. Litvak (N. Novgorod, 1999), 491.
4. *Litvak A. G., Mironov V. A., Fraiman G. M.* JETP Lett., 1975, **22**, 174.
5. *Litvak A. G., Mironov V. A., Feigin A. M.* JETP, 1979, **50**, 684.
6. *Karfidov D. M.* et al., Fizika plazmy, **15**, 797 (1989, in Russian).
7. *Kochetov A. V.* et al., Physica D, 2001, **152–153**, 723.
8. *Kochetov A. V., Mironov V. A., Terina G. I.*, Adv. Space Res., 2002, **29**, 1369.

ELECTROAERODYNAMIC TURBULENCE IN THE ATMOSPHERE AND ITS LABORATORY MODELING

*E. A. Mareev, N. A. Bogatov, A. E. Sorokin, D. I. Iudin,
V. Yu. Trakhtengerts*

Institute of Applied Physics, Russian Academy of Science, Nizhny Novgorod, Russia

Study of generation mechanisms for short period electric field pulsations provides extensive information on the turbulence under different atmospheric conditions and on electrical processes in the atmosphere. Recent measurements in the surface atmospheric layer reveal a frequency range where electric-field pulsations have a power-law spectrum under both fair-weather and fog conditions; intra-cloud electric field balloon-borne measurements give power-law spectra as well. Along with analytical treatment and computer modeling of these spectra we have elaborated the principles of laboratory modeling for collective effects and electroaerodynamical turbulence in a multi-flow system containing highly charged aerosol particles and performed the initial experiments. We can conclude that spectral index of the electric potential fluctuations in the turbulent flow of the weakly ionized air is close to -2 . In the presence of the uncompensated space charge the potential spectrum is slightly deviates from the power law. The performed experiments and their further development seem to be helpful for understanding the nature of space charge structure formation and lightning discharge inception in thunderstorms.

Introduction

The motion of weakly ionized disperse-phase medium leads to the electric charge separation and generation of large-scale quasi-stationary electric field (electric dynamo) [1] as well as to short-period pulsations of electric field, current and space charge density [2]. Their study is of fundamental importance to recognize global and local components of atmospheric electricity, to investigate intra-cloud, cloud-to-ground and high-altitude discharge inception etc. Electroaerodynamical (EAD) turbulence implies a mode of motion, characterized by the mutual transformation of gas mechanical energy and electric field energy. In the present paper we discuss different approaches to the theoretical description of EAD turbulence, its laboratory modeling and experimental data demonstrating EAD turbulence effects, including field measurements showing the aroelectric structures formation.

It is well known that turbulence in the atmosphere leads to Kolmogorov-type spectra of wind and temperature fluctuations. More recently, the spectra of fluctuations of electric field under different atmospheric conditions have been investigated. For the surface atmospheric layer recent measurements show that electric-field pulsations at frequencies 10^{-2} – 1 Hz have a power-law spectrum under both fair-weather and fog conditions, so that the spectral index varies in the range from -2 to -3 depending on particular atmospheric state [2]. Several electric field

soundings through stratiform clouds and convective regions of mesoscale convective systems, made with balloon-borne electric field meters and radiosondes, have been also examined [3]. All these soundings demonstrate the presence of fine structures in the electric field distribution, with characteristic spatial scales of irregularities ranging from hundreds to tens of meters. Fourier analyses of the measured in-cloud electric fields give power-law spectra that depend on the wave number, with the spectral index close to -2 and with the transition to white noise occurring for spatial scales shorter than 30–35 m.

We have started with the analysis of the mechanisms of spectra formation, taking into account specific electrodynamic properties of thunderstorm clouds, arising due to intensive multi-flow motion of charged particles (heavy charged droplets, light ice crystals, etc.) Our studies to date have shown that a thundercloud has the ability to self-organize. This self-organization is manifested as small-scale electrical stratification, where intense electrical cells with the scales of order of 10–100 m are generated [3–5]. The cells are of particular interest in understanding cloud electricity because the electric field within the cells may exceed the average field value substantially.

In addition, we have developed a model that deals with the analysis of a nonlinear diffusion equation for electric field strength evolution [6]. Using this approach, different parameterizations of inductive and non-inductive mechanisms lead to different expressions for the charge separation current. Point discharge dissipation current and turbulent diffusion current are also taken into account. Stationary states and their stability have been investigated with the model. We have found that a nontrivial stationary state is eventually stable with respect to large-scale perturbations, but this large scale state has superimposed on it smaller scale perturbations having characteristic scales that are dependent on the charging intensity parameters. The latter phenomenon has been considered numerically under a more complicated four-component (ions-hydrometeors) model and applied to common thundercloud conditions. Characteristic scales of order of hundred meters have been found for the perturbations of this nonequilibrium system.

Taking into account the random sources of external currents that describe the charge exchange due to particle collisions, we get a Langevine-type equation for electric field. In the framework of this equation and with reasonable assumptions concerning the correlation properties of the source, we are able to get electric field variation spectra close to the experimental ones we have found from the balloon soundings.

Along with analytical treatment and computer modeling of respective field experiments we have elaborated the principles of laboratory modeling for collective effects and EAD turbulence in a multi-flow system, containing charged aerosol particles, and performed the initial experiments. Their results are presented in the following section of the paper.

Experimental results

We have performed laboratory experiments on the study of EAD turbulence in the weakly ionized flow. The scheme of the experimental setup is shown on

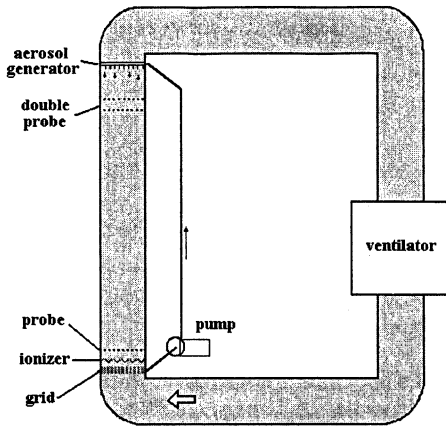


Fig. 1. Scheme of the experimental setup

Fig. 1. The air was pumped along the dielectric tube of $0.4 \times 0.4 \text{ m}^2$ cross section. The flow velocity has been controlled with a help of the grid under 1–5 m/s interval. The ionization was provided with a corona discharge system consisted of 25 needle pairs oriented orthogonal to the airflow. In each pair the needles oriented opposite each to another by their edges, were connected to independent power supplies of opposite polarities. The relation of positive and negative ions in the flow was controlled by the change of voltage on the needles. The air conductivity was

measured by the resistance between two grids separated by 10 cm one from another transverse to the airflow.

The dependence of ion density on the total current of corona discharges is shown on Fig. 2. Distribution of the ion density along the flow in the assumption that the ion mobility was equal $2 \text{ cm}^2 \text{ V}^{-1} \text{ s}^{-1}$ is presented on Fig. 3 for the flow velocity of 5 m/s. Dependence of ion density on the airflow velocity is shown on Fig. 4. It is seen from these figures that the ion density decreases inversely proportional to the distance and increases directly proportional to the flow velocity, which respects to the recombination decay in a case of a neutral ion plasma and to the diffusion charge relaxation in a case of a unipolar plasma.

Local measurements of the potential were carried out with a help of a probe represented a sphere of 1 cm diameter made from a copper wire of 0.3 mm diameter. Such a probe having an extensive effective collecting surface, at the same

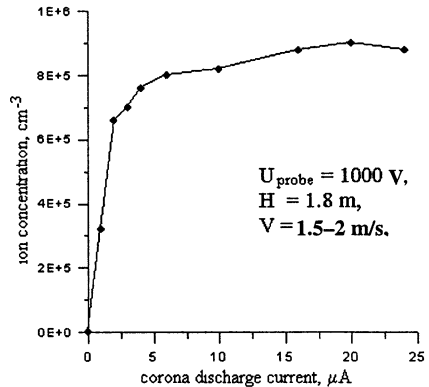


Fig. 2. Dependence of ion density on the total current of corona discharges.

time ensures minimum airflow perturbation. A probe was attached to a glass-made thick-walled tube, oriented across the airflow and penetrated through the setup wall. A copper wire connected a probe to the high-resistor amplifier input, was put inside the glass tube.

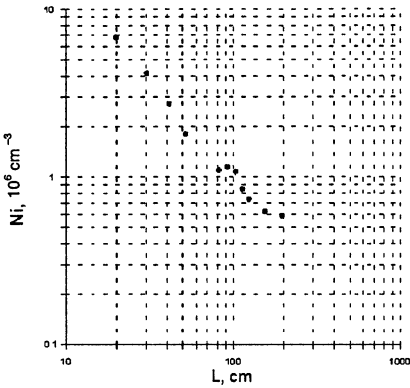


Fig. 3. Ion density as dependent on the distance from the ionizer (for the airflow velocity 5 m/s). The total current of corona discharges was assumed to be 10 μ A, the ion mobility – 2 cm² V⁻¹s⁻¹.

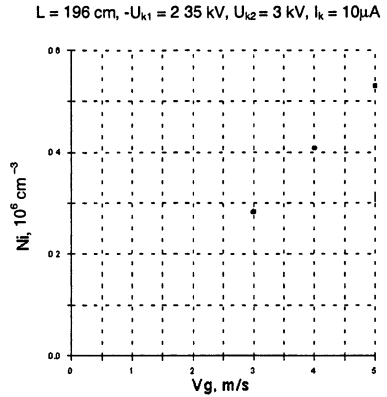


Fig. 4. Ion density as dependent on the airflow velocity (at the point separated by 196 cm from the ionizer).

To minimize the capacitance between the connecting wire and ionized air outside the tube a thin wire of 0.05 mm diameter has been used. The capacitance of the probe, connected to the input of the high-resistor amplifier, was measured according to the upper limit frequency transmission of the signal from the generator connected to the probe through the known resistance. It turned out to be equal to 5 pF, which corresponded to the documented value of the input capacitance of the amplifier. The distance from the ionizer to the probe along the flow was equal to 2.5 m. Two grids noted above used for the conductivity measurements, were situated at the distance of 1 m from the ionizer.

Supplying the voltage between these grids, we have introduced respective perturbations into the airflow and observed their influence on the potential fluctuation spectra in the flow. The signal from the amplifier output was digitized with a help of 12-digit AD converter. One time series length was equal 2¹⁵ values with a sampling rate of 1 ms. The spectrum was calculated on the base of measured data arrays using the fast Fourier transform algorithm. The procedure of a preliminary subtraction of the mean and spectrum smoothing with Hahn's window function has been applied. The examples of the spectra obtained on the base of experimental data analysis, are presented on Fig. 5.

The spectra presented correspond to the following parameters: the total corona current is equal $2 \mu\text{A}$, the airflow velocity is 5 m/s , the mean probe potential is about zero, the voltage between the grids $\varphi = 640 \text{ V}$ for Fig. 5, *a* and $\varphi = 0$ for Fig. 5, *b*.

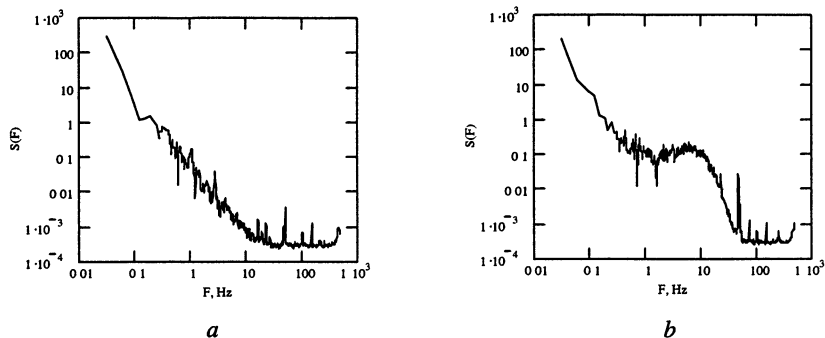


Fig. 5. Potential fluctuation spectra of the EAD turbulence in the airflow: *a* – in the presence of the external electric field, *b* – in the absence of the external electric field.

As a result of laboratory measurements we can conclude that spectral index of the electric potential fluctuations in the turbulent flow of the weakly ionized air is close to -2 . In the presence of the uncompensated space charge the potential spectrum is slightly deviates from the power law.

Superposition of the external electric field along the airflow on the partial section of the tube of 10 cm long leads to the enhancement of fluctuation level in the frequency from 0.5 to 50 Hz (with maximum of the effect on the frequencies $5\text{--}10 \text{ Hz}$). Upper limit of this range corresponds to the inverse path time of the external field region by the airflow.

The following stage of this research implies the addition of aerosol component into the airflow and comparison of respective EAD spectra with the results of field measurements in the atmospheres.

Conclusions

We have elaborated the principles of laboratory modeling for collective effects and electroaerodynamical turbulence in a multi-flow system containing highly charged aerosol particles and performed the initial experiments, which seem to be helpful for understanding the nature of space charge structure formation in the atmosphere. As a result of laboratory measurements we can conclude that spectral index of the electric potential fluctuations in the turbulent flow of the weakly ionized air is close to -2 . In the presence of the uncompensated space charge the potential spectrum is slightly deviates from the power law.

Superposition of the external electric field along the airflow on the partial section of the tube of 10 cm long leads to the enhancement of fluctuation level in the frequency from 0.5 to 50 Hz (with maximum of the effect on the frequencies 5–10 Hz). Upper limit of this range corresponds to the inverse path time of the external field region by the airflow.

Analyzing these spectra and comparing them with generation mechanisms for short period electric field pulsations provides extensive information on the turbulence under different atmospheric conditions and on electrical processes in the atmosphere.

Acknowledgements. This work was supported by the Russian Foundation for Basic Research (project № 00-02-17758) and the Science Support Foundation.

References

1. *Mareev E. A. and Trakhtengerts V. Yu.*, Radiophys. Quant. Elect., 1996, **39**, 797.
2. *Anisimov S. V., Mareev E. A., Bakastov S. S.*, J. Geophys. Res., 1999, **104**, D12, 14359. Ibid: 1994, **99**, 10603. *Anisimov S. V. and Mareev E. A.*, DAN, 2001, **381**, 1. Ibid: 2000, **371**, 101.
3. *Mareev E. A., Sorokin A. E., Trakhtengerts V. Yu., Marshall T. C., Stolzenburg M.*, Fine structure of thunderstorm electric field: spectra from soundings and significance for charge generation mechanisms, Proc. XII Int. Conf. Atm. Electr. (Versalles, France, 2003, accepted).
4. *Trakhtengerts V. Yu.*, Electrical cells in thunderstorm clouds, Doklady Akademii Nauk, 308, 584, 1989 (in Russian).
5. *Mareev E. A., Sorokin A. E., and Trakhtengerts V. Yu.*, Effects of collective charging in a multi-flow aerosol plasma, Plasma Physics Reports, **25** (3), 289–300 (1999).
6. *Mareev E. A., Sorokin A. E.*, Autowave regimes of a thunderstorm electrification, Radiophys. Quantum Elect., **39** (1–2), 797–814 (2001).

STOCHASTIC MODEL OF DUST PARTICLE GROWTH IN PLASMAS

M. V. Shatalina

Institute of Applied Physics, Russian Academy of Science, Nizhny Novgorod, Russia

It is known from the experiments that small growing dust particles in plasma usually form rather complicated resembling fractal clusters. We present a generalized ballistic model of structure formation in dusty plasmas. We develop a numerical model of the growth of a dust grain in plasma and examined its characteristics. The process of dust cloud formation has been investigated as well. In the modeling we took into account different laws of interaction between dust particles. Numerical simulations provide the growth rate of dust particles close to experimental values.

Introduction

In the recent studies dusty plasma is a popular object of theoretical and experimental investigations. Under usual circumstances the dust grains accumulate a negative electrical of the order of 10^2 to 10^4 times the charge of an electron, due to the high mobility of the electrons as compared to ions. Sometimes the presence of dust can essentially influence characteristics of plasma that contains dust particles [1]. It is known from the experiments that small dust particles in plasma occasionally form the fractal structure in the shape of cauliflower when growing [2]. The state of the numerical and theoretical modeling of these dusty plasma phenomena is less developed than the state of experiment up to now, and recently has attracted great attention including particle simulation code development [3]. We investigated a growth rate for dust particles in plasmas under different circumstances and considered fractal properties of growing clusters. Also we discussed the application of the simple stochastic models of fractal clusters (so named DLA-models) for dust structure formation. Macroscopic characteristics of dust structure were examined.

Basic aspects

In our modeling we have generalized the common ballistic a growing model of the Brownian cluster for of structure formation in dusty plasmas. We considered three-component plasma consisted of electrons, ions and dust particles. Dust structure is characterized by its radius R , charge Q and N – the number of particles in a structure. The charge of structure Q can be estimated as $Q \cong C\phi$, where $C = 2R$ – structure capacity [4], $\phi \cong T_e / e$ – thermal potential of the structure.

Dust structure fractal dimension D can be approximated for $N \gg 1$ by the following equation:

$$D = \frac{\ln N}{\ln(R/a)}, \quad (1)$$

where a – radius of a small dust particle [5].

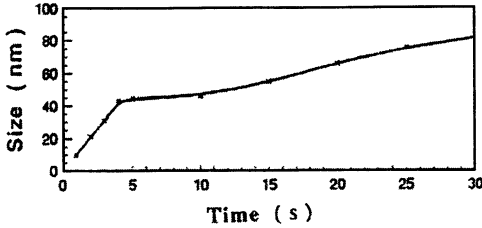


Fig. 1. Average radius dynamic [6]

Experimental observations [6] demonstrated the two regimes of dust grain growth in plasmas (Fig. 1). We have focused on the first stage where radius of a structure increases fast and linear and parameter of non-ideality of dusty plasma

$$\Gamma = \frac{U_{dd}}{E_{kin}} \ll 1, \quad (2)$$

where U_{dd} and E_{kin} is potential and kinetic energy of dust particles interaction. In this case we can use the ballistic model with interaction.

Model

In the modeling we took into account different laws of interaction between dust particles. Absorbing surface of dust particle leads to non-Debye potential [7]:

$$\varphi = \varphi_0 \left[\frac{1}{2} \frac{T_e}{T_e + T_i} \left(1 + \frac{T_i}{2e|\varphi_0|} \right) \frac{a^2}{r^2} + \frac{a}{r} \exp\left(-\frac{r}{r_D}\right) \right]. \quad (3)$$

Also we have taken into account another mechanism of dust particle interaction – effective attraction. This effect may occur due to dust grain adsorption of the plasma particles therefore the resulting interaction force is repulsive at short distance and attracting at remote distance [8].

We assumed that if the particle reaches the structure it will join the structure under the influence of intermolecular forces and occupies a place near the closest point of the structure. The distance between particles in the structure $L = 2a$, $a = 1 \div 10$ nm. Also we take into consideration that adhesion probability of a particle is less than 1. The penetration of small dust particles with high kinetic energy to the growing structure has been specified to characterize various types of dust materials.

For the numerical calculation the time of growth can be estimated as:

$$T_{str} \cong N_{total} v_d^{-1}, \quad (4)$$

where $v_d = n_d \sigma_{str} V_{Td}$ – dust frequency of collision (V_{Td} and n_d – thermal velocity and concentration of dust particles, $\sigma_{str} \cong \pi R^2$ – absorption cross-section of the structure), N_{total} – total number of algorithm steps. Since the adhesion probability is less than 1 we have $N < N_{total}$. From the other hand we can estimate the growth time using simple theoretical approach. Let the rate of particle increasing in the structure is

$$dN / dt = v_d. \quad (5)$$

From (1) and (5) we have

$$R \propto t^{\frac{1}{D-2}}. \quad (6)$$

Numerical simulation results

Using the following parameters of dusty plasma: $T_e = 2\text{eV}$, $T_i \approx T_d = 0.1\text{ eV}$, $n_e = n_i = 10^9\text{ cm}^{-3}$, $n_d = 10^8 \div 10^{10}\text{ cm}^{-3}$ we have found the fractal dimension of the dust structures

$$D = 2.88 \pm 0.06, \quad (7)$$

which characterizes sufficiently dense packing of the cluster. For dust structure radius temporal growth from (6) we have $R \propto t^{1/137}$, that is close to linear. Parameter of non-ideality becomes larger than 1 when dust structure radius reached 40 nm.

3-D view of a spherical dust grain in our model is presented on Fig. 2.

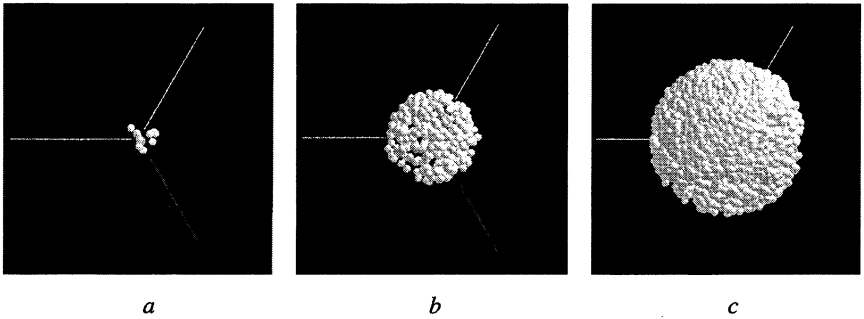


Fig. 2. 3-D view of dust grain simulation: *a* – structure starts growth, *b* – structure is forming the fractal cluster, *c* – fractal cluster for $R \cong 40\text{ nm}$ (end of calculations).

Conclusions

We have presented a model of structure formation in dusty plasmas as a generalized ballistic model of the Brownian cluster. In particular, we built a numerical model of the growth of a dust grain in plasma and examined its characteristics. In the modeling we took into account different laws of interaction between dust particles. The fractal dimension of the dust structures $D = 2.88 \pm 0.06$, which characterized sufficiently dense packing of the cluster. The application of the simple stochastic models of fractal clusters (so named DLA-models) for dust structure growth is discussed.

References

1. *Tsyтович V. N.*, Uspekhi Physicheskikh Nauk, 1997, **167** (1), 57–99
2. *Boufendi and Bouchoule A.*, Plasma Sources Sci Technol., 1994, **3**, 262–267.
3. *Joyce G., Lampe M., and Ganguli G.*, IEEE Transactions on Plasma Science, 2001, **29** (2), 238–246.
4. *Alpert Ya. L., Gurevich A. V., Pitaevsky L. P.*, Artificial Sattelites in Rarified Plasma, M. Nauka, 1964, 298 p.
5. *Smirnov B. M.*, Fractal Cluster's Physic, M : Nauka, 1991.
6. *Garscadden A., Ganguly B. N., Haaland P. D. and Williams J.*, Plasma Sources Sci Technol., 1994, №3.
7. *Khodataev Ya. K., Bingham R., Tarakanov V. P., Tsyтович V. N.*, Phizika plasmy, 1996, **22** (11), 1028–1038.
8. *Ignatov A. M.*, Phizika plasmy, 1998, **24** (8), 731–737.

HOT ELECTRONS AT ELECTRON-ION COLLISIONS IN STRONG LASER FIELDS

A. A. Balakin and G. M. Fraiman

Institute of Applied Physics RAS, Nizhny Novgorod, Russia

Electron-ion collisions in strong electromagnetic fields in non-relativistic and ultra-relativistic cases are considered. Expressions for distribution on energies of the high-energetic electrons, appeared due to collisions, hot electrons density and the rate of the Joule heating are derived. The comparison with experiment is fulfilled.

Recent experiments on the strong (including relativistically strong) laser emission propagation in plasma [1, 2] fixed the presence of the intense generation of fast electrons, distribution function of which has the power law of decrease and reaches oscillatory energies. Peculiarity of the last experiments, as authors noted [1], consists in that spatial and temporal ranges of the interaction of short-pulse (with duration from hundreds femtosecond and higher) laser emission with transparent plasma are small, so collective phenomenon (turbulence) have no time for rise. This is clear also from the physical consideration: there is no cause for the development of such strong small-scale turbulence, which could produce so many high-energetic (with energy of several MeV) electrons in transparent plasma. To our mind the only possible mechanism of such electrons generation is the electron-ion collisions in ultra-relativistic laser field.

Traditional models of electron-ion collisions based on the account of only small-angle scattering [3] can not explain results observed in experiment. They predict lesser number of fast (hot) particles and more rapid law of decreasing of their number in dependence from their energy in comparison with experimental data. Formerly an alternative model of collisions description, including the account of the sufficient particles attraction during the scattering process, have been proposed by the authors [4]. Application of this model results to description of hot electrons generation at electron-ion collisions and comparison with experimental data is the object of the present work.

In the beginning let us determine the range of laser emission parameters, where the presented model is suitable. In further formulas electron temperature T will be measured in eV, the power P will be in 10^{18} W/cm², frequencies in 10^{15} Hz, concentrations n in 10^{18} cm⁻³, all other values are in SGS.

Now let us return ourselves to the main narration. At first, plasma should be cold in comparison with oscillatory energy

$$v \ll v_{osc} = \frac{eE}{m\omega_0} \Leftrightarrow T \ll 6.7 \cdot 10^5 \frac{P}{\omega_0^2}. \quad (1)$$

This is quite an easy condition and it is fulfilled practically for all plasma types at interaction with the short laser pulses (especially on the first stage on the experiment).

Secondly, the laser field intensity should be large enough for the characteristic scale of the scattering b_{osc} to be small in comparison with oscillations radius

r_{osc}

$$b_{osc} = \frac{e^2 Z}{v_{osc} p_{osc}} \ll r_{osc} = \frac{v_{osc}}{\omega_0} \Leftrightarrow \omega_0 \ll 110 \cdot P^{3/8}, \quad (2)$$

where $p_{osc} = eE/\omega_0$ is the oscillatory momentum. This is rather new condition never being considered in electron-ion collisions theory. It may be also rewritten like the condition of smallness of the potential energy of the ion Coulomb field on oscillations radius r_{osc} compared with the oscillatory energy mv_{osc}^2 .

To describe particles scattering in such regime (1), (2) let us use the fact, that the particles collision happens in two stages [4]. In the beginning particle attraction to the ion (i.e., actually, variation of the test particles density) occurs at practically invariable momentum. Then the "hard" collision with strong change of electron momentum, including the scattering on large angles and departure from the Coulomb center, happens.

To determine the particle concentration before the last hard collision $n(\mathbf{r})$ one can use both the results of numerical simulation and/or results of the analysis of mapping [4]. In both cases the dependence $n(\mathbf{r})$ is singular:

$$n = n_e \frac{a}{\rho} \sum_n \delta \left(t - \frac{\pi}{\omega_0} \right), \quad (3)$$

where $\rho = \sqrt{x^2 + y^2}$ is the transversal electron coordinate before the hard collision, $a(v) \geq b_v = e^2 Z / mv^2$ is a some coefficient playing the role of characteristics of the degree of particles attraction to the ion and having abrupt dependence from the initial velocity v direction relatively v_{osc} .

The first term v_{osc}/v corresponds to traditionally considered particles moving along "rectilinear" trajectories. The second term a/ρ describes electrons having experienced the strong attraction to the ion and changed sufficiently their drift velocity. Note, that for every flight for the most of such particles one may consider the scattering on the total velocity $V = v + v_{osc}(t)$ like the small angles scattering! Previously [4] such particles have been called "representative" electrons.

The hard collision may be described by formulas from the Rutherford problem [6]. With accounting of the smallness of the drift velocity (1) momentum

variation here is determined by the oscillatory momentum value at the collision moment and by the impact parameter ρ :

$$\Delta p \underset{\Delta p \ll p_{osc}}{\approx} 2p_{osc} \frac{b_{osc}}{\rho}. \quad (4)$$

At this it is proposed that collisions occur only in maximum of the oscillatory velocity (it is the effect of bunching who provides this [4, 5]) and the collision is momentary. The latter condition implies the limitation on the impact parameter:

$$\rho v_{osc} \ll \pi \omega_0 \Leftrightarrow \rho \ll r_{osc}. \quad (5)$$

Otherwise velocity variation at the scattering is substantial and Rutherford's formulas are not suitable. However, this limitation is not important, since energy variation of such particles in strong fields ($b_{osc} \ll r_{osc}$) is small in comparison with the oscillatory energy.

Relation (4) allows binding the particles distribution on impact parameters with particles distribution on momentum variation in unity of time. Using the distribution (3) we have:

$$f(p) = 4n^2 p_{osc}^2 \frac{vab_{osc}}{p_{osc} p^3}. \quad (6)$$

It is seen, that the dependence of particles distribution on momentum variation from the first term in (6) corresponds to the law of decreasing $\sim 1/p^4$. We should remind, that this term has been derived for rectilinear trajectories. The second term describing representative electrons decreases more slowly – like $\sim 1/p^3$. Note here, that the higher the degree of singularity in correlation function the slower law of decreasing in distribution on energy variation.

So, analysis of the particles distribution on energy variation allows to determine whether the approximation of rectilinear trajectories is suitable. If it is, then the distribution on the momentum variation is one-dimensional and decreases like $\sim 1/p^4$. If the distribution decreases more slowly, then the small angles approximation is not suitable and the singularity is essential in correlation function.

From the relation of the kinetic energy and the particle momentum (m is the rest mass of electron)

$$w = \sqrt{p^2 c^2 + m^2 c^4} \approx \begin{cases} p^2 / 2m, & p \ll mc \\ cp, & p \gg mc \end{cases}$$

It is easy to find the particles distribution on energy in accordance with formula $f(w) = f(p) p dp / dw$ for non-relativistic $w \ll mc^2$

$$f(w) = 8\pi n^2 m p_{osc}^2 \frac{vab_{osc}}{p_{osc} (2mw)^{3/2}} \quad (7)$$

and relativistic cases $w \gg mc^2$

$$f(w) = 8\pi n^2 m p_{osc}^2 \frac{v c a b_{osc}}{p_{osc} w^2}. \quad (8)$$

We shall bring here the dimensional estimation of concentration of particles $n(w) = \int_w^\infty f(w) w dw$ with energies exceeding some limit in relativistic case for the period of field, supposing $w, c p_{osc} \gg mc^2$:

$$n(w)[\text{cm}^{-3} \text{c}^{-1}] \approx 10^{25} \frac{n_e^2 Z}{\sqrt{T} w}. \quad (9)$$

In this relation particles energy w is in MeV, other values are in accordance with agreement before (1). In particular, considering number of particles with energy higher than 1 MeV for plasma¹ with concentration 10^{19} cm^{-3} and volume $300 \times 20 \times 20 \text{ } \mu\text{m}$ at the momentum duration of 10 ps, one find that the hot electrons number is of the order of $10^9 Z$ particles (here $Z \geq 10$ is the charge of ions in plasma) and is coinciding sufficiently with experimental particles number $10^{10} \dots 10^{11}$.

The reduction on 1 of power in (8) in comparison with (6)² is connected with the account of the axial symmetry of the electrons distribution after collision. In reality, in experiments [1, 2] it is the distribution of particles having fly out in the same direction that is measured, i.e., actually, the distribution function on momentum $f(p)$ have been found in (6). With account of aforesaid, superimposing theoretical dependence (6) on the experimental curve one can see the good coincidence (Fig. 1).

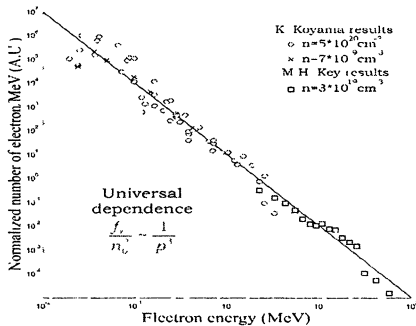


Fig. 1. The comparison of the experimental (Fig. from [1, 2]) and theoretical (full line, (6)) dependencies of hot electrons distribution on energies.

From the Fig. 1 one can once more come to a conclusion in benefit of the collisional nature of hot electrons origin. At the collisional heating there is a natural upper limit of the momentum (and, correspondingly, energy) variation which particles may get. This is doubled oscillatory momentum $2p_{osc}$ corresponding to the experiment [2] (Fig. 1) with energy about 2 MeV. We see, indeed, the abrupt cutting (the decrease of the hot particles number) for energies higher 2 MeV. Similar results has been gotten also in [1].

¹ This data correspond to experiment [1].

² Remind, that in ultra-relativistic case energy and momentum are linearly bound $w = pc$.

Results represented above are obtained in frames of the pair collisions approximation, when it is supposed that the probability of the simultaneous collision of third and more particles at the same point is negligible. The condition of this approximation realization is the smallness of the interaction volume:

$$nV_{\text{int}} \ll 1. \quad (10)$$

Usually (without field) the interaction volume is estimated as $V_{\text{int}} = b_v^3$, that leads to evaluation

$$nb_v^3 \ll 1 \Leftrightarrow nr_D^3 \gg 1, \quad (11)$$

where $r_D = \sqrt{4\pi e^2 n / mv_T^2}$ is the Debye radius. In strong fields the interaction volume is $V_{\text{int}} \approx \sigma_{\text{eff}} r_{\text{osc}}$, that leads to condition:

$$r_E = \sqrt{eZ/E} \ll r_D. \quad (12)$$

But this condition, obviously, may be derived from other considerations. Indeed, new scale r_E , arising at the account of particles attraction, is the scale, from which the particle in oscillation get exactly into the ion (precisely $\sqrt{2\pi}r_E$, see [4]). Effect of attraction will not be "washed off" by the neighboring particles if this scale is lesser than the Debye shielding radius r_D . Hence one again has the condition (12).

So, the supposition about two types of particles being scattered (3) allows to derive the expression for the effective frequency of collisions and hot particles distribution on energies, which agree with experiment sufficiently. More over, the account of "representative" electrons (singular part of (3)) is necessary for the adequate explanation of experimental results. We should stress, that the using of the description with only small-angles collisions account would lead to one-dimensional distribution function of hot particles, that contradicts to the experiment.

This work was performed under the support of RFBR grants No 01-02-16575, 02-02-06005, RAS 1999 (6)-37.

References

1. Key M. H., Cable M. D. et al., Phys. Plasmas, **5**, 1966 (1998); Hatchet S. P., Brown C. G. et al., Phys. Plasmas, **7**, 2076 (2000).
2. Koyama K., Saito N., Tanimoto M., In ICPP 2000, Quebec, Canada, ICPP 4051, page MP1.067 (2000).
3. Shvets G. and Fisch N. J., Phys. Plasmas, **4**, 428 (1997).
4. Fraiman G. M., Mironov V. A., Balakin A. A., Phys. Rev. Lett., **82**, 319 (1999); Fraiman G. M., Mironov V. A., Balakin A. A., Zh. Eksp. Teor. Fiz., **115**, 463 (1999) [J. Exp. Theor. Phys., **88**, 254 (1999)].
5. Fraiman G. M., Mironov V. A., Balakin A. A., Zh. Eksp. Teor. Fiz., **120**, 797 (2001).
6. Landau L. D. and Lifshitz E. M., Mechanics, Pergamon, Oxford, 1969.
7. Lifshitz E. M. and Pitaevski L. P., Physical Kinetics (Pergamon, Oxford, 1981).

OPTICAL-FIELD-INDUCED IONIZATION OF THE GAS BY THE AXICON-FOCUSED LASER PULSES

V. B. Gildenburg, N. V. Vvedenskii

Institute of Applied Physics, Russian Academy of Sciences, Nizhny Novgorod, Russia

Dynamics of the field and plasma at the gas breakdown produced by axicon focusing of high-intensity laser radiation is studied with the effects of natural plasma waves generation and reflected wave spectrum conversion taken into account.

We study in this paper the dynamics of the field and plasma in the discharge column created by axicon focusing [1–3] of a high-intensity laser radiation in homogeneous gas. We focus on the effect of the natural plasma waves generation considered previously for other types of the optical and microwave discharges [4, 5].

The spatiotemporal evolution of the electric field $\tilde{\mathbf{E}} = \text{Re}[\mathbf{E}(\mathbf{r}, t) \exp(-i\omega t)]$ is calculated numerically based on the vector wave equation for the slow time envelope of the field $\mathbf{E}(\mathbf{r}, t)$:

$$\frac{2i}{\omega} \frac{\partial \mathbf{E}}{\partial t} + \delta^2 \nabla (\nabla \cdot \mathbf{E}) + \epsilon \mathbf{E} - \frac{1}{k_0^2} [\nabla \times [\nabla \times \mathbf{E}]] + \hat{\Gamma} \mathbf{E} = 0. \quad (1)$$

This equation takes into account the spatial and time dispersion and allows us to describe the processes of resonance excitation and Landau damping of Langmuir waves in the time-varying plasma. In Eq. (1), $\hat{\Gamma}$ is the model dissipation operator: $\hat{\Gamma} \mathbf{E} = -ia\delta^2 \nabla (\nabla \cdot \mathbf{E})$, $\epsilon = 1 - (N/N_c)(1 - iv/\omega)$ is the complex permittivity of the plasma, $N_c = m(\omega^2 + \nu^2)/4\pi e^2$ is the critical density, ν is the electron collision frequency, a is the coefficient of order 1, $k_0 = \omega/c$, $\delta = \sqrt{3} V_T / \omega$, $V_T \ll c$ is the thermal electron velocity.

Gas breakdown is caused by the optical-field-induced ionization processes. As an example we consider tunnel ionization of hydrogen atoms and determine the time averaged ionization rate by the known expression

$$\frac{\partial N}{\partial t} = 4\Omega (N_g - N) \sqrt{\frac{3E_a}{\pi|\mathbf{E}|}} \exp\left(-\frac{2E_a}{3|\mathbf{E}|}\right). \quad (2)$$

Here $E_a = m^2 e^5 / \hbar^4 = 5.14 \cdot 10^9$ V/cm and $\Omega = me^4 / \hbar^3 = 4.16 \cdot 10^{16}$ s⁻¹ are the atomic field and frequency units, and N_g is the concentration of neutral atoms

before the process of ionization. The parameter range we are interested in here is the following: the wavelength $\lambda \sim 0.6-10 \mu\text{m}$, laser pulse intensity $S \sim 10^{14}-10^{16} \text{ W/cm}^2$, and the gas pressure $p \sim 0.3-60 \text{ atm}$.

We consider the model of the axially symmetric discharge: $N(\mathbf{r}, t) = N(r, t)$ produced by the rotating cylindrical wave with the complex envelope of electric field $\mathbf{E}(\mathbf{r}, t) = \mathbf{E}(r, \varphi, z, t) = \mathbf{E}(r, t) \exp(i\varphi + ik_0 z \cos \theta)$ (r, φ, z are the cylindrical coordinates). Outside the plasma ($r \geq R$, $N(r \geq R) = 0$) the field is a superposition of the converging (incident) and diverging (reflected) TE and TM waves with a given angle of inclination θ to the axis of symmetry z . The incident wave is given by the axial components of electric and magnetic fields: $E_z^{(in)} = C(t) H_1^{(2)}(k_0 r \sin \theta)$, $H_z^{(in)} = -i \cos \theta E_z^{(in)}$, $C(t) = A \exp(-(t-t_0)^2/\tau^2)$, $H_1^{(2)}$ is the first-order Hankel function describing the converging wave. The correlation between the amplitudes of these components (the coefficient $-i \cos \theta$) is chosen so that the transversal components of the fields in the absence of plasma are circular polarized and are the zero-order Bessel function of radius r : $E_\varphi(r) = iE_r(r) \sim J_0(k_0 r \sin \theta)$. In the presence of the plasma the transverse components are always circular-polarized at the axis ($E_\varphi(0) = iE_r(0)$).

Equations (1) and (2) were solved numerically in the space interval $0 \leq r \leq R$ with the initial conditions: $N(r, 0) = 0$, $E_\varphi(r, 0) = iE_r(r, 0) = -2C(0) \cot \theta J_0(k_0 r \sin \theta)$, $E_z(r, 0) = 2C(0) J_1(k_0 r \sin \theta)$ and the following boundary conditions: (i) the solution is analytical at $r = 0$: $E_z = 0$, $\partial E_r / \partial r = \partial E_\varphi / \partial r = 0$, (ii) all field components (including E_r) are continuous at $r = R$ (for detailed expressions and explanation see [6]).

It has been found that the scenario of the breakdown process depends greatly on the convergence angle of the wave. If this angle is less than some critical value $\theta_c \approx 25^\circ$, the maximum plasma density $N_{\text{max}} \sim N_c \theta^2$ that is less than the critical one. However, at the angle exceeding the critical one, the plasma density at the axis increases in the sharpening regime and passes the critical point, after that the fast ionization wave containing the plasma resonance point at the leading front propagates in the radial direction. The results of numerical calculations are presented on Fig. 1 ($\theta = 6^\circ$) and Figs. 2-4 ($\theta = 30^\circ$) in dimensionless variables $k_0 r \rightarrow r$, $\omega t \rightarrow t$, $E/E_a \rightarrow E$, $N/N_c = n$ for the parameter values: $\Omega/\omega = 22$, $k_0 \delta = \sqrt{3} V_T/c = 0.02$, $v/\omega = 0.01$, $a = 0.1$, $N_g = 1.5 N_c$, $t_0 \omega = 100$, $\tau \omega = 50$; in the case $\theta = 6^\circ$: $A/E_a = 0.0037$, $k_0 R = 8$; in the case $\theta = 30^\circ$:

$A/E_a = 0.0204$, $k_0 R = 4$. At the given values of A , the maximum field at the axis in the absence of plasma is the same in both cases: $|E|_{\max}/E_a = 0.1$. The above dimensionless parameters correspond to the vacuum wavelength $\lambda \approx 0.8 \mu\text{m}$, maximum pulse intensity $S \approx 3 \cdot 10^{14} \text{ W/cm}^2$, pulse duration (at the level of $1/e$) $\tau\sqrt{2} \approx 30 \text{ fs}$, and the gas pressure $p \approx 60 \text{ atm}$.

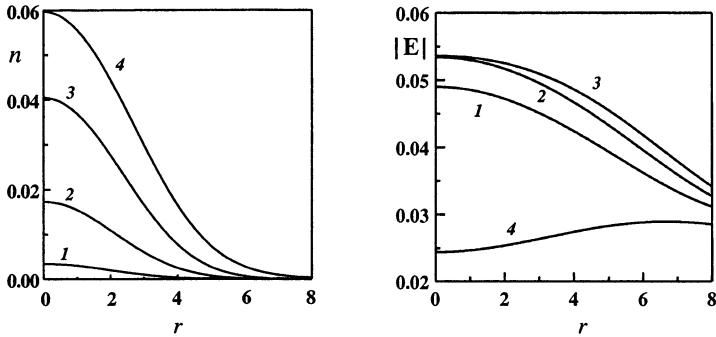


Fig. 1. Evolution of the plasma density $n(r, t)$ and the field amplitude $|E(r, t)|$ at $\theta = 6^\circ$. Curves 1–4 correspond to the time instants $t = 120, 130, 140,$ and 200 , respectively.

The transition of the plasma density through the critical value at $\theta > \theta_c$ (Fig. 2) is accompanied by the excitation of intense Langmuir oscillations, whose amplitude reaches its maximum (twice as high as the amplitude of the unperturbed electric field at the axis) at the front of the ionization wave at $r=1$. The oscillating character of the Langmuir field is clearly seen in Fig. 3. Figure 3, *a* shows the profile of $\text{Re } E_r(r)$ at $t = 150$, and Fig. 3, *b* presents the time behavior of $\text{Re } E_r(t)$ at $r=1$ ($\text{Im } E_r(r, t)$ behaves in a similar way). The wavelength of Langmuir oscillations (the characteristic spatial scale of the field variations) in the region where the gas is completely ionized is on the order of the radius of this region and gradually decreases with decreasing plasma density (Fig. 3, *a*). The oscillation period of the complex amplitude $E_r(t)$ (Fig. 3, *b*) is determined by the frequency shift of the excited Langmuir oscillations with respect to the external field frequency ω . The amplitude of these oscillations exceeds the maximum field amplitude of the Gaussian pulse in the absence of plasma, $|E_{\text{vac}}(t)|$, shown for comparison in Fig. 3, *b* by the dashed line.

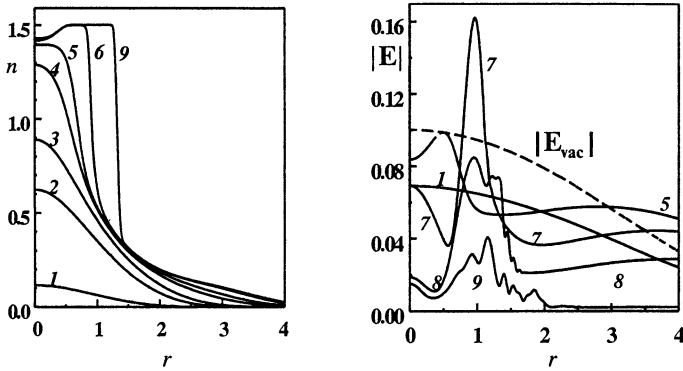


Fig. 2. Evolution of the plasma density $n(r,t)$ and the field amplitude $|E(r,t)|$ at $\theta = 30^\circ$. Curves 1–9 correspond to the time instants $t = 80, 90, 95, 105, 110, 120, 130, 150,$ and 200 , respectively. The dashed curve shows the unperturbed field $|E_{vac}(r)|$ (in the absence of a plasma) at $t \approx t_0 = 100$.

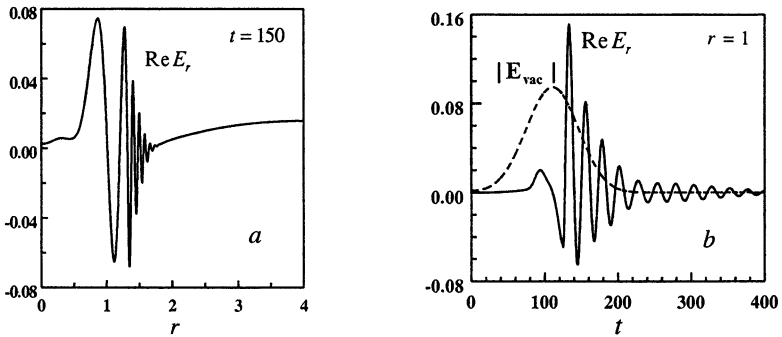


Fig. 3. Spatial and temporal behavior of Langmuir oscillations: a) $Re E_r(r)$ at $t = 150$ and b) $Re E_r(t)$ at $r = 1$. The dashed curve shows the time dependence of the amplitude of the unperturbed Gaussian pulse, $|E_{vac}(t)|$ at $r = 1$.

The coupling of the excited Langmuir oscillations to an external electromagnetic field (due to the presence of a fairly sharp boundary of the ionized region) gives rise to the partial emission of their energy into the surrounding space, i.e., to the occurrence (along with the fundamental frequency component ω) of one or several components at frequencies close to $\omega_{p\max} = \sqrt{4\pi e^2 N_g / m} \approx 1.22\omega$ in the spectrum of the cylindrical wave reflected from the discharge. In view of the

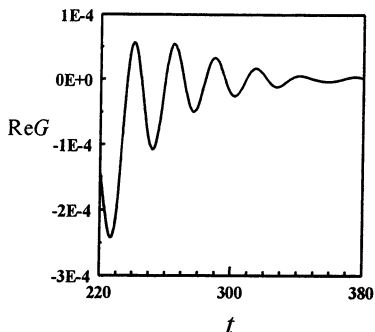


Fig. 4. Time behavior of the amplitude function $\text{Re}G(t)$ of the reflected TE wave at large times. The curve illustrates the radiation from the discharge at the upshifted frequency $\omega_{p \max} \approx 1.22\omega$.

substantially decreased, but the Langmuir oscillations still exist and continue emitting. The transversal wave number at the frequency $\omega_{p \max}$ is

$k_{\perp} = (\omega_{p \max} / c) \sin \theta_p = \sqrt{(\omega_{p \max} / c)^2 - k_0^2 \cos^2 \theta}$, that is the corresponding reflected cylindrical wave is inclined to z -axis at the angle $\theta_p > \theta$ ($\cos \theta_p = (\omega / \omega_{p \max}) \cos \theta$). In the given numerical example, $\theta = 30^\circ$, $\theta_p = 45^\circ$; at $t \approx 250$ the intensity of the frequency shifted component is about 10^{-4} of the maximum intensity of the incident wave.

This work was supported by the Russian Foundation for Basic Research (Grant Nos. 02-02-17271, 01-02-16575, and 02-02-06266) and Russian Academy of Sciences (Grant № 1999 (6) – 37).

References

1. Margolin L. Ya. et al., Sov. Tech. Phys. Lett., 1987, **13**, 89.
2. Milchberg H. M. et al., Phys. Plasmas, 1996, **3**, 2149.
3. Babin A. A. et al., Physics-Uspekhi, 1999, **42**, 74.
4. Gildenburg V. B. and Vvedenskii N. V., Phys. Plasmas, 2001, **8**, 1953.
5. Bakunov M. I. et al., Phys. Plasmas, 2002, **9**, 2803.
6. Vvedenskii N. V. and Gildenburg V. B., JETP Lett., 2002, **76**, 380.

linear character of the "transition" resonant excitation of Langmuir oscillations, the intensities of the shifted spectral components are proportional to the intensity of the incident wave. This linear parametric conversion of the scattered spectrum of an ionizing electromagnetic wave (previously described in the model of a thin gas slab [5]) is illustrated in Fig. 4 by the time dependence of the quantity $\text{Re}G(t)$ determining the amplitude of H_z -component of the reflected wave $H_z^{(r)} = G(t)H_1^{(l)}(k_{\perp}r)$ at large times $t > 220$ (after the end of the incident pulse), when the signal amplitude at the fundamental frequency has already

CHARGED PARTICLE (CP) ACCELERATION BY AN INTENSE WAKE-FIELD (WF) EXCITED IN PLASMAS BY EITHER LASER PULSE (LP) OR A RELATIVISTIC ELECTRON BUNCH (REB)

V. A. Balakirev, I. V. Karas', V. I. Karas', V. D. Levchenko¹,
M. Bornatici²

NSC "Kharkov Institute of Physics & Technology", Kharkov, Ukraine

¹Keldysh Institute of Applied Mathematics of RAS, Moscow, Russia

²INFN, Dipartimento di Fisica "A. Volta", Università degli Studi di Pavia, Pavia, Italy

In the present report the results from theoretical and experimental studies as well as from 2.5-D numerical simulation of both the plasma WF excitation by either REB or LP and the CPWF acceleration are discussed. The results of these investigations make it possible to evaluate the potentialities of the WF acceleration method and to analyse whether it can serve as basis for creating a new generation of devices capable of accelerating CP at substantially higher (by two to three orders of magnitude) rates in comparison with those achievable in classical linear high-frequency (resonant) accelerators.

Collective methods of CP acceleration were proposed by Budker [1], Veksler [2], Fainberg [3]. Budker [1] proposed the CP acceleration in self-stabilized relativistic electron beam; Veksler [2] suggested the method of ion coherent acceleration by relativistic electron ring in longitudinally varying magnetic field; Fainberg [3] proposed the plasma-based scheme for CP acceleration by space-charge waves in plasma and non-compensated beams. At present this is one of the most promising methods for collective acceleration because the electric field amplitude of the space-charge wave (SCW) in a plasma attains a maximum value

$$E_{\max} = n_p / n_0 (4\pi n_0 m c^2)^{1/2} (2\gamma - 1)^{1/2} \quad (1)$$

(formula extended [4] to relativistic case) m is the electron mass; c is the light speed; γ is the relativistic factor; n_p is the maximum density in the SCW; the ratio n_p/n_0 is governed by the way in which the SCW is initiated.

The efficient methods for plasma wave excitation:

– **PWGA** – plasma waveguide accelerator: a) electron beam-plasma interaction in magnetized plasma waveguide (beam-plasma instability); b) external ultra-high oscillator – Fainberg and co-workers (since 1956);

– **PBWA** – plasma beat-wave accelerator: $f_1 - f_2 = f_p$ (f_i is the radiation frequency, f_p is the Langmuir frequency) Tajima and Dawson (1979 a detailed information concerning this and next references you can see in [5]); in BWA, an electric field of $1.8 \cdot 10^9$ V/cm and energy of accelerated particles of 20 MeV were obtained C. Clayton, C. Joshi, C. Darrow, K. A. Marsh, A. Dyson, M. Everett, A. Lai, W. P. Leemans, D. Umstadter, R. Williams, Y. Kitagawa, T. Matsumoto, T. Minamihata, K. Sawai, K. Matsuo, K. Mima, K. Nishihara, H. Azechi, K. A. Tanaka, H. Takabe, and S. Nakai (1992, 1993);

– **SmLWFA** – self-modulated laser wake-field accelerator self-modulation of laser pulse (N. E. Andreev et al. (1992); J. Krall et al. (1993); T. M. Antonsen, P. Mora (1992); P. Sprangle et al. (1992)). The most impressive results on plasma acceleration of CP were obtained in the SmLWFA, i.e. an electric field amplitude of $1.5\text{--}2\cdot 10^8$ V/cm, an energy of accelerated particles of 100–300 MeV (K. Nakajima et al. (1994); A. Modena, Z. Najmudin, A. E. Dangor et al. (1995); D. Umstadter, J. K. Kim, E. Dodd (1996)). The extremely large acceleration gradients generated by laser pulses propagating in plasmas can be used to accelerate electrons. In the standard LWFA a short laser pulse, on the order of a plasma wavelength long, excites a trailing plasma wave that can trap and accelerate electrons to high energy. There are a number of issues that must be resolved before a viable, practical high energy accelerator can be developed. These include Raman, modulation and hose instabilities that can disrupt the acceleration process. In addition, extended propagation of the laser pulse is necessary to achieve high-electron energy. In the absence of optical guiding the acceleration distance is limited to a few Rayleigh ranges, which is far below that necessary to reach GeV electron energies.

– **LPSH** – laser pulse shaping (S. V. Bulanov, T. J. Esirkepov, N. M. Naumova, F. Pegoraro, I. Pogorel'sky, A. M. Pukhov (1996));

– **RLPA** – resonant laser-plasma accelerator: train of laser pulses with independently adjustable pulse widths and interpulse spacing (S. Dalla, M. Lontano (1994); D. Umstadter, E. Esarey, J. Kim (1994));

– **LWFA** – laser wake-fields accelerator: the short laser pulse (T. Tajima, J. M. Dawson (1979); L. M. Gorbunov, V. I. Kirsanov (1987)); for relativistic strong pulse (S. V. Bulanov et al. (1989); P. Sprangle et al. (1990)). To achieve multi GeV electron energies in the laser wakefield accelerator, it is necessary to propagate an intense laser pulse over long distances in a plasma without disruption. The physics of laser beams propagating in plasmas has been studied in great detail and there exists sample experimental confirmation of extended guided propagation in plasmas and plasma channels. In addition to these issues, dephasing of electrons in the wakefield can limit the energy gain. Spatially tapering (2000–2002) the plasma density may be useful for overcoming electron dephasing in the wake-field. P. Sprangle, J. R. Penàno, B. Hafizi, R. F. Hubbard, A. Ting, D. F. Gordon, A. Zigler, T. M. Antonsen proposed and studied guiding and stability of an intense laser pulse in a uniform plasma channel and analyzed the WF acceleration process in an inhomogeneous channel. The coupled electromagnetic and plasma wave equations were derived for laser pulses propagating in a plasma channel with a parabolic radial density profile and arbitrary axial density variation. For a uniform channel, Raman and modulation instabilities were analyzed. For a nonuniform channel the axial and radial electric fields associated with the plasma wave were obtained inside and behind the laser pulse. It was shown that by optimally tapering the plasma density the WF phase velocity several plasma wavelengths behind the laser pulse can be equal the speed of light

in vacuum. A three-dimensional envelope equation for the laser field has been derived that includes nonparaxial effects, WF, and relativistic nonlinearities. In the broad beam, short pulse limit the nonlinear terms in the wave equation that lead to Raman and modulation instabilities cancel. Long pulses (several plasma λ_p wave lengths) experience substantial modification due to these instabilities. The short pulse LWFA, although having smaller accelerating fields, can provide acceleration for longer distances in a plasma channel. By allowing the plasma density to increase along the propagation path electron dephasing can be deferred, increasing the energy gain. A simulation example of a GeV channel guided LWFA accelerator is presented. Simulations also show [6] that multi-GeV energies can be achieved by optimally tapering the plasma channel.

– **PWFA** – plasma wake-fields accelerator: the short rectangular REB or periodic train of REBs (P. Chen, J. M. Dawson, R. M. Huff and T. Katsouleas); blow out regime of PWFA (J. B. Rosenzweig et al. (1991)). In the PWFA an electric field of $6 \cdot 10^4$ V/cm and energy of accelerated particles of 6 MeV (can see in [5] reference J. Rosenzweig, D. Cline, B. Cole et al. (1988)); in blow out regime of PWFA, energy gradients of 700 MeV/m were measured in the experiment E-157 S. Lee, T. Katsouleas, P. Muggli, W. Mori, C. Joshi, R. Hemker, E. S. Dodd, C. E. Clayton, K. Marsh et al. (2000); project "Energy doubler for a linear collider" S. Lee, T. Katsouleas, P. Muggli, W. Mori, C. Joshi, R. Hemker, E. S. Dodd, C. E. Clayton, K. Marsh et al. (2002) [7]. An intense, high-energy electron or positron beam can have focused intensities rivaling those of today's most powerful laser beams. For example, the 5 ps (full-width, half-maximum), 50 GeV beam at the Stanford Linear Accelerator Center (SLAC) at 1 kA and focused to a 3 micron spot size yields intensities of 10^{20} W/cm² at a repetition rate of 10 Hz. Unlike a ps or fs laser pulse which interacts with the surface of a solid target, the particle beam can readily tunnel through tens of cm of steel. However, as it is shown in [7] the same particle beam can be manipulated quite effectively by the plasma that is a million times less dense than air! This is because of the very strong collective fields induced in the plasma by the Coulomb force of the beam. The collective fields in turn react back onto the beam leading to many clearly observable phenomena. The beam particles can be: 1) deflected leading to focusing, defocusing, or even steering of the beam; 2) undulated causing the emission of spontaneous betatron x-ray radiation; 3) accelerated or decelerated by the plasma fields. Using the 28.5 GeV electron beam from the SLAC linac a series of experiments have been carried out that demonstrated clearly many of the above mentioned effects [7]. The results were compared with theoretical predictions and with two-dimensional and three-dimensional, one-to-one, particle-in-cell code simulations [7]. These phenomena may have practical applications in future technologies including optical elements in particle beam lines, synchrotron light sources, and ultrahigh gradient accelerators. As can be seen from spatial distribution of excited WF [7], the electric field can attain high values only over very short distances. Therefore we think that the energy doubler for a linear SLAC collider problem is not very realistic.

An interesting result has been established by us [5]: for a certain relation among the parameters of the plasma bunch magnetic field system, the hybrid nature of the wake waves (which are excited by a REB in a magnetized plasma and are a superposition of the surface and spatial modes) makes it possible to increase the electron energy (EE) of the accelerated bunch to a value that is significantly higher than the initial EE of the accelerating bunch (even when the bunch is initially unmodulated in the longitudinal direction). We have discussed 2.5-dimensional numerical modeling on the formation of an ion channel as a result of the radial ion motion in self-consistent electromagnetic fields excited by a train of REB. The parameters of the fully developed channel are determined by the plasma-to-bunch density ratio and the ratio of the bunch radius to the skin depth. The effective dimensions of the channel and its "depth" (i.e., the high ion density at the channel axis) increase monotonically both in time and in the direction opposite to the propagation direction of the bunches. The formed ion channel stabilizes the propagation of REB, which thus generate stronger accelerating fields. The results of the wake-field excitation during the self-modulation of a long REB has shown that the maximum electron density in the bunch becomes comparable to the plasma density and the amplitude of the plasma density perturbations becomes larger than the initial plasma density by a factor of 4.5. This indicates a very strong modulation of both the bunch density and the plasma density. That is why, even in the above case of a low-density bunch (in which the unperturbed electron density is about two orders of magnitude lower than the plasma density), it is incorrect to describe the plasma in the linear approximation. The amplitude of the longitudinal field is about 0.8 of the maximum electric field that can be generated in the plasma, and the amplitude of the radial field is about 0.4 of the maximum possible field. This shows that the driven bunch needs to be placed in the acceleration stability region. An important point is that the field amplitude increases only over a certain distance along a REB; hence, it would be of no use to operate with bunches whose length exceeds the distance over which the longitudinal field amplitude is maximum, because doing so would provide no additional increase in the excited wake field. The results obtained with allowance for all possible nonlinearities give a better insight into the three-dimensional behaviour of REB in a plasma and may help to ensure the optimum conditions for the wake-field generation during the dynamic self-modulation of the bunches. The results of investigations of the excitation of accelerating fields by an individual REB or by a train of such bunches in a plasma (in particular, in the presence of an external magnetic field) make it possible to evaluate the potentialities of the wake-field acceleration method.

Further more, we discuss the physical mechanism for generation of very high "quasi-static" magnetic fields in the interaction of an ultraintense short laser pulse with an overdense plasma target owing to the spatial gradients and non-stationary character of the ponderomotive force. Numerical (particle-in-cell) simulations by Wilks et al. [8] of the interaction of an ultraintense laser pulse with an overdense

plasma target have revealed nonoscillatory self-generated magnetic fields up to 250 MGs in the overdense plasma, that this non-oscillatory magnetic field is generated around the heated spot in the center of the plasma, the magnetic field generation being attributed to the electron heating at the radiation-plasma interface. The spatial and temporal evolution of spontaneous megagauss magnetic fields, generated during the interaction of a picosecond pulse with solid targets at irradiances above $5 \cdot 10^{18} \text{ W/cm}^2$ have been measured using Faraday rotation with picosecond resolution, the observations being limited to the region of underdense plasma and after a laser pulse [9]. A high density plasma jet has been observed simultaneously with the magnetic fields by interferometry and optical emission and a field value is consistent with field generated by the thermoelectric mechanism (see for example [10]). In paper [11] the first direct measurements of high-energy proton generation (up to 18 MeV) and propagation into a solid target during such intense ($5 \cdot 10^{19} \text{ W/cm}^2$) laser plasma interactions were reported. Measurements of the deflection of these energetic protons were carried out which imply that magnetic fields in excess of 30 MGs exist inside the target. In [12] we solved numerically the problem of high-intensity, linearly polarized electromagnetic pulse incident onto a collisionless plasma layer in a Cartesian coordinate system in a 2.5-D formulation (z is the cyclic coordinate and there are three components of the momentum) by means of COMPASS (COMputer Plasma And Surface Simulation) code. The recent review [5] and references therein combine a detailed information concerning COMPASS code as well as its possibilities and applications. A general advantage of the complete numerical simulation consists of the possibility of obtaining all necessary information concerning spatial and temporal dynamics of both particles and self-consistent electromagnetic fields without requiring additional data (reflection and absorption coefficients, changes of either plasma temperature or different plasma parameters) for a given situation concerning the interaction of an intensive electromagnetic pulse with plasmas. We give only the external parameters, both the initial and boundary conditions for particles and fields, and as results of a numerical simulation we attain all characteristics of the plasma together with pulsed self-consistent electromagnetic fields. The most characteristic feature of the action of an intense, normally incident electromagnetic pulse onto an ultrahigh-density plasma consists in a "well-digging" effect. Worth nothing is the time-growing sharp nonuniformity of the perturbed plasma layer in the transverse direction. As for the magnetic field, we do not observe a change of its direction, but a significant time-variation of its strength varies significantly in time. Hence, the magnetic field cannot be considered as quasi-static because it varies by more than an order of magnitude over a time of $2\pi\omega_{pe}^{-1}$. The magnitude of the "dc" magnetic field is ten times as low as the maximum magnetic field. One should note that in [8, 12] the numerical simulation has been made under very optimal conditions: a uniform plasma density makes it sure a own plasma oscillation resonance with a longitudinal modulation density of particles in a wave as well as a maximum frequency of nonlinear Thomson scatter-

ing spectrum. In experiments, instead, a plasma inhomogeneity is very essential, with the result that resonant conditions are fulfilled only in a small plasma region. Subsequently to the interaction pulse, only the "dc" magnetic field exists, as measured in the underdense plasma region in [9]. On the basis of the formula:

$$B_{dc} \text{ (MGs)} = 4.2 \cdot (10^{-22} I \text{ (W/m}^2))^{1/2} (\lambda \text{ (\mu m)})^{-1} \quad (2)$$

(where I is the intensity of the incident laser radiation) one obtains a "dc" magnetic field magnitude of few MGs for the experimental parameters of [9], and a few tens of MGs for the experimental conditions of [11]. A difference still on order of value is conditioned that at such intensities only 10% of the incident laser radiation is absorbed in agreement with [13]. By means of a 2.5-dimensional numerical simulation on the macroparticles method it is possible to find the magnetic field spatial and temporal distribution without making use of an adapted parameter, in contrast with the conventional $\nabla n \nabla T$ mechanism (see for example [10]). On the other hand, the theoretical model for the generation of a magnetic field proposed by Sudan [14] does not appear to be appropriate, this model being valid for a very large ratio of plasma density to critical density and when the $\nabla n \nabla T$ contribution is not relevant.

The work was supported in part by the Cariplo Foundation (Como, Italy) and INTAS project # 01-233.

References

1. *Budker G. I.* Proceedings of the CERN Symposium on High Energy Accelerators and Pion Physics (Geneva), 1956, **1**, 68.
2. *Veksler V. I.* Ibid, 80.
3. *Fainberg Ya. B.* Ibid, 84.
4. *Akhiezer A. I., Polovin R. V.*, Zh. Esp. Teor. Fiz., 1956, **30**, 696.
5. *Balakirev V. A., Karas` V. I., Karas` I. V.*, Plasma Phys. Rep., 2002, **28**, 125.
6. *Sprangle P., Penano J. R., Hafizi B., Hubbard R. F., Ting A., Gordon D. F., Zigler A., Anton- sen T. M., Jr.* Physics of Plasmas, 2002, **9**, 2364; *Sprangle P.* et al., Phys. Rev. Lett., 2000, **85**, 5110, and references therein.
7. *Joshi C., Blue B., Clayton C. E., Dodd E., Huang C., Marsh K. A., Mori W. B., Wang S., Hogan M. J., O`Connell C., Siemann R., Watz D., Muggli P., Katsouleas T., Lee S.*, Physics of Plasmas, 2002, **9**, 1845; *Clayton C.* et al., Phys. Rev. Lett., 2002, **88**, 154801, and references therein.
8. *Wilks S. C., Krueer W. L., Tabak M., and Langdon A. B.*, Phys. Rev. Lett., 1992, **69**, 1383; *Wilks S. G.*, Phys. Fluids, 1993, **B5**, 2603; *Mason R. J. and Tabak M.* Ibid. **80**, 524 (1998).
9. *Borghesi M., MacKinnon A. J., Bell A. R., Gailard A., and Willi O.*, Phys. Rev. Lett., 1998, **81**, 112.
10. *Haines M. G.*, Phys. Rev. Lett., 1997, **78**, 254.
11. *Clark E. L., Krushelnick K., Davies J. R., Zepf M., Tatarakis M., Beg F. N., Machcek A., Norreys P. A., Santala M. I. K., Watts I., and Dangor A. E.*, Phys. Rev. Lett., 2000, **84**, 670.
12. *Batishchev O. V., Karas` V. I., Levchenko V. D., and Sigov Yu. S.*, Plasma Phys. Rep., 1994, **20**, 587.
13. *Price D. F., More R. M., Walling R. S., Guethlein G., Shepherd R. L., Stewart R. E., and White W. E.*, Phys. Rev. Lett., 1995, **75**, 252.
14. *Sudan R. N.*, Phys. Rev. Lett., 1993, **20**, 3075.

BOHM CRITERION FAILURE AND PERIODIC OSCILLATIONS OF THE PLASMA SHEATH IN NONSTATIONARY PLASMAS

Ya. Z. Slutsker, Yu. P. Bliokh, J. Felsteiner, and P. M. Vaisberg

Department of Physics, Technion – Israel Institute of Technology, Haifa, Israel

The plasma sheath resonance and its instability were found to be in certain disagreement with theoretical assertions based on the Bohm criterion. Powerful RF oscillations appear in the discharge circuit when the Bohm criterion is not satisfied.

The significance of the Bohm criterion is clear because it determines the plasma-sheath formation near the walls. This criterion states that for the formation of a stationary sheath the ions must arrive at the sheath edge with velocity $v_i \geq c_s$, where c_s is the ion sound velocity. This criterion is widely used as a boundary condition at the sheath edge. It is used there in its marginal form $v_i = c_s$ [1].

The results of experimental and theoretical studies of a low-pressure pulsed hollow-cathode discharge are presented here. We studied the dynamics of the cathode sheath and probes located in the discharge plasma. A number of phenomena have been found to be in certain disagreement with statements and calculations based on the Bohm criterion. A sketch of the experimental setup is shown in Fig. 1. The results presented here were obtained mainly with an open cylinder with 13.5 cm diameter and 17 cm length. It was filled with He up to 80–100 mTorr. When necessary other gases and cylinders were used. We interpret the voltage across the discharge as a cathode fall because the anode fall together with the plasma fall were very small. For the plasma diagnostics we used single and double floating probes and a multigrid plasma analyzer. The microwave cutoff method was employed. The plasma analyzer was located at the cathode wall. For a more detailed apparatus description see [2–4]. The discharge driving current was varied in the range of 5–100 A. The corresponding plasma density was $n_0 \sim (0.5\text{--}10) \cdot 10^{11} \text{ cm}^{-3}$. The electron temperature was about 7–8 eV. The time needed to fill the device with plasma due to ionization never exceeded 0.5 μs . This means that the plasma density almost instantly followed the discharge driving current.

The discharge current pulse is shown in Fig. 2 (bold line). It is seen here that the driving current kept almost constant during the pulse. The voltage fall across the cathode sheath is shown in Fig. 2 (dashed line). It is clearly seen that the cathode fall voltage reduces by about three times till it achieves the steady state, from about 2 kV to 700 V. The time needed to achieve the steady state, which is about 0.5 μs , is remarkably longer than the ionization time ($\sim 10 \mu\text{s}$). A similar transition period was found in the probe measurements. In Fig. 3 we show the scope trace of the single probe saturation current. It reaches the stationary value during about 15 μs in a non-monotonic way.

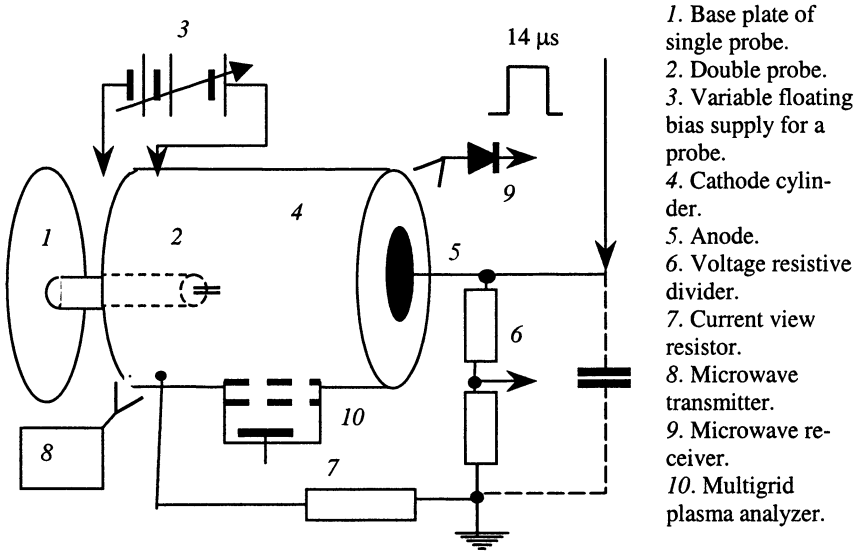


Fig. 1. Experimental setup

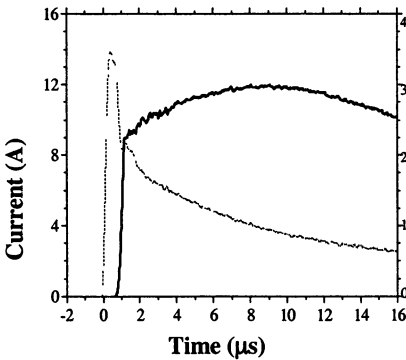


Fig. 2. Driving current (bold line), cathode voltage fall (dashed line).

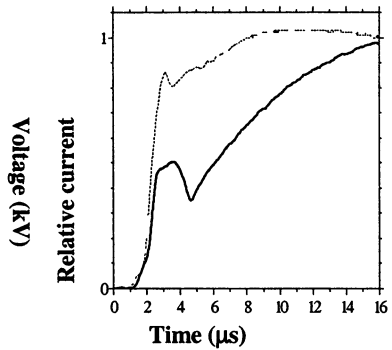


Fig. 3. Ion saturation current of single (bold line) and double (dashed line) probes.

Another remarkable phenomenon appeared when we increased the discharge driving current. Above a certain threshold (typically 12–15 A) the cathode sheath became unstable during the transition period [2, 5]. This instability induced a strong RF current in the discharge circuit, which is very well seen in Fig. 4. The value of this RF current could exceed the discharge driving current by several

times, up to 5.5 times. These oscillations were indeed sinusoidal and their frequency was about $(0.6-0.9)\omega_i$, where ω_i is the ion plasma frequency. The whole range of measured frequencies for all tested cylinders and filled gases was from 15 MHz up to 100 MHz [6]. This frequency did not depend on the external circuit, cathode or anode materials, anode size or location, etc. The only requirement to the external circuit was to close the way of the RF current, e.g. with a capacitor shunt between the anode and the cathode (see dashed lines in Fig. 1). Its capacitance should exceed a few hundred pF and it did not have any influence on the frequency.

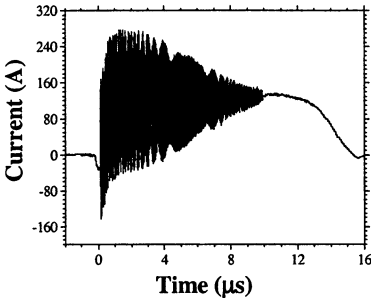


Fig. 4. Discharge driving current with RF instability.

As we noted before, the anode itself and the quasineutral plasma parameters did not have any influence on the instability. Consequently just the cathode sheath could be "responsible" for this phenomenon. The experimental evidence that the cathode-fall voltage collapsed to the plasma electron energy during each oscillation cycle was obtained with the electrostatic plasma analyzer [2]. Indeed, when this RF instability appears, in certain phase of the RF oscillations the plasma electrons start to penetrate into the cathode sheath up to the cathode wall (Fig. 5, *b*). It means that at this moment the cathode fall was reduced to the energy of the plasma electrons, which is much less than the cathode fall. Moreover the maximum of the ion current corresponds to the minimum of the cathode fall as it is seen in Fig. 5, *a*. This means that they are in opposite phases. This is understood qualitatively because the RF frequency is about ω_i and the ion inertia must be taken into account. Note that it is impossible to obtain a sinusoidal RF component of the

The gas pressure below a certain value did not play any role but above that critical value the threshold for the instability rose steeply. We found out that the product PD , where P is the pressure and B is the cylinder diameter, kept constant and depended just on the sort of gas. For He it was about 2.5, for Xe ~ 0.3 , for other noble gases (Ne, Ar, Kr) it was somewhere in between. This critical pressure corresponds to the ion-neutral collision frequency, which is approximately equal to ω_i [2, 3].

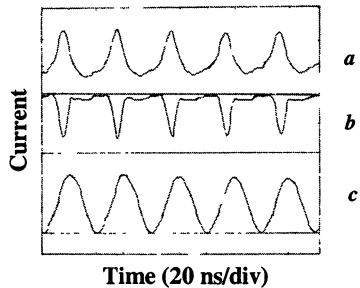


Fig. 5. Scope traces of: *a*) the ion current to the analyzer; *b*) the electron current to the analyzer; *c*) the RF current.

discharge current (Fig. 5, c) by combining the electron and ion currents which are conductive currents. This means that there should be a significant additional reactive RF current component through the sheath.

Recalling that this instability appears just during the transition period T_s , we found out that this T_s depends on the ion mass M and on the cylinder diameter D . Namely it is approximately equal to the time needed by the ion sound to propagate across the cathode radius: $T_s \approx D/2c_s$, $c_s = \sqrt{T_e/M}$, where T_e is the electron temperature [6, 7]. Note that this is also the time needed to accelerate the ions coming from the plasma volume to the walls, base electrodes, probes, etc. It is understood that when plasma appears instantly, like in our case, this time is needed for the stationary ion flux formation. Therefore during this transition period the Bohm criterion $v_i \geq c_s$ should not be valid. As it is shown in Ref. [1] the plasma ions are accelerated because a small amount of the whole potential fall penetrates into the bulk plasma. The value of this amount is about T_e . The distance of this penetration may be different in different cases. When the plasma size is much larger compared to the electrode size, say a miniature double probe, this distance may be considered as the probe size. In case of large electrodes comparable to the plasma size, say the single-probe base plate or the cathode cylinder itself, this distance is the plasma size, which is the cylinder radius. Therefore the time needed to achieve a stationary current in case of a large electrode should be much longer than for the small electrodes of the double probe. This is clearly seen in Fig. 3 (dashed line).

Concerning the RF instability one may assume that when the Bohm criterion is not satisfied something like unstable resonance should appear in the cathode sheath near the ion plasma frequency. On the other hand theories concerning the plasma-sheath stability near a negative wall ruled out even a stable resonance near ω_i [8]. The point is that these theories included the Bohm criterion as a boundary condition. So to explain the RF instability (and probe distortions as well) we derived a theory which includes the temporal evolution of the ion velocities at the sheath edge from a low value up to c_s [4].

Qualitatively the plasma sheath consists of three regions. The first one is a quasineutral plasma. The potential fall here does not exceed $\Delta\phi \sim T_e/e$. Then follows a narrow area where the electron density falls down abruptly. The potential fall here is also a few T_e and is much lower than U . The width of this area does not exceed a few r_d , where r_d is the electron Debye length. The third region is an electron-free sheath. It is electron free because the cathode fall U is much higher than T_e .

The ion motion in the electron-free sheath is described by the well-known Llewellyn equation (1). To derive the boundary conditions we will make a sim-

plification, which is shown in Fig. 6. In the plasma body we put $n_e = n_i = n_0$. It means that here the electric field $E = 0$ and therefore in our model $\Delta\phi = 0$ in a quasineutral plasma. However, this electric field has to accelerate the plasma ions toward the sheath edge. The role of this electric field in our model will be simulated with a given ion velocity function $v_0(t)$. This function grows up monotonically to its asymptotic value c_s . We will eliminate the second very narrow area and introduce instead a potential discontinuity $\Delta\phi$ and a step-like fall $n_e \rightarrow 0$. Then the set of equations (1)–(4) can be written, describing the ion motion in the electron-free sheath [9]:

$$\frac{d^3 x}{dx^3} = \frac{4\pi e}{M} j(t), \tag{1}$$

$$\left. \begin{aligned} \frac{d^2 x}{dt^2} \Big|_L &= \frac{e}{M} E \Big|_L = 0, \\ \frac{dx}{dt} \Big|_L &= v_i \Big|_L = v_i \left(v_0(t), v_b = \frac{dL}{dt} \right), \\ x(t = t_0) &= L(t), \end{aligned} \right\} \tag{2}$$

$$\int_{L(t)}^0 E(x,t) dx = U(t), \tag{3}$$

$$n_0 v_0(t) = n_i v_i. \tag{4}$$

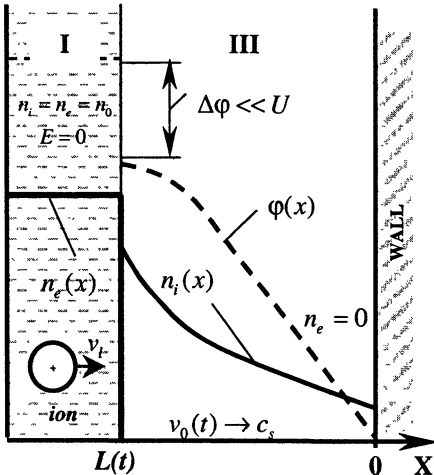


Fig. 6. Idealized plasma sheath

In the above equations $x(t)$ is the ion position inside the sheath and $j(t)$ is the total current density through the sheath. The main difference of our model compared to all others is that in our case the ion velocity in the sheath entrance depends on the sheath boundary motion. It happens because we introduced the finite potential discontinuity $\Delta\phi$. This is clearly seen from the energy conservation law:

$$v_i(t) = v_b(t) + \sqrt{\frac{2e\Delta\phi}{M} + (v_0(t) - v_b(t))^2}. \quad (5)$$

Namely this dependence is "responsible" for additional reactive currents and the resonance creation.

To compare the experimental and theoretical data these equations were solved numerically. Two kinds of solutions were obtained. The first one corresponds to the case when the current through the sheath is limited by the external circuit, which is typical for any discharge power supply. The transition period corresponds to about 10 μs , which is quite reasonable. Also the voltage drops down similarly, i.e. about 2.5 times. The second one corresponds to the case when the voltage across the sheath is kept constant. This is typical for probe measurements. A reasonable agreement with experiment was obtained here, even the current minimum is located in the "correct" place (see Fig. 3). The point is that in order to get this quantitative agreement we had to insert in our computation a non-zero initial ion velocity. Its value should be somewhere in range $(0.3 - 0.5)c_s$, which is comparable to the ion thermal velocity.

In order to study further the RF instability one should regard the sheath as stationary at any moment. Then the linear current density response δj to a small harmonic perturbation of the cathode voltage $\delta U = Z(\omega)\delta j$ should be calculated, where $Z(\omega)$ is the sheath impedance. The value of $Z(\omega)$ was derived from Eqs.

(1)–(4). It was found that the resonance in the sheath impedance appears by just considering the finite energy spread of the incoming ions. This is reasonable because any energy spread of ions causes the ion current to pulsate when the ions penetrate through the moving energy step $\Delta\phi$. The real and imaginary parts of the sheath impedance are presented in Fig. 7. It is seen there that the resonance appears when the transit angle $\theta \approx 0.7\pi$:

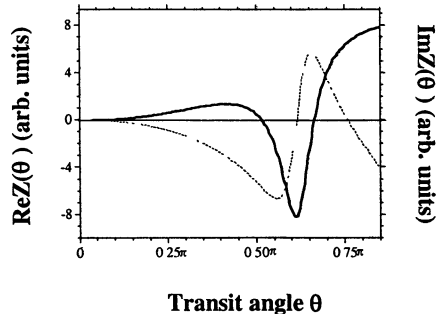


Fig. 7. The real (bold line) and imaginary (dashed line) parts of the sheath impedance.

$$\theta = \frac{\omega}{\omega_i} \left(\frac{8e^3 n_0^2 U}{Mj^2} \right)^{1/4}, \quad (6)$$

and this resonance is unstable because $\text{Re} Z(0.7\pi) < 0$. This is in a reasonable agreement with the experiment, which shows the opposite phases of the RF voltage the ion current (Fig. 6). Inserting the plasma and the discharge parameters in the transit-angle formula of Eq. (6), it is easily seen that $\theta \approx 0.7\pi$ corresponds to $\omega \sim 0.7\omega_i$, which is also quite reasonable.

This hollow-cathode device was used to construct a powerful pulsed RF oscillator [10]. Four different oscillators have been tested and the following results were obtained:

1. Max RF power (pulsed)	120 kW
2. Max efficiency	30%
3. Max RF pulse duration	13 μ s
4. Max repetition rate	
limited by our power supply	300 Hz
estimated as $\sim 10 D/c_s$	approx. 7 kHz
5. Optimal loading	$50 \pm 20 \Omega$
6. Whole frequency range for 4 tested oscillators	25–57 MHz
7. Level of harmonics	(5–7)%

To conclude we can state:

- (a) In pulsed plasmas the Bohm criterion is not valid during the period needed by the ion sound to propagate across the plasma.
- (b) The Bohm criterion failure causes plasma-sheath instabilities and probe characteristics distortions.
- (c) A powerful, pulsed RF generator was designed using the plasma–sheath instability.

References

1. Riemann K.-U., *J. Phys. D*, 1991, **24**, 493.
2. Arbel D., Bar-Lev Z., Felsteiner J., Rosenberg A., and Slutsker Ya. Z., *Phys. Rev. Lett.*, 1993, **71**, 2919.
3. Arbel D., Bar-Lev Z., Felsteiner J., Rosenberg A., and Slutsker Ya. Z., *Phys. Rev. Lett.*, 1997, **78**, 66.
4. Bliokh Yu. P., Felsteiner J., Slutsker Ya. Z., and Vaisberg P. M., *Phys. Plasmas*, 2002, **9**, 3311.
5. Bliokh Yu. P., Felsteiner J., and Slutsker Ya. Z., *Europhys. Lett.*, 1999, **46**, 735.
6. Arbel D., Bar-Lev Z., Felsteiner J., Rosenberg A., and Slutsker Ya. Z., *Appl. Phys. Lett.*, 1995, **66**, 1193; Felsteiner J., Ish-Shalom S., and Slutsker Ya. Z., *J. Appl. Phys.*, 1998, **83**, 2940.
7. Bliokh Yu. P., Felsteiner J., Slutsker Ya. Z., and Vaisberg P. M., *Proc. 13th Intern. Conf. on Gas Discharges and Their Applications*. Ed. S. J. MacGregor. Glasgow, 2000, 965.
8. Rosa R., *J. Phys. A*, 1971, **4**, 934; Oliver B. M. and Clements R. M., *J. Appl. Phys.*, 1973, **44**, 1128.
9. Birdsall C. K. and Bridges W. B., *Electron Dynamics of Diode Regions* (Academic, New York, 1966), Chap. 2.
10. Bliokh Yu. P., Felsteiner J., Slutsker Ya. Z., and Vaisberg P. M., *IEEE Trans. Plasma Sci.*, 2001, **29**, 895.

THE PARAMETRIC INSTABILITY OF THE CYCLOTRON RADIATION IN REACTIVE ELECTRON MEDIUM

M. A. Erukhimova, M. D. Tokman

IAP RAS, Nizhny Novgorod, Russia

The effect of the simultaneous amplification of two waves due to their parametric cyclotron interaction with modulated ensemble of nonresonant particles is investigated. The mechanism of energy exchange between field and particles in this effect is clarified by solving of nonlinear equations of particle motion in the wave field in one-frequency frame of references.

Introduction

This work continues theoretical investigations of unusual regimes of generation of coherent radiation by ensembles of classical charged particles started a few years ago. In these new regimes the simultaneous amplification of two HF waves is provided by their parametric cyclotron interaction with modulated electron ensemble which is stable against generation of these waves separately. The main interest was attracted by so-called maser without inversion (MWI) [1–4], classical analog of quantum effect of inversionless amplification [5]. In this regime the parametric instability of two HF waves is due to their interaction with modulated ensemble of resonant particles, i.e. such particles that stay in cyclotron (or Doppler) synchronism with HF waves during interaction, so that there is effective energy exchange between these particles and waves. Unlike the usual maser in MWI the distribution function of electrons is "noninverted" at the resonance, but modulated, so that bichromatic (*not monochromatic*) field is amplified due to optimal synchronization of the beats of HF waves with periodic "inversion" of distribution function.

This paper is devoted to the investigation of another interesting regime of such parametric instability. It is the amplification of bichromatic cyclotron radiation in the absence of resonant particles [2]. The second regime in contrast to the first one where the amplification mechanism corresponds to the parametric interaction with modulated *active susceptibility* can be named as the amplification in *reactive medium*. To avoid contradictions with common sense the term reactivity must be applied to the medium without modulation, besides it should be taken into account that in the medium with spatial or temporal dispersion the modulation of any parameter leads to the complex response.

The scheme

The effect of amplification of coherent radiation by ensemble of nonresonant particles was revealed in paper [2]. In that particular scheme two Brilluin compo-

nents of the waveguide mode with the same transverse structure (with respect to the constant magnetic field $\mathbf{B} = \mathbf{z}_0 B_0$) and different (but close) frequencies

$\mathbf{E} = \sum_{j=1}^2 \mathbf{E}_j \exp(ik_{\perp} x + ik_{\parallel j} z - i\omega_j t)$, that are resonant to the electrons with momen-

tum components $p_{\parallel}^R, p_{\perp}^R$ at the first harmonic of the cyclotron frequency

$\omega_j = \frac{eB_0}{mc\gamma_R} + k_{\parallel j} v_{\parallel}^R$, interact with ensemble of electrons with momentum compo-

nents close (*but not equal*) to the resonant values. The electron ensemble is described by the unperturbed distribution function, modulated on the longitudinal coordinate at the initial moment providing the parametric coupling of HF waves

$f = f_0(p_{\parallel}, p_{\perp}^2/2) + f_M(p_{\parallel}, p_{\perp}^2/2) \cos(\varphi_M + (k_{\parallel 1} - k_{\parallel 2})z)$. The analysis in [2] was

based on solving in linear approximation of kinetic equation in truncated variables, which submit under the resonant approximation to the equations of "nonlinear pendulum", and wave excitation equations with resonant harmonics of the current, expressed in terms of the distribution function. It was shown that due to the specific dependence of synchronism detunings on momentum which takes into account both relativistic cyclotron detuning and Doppler shift:

$\Delta_j = \omega_j - eB_0/mc\gamma - k_{\parallel j} v_{\parallel}$ it is possible to set such modulation of distribution function in vicinity of common resonant point $p_{\parallel}^R, p_{\perp}^R$, that particle density in momentum space expressed via Δ_1 and Δ_2 will oscillate in opposite phase. The dependence $f_M(p_{\parallel}, p_{\perp}^2/2)$ must be the antisymmetric function of $(p_{\parallel} - p_{\parallel}^R)$:

$f_M(p_{\parallel} - p_{\parallel}^R, p_{\perp}^2/2) = -f_M(p_{\parallel}^R - p_{\parallel}, p_{\perp}^2/2)$. As consequence the oscillations of corresponding susceptibilities (medium responses on the first and second field) will be "antiphase". Then if all particles are out of the resonance with waves (there is no partial synchronism), i.e.

$$\Delta_j(p_{\parallel}, p_{\perp})t \gg 1, \quad (1)$$

but there is parametric synchronism

$$(k_{\parallel 1} - k_{\parallel 2})(V_{\parallel} - V_{\parallel}^R)t \ll 1, \quad (2)$$

the parametric coupling of two waves will assume their simultaneous amplification. The linear increment of such amplification is found in [2].

The mechanism of energy exchange

The result of linear kinetic theory [2] does not make clear the mechanism of energy exchange between dichromatic field and electrons in the absence of par-

tial synchronism. Note that this effect is accompanied by amplification of two waves simultaneously but not by scattering from the field of one frequency to another, as in standard induced scattering, where the energy exchange is connected with the frequency transformation in scattering process. In order to clarify this effect we solve nonlinear equations of particle motion going to the accompanying frame of references where the frequencies of two waves are equal, thus excluding the interpretation of this energy exchange as change of photon energy in scattering process.

Consider two circularly polarized waves propagating for simplicity along the constant magnetic wave. So the electric and magnetic field can be written as: $\mathbf{E} = \text{Re} \mathbf{e}_+ E(z) e^{-i\omega t}$, $\mathbf{B} = \text{Re} \mathbf{e}_+ B(z) e^{-i\omega t} + B_0 \mathbf{z}_0$, $E(z) = E_0 (e^{ikz} + e^{-i\varphi_0 - ikz})$, $B = -(c/\omega) \partial E(z) / \partial z$, $\mathbf{e}_+ = \mathbf{x}_0 + iy_0$. Consider the relativistic equations of particle motion in this field

$$\begin{cases} \frac{d}{dt} \mathbf{p} = \text{Re} \left\{ -eE(z) \mathbf{e}_+ e^{-i\omega t} - \frac{e}{c} [\mathbf{v}, B(z) \mathbf{e}_+ e^{-i\omega t} + B_0 \mathbf{z}_0] \right\} \\ \frac{d}{dt} \mathbf{r} = \mathbf{v} = \frac{\mathbf{p}}{m\gamma} \end{cases}$$

with initial conditions: $p_{\parallel}(t=0) = P_{\parallel}^0 = m\gamma_0 V_{\parallel}^0$, $\mathbf{p}_{\perp}(t=0) = \mathbf{P}_{\perp}^0 = m\gamma_0 \mathbf{V}_{\perp}^0$, $z(t=0) = Z_0$. Suppose that momentum components of relativistic particles are close to the resonant values so that resonant parameter is large:

$$R = \frac{|V_{\perp}|^2}{c^2} \frac{\omega}{\Delta_0} \gg 1$$

and Doppler shift is much smaller than cyclotron detuning:

$$|kV_{\parallel}| \ll |\Delta_0|.$$

Here $\Delta_0 = \omega - eB_0/mc\gamma$. Since the electron is not resonant to the field, so that $t\Delta_0 \gg 1$ (see condition (1)), the electron makes large number of oscillations in the wave, so its motion can be presented as superposition of slow part and term oscillating in the wave field:

$$\mathbf{p} = (P_{\parallel} + \tilde{p}_{\parallel}) \mathbf{z}_0 + \text{Re} (P_{\perp} + \tilde{p}_{\perp}) \mathbf{e}_+ \exp(-ieB_0 t/mc\gamma_0).$$

The aim is to obtain that the averaged over large number of oscillations energy of electron changes under action of the standing wave and to get that the full energy of electron ensemble decreases.

We develop the theory of successive approximations. Setting the wave amplitude to be rather small so that $\frac{1}{\gamma_0} \frac{e|E_0|}{mc} \frac{\omega}{\Delta_0^2} \frac{|V_\perp^0|}{c} \ll 1$, we can write

$E(z) = E(Z) + \xi \frac{\partial E(Z)}{\partial Z}$, where $Z = V_\parallel^0 t + z_0$, $z = Z + \xi$. In linear approximation the averaged values for squared oscillating parts of momentum are found:

$$\langle \tilde{p}_\parallel^2 \rangle = e^2 |E_0|^2 \frac{|V_\perp|^2}{c^2} \frac{1}{\Delta_0^2} (1 - \cos(2kZ + \varphi_0)), \quad (3)$$

$$\langle |\tilde{p}_\perp|^2 \rangle = e^2 |E_0|^2 \frac{1}{\Delta_0^2} (2 + R^2 - 2R) (1 - \cos(2kZ + \varphi_0)). \quad (4)$$

In the square approximation we derive the equation for slow longitudinal motion:

$$dP_\parallel/dt = -R 2e^2 |E_0|^2 / (\gamma_0 mc \Delta_0) \sin(2kZ + \varphi_0) \quad (5)$$

and for the slow variation of the amplitude of gyro-rotations:

$$|P_\perp|^2/dt = (2kV_\parallel e^2 |E_0|^2 / \Delta_0^2) \sin(2kZ + \varphi_0) (R^2 + 2R). \quad (6)$$

Then it becomes possible to find the expression for the evolution of electron energy averaged over large number of oscillations in wave field in the square approximation:

$$\frac{d}{dt} \langle w \rangle \approx \frac{1}{2m\gamma_R} \left\{ \frac{d}{dt} |P_\perp|^2 + \frac{d}{dt} P_\parallel^2 + \frac{d}{dt} \langle |\tilde{p}_\perp|^2 \rangle + \frac{d}{dt} \langle \tilde{p}_\parallel^2 \rangle \right\}. \quad (7)$$

It can be found from (3)–(7) that the change of transverse energy is $4\omega/\Delta_0 \gg 1$ times larger than change of longitudinal energy. In term averaged transverse energy consists of energy of gyrorotations w_\perp^{st} and averaged oscillatory energy

$$\langle \tilde{w}_\perp \rangle. \quad \text{Their time derivatives} \quad \frac{d}{dt} w_\perp^{st} \propto (-R^2 - 2R) \left(V_\parallel \frac{\partial |E|^2(Z(t))}{\partial Z} \right),$$

$$\frac{d}{dt} \langle \tilde{w}_\perp \rangle \propto (R^2 - 2R) \left(V_\parallel \frac{\partial |E|^2(Z(t))}{\partial Z} \right) \quad \text{approximately compensate each other.}$$

The remainder of this compensation defines the change of full electron energy:

$$\frac{d}{dt} \langle w \rangle \approx -\frac{\omega}{\Delta_0^3} \frac{e^2}{m\gamma_0} \frac{|V_\perp|^2}{c^2} \left(V_\parallel \frac{\partial}{\partial Z} |E|^2(Z(t)) \right). \quad (8)$$

So we have found that the alteration of the mean electron energy under action of the standing wave is not zero unlike more simple situations, for example system without magnetic field, where the full electron energy is the integral of particle motion in the field with time-independent amplitude. Taking in to account periodic dependence $|E|^2 = 2|E_0|^2 (1 + \cos(2kz + \varphi_0))$ we can see from (8) that the sign of energy change is constant if $kV_{\parallel}t \ll 1$. (It is the condition (2).) This sign depends on the sign of synchronism detuning. If $\Delta_0 > 0$ the energy of particle decreases if it moves in direction of stronger field. In this case the decrease of energy of gyro-rotations prevails over increase of averaged oscillatory energy. If $\Delta_0 < 0$ the situation is opposite.

Now the role of modulation of electron ensemble on the longitudinal momentum becomes obvious. If at every position Z electrons moves with the same longitudinal velocity (no modulation) number of electrons receiving and losing energy are equal. But setting the initial modulation on z of longitudinal velocity of electrons in ensemble in correspondence with spatial dependence of field amplitude, so that $\varphi_0 = \varphi_M + \pi/2 + \text{Sign } \Delta_0$ (φ_M - phase of modulation) the decrease of the energy of electron ensemble due to its interaction with nonresonant wave field is obtained. It is worth to note, that if $\Delta_0 > 0$ the source of field amplification is energy of gyro-rotations, but if $\Delta_0 < 0$ the source is averaged energy of transverse oscillations in the wave field. The calculation of the evolution

$$\begin{aligned} & \text{of energy of electron ensemble by the formula } \frac{d\langle W \rangle}{dt} = \\ & = \int dP_{\parallel}^0 d \frac{|P_{\perp}^0|^2}{2} dz_0 \left\{ \frac{d\langle w \rangle(P_{\parallel}^0, P_{\perp}^0, z_0, t)}{dt} \left(f_0 \left(P_{\parallel}^0, \frac{|P_{\perp}^0|^2}{2} \right) + f_M \left(P_{\parallel}^0, \frac{|P_{\perp}^0|^2}{2} \right) \cos(\varphi_M + 2kz_0) \right) \right\} = \\ & = -\mu |E_0|^2 \quad \text{gives the same result for increment } \mu = \frac{2e^2 \omega |V_{\perp}^R|^2}{m\gamma_R^2 c^2} \times \\ & \times \left| \int \frac{P_{\parallel}}{mc} f_M \left(p_{\parallel}, \frac{|p_{\perp}|^2}{2} \right) \frac{1}{\Delta_0^3} dp_{\parallel} d \frac{|p_{\perp}|^2}{2} \right| \text{ as that obtained in [2] from linear theory.} \end{aligned}$$

Paying our attention on energy exchange during nonresonant interaction when $\Delta_0 t \gg 1$ we missed that during short time period $\Delta_0 t < 1$ the standard mechanism of energy exchange between wave and still synchronized particles works. It is important to compare two quantities: the energy extracted from the medium during parametric "nonresonant" interaction $\Delta\langle W \rangle$ and "quasi resonant" energy exchange $\delta\langle W \rangle = \langle W \rangle_{t=0} - W_0$. The investigated effect is worth to be spo-

ken about if the field derives energy from the medium integrally over all time of interaction. The analysis shows that the ratio $\Delta\langle W\rangle/\delta\langle W\rangle$ has order of $R(\kappa V_{\parallel}t)$. It can be more than 1, so the energy exchange during parametric interaction without partial resonances can be the dominant effect.

The main results

The theory of the parametric instability of the cyclotron interaction in the absence of resonant particles is developed. The nonlinear equations of particle motion in the wave field in one-frequency frame of references are investigated with aim to explain the energy exchange mechanism in this regime.

It is obtained that the source of field amplification is the energy of transverse motion.

It is shown that the energy extracted from the medium during nonresonant interaction exceeds initial "quasi-resonant" energy exchange.

References

1. *Gaponov-Grekhov A. V., Tokman M. D.*, JETP, 1997, **85**, 640.
2. *Erukhimova M. A., Tokman M. D.*, JETP, 2000, **91**, 255.
3. *Erukhimova M. A., Tokman M. D.*, Radiophysics and Quantum Electronics, 2001, **44**, 176.
4. *Erukhimova M. A., Tokman M. D.*, Plasma Physics Reports, 2001, **27**, 868.
5. *Kocharovskaya O.*, Phys. Rep., 1992, **219**, 175.

PENETRATION OF A MICROWAVE WITH A STOCHASTIC JUMPING PHASE (MSJP) INTO OVERDENSE PLASMAS AND ELECTRON COLLISIONLESS HEATING BY IT

V. I. Karas', V. D. Levchenko¹

NSC "Kharkov Institute of Physics & Technology", Kharkov, Ukraine

¹Keldysh Institute of Applied Mathematics of the RAS, Moscow, Russia

In present report the results from a theoretical study as well as from numerical simulation of either direct or inclined incident to boundary vacuum-overcritical density plasma of the linearly polarized electromagnetic waves are discussed. The chief results of our studies are the following: (i) at considered parameters the penetration coefficient (PC) of the MSJP is about one order of magnitude higher than a PC of the wide-band regular electromagnetic wave (WREW); (ii) in particular, at inclined incident of the MSJP a electron heating is most essential and besides the electron distribution function has high energy "tail". This anomalous behavior of a penetration coefficient as well as the electron heating are connected with a jumping phase of MSJP.

Litvak and Tokman [1] have been demonstrated the useful possibility to transport waves through the region of their absorption owing use of a classical analog of quantum electromagnetic induced transparency. Fainberg et al [2] shown that the stochastic electric fields with a finite time of a phase correlation can effective heat the particles of the collisionless plasma because the inverse correlation time at interaction particle-wave in fact have a physical sense of some effective collision frequency.

In present report the results from a theoretical study as well as from numerical simulation of either direct or inclined incident to boundary vacuum-overcritical density plasma of the linearly polarized electromagnetic waves are discussed. The dynamics of plasma electrons is described by the relativistic Vlasov equation for the distribution function and by Maxwell's equations for the self-consistent electric and magnetic fields. Ions are immobile. Our method [3] allows a fully nonlinear kinetic treatment of electron dynamics for arbitrary densities and wave intensities provided that the time step is small compared to the electron plasma period. We considered a penetration into overdense plasmas of the MSJP as well as the wide-band regular electromagnetic wave (WREW), which has the identical spectral density of signal.

The plausible mechanisms of a wave passage through a wave barrier are following:

- linear and nonlinear transformation of different waves;
- linear and nonlinear echo with help of van Kampen waves;
- linear "enlightenment" of a wave barrier ("beam antenness");
- collisional penetration of a wave into a wave barrier;

- penetration of a wave is due to the jumps of a wave phase because a penetration coefficient is proportional a phase derivative that result from a electric field derivative.

It is well to bear in mind the following mechanisms of a particle heating by waves:

- resonant absorption that is effective as result of synchronism between a wave and a particle, i.e. a temporal shift of a phase difference is equal to zero;
- collision absorption is conditioned by losing of particle-wave synchronism (therefore, efficiency is proportional to ratio of a collision frequency to a wave frequency);
- linear and nonlinear absorption into a inhomogeneous wave;
- wave absorption is due to jumps of a wave phase as result of losing of a wave-particle synchronism.

Physical model

Consider the case where the electron plasma is initially homogeneity and ions are immobile (Fig. 1). The electron distribution function is Maxwellian with a thermal velocity V_T . Plasma density is $n(x) = n_0 \theta(x)$ (where $\theta(x)$ is Heviside function; $(\omega_p > \omega_0)$; ω_p and ω_0 are the electron plasma frequency and the wave frequency, respectively). Electromagnetic wave have $\vec{k} = (k_x, k_y, 0)$, $\vec{E} = (E_x, E_y, 0)$, $\vec{B} = (0, 0, B_z)$. At $x = x_L$

$$E_y^{sf}(t) = B_z^{sf}(t) = F_0 \cos(\omega_0 t + \tilde{\varphi}(t)), \tag{1}$$

where $\tilde{\varphi}(t)$ is steady state Poisson's stochastic process with a frequency $1/\tau_0$ and into a interval $[-\pi, \pi]$. Correlation coefficient of such stochastic process is:

$$R(t) = \exp\left(-\frac{|t|}{\tau}\right) \cos \omega_0 t, \tag{2}$$

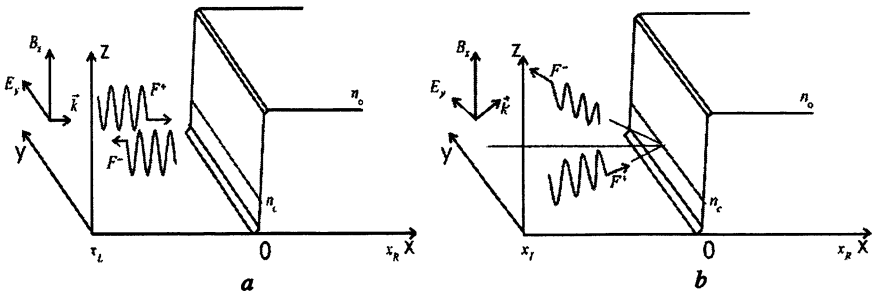


Fig. 1. Scheme of a model region: *a* – direct wave incident upon the surface; *b* – inclined wave incident upon the surface

Spectrum density [3]

$$G(\omega) = \frac{1}{(1/\tau)^2 + (\omega - \omega_0)^2}. \quad (3)$$

In the plane case Maxwell equations for self-consistent electromagnetic fields have a form

$$\frac{1}{c} \frac{\partial E_y}{\partial t} + \frac{\partial B_z}{\partial x} = -\frac{4\pi}{c} j_y, \quad \frac{1}{c} \frac{\partial B_z}{\partial t} + \frac{\partial E_y}{\partial x} = 0,$$

and, if we enter the auxiliary fields $F^\pm = E_y \pm B_z$, are split in two of the such equations

$$\left(\frac{1}{c} \frac{\partial}{\partial t} \pm \frac{\partial}{\partial x} \right) F^\pm = -\frac{4\pi}{c} j_y,$$

where the charge density ρ and the transversal current density j_y are defined as

$$\rho = e \left(n_0 - \int f(x, \vec{p}) d\vec{p} \right), \quad (4)$$

$$j_y = e \int (V_y(x) f(x, \vec{p}) d\vec{p}). \quad (5)$$

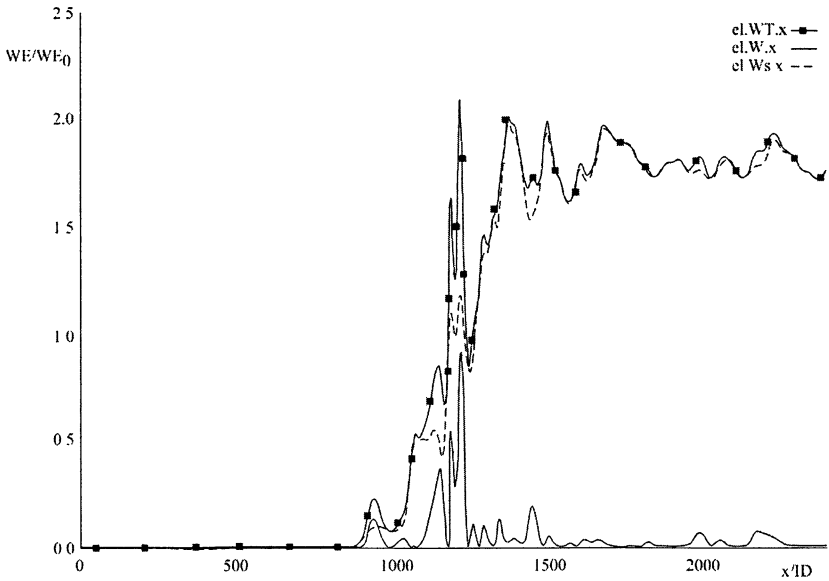
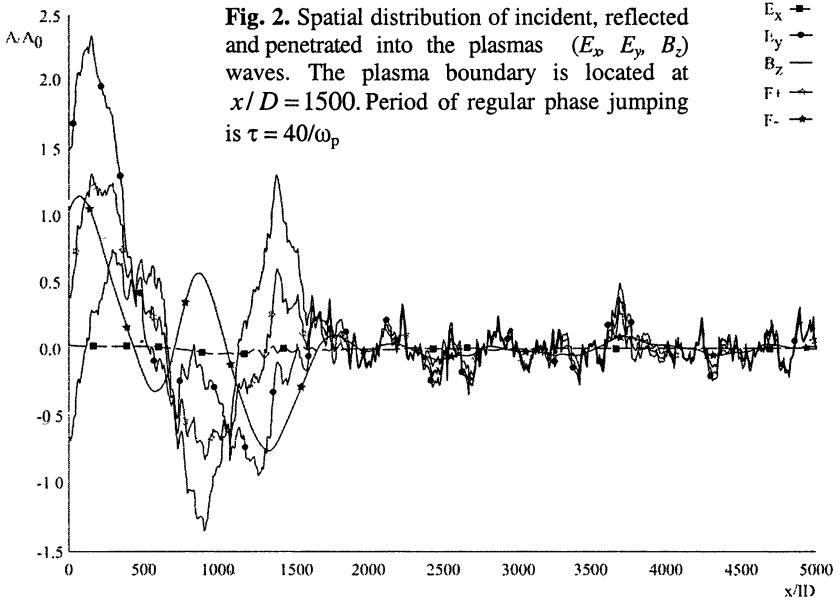
The boundary conditions to transversal and longitudinal E_x fields have a form:

$$E_x|_{x=x_L} = 0, \quad F^+|_{x=x_L} = F(t), \quad -F^-|_{x=x_R} = 0, \quad (6)$$

where $F(t)$ is a relation from (1). To a numerical simulation we used our code SUR [4, 5] at following parameters: $V_y^{osc} = 3V_T$, $\omega_0 = 0.5\omega_p$, $\tau = 40/\omega_p$, $x_L = -1000\lambda_D$, $x_R = 1000\lambda_D$, fall length of a ion profile $\Delta L = 50\lambda_D$, $L = 5000$, λ_D Debye length. The results of numerical simulation exhibited in Figs. 2, 3. The penetration coefficient defined as ratio of a penetration-wave energy flow (at $x = x_R$) to incident-wave energy flow (at $x = x_L$) with a corresponding time shift.

To numerical simulation of inclined incident of electromagnetic radiation to boundary vacuum-plasma the such parameters were used as to direct incident with the exception only of plasma size that was $L = 2500$. In this case an incident electromagnetic radiation render a strong influence to plasma electrons (in particular at big incident angles. The longitudinal fields are close to transversal one`s. The longitudinal electron energy (and their temperatures) grows more than once. The electron distribution function is non-Maxwellian function because the accelerated electron "tail". The incident transversal electromagnetic waves is transformed partially in a longitudinal wave as well as electron energy.

To illustration we depicted a character experimental oscilloscope of the stochastic signal realization (Fig. 4).



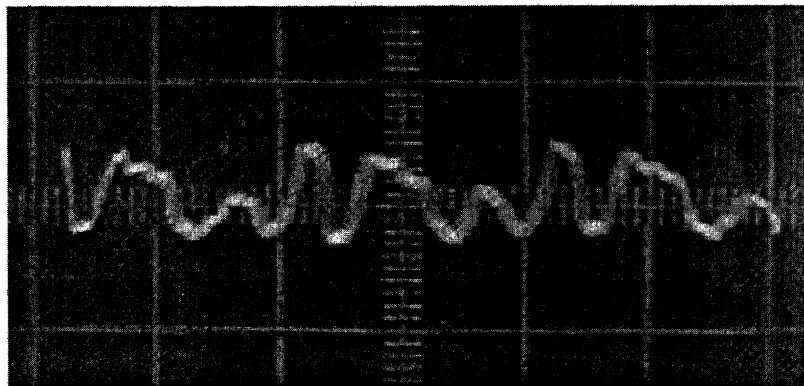


Fig. 4. Some experimental realizations of microwave with a stochastic-jumping phase

Conclusions

The chief results of our studies are the following: (i) at considered parameters the penetration coefficient (PC) of the MSJP is about one order of magnitude higher than a PC of the WREW; (ii) in particular, at inclined incident of the MSJP a electron heating is most essential and besides the electron distribution function has high energy "tail". This anomalous behavior of a penetration coefficient as well as the electron heating are connected with a jumping phase of MSJP.

The work was supported in part by INTAS project № 01-233.

References

1. *Litvak A. G. and Tokman M. D.*, Phys. Rev. Lett., 2002, 88, 095003.
2. *Fainberg Ya. B., Bass F. G., Shapiro V. D.*, Zh. Eksp. Teor. fiz., 1965, 49, 329.
3. *Akhmanov S. A., D'yakov Yu. E., Chirkin A. S.* Vvedenie v statisticheskuyu radiofiziku i optiku. M.: Nauka, 1981.
4. *Levchenko V. D., Sigov Yu. S.*, In: Dynamics of Transport in Fluids, Plasmas and Charged Beams. Ed. G. Maino and A. Provenzale. World Scientific: Singapore, 1995, 121.
5. *In'kov L. V., Levchenko V. D.* Optimizatsiya PIC metoda v ramkakh ob'ektno-orientirovannoy modeli plazmy v kode SUR. Preprint 133, IPM im. M. V. Keldysha RAN, Moskva, 1995.

DYNAMICS OF POWERFUL PLASMA WAVE BREAKING AND REFLECTION PHENOMENA

V. I. Arkhipenko, E. Z. Gusakov¹, V. A. Pisarev, L. V. Simonchik

Institute of Molecular and Atomic Physics NASB, Minsk, Belarus

¹Ioffe Physical-Technical Institute RAS, St. Petersburg, Russia

Interaction of powerful electromagnetic waves with plasma is accompanied by wave breaking phenomenon and fast electron generation. Both these effects attract considerable attention at present as a possible way of strong electric field production and further ion acceleration. In this paper we describe results of a model experiment in which propagation and absorption of strong electrostatic wave pulse in inhomogeneous magnetised plasma is studied and substantial electron acceleration effect is observed under conditions, when the wave breaking should occur according to estimations.

The experiments were performed in a linear plasma device "Granite" [1] where plasma was produced using the electron cyclotron discharge in a tube 2 cm in diameter and 100 cm in length. The experiment parameters are as follows: magnetic field $H = 3500$ Oe, the argon gas pressure is 10^{-2} Torr, the plasma inhomogeneity scale along magnetic field and across it are $a = 5$ cm and $b = 0.4$ cm accordingly, the maximal electron density is $n_e \sim 5 \cdot 10^{12}$ cm⁻³, electron temperature is $T_e = 2$ eV. An electron plasma wave (EPW) at frequency $f = \omega/(2\pi) = 2.84$ GHz in the form of the fundamental Trivelpiece-Gould mode was launched into the plasma by waveguide.

The dispersion relation for this wave is $k_{\perp}^2 = [\omega_{pe}^2(r, z) / \omega^2 - 1] k_{\parallel}^2$, where k_{\parallel} and k_{\perp} are the components of the wave vector parallel and transverse to the magnetic field. The high density plasma ($n_e(r, z) > n_c$, where n_c – critical electron density) creates a plasma waveguide for EPW shown in Fig. 1. It is weakly inhomogeneous in axial direction. Propagating towards decreasing electron density to a point of a plasma resonance (focal point), where $\omega = \omega_{pe}(0, z)$ the wave slows down and its electric field increases drastically. This electric field growth is so significant, that the incident wave power of 10 mW is enough for the parametric decay instability of stimulated back scattering excitation [2].

At higher pump power the electron redistribution due to the ponderomotive force should come into play, leading to quasi-static electric potential enhance-

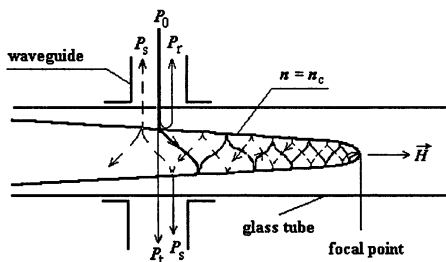


Fig. 1. Scheme of excitation and propagation of the EPW. P_0 , P_r , P_s , P_r are incident, transient, scattered and reflected power correspondingly.

ment in the resonance point vicinity. The oscillatory energy of electrons given, according to [2], by $W_- = \frac{P}{\pi\omega n_e} k_{\parallel}^3 \exp\left(-2ak_{\parallel} \frac{v}{\omega}\right)$ at power ~ 5 W exceeds the ionisation energy of argon atoms. At power about 20 W the electron oscillatory velocity is already close to the phase velocity of wave $\omega/k_{\parallel} = 4 \cdot 10^8$ cm/s. At this condition intensive resonance interaction of wave with electrons and, as a consequence, the capture of electrons and wave breakdown should take place. The energy of captured electrons is close to double oscillatory energy in the breaking point and scales as $W^* [\text{eV}] \approx 90 P^{0.4} [\text{W}]$. The dependence of the fast electron energy on pump power obtained in our previous experiments [3] is in agreement with this scaling. It was shown that at available power of 10 kW electrons with energy higher than 500 eV are generated in initial stage of pulses ($t < 100$ ns). The density of accelerated electrons was estimated at the level ~ 25 % of total density in focal point [4].

In the present paper the detailed study of dynamics of interaction of strong EPW pulses with plasma was performed at pump power less than 200 W. A number of diagnostics, possessing sufficient time resolution such as: multi-grid analyser and spectroscopic, cavity, magnetic diagnostics – were used in the experiment. Parameters of microwave pump in present experiments are as follows: incident pulse power is $P \sim 50\text{--}200$ W, pulse duration is up to $2.5 \mu\text{s}$, pulse rise time is $t_f \sim 40$ ns, repetition frequency is 300 Hz. The oscillogram of incident pulse is shown in Fig. 2, *a*.

As it is seen in oscillograms of both the multi-grid analyser (Fig. 2, *c*) and Rogovskii's coil (Fig. 2, *d*) two

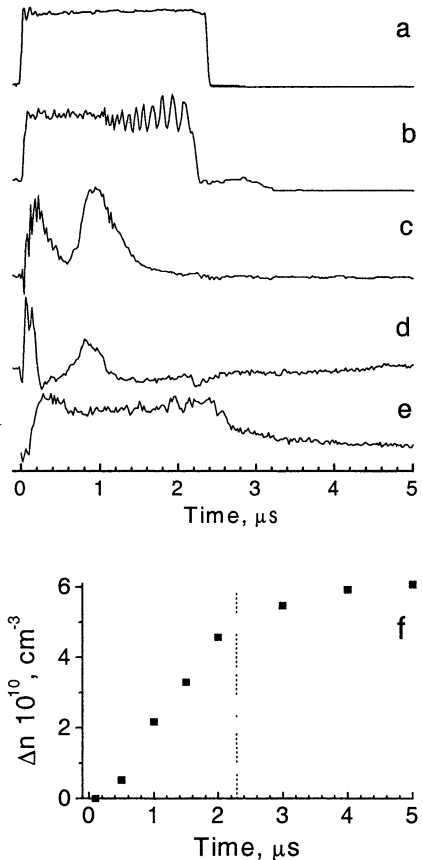


Fig. 2. Oscillograms of incident (*a*) and scattered (*b*) pulses, currents of multi-grid analyser (*c*) and Rogovskii's coil (*d*), light intensity (*e*) and time behavior of electron number density (*f*) in focal region.

separate bursts of electron current are generated in plasma after the microwave pulse is on. The first one is observed immediately after the application of RF power, whereas the position of the second is determined by the pump power. The delay of the second burst is higher than $1 \mu\text{s}$ for $P = 50 \text{ W}$ and decreases with growing power. The bursts overlap at $P = 1 \text{ kW}$. The maximal electron current in both bursts increases with microwave power.

The electron distribution function measured by the analyser has a pronounced tail at energy $W \gg T_e$, which can be characterised by effective temperature T_h . The effective temperature T_h depends on the time and pulse power. The time variation of voltage-characteristics of multi-grid analyser is shown in Fig. 3. As it is seen, the first electron current burst is caused by the high energy electrons with effective temperature T_h higher than 350 eV . The effective temperature in the second burst is significantly smaller and has value of $\sim 50 \text{ eV}$. After the termination of the second burst the further decrease of the fast electron's temperature to the level $T_h = 20 \text{ eV}$ is observed. The above mentioned fast electrons disappear during $1\text{--}1.5 \mu\text{s}$ after the pulse switch off.

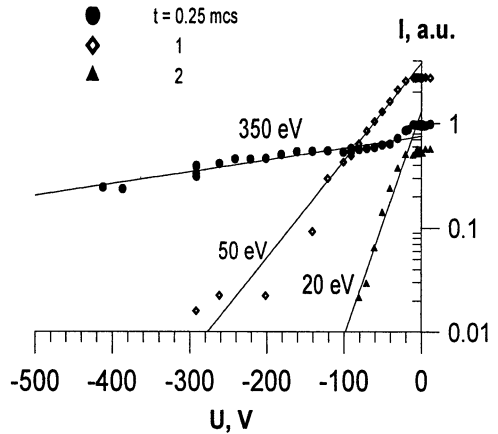


Fig. 3. Voltage-current characteristics at different time.

It should be mentioned that the termination of the second fast electron current burst is always accompanied by oscillations observed on the microwave detector in the waveguide Fig. 2, *b*. These oscillations indicate the wave reflected in plasma, which is up-shifted in frequency. The power of this wave is comparable to the launched one.

High energetic electrons produce increased excitation and ionisation of argon atoms. Therefore the significant growth of light intensity is observed in the focal region just after the pulse is on (Fig. 2, *e*). Fast intensity fall after a pulse termination is also correlated to the behaviour of energetic electrons. On contrary, the electron density increased both during the pulse impact (Fig. 2, *f*) and $1\text{--}2 \mu\text{s}$ after a pulse termination. After that the electron density was practically constant for a long time and then decreases slowly to the initial condition during 1 ms .

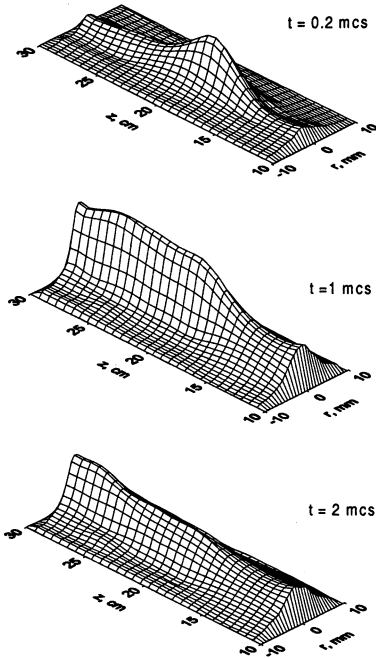


Fig. 4. Spatial distributions of ArII 454.5 nm line intensity at different time.

the obtained electron density is averaged over a cavity volume. To obtain the absolute spatial density distribution we used the data for average electron density and radial distribution of luminosity integrated in visible spectral region, as radial distribution of plasma density. This method was tested earlier in [1]. The contours of electron density distribution at different time, calculated in this way, are plotted in Fig. 6. Ten grey gradation were used in these pictures to scale the plasma density magnitudes. Maximal light hue corresponds to electron number density of $5 \cdot 10^{11} \text{ cm}^{-3}$.

These pictures obviously illustrate

The spatial distributions of the ArII 454.5 nm line intensity at different time are shown in Fig. 4. As it seen the intensity growth in vicinity of focal point is observed at the pulse start (Fig. 4, $t = 0.2 \mu\text{s}$). Then the fast growth of luminosity begins in region of lower density plasma ($t = 1 \mu\text{s}$) and a long narrow luminous channel is formed at the pulse termination time ($t = 2 \mu\text{s}$).

In Fig. 5 the axial distributions of averaged electron density measured with the cavity diagnostics at different moments are pictured. One can see that the density distribution evolution under the influence of microwave power is similar to that, observed in Fig. 4 for plasma luminosity. The density increases at first in the vicinity of focal point ($z = 24 \text{ cm}$). Later on the growth of density in a wider region along discharge axis is observed. As far as the density measurements were performed using the cavity diagnostic,

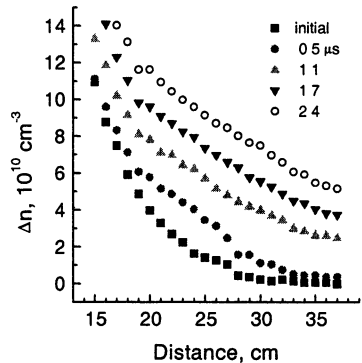


Fig. 5. Axial distribution of average electron number density at different time.

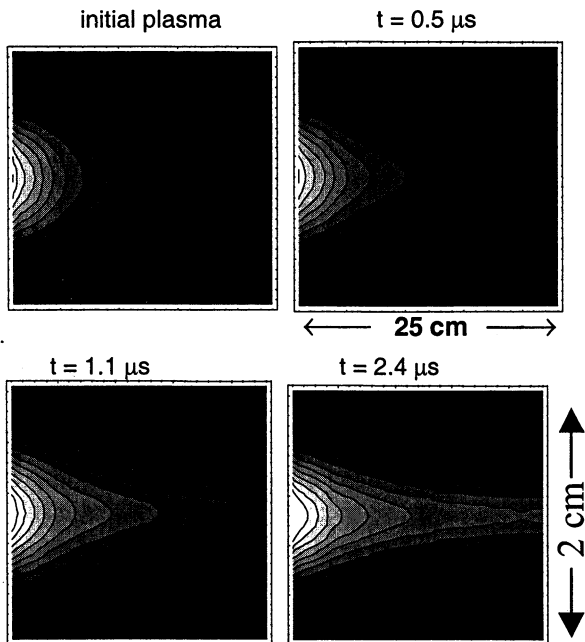


Fig. 6. Contours of the electron density distribution

formation of longitudinal plasma channel, which serves as a waveguide for EPW. When the channel propagates down to the distance of 45 cm from the launcher it goes out from the magnetic system. The magnetic field quickly decreases and conditions for the EPW change drastically leading to its reflection. The reflection takes place also if the multi-grid analyzer is placed at distance less than 45 cm. Reflected wave propagates in opposite direction towards the launcher in non-stationary narrow channel with increasing density (see Fig. 6). That leads to an additional phase taper and, correspondingly, to the frequency up-shift of the wave. In turn it causes low frequency oscillations of the homodyne detector signal (Fig. 2, *b*). The time resolved spectral analysis of the reflected microwave signal performed using spectrum analyzer with window of $0.4 \mu\text{s}$ allowed to display the satellite close to pump wave line in the anti-Stokes region of its spectrum (Fig. 7). The satellite frequency shift depends on both the time

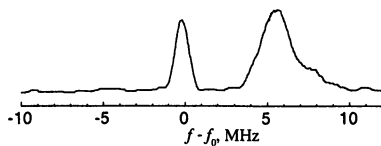


Fig. 7. Spectrum of scattered signal

and pulse power (Fig. 8). It exceeds 20 MHz at the oscillation onset and then falls sharply to the frequency shift of ~ 5 MHz, which is weakly changed down to pulse termination. The onset time of oscillations decreases with the pump power, which can be explained by quicker channel formation due to growth of electron energy and, as consequence, increasing of ionisation rate.

In conclusion we should underline that the interaction of a strong microwave pulse at power up to 200 W with inhomogeneous magnetised plasma resulting in the electron acceleration takes place during the period less than $0.5 \mu\text{s}$. This acceleration, in our opinion, is produced by the wave breaking.

For longer time the narrow homogeneous plasma channel is formed due to the fast ionisation caused by oscillating electrons. It leads to growth of collision wave absorption and suppression of the electron acceleration.

Reflection of the powerful wave at the edge of plasma waveguide is observed at the later stage of interaction ($t > 1 \mu\text{s}$). It is likely that at first stage of interaction ($t < 0.5 \mu\text{s}$) the high electrostatic potential is formed in the vicinity of resonance point due to the electron redistribution in the ponderomotive potential.

The work was supported by RFBR-BRFBR collaborative grant (02-02-81033 Bel 2002_a, F02P-092) and grant INTAS-01-0233.

References

1. Arkhipenko V. I. et al., Plasma Physics Reports, 1981, **7**, 396–404.
2. Arkhipenko V. I. et al., Plasma Physics Reports, 1987, **13**, 693–707.
3. Arkhipenko V. I. et al., Proc. of the III Intern. Workshop "Strong microwaves in plasmas", Nizhny Novgorod, 1996. V. 2, p. 516–521.
4. Arkhipenko V. I. et al., 29th EPS Conference on Plasma Phys. and Contr. Fusion Montreux (17–21 June 2002 ECA). V. **26B**, P-5.009 (2002).

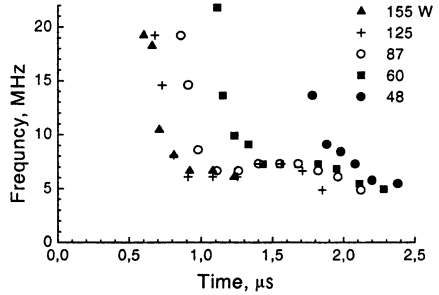


Fig. 8. Temporal dependencies of oscillation frequency at different pump power.

THE UPPER HYBRID RESONANCE IN THE TURBULENT PLASMA

E. Z. Gusakov, A. V. Surkov

Ioffe Physico-Technical Institute, St.-Petersburg, Russia

The long-scale plasma turbulence influence on the enhanced scattering (ES) diagnostics, which is sensitive to small-scale fluctuations, is investigated. The probing and scattered extraordinary wave frequency spectrum formation due to multiple small-angle scattering during the wave propagation in the upper hybrid resonance region is studied. The correlation ES diagnostics radial wavenumber resolution, which is determined by multiple small-angle scatterings effect, is analyzed.

The enhanced microwave scattering technique is an efficient tool for the small-scale plasma turbulence investigations. This method is based on the measurement of the signal, which is Back Scattered (BS) off the plasma density fluctuations in the Upper Hybrid Resonance (UHR) vicinity. The enhancement effect is associated with probing and scattered extraordinary waves electric field potential component growth in the UHR vicinity. This circumstance provides extreme sensitivity and high spatial resolution of the ES diagnostics. The increase of the probing wave wavenumber in the UHR region causes the sensitivity to the small-scale plasma density fluctuations.

At first this technique was applied to small-scale oscillations and waves investigations in quiet plasma of linear laboratory devices [1]. But now this method is introduced for a study of plasma small-scale turbulence and wave propagation in the tokamak plasma [2]. In this case the incident wave propagation and the scattering take place in the plasma with dominating long-scale density fluctuations in the background, which can modify the BS spectra. The BS wave frequency spectrum broadening can be associated not only with the frequency of the small-scale fluctuations, but also with spectral broadening of incident and BS waves due to small-angle scattering off the long-scale turbulence component. As it was shown in [3] the small-angle scattering cross-section increases sharply in the vicinity of the UHR as well as the BS one. Owing to this cross-section growth a non-linear regime of a multiple small-angle scattering arises.

In the present paper the effect of the multiple small-angle scatterings due to the density fluctuations in the UHR vicinity on incident and BS wave spectrum is analyzed. The multiple small-angle scatterings influence on enhanced scattering correlation analysis [4] is also considered.

1. The probing wave frequency broadening

The effect of small-angle scattering has the nature of a phase modulation. So it can be taken into account by the inserting of the turbulent phase variation in the expressions for the wave electric field in the eiconal approximation. The phase variation has the form of an integral of the density fluctuation along the wave ray trajectory with a weight factor, which takes into account the enhancement of the small-angle scattering. For the extraordinary wave in the UHR vicinity it takes form

$$\delta\Psi(x, t) = -\frac{k_c}{2n_{UH}} \int_0^x d\chi \frac{\delta n(\chi, t)}{(-\varepsilon(\chi))^{3/2}}, \quad (1)$$

where $k_c = \omega_{ce}(x_{UH})/c$; $\varepsilon = (x - x_{UH})/\ell$ is an element of permittivity tensor (the plasma density profile is assumed to be linear), $x = 0$ is an antenna position and $\delta n/n_{UH}$ is the relative density fluctuation in the UHR.

For example, this approach allows calculating the averaged electric field extinction due to the multiple small-angle scattering. Assuming a normal distribution of a random value $\delta\Psi$ the averaged electric field is given by:

$$\langle E \rangle \propto \langle e^{i\delta\Psi} \rangle = e^{-\langle \delta\Psi^2 \rangle / 2} = \exp \left\{ -\frac{\langle \delta n^2 \rangle}{n_{UH}^2} R(x) \right\}, \quad (2)$$

$$R(x) = \begin{cases} \ell \ell_c k_x^4(x) / 16k_c^2, & x_{UH} - x \gg \ell_c, \\ \ell^2 k_x^2(x) / 2, & x_{UH} - x \ll \ell_c, \end{cases}$$

where $k_x(x) = k_c \sqrt{\ell} / \sqrt{x_{UH} - x}$ is the extraordinary wave wavevector projection on the inhomogeneity direction x , and ℓ_c is the long-scale fluctuations correlation length.

The correlation function

$$K(x, \tau) = \frac{\langle A(x, t) A^*(x, t + \tau) \rangle - \langle A(x, t) \rangle \langle A(x, t + \tau) \rangle^*}{\langle |A(x, t) - \langle A(x, t) \rangle|^2 \rangle}, \quad (3)$$

where $A(x, t) = e^{i\delta\Psi(x, t)}$, allows evaluating the frequency spectrum of the multiple small-angle scattered wave. Assuming the normal distribution of $\delta\Psi$ we get following expression for this correlation function:

$$K(x, t) = \left(e^{\langle \delta\Psi(x, t) \delta\Psi(x, t + \tau) \rangle} - 1 \right) / \left(e^{\langle \delta\Psi^2 \rangle} - 1 \right). \quad (4)$$

In a non-linear case, when the field correlation time is much less then the fluctuations correlation time $\tau/t_c \ll 1$, the correlation function takes the following simple form:

$$K = \exp \left\{ -\frac{\langle \delta n^2 \rangle}{n_{UH}^2} R(x) \langle \Omega^2 \rangle \tau^2 \right\}, \quad (5)$$

where $\langle \Omega^2 \rangle$ is the averaged square of the long-scale fluctuations frequency. The corresponding probing wave spectrum width is given by

$$\Delta\omega \approx 2\sqrt{R(x) \langle \Omega^2 \rangle \langle \delta n^2 \rangle / n_{UH}^2}. \quad (6)$$

It is well known that in the UHR vicinity, when $k_x \sim \omega/c \cdot \sqrt{c/v_{Te}}$, the extraordinary wave transforms into Bernstein mode, which propagates from the UHR. Near the UHR the wavenumber of Bernstein wave takes form: $k_x = \sqrt{-\varepsilon(x)}/\ell_T$, where ℓ_T is associated with the thermal particle motion, $\ell_T \sim \rho_{ce}$, where ρ_{ce} is the electron cyclotron radius.

The Bernstein wave can be back scattered off the small-scale fluctuations and then, after the reverse transformation it gives the contribution in the registered signal. So, the spectral broadening of the Bernstein wave is also essential. The Bernstein wave spectrum width can be evaluated with the same method. Near the UHR it is proportional to the wavenumber and equal to the extraordinary wave spectrum width in this region:

$$\Delta\omega \approx \ell k_x(x) \sqrt{2 \langle \Omega^2 \rangle \langle \delta n^2 \rangle / n_{UH}^2}, \quad x_{UH} - x \ll \ell_c. \quad (7)$$

And during the propagation from the UHR the broadening increase practically stops:

$$\Delta\omega \approx \sqrt{\frac{\ell \ell_c}{\ell_T^2} \ln(k_x^2(x) \ell_T^2 / \ell_c) \langle \Omega^2 \rangle \langle \delta n^2 \rangle / n_{UH}^2}, \quad x_{UH} - x \gg \ell_c. \quad (8)$$

2. The correlation technique wavenumber resolution

As we have shown the small-angle scattering effects disturb the probing wave propagation determining the formation of the BS wave frequency spectrum. So we can anticipate that the long-scale turbulence influence on the correlation ES diagnostics is essential too. This method is based on the dependence of the BS signal on the fluctuation phase in the scattering point and allows getting the fluctuations wavenumber spectrum [4]. Taking into account that the main input into BS signal is produced by the linear conversion point, where the eiconal approximation fails, we shall use the accurate expressions for resonant component of the electric field [1]:

$$E(\xi) = \sqrt{\frac{8}{\gamma^2 \ell \omega_0}} \int_0^\infty d\kappa \exp \left[i \left(\frac{\kappa^3}{3} - \frac{b}{\kappa} + \xi \kappa \right) \right], \quad (9)$$

$$\gamma = (\ell_T / \ell)^{2/3}, \quad \xi = (x - x_{UH}(t)) / (\gamma \ell), \quad b = (k_c \ell)^2 \gamma,$$

where the long scale fluctuations are accounted for by using a long-scale approximation:

$$x_{UH}(t) = x_{UH} - \ell \delta n(t) / n_{UH}, \quad (10)$$

modeling the movement of the UHR due to the long-scale fluctuations but neglecting their influence on the density gradient. Substituting expressions (9), (10), for the probing wave field into the reciprocity theorem in the form proposed by Piliya in [1] we obtain the following formula for the cross-correlation function of BS signals at two probing frequencies

$$\begin{aligned} \langle A_{s1}(t) A_{s2}(t + \tau) \rangle &= \frac{1}{\gamma^2 n_{UH}^2} \int_{-\infty}^\infty \frac{d\bar{Q}}{(2\pi)^3} |\delta n_{\bar{Q}, \Omega}|^2 |U(\gamma \ell Q_x)|^2 \times \\ &\times e^{iQ_x \Delta x_{UH}} F(Q_y, Q_z) K(Q_x, \Delta x_{UH}, \tau). \end{aligned} \quad (11)$$

Here $|U(\gamma \ell Q_x)|^2$ is the factor, which describes the scattering enhancement [1], Δx_{UH} is the distance between UHR positions for two probing waves, $F(Q_y, Q_z)$ is the term, which is determined by the antenna diagram, and $K(Q_x, \Delta x_{UH}, \tau)$ is the additional factor, which is caused by the multiple small-angle scattering. The last term describes the correlation decay due to long-scale turbulence and has a following form:

$$K = \exp \left\{ -(\Delta x_{UH})^2 \delta Q_x^2 - \tau^2 \Delta \omega^2 \right\}, \quad (12)$$

where δQ_x determines the wavenumber resolution of the diagnostics and $\Delta \omega$ corresponds to the frequency spectrum broadening. For the BS wave in the region of the maximum efficiency of BS we have the BS wave spectrum width:

$$\Delta \omega \approx \frac{1}{\sqrt{2}} \ell Q_x \sqrt{\langle \Omega^2 \rangle \langle \delta n^2 \rangle} / n_{UH}, \quad (13)$$

where Q_x is the radial wavenumber of the fluctuation. This expression matches formulas (4) and (5) after the substitution of the Bragg condition $2k_x = -Q_x$. The prescribed behavior of the broadening agrees with one, which was observed in the experiments on FT-1 tokamak [2]. Using the observed spectrum width

$\Delta f = \omega / (2\pi) \approx 5.4 \cdot 10^5 \text{ Hz}$, $Q_x \sim 100 \text{ cm}^{-1}$, assuming the drift nature of the long-scale turbulence: $\bar{\Omega} \approx v_d q_0$ and FT-1 tokamak parameters, which give the characteristic wavenumber of the long-scale turbulence $q_0 \sim 2 \text{ cm}^{-1}$, and the drift velocity $v_d \sim 2 \cdot 10^5 \text{ cm/s}$, we get a sensible estimation for the relative amplitude of the long-scale fluctuations: $\delta n / n_{UH} \sim 0.1$.

The diagnostics radial wavenumber resolution in the region of the maximum efficiency of BS takes the following simple form

$$\delta Q_x \approx \frac{1}{\sqrt{2}} \ell Q_x \sqrt{\langle q_x^2 \rangle \langle \delta n^2 \rangle} / n_{UH}, \quad (14)$$

where q_x is a radial wavenumber of the long-scale fluctuations. So the multiple small-angle scattering limits the wavenumber resolution of the diagnostics and must be taken into account for a proper interpretation of the diagnostics results.

3. Conclusions

In this paper the influence of the long-scale turbulence on the ES diagnostics is investigated. The unusual behavior of the BS wave frequency spectrum, which was observed on FT-1 tokamak, is explained. The influence of the multiple small-angle scattering on the wavenumber resolution of correlation ES technique is analyzed. The additional possibility to get some local information about the long-scale turbulence from the ES diagnostics results arises.

Acknowledgements. The paper was supported by the RFBR grants 00-15-96762, 01-02-17926, 02-02-17589, 02-02-17591, 02-02-06632-mas, INTAS grant 01-2056 and RFBR-NWO grant 047.009.009.

References

1. *Novik K. M., Piliya A. D.*, Plasma Phys. Control Fusion, 1993, **35**, 357.
2. *Bulygin'skiy D. G., Gur'chenko A. D., Gusakov E. Z. et al.*, Phys. of Plasmas, 2001, **8**, 2224.
3. *Gusakov E. Z., Surkov A. V.*, Plasma Phys. Rep., 2001, **27**, 971.
4. *Gusakov E. Z., Kaganskaya N. M., Krämer M. et al.*, Plasma Phys. Control. Fusion, 2000, **42**, 1033.

THE NONLINEAR REGIME OF A RESONANCE MICROWAVE PROBE BASED ON A TWO-WIRE LINE SECTION

*I. G. Kondrat'ev, A. V. Kostrov, A. I. Smirnov,
A. V. Strikovskiy*

Institute of Applied Physics, Russian Academy of Sciences, Ulyanov str. 46,
603950 Nizhny Novgorod, Russia

Resonance probes often used for plasma diagnostics are very sensitive even to minor changes in parameters of the media. Main sources of information in such sensors are shifting and expanding of the resonance curve. The report proposed describes a plasma resonance microwave probe based on a section of the two-wire line. It is shown that the nonlinear regime can be used successfully not only to measure plasma density, but also plasma temperature as well.

The basic scheme of the resonance microwave probe used in the experiments described below is shown in Fig. 1.

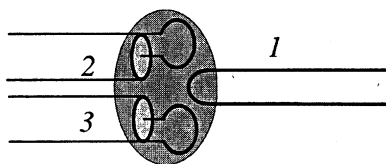


Fig. 1. Quarter-wave resonator (1), exciting (2) and receiving (3) lines.

l is the length of the two-wire line section; d is the distance between the wires; a is the radius of the wires: $a/d \ll 1$, $d/l \ll 1$, $M_{2,3}$, $M_{2,1} = M_{3,1} = M$ are the coefficients of mutual inductance between the coupling loops, coupling loops and the two-wire line; L_c is the coefficient of inductance of the coupling loops; ρ , ρ_c are the wave resistances of the two-wire line and the coaxial cables $c^{-2}\omega L_c \ll \rho_c$, $c^{-2}\omega M \ll \rho$.

Behaviour of the current, $I(z)$, and voltage, $U(z)$, in long line 1 (co-ordinate z is counted from its short-circuited end) can be described by means of telegraph equations:

$$\frac{dU}{dz} = -\frac{i}{c^2} \omega \tilde{L} \cdot I + \varepsilon \cdot \delta(z+0), \quad (1)$$

$$\frac{dI}{dz} = -i\omega \tilde{C} U \quad U(0) = 0, \quad I(z=l) = 0,$$

where \tilde{L} and \tilde{C} are inductance and capacity of line 1 per unit length, respectively, $\varepsilon = -\frac{i}{c^2}\omega M(I_2 + I_3)$ is e.m.f. of mutual induction concentrated near the short-circuited end ($z = 0$), and $\delta(z)$ is delta function. $\omega \gg \omega_p$, ω_{He} , ω_{pe} and ω_{He} are plasma frequency and gyrofrequency of electrons, respectively.

$$\tilde{L} = \tilde{L}_0 \approx 4 \ln(d/a), \quad \tilde{C} = \tilde{C}_0(1 + \delta C), \quad \tilde{C}_0 \approx [4 \ln(d/a)]^{-1}, \quad |\delta C| \ll 1$$

(here \tilde{L}_0 and \tilde{C}_0 are inductance and capacitance per unit length of line 1 in vacuum).

In the presence of plasma the amplitude of the current in the line is defined by the coupling Q -factor, Q_0 , and the following parameter:

$$q = \frac{1}{\ell} \int_0^\ell \delta C \sin^2\left(\frac{\pi z}{2\ell}\right) dz. \quad (2)$$

The transmission coefficient ($\delta\omega = \frac{\omega - \omega_0}{\omega_0}$, $\delta C \ll 1$):

$$\beta = \frac{I_3}{I_0} = \frac{1}{\frac{1}{4}Q_0^2(\delta\omega + \text{Re } q)^2 + \left(1 + \frac{1}{2}Q_0 \text{Im } q\right)^2}. \quad (3)$$

The case of collisionless plasma:

$$\varepsilon = 1 - \frac{N}{N_c}, \quad N_c = \frac{\omega^2 m_e}{4\pi e^2}$$

(N is plasma density, m_e is electron mass, and e is electron charge).

The influence of striction nonlinearity:

$$N = N_0 \exp\left(-\frac{|\bar{E}|^2}{E_c^2}\right), \quad E_c = \left(\frac{4(T_e + T_i)m_e\omega^2}{e^2}\right)^{1/2} \text{ is critical field of striction}$$

effects, T_e and T_i are electron and ion temperatures.

The characteristic parameter of striction nonlinearity looks as, $g_m = E_0^2 / E_c^2$, here E_0 is maximum value of the electric field on the surface of microwave resonator wires.

In the linear regime, $g_m \ll 1$, $N \approx N_0$, $q \approx -\frac{1}{2} \frac{N_0}{N_c}$.

In this case the shape of the resonance curve, $\beta(\omega)$, coincides with the vacuum one, but the curve *per se* moves as a whole along the frequency axis to the value of $\Delta\omega_m \approx \frac{1}{2} \frac{N_0}{N_c} \omega_0$.

In non-linear regime, $g_m > 1$, the striction nonlinearity lead to displacement of the resonance curve and also to its deformation.

When frequency $\delta\omega$ is fixed, and the plasma density changes with time, it is more convenient to analyse dependencies $\beta(N)|_{\delta\omega=\text{const}}$ instead of resonance curves $\beta(\delta\omega)|_{N=\text{const}}$. Such dependencies for the values of $\Omega = \frac{Q_0}{2} \delta\omega = 50$ and $\Omega = 100$ are shown in Fig. 2.

When $1 < g_m < \left(\frac{3\Omega}{2 \ln d/a}\right)^{1/2}$, the following equation is valid, which links the bottom bifurcation value of $n = n_b$, ($n = \frac{Q_0}{4} \frac{N_0}{N_c}$) with g_m , and, hence, with plasma temperature:

$$n_b - \Omega \approx \left(\frac{3\Omega}{2 \ln d/a} g_m\right)^{1/3}. \quad (4)$$

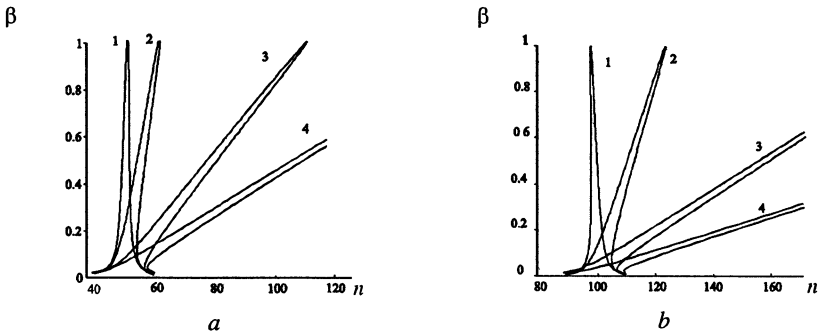


Fig. 2. Family of resonance curves $\beta(n)$, where $n = \frac{Q_0}{4} \frac{N_0}{N_c}$, calculated for the line $d/a = 20$ at fixed values of a) $\Omega = \frac{Q_0}{2} \delta\omega = 50$ and b) $\Omega = 100$ for various values of g_m : 0,1; 1; 10; 50 (curves 1-4).

The experimental setup was made as a vacuum chamber 3 m in diameter and 10 m long. The plasma was produced by means of an induction high-frequency breakdown ($f = 5$ MHz, $\tau_p \approx 1.6$ ms, $H_{magn.f.} \approx 200$ Oe) in the argon atmosphere under the pressure of $5 \cdot 10^{-4}$ Torr. The experiments were performed in the regime of decaying plasma, i.e. after the high-frequency source had been switched off.

The resonator of the microwave probe: $l = 8$ mm, $a = 0.1$ mm, $d = 2$ mm; $f_0 = 8$ GHz and $Q_0 \approx 100$.

The oscillograms of the response of the resonance microwave probe at a low power level of the input signal were used to measure dependence on plasma density on time.

Higher power fed to the microwave probe resulted in aberrations in the shape of its resonance responds. The oscillograms of the output signal for three values of the microwave power are shown in Fig. 3.

As the input power was growing, the position of the step, $N = N_b$, shifted into denser plasma. The dependence of N_b on P was used to determine the electron temperature, T_e ($T_e \gg T_i$) by means of Eq. (4).

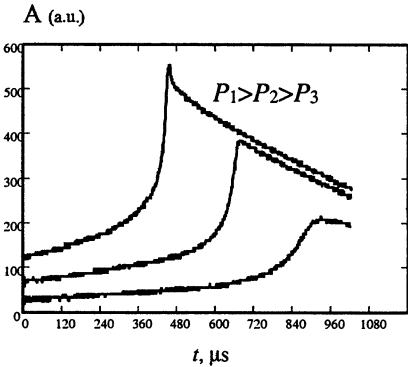


Fig. 3. Oscillograms of the output signal at a fixed frequency for three values of the input power ($P_1 > P_2 > P_3$) in the regime of plasma decay.

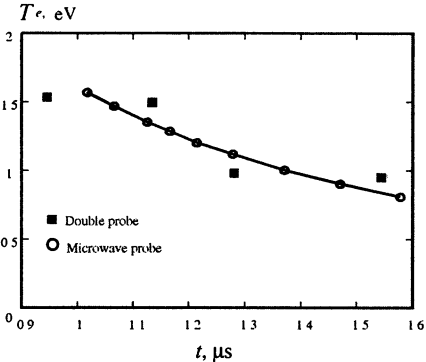


Fig. 4. Results of measuring time dependence of the electron temperature obtained by means of a double probe and a microwave probe.

Figure 4 shows the results of measuring the temperature of electrons with a microwave probe and by means of a double probe. They agree well with each other.

The work reported in this paper was supported by Russian Department of Science on "KROT" set-up (registr. 01-18) and by Ministry of Industry, Science and Technology grant № 40.020.1.1.1171.

EXCITATION OF MAGNETIC FIELDS CORRELATED WITH INTENSE LOWER-HYBRID WAVES IN PLASMAS

S. I. Popel, K. Elsässer¹, Y. Takeda², H. Inuzuka³

Institute for Dynamics of Geospheres RAS, Moscow, Russia

¹Ruhr-University Bochum, Bochum, Germany

²Nihon University, Tokyo, Japan

³Shizuoka University, Hamamatsu, Japan

Theoretical description of the experiments on excitation of magnetic fields related to intense lower-hybrid turbulence is presented. The main experimental results are explained under the assumption that the waves propagate in one plane.

1. The experiments in a high-current linear plasma discharge carried out at the Nihon University [1] have shown the possibility of the excitation of magnetic field perturbations related to intense lower-hybrid turbulence. The value of the magnitude of the perturbations is $|\delta\mathbf{B}| \approx 10$ Gs and $|\delta\mathbf{B}|/|\mathbf{B}_0| \approx 0.01$, where \mathbf{B}_0 is the unperturbed magnetic field. The characteristic features of the observations are: 1) the magnetic field perturbations are excited in the experiments mostly in the paramagnetic sense; 2) there is a correlation between the magnetic field perturbations and the electron density perturbations; 3) the power spectrum of the associated electric field fluctuations shows widely broadened profile and has multiple peaks around the lower-hybrid (LH) frequency.

All the results show that the excitation of the magnetic field perturbations can be associated with the development of the magneto-modulational processes [2]. We check this assumption.

2. The theoretical investigation of the magneto-modulational processes with the participation of LH waves has been performed for tokamak plasmas [3, 4]. The conditions of the laboratory experiments [1] differ strongly from those of tokamak plasmas. In particular, in the case of the laboratory experiments [1] the electron plasma frequency ω_{pe} is far higher than the electron gyrofrequency ω_{Be} . The equation for the magneto-modulational processes given in Refs. [3, 4] assumes that the inequality $\omega_{pe} < \omega_{Be}$ is fulfilled. Here we present the main steps of the derivation of the equation for the magneto-modulational perturbations caused by LH waves in general case.

Although LH waves are "almost" electrostatic, we are interested in the modulational excitation of the magnetic field perturbations. This means that we have to take into account low-frequency (with the frequencies much less than those of LH waves) transversal fields which can appear in process of the modulational interactions. We start from Maxwell's equations, which in Fourier representation take the form (see, e.g., [2])

$$\left[\frac{\omega^2}{c^2} \varepsilon_{ij} + k_i k_j - \delta_{ij} k^2 \right] E_{k,j} = -\frac{4\pi i \omega}{c^2} (j_{k,i}^{(2)} + j_{k,i}^{(3)} + \dots), \quad (1)$$

where $j^{(2)}$, $j^{(3)}$, ... are the quadratic, cubic, etc. (in LH electric field \mathbf{E}) currents, respectively, $\varepsilon_{ij}(\omega, \mathbf{k})$ is the dielectric permittivity tensor, the subscript $k = \{\omega, \mathbf{k}\}$ is a four-vector characterizing the Fourier component, ω is the frequency, \mathbf{k} is the wave vector, δ_{ij} is the Kronecker symbol, and c is the velocity of light.

To denote the low-frequency fields we use the symbol tilde. The direction of the unperturbed magnetic field \mathbf{B}_0 is chosen along the axis Oz . Assuming that the low-frequency fields obey the inequality $\tilde{\omega} \ll \tilde{k}_z v_{Te}$, taking into account only the quadratic current $j^{(2)}$, and using the following relationship for the components of ε_{ij} under the condition $\omega \ll k_z v_{Te}$ [5]

$$\varepsilon_{xx} = \varepsilon_{yy} = 1, \quad \varepsilon_{zz} \approx 1 + \frac{\omega_{pe}^2}{k_z^2 v_{Te}^2}, \quad (2)$$

$$\varepsilon_{xy} = \varepsilon_{yx} = \varepsilon_{xz} = \varepsilon_{zx} = \varepsilon_{yz} = \varepsilon_{zy} = 0,$$

we find the relationship

$$\mathbf{E}_{\tilde{k}} = \frac{4\pi i}{\tilde{\omega}} \left[\frac{\tilde{\omega}^2 \mathbf{j}_{\tilde{k},\perp}^{(2)}}{\tilde{\mathbf{k}}^2 c^2} - \frac{\tilde{\mathbf{k}}(\tilde{\mathbf{k}} \cdot \mathbf{j}_{\tilde{k},\perp}^{(2)})}{\tilde{k}_z^2 \varepsilon_{zz}} + \frac{\tilde{\omega}^2 \tilde{\mathbf{k}}_{\perp}(\tilde{\mathbf{k}} \cdot \mathbf{j}_{\tilde{k},\perp}^{(2)})}{\tilde{k}_z^2 \tilde{\mathbf{k}}^2 c^2} \right]. \quad (3)$$

Here v_{Te} is the electron thermal velocity, the subscript \perp denotes the vector component perpendicular to the unperturbed magnetic field. Thus if $\mathbf{j}_{\tilde{k},\perp}^{(2)} \neq 0$ then the presence of LH waves results in the excitation of magnetic field perturbations

$$\delta \mathbf{B}_{\tilde{k}} = \frac{c}{\tilde{\omega}} (\tilde{\mathbf{k}} \times \mathbf{E}_{\tilde{k}}). \quad (4)$$

To determine $\mathbf{j}_{\tilde{k},\perp}^{(2)} \equiv -e \int \mathbf{v}_{\perp} f_{\tilde{k}} d\mathbf{p} / (2\pi)^3$ the kinetic equation for the electron distribution function $f(t, \mathbf{r}, \mathbf{p})$ is used (as it can be shown by direct calculations, the ion contribution to the magneto-modulational processes with participation of LH waves is negligibly small in comparison with the electron one). Here, $-e$ is the electron charge, \mathbf{p} (\mathbf{v}) is the electron momentum (velocity). The distribution function f is normalized as follows $n_e = \int f(t, \mathbf{r}, \mathbf{p}) d\mathbf{p} / (2\pi)^3$, where n_e is the electron density. We assume that LH wave frequency ω_0 is much less than ω_{Be} .

We solve the kinetic equation using the theory of perturbations in powers of LH wave electric field and following the standard procedure of separation of high-frequency electric fields (which are associated with LH field) and low-frequency those [2]. We find

$$j_{\vec{k},x}^{(2)} \approx \frac{i}{4\pi} \frac{c\omega_{pe}^2}{|\mathbf{B}_0| \omega_0^2} \int (k_{1,z} E_{k_1,y}^+ E_{k_2,z}^- + k_{1,z} E_{k_2,y}^- E_{k_1,z}^+ + k_{2,z} E_{k_1,y}^+ E_{k_2,z}^- + k_{2,z} E_{k_2,y}^- E_{k_1,z}^+) \delta(\vec{k} - k_1 - k_2) dk_1 dk_2, \quad (5)$$

$$j_{\vec{k},y}^{(2)} \approx -\frac{i}{4\pi} \frac{c\omega_{pe}^2}{|\mathbf{B}_0| \omega_0^2} \int (k_{1,z} E_{k_1,x}^+ E_{k_2,z}^- + k_{1,z} E_{k_2,x}^- E_{k_1,z}^+ + k_{2,z} E_{k_1,x}^+ E_{k_2,z}^- + k_{2,z} E_{k_2,x}^- E_{k_1,z}^+) \delta(\vec{k} - k_1 - k_2) dk_1 dk_2, \quad (6)$$

where the superscripts "+" and "-" denote the positive- and negative-frequency parts of the electric field, respectively.

Using (3), (5), and (6), we obtain from (4) the equation determining the amplitude of the quasistationary magnetic field perturbations $\delta\mathbf{B}$ excited by intense LH waves of a given frequency ω_0

$$\Delta\delta\mathbf{B} = \frac{1}{|\mathbf{B}_0|} \frac{\omega_{pe}^2}{\omega_0^2} \nabla \times \nabla \times (\mathbf{E}_\perp (\mathbf{b} \cdot \mathbf{E}^*) + \mathbf{E}_\perp^* (\mathbf{b} \cdot \mathbf{E})), \quad (7)$$

where Δ is the Laplace operator; $\mathbf{b} = \mathbf{B}_0/|\mathbf{B}_0|$ is a unit vector along the unperturbed magnetic field; \mathbf{E} is the complex amplitude of LH field, the field itself is $\text{Re}(\mathbf{E} \exp\{-i\omega_0 t\})$; the asterisk stands for the complex conjugate. Equation (7) is valid for the case $\omega_0 \ll \omega_{Be}$. This means that for LH waves, when $\omega_0 \sim \omega_{LH} \equiv \omega_{pi} / \sqrt{1 + \omega_{pe}^2 / \omega_{Be}^2}$ (ω_{pi} is the ion plasma frequency), Eq. (7) is valid for arbitrary relationship between ω_{pe} and ω_{Be} .

3. Here we compare the results obtained on the basis of (7) with the data [1]. In general, Eq. (7) describes the excitation of the magnetic field perturbations which have the components both parallel and perpendicular to the unperturbed magnetic field \mathbf{B}_0 . Let us find the condition of the excitation of the magnetic field perturbations mostly in the paramagnetic sense, i.e., when the perturbations are "almost" parallel to \mathbf{B}_0 . We denote

$$\mathbf{a}_\perp \equiv \frac{1}{|\mathbf{B}_0|} \frac{\omega_{pe}^2}{\omega_0^2} (\mathbf{E}_\perp (\mathbf{b} \cdot \mathbf{E}^*) + \mathbf{E}_\perp^* (\mathbf{b} \cdot \mathbf{E})). \quad (8)$$

Eq. (7) have solutions obeying the relationship

$$\nabla \delta B_z = \frac{\partial \mathbf{a}_\perp}{\partial z}. \quad (9)$$

This means that δB_z does not depend on z , while

$$\frac{\partial \delta B_z}{\partial x} = \frac{\partial a_x}{\partial z}, \quad \frac{\partial \delta B_z}{\partial y} = \frac{\partial a_y}{\partial z}. \quad (10)$$

Using the fact that $\partial \delta B_z / \partial z = 0$ and the relationships (10) we find from Eq. (7)

$$\Delta\delta\mathbf{B}_\perp = \mathbf{i} \frac{\partial}{\partial y} \left[\frac{\partial a_y}{\partial x} - \frac{\partial a_x}{\partial y} \right] - \mathbf{j} \frac{\partial}{\partial x} \left[\frac{\partial a_y}{\partial x} - \frac{\partial a_x}{\partial y} \right], \quad (11)$$

where \mathbf{i} and \mathbf{j} are unit vectors in the directions of the axes Ox and Oy , respectively. Using Fourier representation we find

$$\begin{aligned} \frac{\partial a_y}{\partial x} - \frac{\partial a_x}{\partial y} \propto \int d\mathbf{k}_1 d\mathbf{k}_2 (E_{k_1} E_{k_2}^* e^{i(\mathbf{k}_1 - \mathbf{k}_2) \cdot \mathbf{r}} + \\ + E_{k_2} E_{k_1}^* e^{i(\mathbf{k}_2 - \mathbf{k}_1) \cdot \mathbf{r}}) [k_{2y} k_{1x} - k_{1y} k_{2x}], \end{aligned} \quad (12)$$

where we take into account the longitudinal character of LH waves ($E_{k_i} = (k_z/|\mathbf{k}|)E_k$, $E_{k_i}^* = (k_z/|\mathbf{k}|)E_k^*$). If for two arbitrary LH waves with the wave vectors \mathbf{k}_1 and \mathbf{k}_2 the relationship

$$k_{1y}/k_{1x} = k_{2y}/k_{2x} = \text{const} \quad (13)$$

is fulfilled, then the excitation of the magnetic field perturbations in the direction perpendicular to the unperturbed magnetic field is negligible, and the magnetic field perturbations can be excited in the paramagnetic sense. This relationship means that LH wave spectrum consists of the waves propagating in one plane. In this case we obtain

$$\delta B_z \propto \frac{\omega_{pe}^2}{\omega_0^2} \frac{\mathbf{E}^2}{|\mathbf{B}_0|} \cos^2 \theta_0, \quad (14)$$

where $\cos \theta_0 = k_z/|\mathbf{k}|$. The estimate (14) is valid for the spectrum which is rather broad and/or consists of several peaks. The width of LH wave spectrum in \mathbf{k} -space determines the characteristic wave vector of the low-frequency magnetic field perturbations. For the data of the experiments [1] (the characteristic frequency $f \approx 55$ MHz, $\omega_0 = 2\pi f \approx 3.46 \cdot 10^8$ s $^{-1}$, $|\mathbf{E}| \sim 10$ kV/cm, $|\mathbf{B}_0| \approx 1.2$ kGs, the electron density $n_e \sim 10^{12}$ cm $^{-3}$) under the assumption that $\cos \theta_0$ takes the typical (for LH waves) magnitude $\cos \theta_0 \sim \sqrt{m_e/m_i}$, we get from Eq. (14): $\delta B_z \sim 18$ Gs for hydrogen plasmas; $\delta B_z \sim 9$ Gs for deuterium plasmas. We see a good agreement of this estimate with the experimental data $\delta B_z \sim 10$ Gs.

4. The electron density perturbations δn are related to the usual development of the modulational processes with the participation of LH waves. They appear in the places of LH field localization (see, e.g., [2]). Let us determine δn using the theory of perturbations. The dielectric permittivity for LH waves propagating under the angle θ_0 with respect to the external magnetic field is

$$\varepsilon_k = (\varepsilon_0)_k - \frac{\delta n}{n_0} \equiv 1 - \frac{\omega_{pe}^2}{\omega^2} \cos^2 \theta_0 - \frac{\omega_{pi}^2}{\omega^2} + \frac{\omega_{pe}^2}{\omega_{Be}^2} - \frac{\delta n}{n_0}, \quad (15)$$

where the electron (ω_{pe}) and ion (ω_{pi}) frequencies correspond to the unperturbed electron and ion densities ($n_{e0} = n_{i0} = n_0$), respectively, $(\epsilon_0)_k$ is the unperturbed dielectric function. Poisson's equation can be written in the form

$$(\epsilon_0)_k E_k^+ = -\frac{1}{n_0 \|\mathbf{k}\|} (\mathbf{k} \cdot [\delta n \mathbf{E}]_k^+) = \int \frac{\delta n_{k-k_1} (\mathbf{k} \cdot \mathbf{k}_1)}{n_0 \|\mathbf{k}\| \|\mathbf{k}_1\|} E_{k_1}^+ dk_1. \quad (16)$$

From the other hand, we have (see, e.g., [2])

$$(\epsilon_0)_k E_k^+ = 2 \int \Sigma_{k_1, k_2, k_3}^{eff} E_{k_1}^+ E_{k_2}^+ E_{k_3}^- \delta(k - k_1 - k_2 - k_3) dk_1 dk_2 dk_3, \quad (17)$$

where $\Sigma_{k_1, k_2, k_3}^{eff}$ is the effective nonlinear third-order response in the fields of LH waves. The derivation of the response $\Sigma_{k_1, k_2, k_3}^{eff}$ for the case $\omega_{pe} < \omega_{Be}$ is presented, e. g., in [2]. Deriving this response for the case $\omega_{pe} > \omega_{Be}$ we use the same procedure as in [2]. We find

$$\begin{aligned} \Sigma_{k_1, k_2, k_3}^{eff} = & -\frac{e^2}{2m_e^2} \frac{|\mathbf{k}_2 + \mathbf{k}_3|^2}{\|\mathbf{k}\| \|\mathbf{k}_1\| \|\mathbf{k}_2\| \|\mathbf{k}_3\|} \frac{\epsilon_{k_2+k_3}^{(i)}}{\epsilon_{k_2+k_3}} (\epsilon_{k_2+k_3}^{(e)} - 1) \times \\ & \times \left[\frac{k_z k_{1z}}{\omega^2} + \frac{i(\mathbf{k}_\perp \times \mathbf{k}_{1\perp})_z}{\omega \omega_{Be}} - \frac{(\mathbf{k} \cdot \mathbf{k}_1)}{\omega_{Be}^2} \right] \left[\frac{k_{2z} k_{3z}}{\omega^2} - \frac{i(\mathbf{k}_{2\perp} \times \mathbf{k}_{3\perp})_z}{\omega \omega_{Be}} - \frac{(\mathbf{k}_2 \cdot \mathbf{k}_3)}{\omega_{Be}^2} \right], \end{aligned} \quad (18)$$

where $\epsilon^{(e)}$ and $\epsilon^{(i)}$ are the electron and ion parts of the unperturbed dielectric permittivity ϵ (the subscript 0 is omitted).

Using the explicit values of $\epsilon^{(e)}$ and $\epsilon^{(i)}$ in the low-frequency limit $\tilde{\omega} = |\omega - \omega_1| = |\omega_2 + \omega_3| \ll \tilde{k}_z v_{Te}$ ($\tilde{\mathbf{k}} = \mathbf{k} - \mathbf{k}_1 = \mathbf{k}_2 + \mathbf{k}_3$), the fact that under the experimental conditions [1] $\omega_{pe}^2 \gg \omega_{Be}^2$, and the condition (13), we find that the main contribution to the effective response is made by the terms which do not contain the gyrotropic nonlinearity (proportional to vector products). Then Eq. (17) can be presented in the form (16), where

$$\frac{\delta n}{n_0} = -\frac{|\mathbf{E}|^2}{4\pi n_0 (T_e + T_i)}. \quad (19)$$

Comparing (19) and (14), we find

$$\frac{\delta n}{n_0} \propto \frac{2}{\beta} \frac{\omega_0^2}{\omega_{pe}^2} \frac{\delta B_z}{|\mathbf{B}_0|} \sec^2 \theta_0, \quad (20)$$

where $\beta = 8\pi n_0 (T_e + T_i) / |\mathbf{B}_0|^2$. For the typical data of the experiments [1] ($\omega_{LH}/2\pi = 55$ MHz, $\omega_{pe}/2\pi = 15$ GHz, $\beta \sim 0.001$, $\delta B_z / |\mathbf{B}_0| \sim 0.01$, $\cos \theta_0 \sim \sqrt{m_e / m_i}$) this estimate gives the value of $\delta n / n_0 \sim 0.5$. So this is in accordance with the experimental data $\delta n \sim 0.5 n_0$ measured by the microwave interferometer when strong electric field bursts give rise to enhanced electron density modulation [6].

5. Thus the theory developed here allows us to explain the main experimental results [1] under the assumption that LH wave spectrum consists of the waves propagating in one plane. The most probable reason for the excitation of the magnetic field perturbations in these experiments is the development of the magneto-modulational processes.

References

1. *Takeda Y., Inuzuka H., and Yamagiwa K.*, Phys. Rev. Lett., 1995, **74**, 1998; *Takeda Y. and Inuzuka H.*, Phys. Lett. A, 2000, **265**, 282; *Takeda Y. and Inuzuka H.* in Proc. 2000 Int. Congress Plasma Phys. (Quebec City, Canada, 2000), Vol. 1, p. 320.
2. *Vladimirov S. V., Tsytovich V. N., Popel S. I., and Khakimov F. Kh.*, Modulational Interactions in Plasmas, Kluwer Academic Publishers, Dordrecht (1995).
3. *Tsytovich V. N. and Bel'kov S. A.*, Comments Plasma Phys. Controlled Fusion, 1980, **5**, 219.
4. *Popel S. I. and Elsässer K.*, Comments Plasma Phys. Controlled Fusion, 1994, **16**, 79.
5. *Lifshitz E. M. and Pitaevskii L. P.*, Physics Kinetics, Nauka, Moscow (1979) (in Russian).
6. *Inuzuka H., Takeda Y., and Yamagiwa K.*, Phys. Lett. A, 1997, **234**, 219.

EXCITATION OF A WAKE FIELD BY A RECTANGULAR MICROWAVE PULSE IN A RECTANGULAR WAVEGUIDE

H. K. Malik¹, H. Ito, N. Yugami, Y. Nishida

Energy and Environmental Science, Graduate School of Engineering
Utsunomiya University, Utsunomiya, Tochigi 321-8585, Japan

¹Department of Physics, Indian Institute of Technology Delhi, New Delhi – 110 016, India

Analytical expressions are obtained for the longitudinal field (wake field), density perturbation and the potential behind high intensity microwave pulse propagating in a plasma filled rectangular waveguide with the pulse duration half of the electron plasma period. A feasibility study on wake field is carried out with rectangular pulse under the effects of microwave pulse parameters and waveguide dimensions. A 1 ns short rectangular pulse with intensity 250 kW/cm² at the frequency of 5.03 GHz can excite the wake field of 1.0 MV/m in a waveguide of width 6 cm and height 4 cm. The field of wake gets weakened at higher microwave frequency and larger dimensions of the waveguide for other fixed parameters; but larger field is achieved when the pulse length of the microwave pulses is made shorter and/or intensity of the pulses is increased.

1. Introduction

The charged particle acceleration has been the subject of great interest for the experimental as well as the theoretical research and appreciable attempts have been made to achieve compact ultra high gradient accelerators using high intensity short pulse lasers in the plasmas ([1], [2] and references therein). Most widely investigated plasma based acceleration schemes mainly include the plasma beat wave accelerator, laser wake field accelerator, $v_p \times B$ accelerator and the plasma wake field accelerator. Investigations on the plasma wake field began with the pioneering work of Chen *et al.* [3] and the first experimental evidence was reported by Rosenzweig *et al.* [4], where they employed super relativistic electron bunches of short pulse duration in a high density plasma. Nishida *et al.* [5] have succeeded in exciting a wake field in the ion wave regime with long pulse duration by employing a variety of driving bunch shapes. Later, Aossey *et al.* [6] observed such type of wake field in three-component plasma also.

In laser wake field acceleration, a large amplitude wake field is excited by a high intensity short pulse when its length matches with half of the plasma wavelength and the injected electrons can be accelerated to high energies [7, 8]. However, the diffraction of the laser propagation limits the laser plasma interaction distance to the extent of the vacuum Rayleigh length and this effect eliminates the advantage of ultrahigh gradient acceleration from laser driven accelerator. In order to achieve higher acceleration, the laser plasma interaction length as well as the amplitude of the wake field should be maintained at higher magnitudes. The

wake fields can be enhanced by the nonlinearities in response of the plasma to the pondermotive force of a long smooth laser pulse of relativistic intensity whose length is much larger than half of the plasma wavelength [9]. The amplitude of the laser wake field has also been found to increase by the ionization processes of the gases at comparatively higher laser peak intensities [10]. A capillary tube can be used as a waveguide in order to enhance the interaction length [11]. Tapered plasma channels have recently been proposed to achieve greater electron acceleration in laser wake field mechanism by enhancing the interaction length of the laser pulse with the plasma [12].

It can be noted that generally the lasers due to their high intensities and ultra short pulse durations have been employed for the wake field excitation and appreciable energy gradients for electrons have been achieved. However, it will be of much importance if high power microwaves could be used in place of lasers for the wake field excitation. The group of present authors has done extensive studies on microwave plasma interaction in view of particle acceleration via the resonant wave particle interaction, $\mathbf{v}_p \times \mathbf{B}$ acceleration and the wake field excitation schemes [13–15]. In the present paper, our aim is to carry out a feasibility study on wake field excitation by the microwave (rectangular pulse) in a plasma filled rectangular waveguide.

2. Wake field in plasma filled rectangular waveguide

A rectangular waveguide is considered with its inner width "a" along x-axis and inner height "b" along y-axis filled with isotropic unmagnetized plasma, and a high intensity short microwave pulse is assumed to propagate along z-axis. In addition, the ions in the plasma are taken to be immobile on the time scale of the interest. The plasma response to the electromagnetic field is given by the cold, collisionless, nonrelativistic electron fluid equations. The propagation of the microwave in the waveguide is analyzed by assuming that the electromagnetic field is a superposition of modes with a dependence along the propagation axis as $e^{-i\beta z}$ [16], where the propagation constant $\beta = (\omega^2 \epsilon_p / c^2 - k_c^2)^{1/2}$ together with k_c as the wave number corresponding to the cutoff condition and ϵ_p as the plasma dielectric constant given by $\epsilon_p = 1 - \omega_{pe}^2 / \omega^2$ with ω_{pe} as the plasma frequency. The Maxwell's equations are solved along with the electron fluid equations under the conditions that the tangential components of the electric field are continuous at the walls of the waveguide. This procedure leads to the following dispersion relation

$$\omega^2 = c^2 \beta^2 + \omega_{pe}^2 + c^2 k_c^2. \quad (1)$$

Here $k_c^2 = (m\pi/a)^2 + (n\pi/b)^2$ and m and n are the integers occurring in the field solutions that describe the variation of the fields along the two transverse coordinates. The cutoff frequency f_c for the propagation of the microwave is obtained as $f_c = \{f_{pe}^2 + (c^2/4)[m^2/a^2 + n^2/b^2]\}^{1/2}$ and the group velocity v_g as

$$v_g = c \{1 - f_{pe}^2/f^2 - (c^2/4f^2)[m^2/a^2 + n^2/b^2]\}^{1/2}. \quad (2)$$

This can be noted here that the group velocity of the microwave in the plasma filled waveguide depends on the waveguide dimensions in addition to the plasma density and is less than the speed of light.

Now considering the one-dimensional case [17], we derive analytical expressions for the wake field, density perturbation and the potential behind the microwave pulse propagating along z -axis in the waveguide. The Maxwell's equations and the electron fluid equations are resolved into parallel (z -axis) and perpendicular components. The system is considered to be nonevolving, i.e. all the quantities depend only on $\xi = z - v_g t$ and the electron density is taken to be $n_0 + n_e'$, where n_e' is the density perturbation due to the microwave pulse and n_0 is the unperturbed density. Moreover, under the conditions that the perturbation n_e' in the density and the parallel component of the electron fluid velocity v_{\parallel} vanish when $\xi \rightarrow \infty$, and if the perturbations in the density are not so great, i.e. $n_e' < n_0$, the Poisson's equation together with the use of Maxwell's equations yields the following

$$\partial^2 \phi / \partial \xi^2 + (\omega_{pe}^2 / v_g^2) \phi - (c^2 e / 2 m_e v_g^4) E^2 = 0. \quad (3)$$

This is interesting to note here that the above equation allows us to obtain the expression for the electrostatic potential ϕ for the different envelopes of E , i.e. for different shapes of the pulse; however, our aim in the present paper is to make calculations for rectangular pulse only.

Rectangular (RP) pulse. For a rectangular pulse of pulse length L we take its field E as $|E(\xi)|^2 = E_0^2 [H(\xi + L/2) - H(\xi - L/2)]$ for $-L/2 < \xi < L/2$, where H is the Heaviside unit step function. Then (3) is solved together with this shape of E under the condition that at the center of the pulse (i.e. at $\xi = 0$), where E is maximum, the potential ϕ is zero. Finally we obtain the following expression for the electrostatic potential ϕ (ϕ_{RP} for rectangular pulse) behind the pulse for $\xi < -L/2$:

$$\phi_{RP}(\xi) = (c^2 e E_0^2 / m_e v_g^2 \omega_{pe}^2) \sin(k_p L/2) \sin(k_p \xi). \quad (4)$$

The above equation readily gives the expression for the wake field E_{zRP} behind the pulse for $\xi < -L/2$

$$E_{zRP}(\xi) = -(c^2 e E_0^2 / m_e v_g^3 \omega_{pe}) \sin(k_p L/2) \cos(k_p \xi). \quad (5)$$

Here $k_p = \omega_{pe} / v_g = 2\pi / \lambda_p$ together with λ_p as the plasma wavelength, which is described by the group velocity of the microwave pulse in the plasma filled waveguide. Now with the help of (4) and (5) one can derive the expression for the density perturbations behind the pulse as

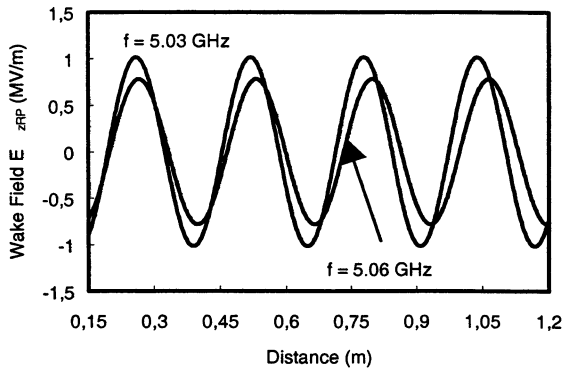
$$n_{eRP}'(\xi) / n_0 = (c^2 e^2 E_0^2 / 2 m_e^2 v_g^4 \omega_{pe}^2) [1 - 2 \sin(k_p L/2) \sin(k_p \xi)]. \quad (6)$$

3. Results and discussion

Now by giving typical values to the microwave intensity, waveguide dimensions, microwave frequency and the plasma density we examine the wake field excited by rectangular (*RP*) pulse for $\xi < -L/2$ in the waveguide. Since the present theory considers a weakly nonlinear case, the density perturbations n_e'/n_0 will be kept less than unity for presenting the results graphically.

Effect of microwave frequency. Figure 1 shows the effect of microwave frequency f on the wake field E_{zRP} behind the rectangular pulse. Here we take typically the duration (length) of the pulse as 1 ns and the intensity as 250 kW/cm^2 in a waveguide of width $a = 6 \text{ cm}$ and height $b = 4 \text{ cm}$. The plasma density n_0 for 1 ns pulse duration comes out to be $3.10 \cdot 10^{15} \text{ m}^{-3}$ as per the condition that the pulse duration be half of the electron plasma period. The cutoff frequency for the microwave propagation in the waveguide for these values of a , b , n_0 and $m = 1$ and $n = 1$ is $f_c = 4.53 \text{ GHz}$. We have therefore selected the microwave frequency $f = 5.03 \text{ GHz}$ in view of $n_e'/n_0 \approx 0.9$ for maximum attainable wake fields. This is clear from the figure that the wake field behind the microwave pulse goes down for the higher microwave frequency.

Fig. 1. Effect of microwave frequency f on wake field E_{zRP} excited by rectangular pulse when a 1 ns pulse with intensity of 250 kW/cm^2 is used in a waveguide of width 6 cm and height 4 cm.



Effect of waveguide dimensions. The effect of waveguide width a on the wake field E_{zRP} is shown in Fig. 2. Here the microwave frequency f is 5.03 GHz and other parameters are taken the same as in Fig. 1. It is evident from this figure that the wake field E_{zRP} is significantly decreased for the larger width of the waveguide. This dominant effect of waveguide width can be explained on the basis of expressions (5), which shows that the field E_{zRP} varies as $1/v_g^3$. Since the group velocity v_g has a strong dependence on the waveguide width, it is increased significantly for the increasing width and hence the decrease in the wake field is faster. The similar effects are obtained for the increasing height of the waveguide.

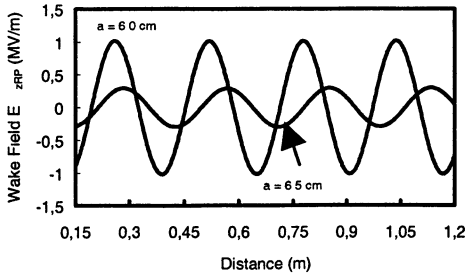


Fig. 2. Effect of waveguide width a on wake field E_{zRP} excited by rectangular pulse at frequency $f = 5.03$ GHz. Other parameters are the same as in Fig. 1.

Effect of pulse duration: plasma density. In the above studies we have kept fixed the microwave pulse durations as 1 ns. However, now we examine the effect of shorter pulse (in comparison to 1ns) on the strength of the wake fields E_{zRP} . Here we evaluate for 0.5 ns pulse duration, which corresponds to the plasma density $n_0 = 1.24 \cdot 10^{16} \text{ m}^{-3}$. This increased plasma density has a direct bearing on the cutoff frequency f_c and for the same waveguide (4 cm \times 6 cm) the frequency f_c is increased from 4.53 GHz to 4.62 GHz, when the plasma density (pulse duration) is increased (reduced) from $3.10 \cdot 10^{15} \text{ m}^{-3}$ (1 ns) to $1.24 \cdot 10^{16} \text{ m}^{-3}$ (0.5 ns). The effect of pulse duration on the maximum attainable wake field E_{zRP} is displayed in Fig. 3, where the microwave frequency for 0.5 ns is set as 4.911 GHz and other parameters are taken the same as in Fig. 2. One can note from Fig. 3 that the wake field is increased for the shorter lengths of the pulses or increased plasma density.

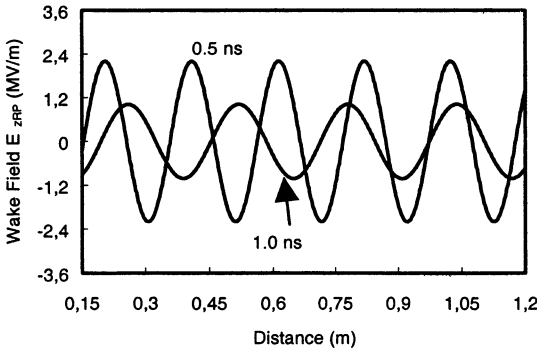


Fig. 3. Effect of pulse duration (length L) on wake field E_{zRP} excited by rectangular pulse at frequency $f = 4.911$ GHz for 0.5 ns. Other parameters are the same as in Fig. 2.

Finally we concentrate on (5) and note that the field E_{zRP} contains a term $\sin(k_p L/2)$. Since this term vanishes when the pulse length L is exactly equal to the plasma wavelength $\lambda_p (= 2\pi/k_p)$, the field E_{zRP} tends to zero near $L = \lambda_p$. Hence, it is concluded that the wake field cannot be attained in a rectangular waveguide when a rectangular microwave pulse of length exactly equal to the plasma wavelength is employed.

4. Concluding remarks

In the present paper we have attempted for the wake field excitation using high intensity microwave in a plasma filled rectangular waveguide with rectangular pulse. The present analysis reveals that a rectangular pulse can provide best results if the microwave with shorter pulse duration is available; wake field increases from 1 MV/m to 2.2 MV/m if the pulse duration is reduced from 1 ns to 0.5 ns.

Acknowledgement. The author HKM acknowledges the *Japan Society for the Promotion of Science (ID № P00100)* for providing the financial assistance.

References

1. Esarey E., Sprangle P., Krall J., and Ting A. IEEE Trans. Plasma Sci., 1996, **24**, 252.
2. Unstaeter D. Phys. Plasmas, 2001, **8**, 1774.
3. Chen P., Dawson J. M., Huff R. W., and Katsouleas T. Phys. Rev. Lett., 1985, **54**, 693.
4. Rosenzweig J. B., Cline D. B., Cole B., Figueroa H., Gai W., Konecny R., Norem J., Schoes-sow P., and Simpson J. Phys. Rev. Lett., 1988, **61**, 98.
5. Nishida Y., Okazaki T., Yugami N., and Nagasawa T. Phys. Rev. Lett., 1991, **66**, 2328.
6. Aossey D. W., Williams J. E., Kim H. S., Cooney J., Hsu Y. C., and Lonngren K. E. Phys. Rev. E, 1993, **47**, 2759.
7. Leemans W. P., Volfbeyn P., Guo K. Z., Chattopadhyay S., Schroeder C. B., Shadwick B. A., Lee P. B., Wurtele J. S., and Esarey E. Phys. Plasmas, 1998, **5**, 1615.
8. Dorchies F., Amiranoff F., Malka V., Marques J. R., Modena A., Bernard D., Jacquet F., Mine Ph., Cros B., Matthieussent G., Mora P., Solodov A., Morillo J., and Najmudin Z. Phys. Plasmas, 1999, **6**, 2903.
9. Kingham R. J. and Bell A. R. Phys. Rev. Lett., 1997, **79**, 4810.
10. Andreev N. E., Chegotov M. V., and Veisman M. E. IEEE Trans. Plasma Sci., 2000, **28**, 1098.
11. Cros B., Courtois C., Malka G., Matthieussent G., Marques J. R., Dorchies F., Amiranoff F., Rebibo S., Hamoniaux G., Blanchot N., and Miquel J. L. IEEE Trans. Plasma Sci., 2000, **28**, 1071.
12. Sprangle P., Hafizi B., Penano J. R., Hubbard R. F., Ting A., Moore C. I., Gordon D. F., Zigler A., Kaganovich D., and Antonsen Jr. T. M. Phys. Rev. E, 2001, **63**, 056405-1.
13. Nishida Y. and Shinozaki T. Phys. Rev. Lett., 1990, **65**, 2386.
14. Nishida Y. and Sato N. Phys. Rev. Lett., 1987, **59**, 653; Nishida Y., Yoshizumi M., and Sugi-hara R. Phys. Fluids, 1985, **28**, 1574, and references therein.
15. Nishida Y., Kusaka S., and Yugami N. Phys. Scr., 1994, **T52**, 65.
16. Marcatili E. A. J. and Schmeltzer R. A. Bell Syst. Tech. J., 1964, **43**, 1783.
17. Gorbunov L. M. and Kirsanov V. I. Sov. Phys. JETP, 1987, **66**, 290.

INHOMOGENEOUS PLASMA PARAMETRIC DECAY INSTABILITY DRIVEN BY A FREQUENCY MODULATED PUMP

*V. I. Arkhipenko, V. N. Budnikov¹, E. Z. Gusakov¹, V. A. Pisarev,
L. V. Simonchik, B. O. Yakovlev¹*

Institute of Molecular and Atomic Physics Minsk, Belarus
¹Ioffe Institute St.-Petersburg, Russia

In the present paper it is shown both experimentally and in theory that inhomogeneous plasma parametric decay instability (PDI) is very stable to pump frequency modulation such non-sensitivity holds only for the pump frequency modulation faster than the decay wave transient time. In the case of slower modulation, both harmonic and stochastic, the PDI enhancement may take place instead.

The pump phase modulation was discussed as a possible way of parametric decay instability (PDI) suppression starting from 60th. According to results of homogeneous plasma theory [1], it can serve as an effective method for parametric instability control. However the analysis carried out in inhomogeneous plasma model for stochastic pump phase modulation have revealed high stability of convective amplification coefficient, which appeared to be non-sensitive to modulation [2]. Such stability was recently confirmed in experiment [3] and shown in numerical computations also for absolute PDI [4], where the threshold conditions for instability suppression in inhomogeneous plasma were determined.

It should be mentioned that theoretical conclusion [2] was obtained under the supposition of very fast (delta-correlated) pump phase modulation. It was confirmed in experiment for modulation quicker than the transient time of the slow daughter wave in the decay region as well. In the present paper the case of slower pump frequency modulation is considered both experimentally and in theory. The experiment was carried out in the linear plasma device "Granit" [3]. The Trivelpiece-Gould (TG) pump wave ($f_0 = 2480$ MHz) was excited in the inhomogeneous plasma with a waveguide. The backscattering parametric instability $l_0 \rightarrow l_0' + s$ was observed under these conditions in previous experiments [3], utilizing a monochromatic pump. The reflected fundamental TG mode l_0' and ion acoustic wave, propagating along the magnetic field in the direction of decreasing plasma density, are produced by this decay. The satellite, red-shifted by 3 MHz, appears in the spectrum of the signal reflected by the plasma. The effect of the harmonic pump frequency modulation on this PDI was investigated in wide modulation frequency region for $0.1 \text{ MHz} < f_m < 10 \text{ MHz}$ [3]. The suppression was observed only for $f_m > 0.8 \text{ MHz}$ and for large frequency deviations $\Delta f > 50 \text{ MHz}$. The effect was strong close to the instability threshold, which was increased by a factor of 3 for $\Delta f = 150 \text{ MHz}$. Far from instability threshold the influence of modulation on the instability was weaker. At smaller modulation frequencies $f_m < 0.5 \text{ MHz}$ there was no suppression of PDI, on contrary, a pro-

nounced growth of the ion acoustic wave was observed. A more detailed investigation of this wave in a specially performed scattering experiment revealed its strong amplitude modulation at frequency f_m . The results of time resolved stroboscopic measurements of the amplitude of the scattering signal are shown in Fig. 1, *a*, *b* for modulation frequencies $f_m = 0.2$ MHz and $f_m = 0.35$ MHz.

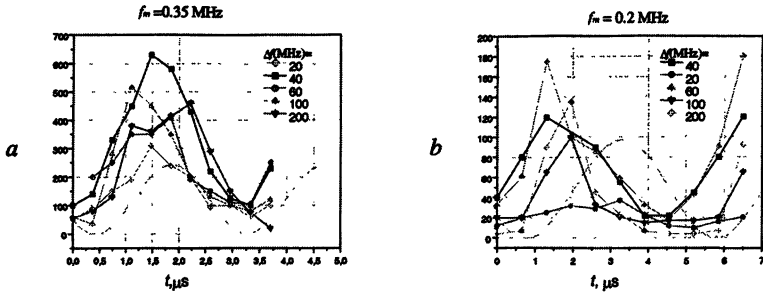


Fig. 1. Experimentally observed PDI wave amplitude behavior for different frequency deviation Δf

As it is seen, the amplitude modulation is especially pronounced for specific frequency deviations ($\Delta f = 60$ MHz for $f_m = 0.2$ MHz and $\Delta f = 40$ MHz for $f_m = 0.35$ MHz), for which the non-harmonic distortions are maximal. The observed phenomena looks like a resonance effect for which the condition $\Delta f f_m = \text{const}$ holds.

The theoretical investigation of this resonance phenomenon is carried out in the framework of coupled equations for slow varying wave amplitudes a_1 and a_2 of oppositely propagating plasma waves:

$$\begin{aligned} \frac{\partial a_1}{\partial t} + v_1 \frac{\partial a_1}{\partial x} + v_1 a_1 &= \gamma_0 a_2 e^{i\Phi(x,t)}, \\ \frac{\partial a_2}{\partial t} + v_2 \frac{\partial a_2}{\partial x} + v_2 a_2 &= \gamma_0^* a_1 e^{-i\Phi(x,t)}, \end{aligned} \quad (1)$$

where $\Phi(x,t) = \int^x \Delta\kappa(x') dx' + \delta\Phi(x - v_0 t)$ is a phase mismatch caused by plasma inhomogeneity and pump wave frequency modulation, v_j – group velocities, v_0 – pump wave group velocity, v_j – damping coefficients, γ_0 – is maximal PDI growth rate, proportional to the pump wave amplitude. Here and below dimensionless parameters are used $t = t v_1 / \ell$, $v_i = v_i / |v_0|$, $x = x / \ell$, $v_i = v_i \ell / |v_0|$, $i = 0, 1, 2$. It is supposed that $v_1 > 0$, $v_2 < 0$, $v_0 < 0$ and $|v_0| = v_1$.

The results of numerical modeling in the decay point $x_d = 0$ vicinity, where $\Delta\kappa(x) = x / \ell^2$ for harmonic frequency modulation resulting in

$$\Phi(x, t) = x^2 / 2\ell^2 + (A/\Omega) \cos[\Omega(t - x/v_0)] \quad (2)$$

are shown in Fig. 2 for $v_2 = -0.2$, $\gamma_0 = 0.65$ and $A = 1$.

At high modulation frequency $\Omega > 0.5$ decay wave amplification is not affected by modulation. On contrary, at lower modulation frequency $\Omega < 0.4$ the amplification is much higher, moreover it demonstrates well pronounced modulation at frequency Ω , which has much in common to that observed in Fig. 1.

The physical reason for this effect is convective losses suppression occurring when the decay point velocity, moving under pump frequency modulation, coincides with decay wave group velocity [5]. The amplification coefficient in this case, according to [5] takes form

$$S = \exp\left\{\left[\pi\gamma_0^2\ell^2\right] / \left[|v_1 - v_d||v_2 - v_d|\right]\right\}, \quad (3)$$

where v_d is the decay point velocity. In the case the frequency of wave a_2 is prescribed by thermal fluctuations, modeled by the source term in (1), the decay point velocity is given by simple condition $v_d = -\frac{2\ell^2}{v_0} \frac{d\omega_0}{dt}$. For harmonic frequency modulation (2) the resonant increasing of amplification is expected at $(2\ell^2/v_0)A\Omega \cos[\Omega(t - x/v_0)] = v_2$. At $v_2v_0 < 2\ell^2A\Omega$ such increases should occur twice each period of modulation, but the strongest amplification is foreseen for:

$$A\Omega = v_2v_0 / \left[2\ell^2(1 - v_2/v_0)\right], \quad (4)$$

when the two resonance are overlapped. The last conclusion is in a nice agreement with above experimental observation $\Delta f f_m = \text{const}$ and numerical calculations (see Fig. 1, *a, b* and Fig. 3).

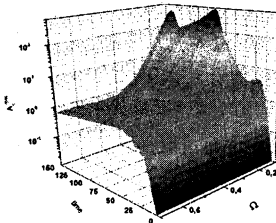


Fig. 2. Decay wave amplitude dependence on time and modulation frequency Ω for $V_1 = 1.0$, $V_2 = -0.2$, $\gamma_0 = 0.65$.

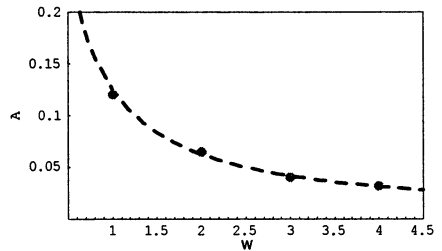


Fig. 3. $V_d = V_2$ modulation rate A vs modulation frequency; --- — analytical curve (4), \bullet — numerical calculations.

According to (3), amplification in the resonance case is formally infinite. However in reality it will be saturated either due to the finite interaction time, or by nonlinearities of the pump frequency modulation. In the later case the substi-

tution $a_j = b_j \exp \left\{ i \frac{v_k v_0}{(v_j - v_0)(v_k - v_j)} \frac{(x - v_j t)^2}{2\ell^2} \right\}$, $k \neq j$ and transition to the

moving coordinate system $y = x - v_0 t$ converts system (1) into the form suitable for analytical treatment:

$$\frac{\partial b_1}{\partial t} + (v_1 - v_0) \frac{\partial b_1}{\partial y} = \gamma_0 b_2 e^{i\phi(y)},$$

$$\frac{\partial b_2}{\partial t} + (v_2 - v_0) \frac{\partial b_2}{\partial y} = \gamma_0^* b_1 e^{-i\phi(y)},$$

where $\phi(y) = \frac{y^2}{2\ell_*^2} + \delta\phi(y)$, $\ell_*^2 = \ell^2 \frac{(v_1 - v_0)(v_2 - v_0)}{v_1 v_2}$ and damping, source terms are omitted. The amplification coefficient is estimated from this system in WKB approximation as:

$$S = \exp \left(\int_{y_1}^{y_2} \sqrt{\frac{1}{\ell_d^2} - \frac{1}{4} (\phi'(y))^2} dy \right), \quad (5)$$

where $\ell_d^2 = \gamma_0^{-2} (v_1 - v_0)(v_2 - v_0)$ and y_i are zeros of the square root. In case $\delta\phi = y^4 / 12L^4$, modeling situation of the most effective interaction for harmonic modulation, we compare (see Fig. 4) expression (5) predictions and computational results based on (1).

It should be stressed that resonant enhancement of convective amplification coefficient is possible not only for linear or harmonic pump frequency modulation, but also for stochastic modulation as it was shown in numerical modeling. The pump phase modulation was taken in the form:

$$\begin{aligned} \delta\Phi_\Omega(x, t) = & -(32\pi)^{1/4} (\tau_c/T)^{1/2} \Delta \times \\ & \times \sum_{j=1}^{\infty} \exp \left\{ -(\omega_j \tau_c)^2 / 4 \right\} \cos(\omega_j (t - x/v_0) + \vartheta_j) / \omega_j, \end{aligned}$$

where $\omega_j = 2\pi j/T$, T is time longer than any time scale of the problem, ϑ_j is a random phase from $[0, 2\pi]$ interval. This representation provides statistically

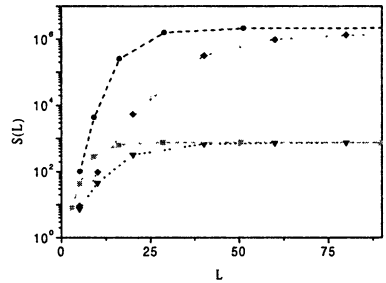


Fig. 4. Amplification coefficient dependence on the nonlinear phase mismatch parameter L for code calculations: \cdots $V_d = 0.0$, \blacklozenge $V_d = -0.12$, analytical results: \blacksquare $V_d = 0.0$, $-\blacklozenge$ $V_d = -0.12$.

uniform, gaussian frequency modulation possessing correlation function $\langle \delta\Omega(t)\delta\Omega(t') \rangle = \Delta^2 \exp\left(-\frac{(t-t')^2}{2\tau_c^2}\right)$, $\langle \delta\Omega \rangle = 0$, $\langle \delta\Omega^2 \rangle^{1/2} \equiv \Delta$. As it is seen in Fig. 5, where variation of decay wave amplitude is shown for different random phase sets, in the case of fast phase modulation ($\tau_c = 1$) amplitude growth is much slower than that associated with growth rates γ_0 or $\gamma_0\sqrt{\nu_2/\nu_1}$ and saturates at level prescribed by amplification coefficient $\exp\left[\frac{\pi\gamma_0^2\ell^2}{\nu_1\nu_2}\right]$ in agreement with [2]. On contrary, for slow modulation ($\tau_c = 16$) shown in Fig. 6, fast bursts of growth are observable and average level of amplification is much higher.

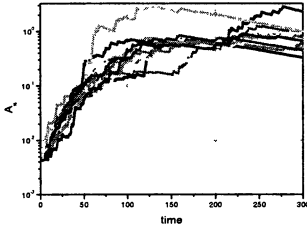


Fig. 5. Slow wave amplitude behavior for different stochastic phase realization, $\tau_c = 1.0$, $\Delta = 9.6$.

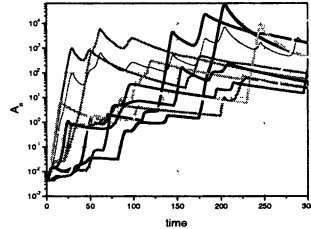


Fig. 6. Slow wave amplitude behavior for different stochastic phase realization, $\tau_c = 16.0$, $\Delta = 9.6$.

Conclusions

The prediction of weak influence of the pump frequency modulation on the inhomogeneous plasma PDI level is applicable only to the case of modulation faster than transient time of daughter waves in the decay region. If this condition is violated, the significant PDI enhancement becomes possible due to the effect of resonant suppression of the convective losses from the moving decay region. This effect manifests itself in the form of short giant bursts of decay wave amplitudes. It can be used for selective excitation of PDI in experiment with chirped frequency laser pulses.

Acknowledgements. This work was supported by grants of RFBR-BRFBR 02-02-81033 F02P-092, INTAS-01-0233.

References

1. Valeo E., Oberman C., Phys. Rev. Lett., **30**, 1035 (1973).
2. Laval G., Pellat R., Pesme D., Phys. Rev. Lett. **36**, 192 (1976).
3. Arkhipenko V. I., Budnikov V. N., Gusakov E. Z. et al., Plasma Phys. Reports, **26**, 314 (2000).
4. Gusakov E. Z., Yakovlev B. O., ICPP, **1**, 17 (2000).
5. Arkhipenko V. I., Budnikov V. N., Gusakov E. Z. et al., JETP Lett., **60**, 843 (1994).

THE EFFECT OF THE ELECTROMAGNETICALLY INDUCED TRANSPARENCY IN MAGNETOACTIVE PLASMAS

A. Yu. Kryachko, M. D. Tokman

Institute of Applied Physics Russian Academy of Sciences, Nizhny Novgorod, Russia

The effect of electromagnetically induced transparency (EIT) is investigated for the electron-cyclotron waves in warm plasma. It is shown, that the thermal motion drastically changes the behavior of dispersive curves of the probe wave in the EIT regime in comparison with the cold plasma. Also the features of transverse propagation of the probe wave in "quasi-EIT" regime are investigated for the cold plasma.

Introduction

An interesting parametric effect in contemporary coherent and nonlinear optics is electromagnetically induced transparency (EIT) in ensembles of three-level atoms caused by interference of the quantum states of electrons. This effect manifests itself as formation of a "transparency window" within the zone of resonance absorption of the probe light wave in the presence of high-power pumping wave, which is accompanied, at the same time, by extremely slow group velocity of the probe wave [1].

The classical analogs of this effect in wave systems were investigated in [2, 3] for the electromagnetic waves in isotropic plasma and in [4, 5] for the longitudinal propagation of electron cyclotron waves in magnetoactive one. In both cases the cold plasma was considered.

In this paper we investigate two basic problems: 1) we consider the influence of the thermal motion in plasma on EIT effect for the EC waves, investigated in [4]. We have shown that the thermal dispersion, provoked by the thermal motion, changes the manifestation of EIT drastically; 2) we investigate the interesting features of transverse propagation of the probe EC wave in cold plasma in quasi-EIT regime. It is shown that in such regime the effect of depression of the resonant component can be eliminated for the probe wave.

Effect of EIT in high-temperature plasma

When the thermal motion is considered, the collisionless absorption of the waves is the principal effect. Hence, we can investigate this problem correctly only within the framework of kinetic theory. Following the work [4], we will investigate the propagation of two circularly polarized extraordinary waves along the static magnetic field $\mathbf{H} = H\mathbf{z}_0$ in magnetized plasma:

$$\mathbf{E}_\perp(z, t) = \text{Re} \left\{ \mathbf{e}_+ \left[E_1 \exp(-i\omega_1 t + ik_1 z) + E_2 \exp(-i\omega_2 t + ik_2 z) \right] \right\}. \quad (1)$$

Here $\mathbf{e}_+ = 2^{-1/2}(\mathbf{x}_0 + i\mathbf{y}_0)$ is the polarization vector of extraordinary wave, \mathbf{x}_0 , \mathbf{y}_0 and \mathbf{z}_0 are the basis vectors of coordinate system. We will consider the range of parameters:

$$|\omega_1 - \omega_H|, \gamma \ll \omega_1, \omega_H, \quad (2a)$$

$$|\omega_L - \omega_p|, \gamma \ll \omega_L, \omega_p, \quad (2b)$$

$$k_{1,2,L} V_T \ll \omega_{1,2,L}, \quad (2c)$$

corresponding to the conditions of electron cyclotron resonance for probe wave (2a), effective excitation of plasma waves by the beat wave (2b) and weak thermal dispersion (2c) respectively. Here $\omega_L = \omega_1 - \omega_2$ and $k_L = k_1 - k_2$ are the frequency and the wavenumber of the beat wave, excited by probe and pumping waves, $\omega_p = (4\pi e N_0/m)^{1/2}$ is the electron plasma frequency, $V_T = (T/m)^{1/2}$ and T are the thermal velocity and the temperature of electrons respectively.

The kinetic equation for the electrons' distribution function f has the following form:

$$\frac{\partial f}{\partial t} + \mathbf{V} \frac{\partial f}{\partial \mathbf{r}} - \omega_H [\mathbf{V}, \mathbf{z}_0] \frac{\partial f}{\partial \mathbf{V}} - \frac{e}{m} \left(\mathbf{E} + \frac{1}{c} [\mathbf{V}, \mathbf{B}] \right) \frac{\partial f}{\partial \mathbf{V}} = -\gamma (f - f_0). \quad (3)$$

Here f_0 is the unperturbed distribution function, $\omega_H = eH/mc$ is the electron gyrofrequency, e and m are the electron charge ($e > 0$) and mass. Including the non-zero value of γ in Eq. (3), we automatically agree the "Landau pole rule", when calculating the collisionless decrement of the waves. Since the frequency ω_1 is close to ω_H , the collisionless decrement of probe wave is significantly greater, than the transport frequency of Coulomb collisions for thermal particles. At the same time, according to the Eq. (2c), the value of collisionless decrement for pumping and plasma waves is exponentially small and it is much less, than transport frequency (for the parameters considered). Therefore, it is reasonable to take γ to be equal to the transport frequency of Coulomb collisions for the given temperature.

Kinetic equation should be supplemented with the equation, describing the excitation of plasma waves:

$$\partial E_p / \partial t = -4\pi j_z = 4\pi e \int V_{\parallel} f d^3V. \quad (4)$$

Here E_p is the electric field of plasma wave and j_z is the longitudinal component of the electron current. We will assume that the ion density N_0 is constant and the plasma is quasi-neutral.

Considering the Eqs. (2a) and (2b), we can use the technique of "reduced" equations [5, 6], i.e. neglect all "non-resonant" terms in Eqs. (3) and (4). Solving the obtained system of equations, one can find the expression for the effective refractive factor of the probe wave:

$$N_{EIT}^2 = N_0^2 - \xi_{EC} \frac{A(\omega_1, k_1)}{D(\omega_L, k_L) - \xi_{EC} \cdot B(\omega_1, k_1)}. \quad (5)$$

Eq. (5) generalizes the expression for N_{EIT}^2 in cold plasma [4]. Here $\xi_{EC} = |eE_2/2m(\omega_2 - \omega_H + i\gamma)|^2 (k_2/\omega_2)^2$ is the ratio of squares of the oscillatory and phase velocities for the pumping field (i.e. ξ_{EC} is the dimensionless pumping intensity), N_0^2 is the "linear" refractive factor of extraordinary wave in warm plasma within the kinetic theory (e.g. see [7]):

$$N_0^2 = 1 - \frac{\omega_p^2}{\omega_1^2} \int_{-\infty}^{+\infty} \frac{(\omega_1 - k_1 V_{\parallel}) F_0 - k_1 \partial (\langle V_{\perp}^2 \rangle F_0) / \partial V_{\parallel}}{\omega_1 - \omega_H - k_1 V_{\parallel} + i\gamma} dV_{\parallel}. \quad (6)$$

$D(\omega_L, k_L)$ is the "longitudinal" dielectric permittivity of warm plasma [7]:

$$D(\omega_L, k_L) = 1 + \frac{\omega_p^2}{\omega_L} \int_{-\infty}^{+\infty} \frac{(\partial F_0 / \partial V_{\parallel}) V_{\parallel}}{\omega_L - k_L V_{\parallel} + i\gamma} dV_{\parallel}. \quad (7)$$

In particular, equation $\text{Re}D(\omega_L, k_L) = 0$ is the dispersive relation for the plasma waves. Here $F_0(V_{\parallel}) = N_0^{-1} \int f_0 d^2 V_{\perp}$ is the unperturbed distribution function for longitudinal velocities, normalized to unity, $\langle V_{\perp}^2 \rangle = \int f_0 V_{\perp}^2 d^2 V_{\perp} (\int f_0 d^2 V_{\perp})^{-1}$. A and B are the functions, not containing the ξ_{EC} parameter [6]. They are very cumbersome and not shown here.

Dispersion and dissipation of the probe wave in EIT regime

The value of ξ_{EC} is the small parameter: for moderate pumping intensity (in order of 100 kW/cm^2) it is equal to the $10^{-4} \div 10^{-6}$. Hence, the contribution of the second term in Eq. (5) is significant only if the value of $D(\omega_L, k_L)$ is small enough and the criterion of EIT can be written as:

$$\xi_{EC} \gg \max \{ \text{Re} D(\omega_L, k_L), \text{Im} D(\omega_L, k_L) \}. \quad (8)$$

From the Eq. (8) one can see, that the dispersive curves of the probe wave in EIT region are determined by dispersive curves of plasma wave ($\text{Re}D(\omega_L, k_L) = 0$), in contrast to the case of cold plasma, where their behavior was determined by pumping intensity [4]. This physical effect is rather obvious: as shown in [5], the effect of EIT in cold plasma can be observed only if the collective degrees of freedom are effectively excited in plasma. In our case collective oscillations correspond to the plasma waves and are determined by the dispersive relation $\text{Re}D(\omega_L, k_L) = 0$.

We investigated the law of dispersion of the probe wave within the EIT regime, using numerical calculations for Eq. (5) and assuming that distribution function F_0 is Maxwellian and isotropic. Dispersive curves are shown in Fig. 1 for different values of pumping intensity I_2 . One can see that their behavior is mainly determined by the structure of the plasma waves' dispersion curves, as predicted above. In particular, dispersive curves have points with zero group velocity (which is impossible for quantum system and cold plasma), corresponding to the minimum of the dispersive curves of plasma wave: $\omega_1 = \omega_2 + \omega_p + O(\xi_{EC})$

and $k_1 = k_2 + O(\xi_{EC})$. Fig. 2 demonstrates the modification of the absorption band within the EIT region. As follows from this figure, there is the frequency range, approximately corresponding to the point with zero group velocity on the dispersive curve, where the dissipation of the probe wave is reduced.

Let us estimate the width of transparency window $\Delta\omega$ in EIT regime. In cold plasma [4] the value of $\Delta\omega$ can be estimated as $\Delta\omega \sim (\omega_p \omega_H \xi_{EC})^{1/2}$. For the warm plasma it is possible to obtain the analytical estimation for $\Delta\omega$ only in the context of the hydrodynamic theory [6]. In that case the expression for $\Delta\omega$ has the following form:

$$\Delta\omega \sim \max \left\{ (\omega_p \omega_H \xi_{EC})^{1/2}, k_L^2 V_T^2 / \omega_p \right\}. \quad (9)$$

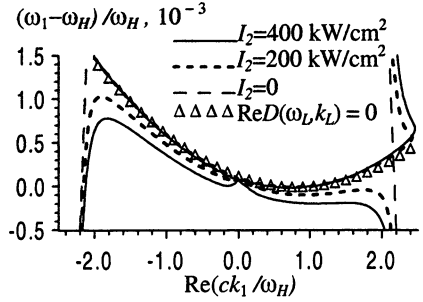


Fig. 1. Dispersion of probe wave. $\omega_2/\omega_H = 0.7$, $\gamma/\omega_H = 4.0 \cdot 10^{-6}$, $T = 30$ eV, $N_0 = 10^{13}$ cm^{-3} , $H = 35$ kGs ($\omega_H/2\pi = 94$ GHz).

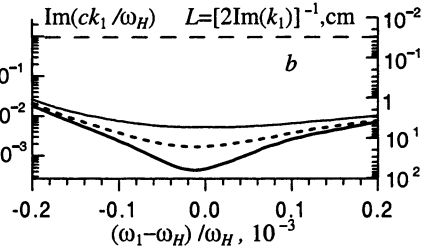
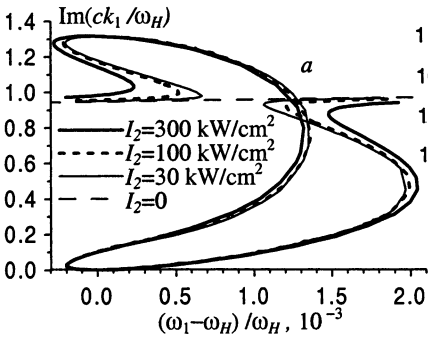


Fig. 2. Transparency window. $\omega_2/\omega_H = 0.72$, $\gamma/\omega_H = 4.0 \cdot 10^{-8}$, $T = 610$ eV, $N_0 = 10^{13}$ cm^{-3} , $H = 35$ kGs ($\omega_H/2\pi = 94$ GHz).

Since the Eqs. (5)–(7) for N_{EIT}^2 are very cumbersome, the analytical result for $\Delta\omega$ in the kinetic theory can not be obtained. But it can be shown via numerical calculations, that the Eq. (9) is valid in the kinetic theory also. As follows from Eq. (9), the transparency window in warm plasma can be significantly wider, than in cold one, if the temperature is high enough:

$$T/(mc^2) > \omega_p^2 (ck_L)^{-2} (\omega_H \xi_{EC} / \omega_p)^{1/2}. \quad (10)$$

For example, for the pumping intensity of 100 kW/cm^2 and other parameters, corresponding to the Fig. 2, the temperature should exceed 150 eV. Moreover, if

the Eq. (10) is fulfilled, the value of $\Delta\omega$ does not depend on the pumping intensity (Fig. 2). At the same time, as it can be seen from Fig. 2, *b*, the dissipation and the maximum propagation length $L = [2\text{Im}(k_1)]^{-1}$ of the wave strongly depend on the pumping intensity.

Possible applications of the EIT in ensembles of classical oscillators include the spectroscopy of thermonuclear plasma and the realization of EIT in different devices of microwave plasma electronics (e.g. for the purpose of pulse compression). For more detailed proposals, however, it is necessary to generalize our theory for the non-longitudinal propagation of the waves in inhomogeneous plasma.

Quasi-EIT regime for transverse probe wave

Having continued the investigation of the EIT for extraordinary EC waves, we considered the transverse propagation of the probe wave in cold plasma. For pumping wave we assume, that its wavevector \mathbf{k}_2 has the finite angle Θ_2 relatively to the magnetic field \mathbf{H} , such that the wavevector \mathbf{k}_L of the beatwave is directed close to the magnetic field \mathbf{H} for the effective excitation of longitudinal plasma oscillations at plasma frequency ω_p : $|k_{Lx}| = |k_1 - k_2 \sin(\Theta_2)| \ll |k_1|, |k_2|, |k_L|$.

We investigated this problem in the framework of hydrodynamic theory, using the technique of "reduced" equations very similar to the approach, used in [5]. The results obtained are quite obvious from the physical point of view. It is well known, that in linear regime the maximum dissipation of transversally propagating extraordinary wave (probe wave) corresponds to the upper-hybrid frequency $\omega_{uh} = (\omega_p^2 + \omega_H^2)^{1/2}$ and at gyrofrequency its dissipation is very small:

$$\text{Im } k_1(\omega_1 = \omega_H) / \text{Im } k_1(\omega_1 = \omega_{uh}) \sim (\gamma/\omega_1)^{3/2} \ll 1, \quad (11)$$

because for $\omega_1 = \omega_H$ the amplitude of the resonant component $\mathbf{E}_1^{(\text{res})}$ of the wave (having circular polarization with electric field vector rotating in the direction of the electrons' motion) is also very small due to the so-called effect of depression of the resonant component:

$$|\mathbf{E}_1^{(\text{res})}| / |\mathbf{E}_1| \sim \gamma/\omega_1 \ll 1. \quad (12)$$

But when the amplitude of the pumping wave is finite, because of the nonlinear interaction between pumping and plasma waves, the wave with different polarization is generated at frequency ω_1 . Therefore, the non-zero resonant component appears for the probe wave, when pumping intensity is increased (see Fig. 3, *a*). And the appearance of this component is accompanied by the increasing of dissipation for the wave (Fig. 3, *b*).

Therefore, this regime of parametric wave interaction can not be called "electromagnetically induced transparency", because instead of transparency we have

the increasing of dissipation. But this regime is nevertheless very interesting. Here we still have the nonlinear regime of wave interaction and effective excitation of collective degrees of freedom, which lead to the strong polarization effects and significant modification of the probe wave's dissipation. And this regime, in principal, can be used for the elimination of the depression and for the increasing of cyclotron dissipation of the waves in plasma.

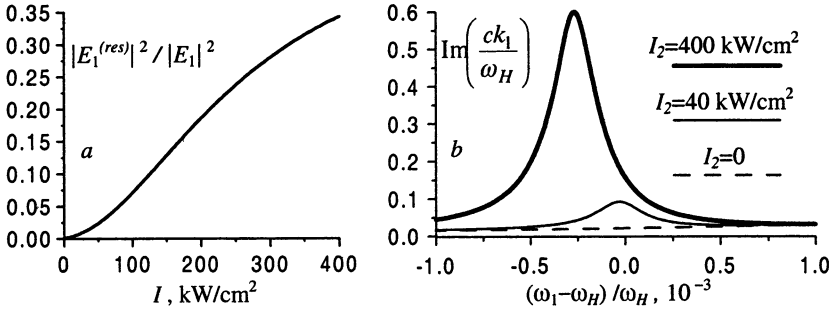


Fig. 3. Resonant component (a) and dissipation (b) for transversal probe wave. $N_0=10^{12} \text{ cm}^{-3}$, $H_0=35 \text{ kGs}$ ($\omega_H/2\pi=94 \text{ GHz}$), $\gamma/\omega_H=3.0 \cdot 10^{-4}$, $\omega_2/\omega_H=0.9$, $\Theta_2=17^\circ$

This work was supported by the grants of Russian Foundation for Basic Research (№ 01-02-17388 and № 01-02-17779).

References

1. Harris S. E., Phys. Today, July 1997, **50**, 36.
2. Harris S. E., Phys. Rev. Lett., 1996, **77**, 5357.
3. Gordon D. F., Mori W. B., Joshi C., Phys. of Plasmas, 2000, **7**, 3145, 3156.
4. Litvak A. G., Tokman M. D., Phys. Rev. Lett., 2002, **88**, 095003.
5. Litvak A. G., Tokman M. D., Radiophysics and Quantum Electronics, 2001, **44**, 375.
6. Kryachko A. Yu., Litvak A. G., Tokman M. D. Preprint of IAP RAS № 575 (in Russian), 2001.
7. Akhiezer A. I., Akhiezer I. A., Polovin R. V. et al., Plasma Electrodynamics, Nauka, Moscow, 1974; Pergamon, Oxford, 1975.

SELF-CHANNELING OF HIGH POWER MICROWAVES IN A PREFORMED PLASMA WAVEGUIDE

C. Rajyaguru, T. Hosoya, H. Ito, N. Yugami, Y. Nishida

Energy and Environmental Science, Graduate School of Engineering,
Utsunomiya University 7-1-2 Yoto, Utsunomiya, Tochigi 321-8585, Japan

Propagation characteristics of high power microwaves are investigated in preformed plasma density channel. Plasma density channel is formed by inserting a thin glass strip along the axis of the chamber. The width and depth of the density channel can be adjusted by changing the background plasma density. When incident microwaves with power more than 50 kW are launched, density channel is expanded and microwaves penetrate for almost five Rayleigh lengths (~50 cm) in the channel. This way, preformed density channel acts as a waveguide to guide the high power microwaves. The width of the density channel increases and that of electric field decreases with increase in the incident microwave power. This shows that microwaves modifies the refractive index of the density channel to increase it at the center and remains trapped in the region of higher refractive index. Analytical treatment to the propagation of electromagnetic waves in a dielectric waveguide having step-index profiles shows good agreement with the experimentally measured electric field profiles.

Introduction

Now that lasers employing CPA [1] (Chirped Pulse Amplification) technique have become readily available, a new era of discovery, similar to that following the invention of the laser itself, has begun. Topics like, fast ignition [2], plasma based accelerators (typically laser wake-field accelerators) [3, 4] and tunable radiation sources [5] gained real acceleration after the availability of, so called table top lasers. Plasma based accelerators are of particular interest as they can hold acceleration gradients almost three orders of magnitude greater than the conventional RF accelerators. However, plasma based accelerators require long interaction lengths between laser pulse and plasma. Usually interaction lengths are severely limited by vacuum diffraction [6] and other instabilities [7] of laser pulse. Several schemes like self focusing [8], optical guiding [9] and preformed channels [10] are proposed to achieve longer interaction lengths. Guiding of laser pulse by preformed channel is the best candidate among all as self focusing and optical guiding concepts are ineffective for short laser pulses and work only for long laser pulses [11].

In present experiment we study the propagation characteristics of strong microwaves in preformed channel to avoid usually complicated experimental setup and diagnostics involved in laser experiment. Complex problem of channel formation and study of propagation characteristics have been isolated to concentrate more on the physics involved in propagation of microwaves inside the channel rather than solving for the technical problems associated with evolving (in time) channels usually created in guiding experiments involving lasers.

Experimental setup

The experimental setup used in the present investigation is shown schematically in Fig. 1. Unmagnetized argon plasma is produced in a stainless-steel chamber of 100 cm length and 60 cm diameter.

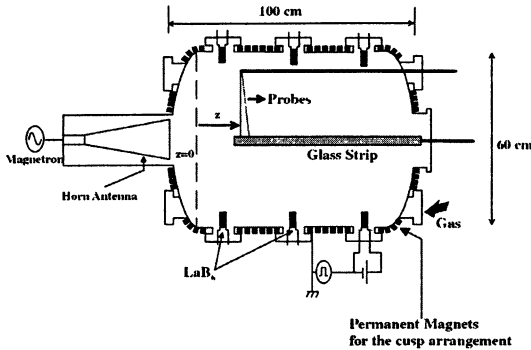


Fig. 1. Experimental setup used in present study

Outside surface of the vacuum chamber is covered, for improved plasma confinement, with line cusp arrangements, made from permanent magnets having surface magnetic field strength of 4 kGs. Plasma is produced by a pulsed discharge between six LaB_6 cathodes and the grounded chamber wall acting as anode. Typical discharge voltage and discharge duration

are 180 V and 1.5 ms, respectively, with the repetition rate of 10 Hz. Typical plasma parameters are, $n_e \approx 1 \sim 1.5 \cdot 10^{12} \text{ cm}^{-3}$, $T_e \approx 2 \text{ eV}$. Microwave used in the present study has central frequency, $f_0 = 9 \text{ GHz}$ (corresponding to cut-off density, $n_c \approx 1 \cdot 10^{12} \text{ cm}^{-3}$) and maximum power, 250 kW. The microwave pulse duration is about $1 \mu\text{s}$, full width at half maximum (FWHM), with rise and fall time of 100 ns and repetition rate of 10 Hz.

The entrance of the channel is adjusted at such a distance that microwave can enter it before diverging significantly from its beam size at the aperture of the horn antenna. Density channel is formed by introducing a glass strip having dimensions $50 \times 1 \times 0.1 \text{ cm}$. Surface of the glass strip acts as a dielectric boundary in plasma reducing the plasma density near its surface. This way, one would have minimum density at the center and gradually increasing for higher radial positions. Channel width can be varied by adjusting the background plasma density.

Results and discussion

When 0.1 cm thick, 1 cm wide and 70 cm long glass strip is introduced along the axis of the chamber up to 20 cm from the horn antenna. Typical density distribution measured in r - z plane is shown in Fig. 2. As the plasma around the glass strip is symmetric, all measurements are shown only on one side of the glass strip. Horn antenna orientation is such that the direction of electric field is perpendicular to smallest dimensions ($\sim 1 \text{ mm}$) of the glass strip. Propagation characteristics of microwaves within the channel are studied for different channel

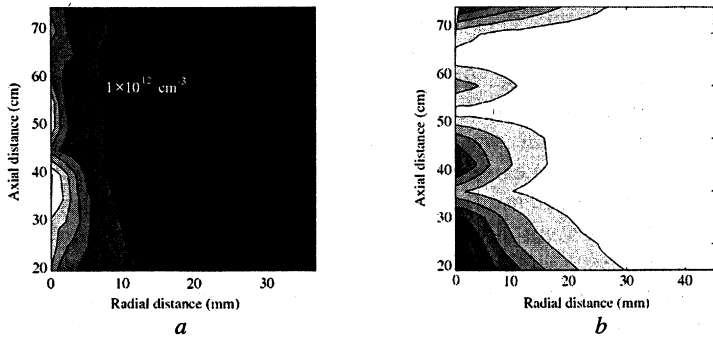


Fig. 2. Contour plot of plasma density and microwave electric field intensity: *a* – plasma density in the absence of microwaves in *r-z* plane; *b* – microwave electric field intensity within the density channel.

widths. It is observed that for smallest possible channel widths (≈ 1.6 cm), high power microwaves (~ 250 kW) expands the channel and propagate for approximately 50 cm which is five times the Rayleigh length (~ 10 cm in present case). The smallest cut-off dimension, for the 9 GHz microwaves used in present case, is estimated to be 2 cm. Though the channel width, in absence of microwaves as shown in Fig. 2, *a*, is less than the cut-off width microwaves can be seen to expand the channel and propagate in the preformed channel in Fig. 2, *b*. Figure 3 shows the radial density profile at $z = 60$ cm and corresponding microwave electric field intensity profile for different incident microwave powers.

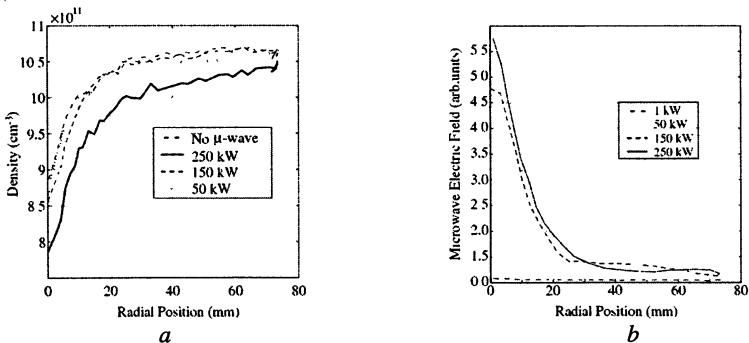


Fig. 3. Expansion of density channel and penetration of microwave energy: *a* – density profile for different incident powers at $z = 60$ cm; *b* – microwave electric field intensity for different incident powers at $z = 60$ cm.

However, the expansion of the channel is observed less (not shown in the figure) for greater channel widths. We have also observed that radial half width of plasma density increases as incident microwave power is increased. Maximum

expansion of the channel occurs around $z = 60$ cm as the radial width (in absence of microwaves) at $z = 60$ cm is smallest (see Fig. 2, a) and greater ponderomotive force is exerted. In addition, for spatial locations deeper into the channel, power required to expand the channel also increases which is natural due to the intensity depletion occurring as microwaves penetrate deeper in the channel. As the initial channel width is wider near $z = 42$ cm as compared to that at $z = 60$ cm, radial extent of microwave electric field is also wider, hence increase in incident power beyond 50 kW does not significantly alter the channel width. However, initial channel width near $z = 60$ cm is already smaller, thus greater ponderomotive force is exerted leading to drastic widening of the channel when incident power is increased beyond 50 kW. This is the reason why fractional change in the radial half width of density is more for deeper locations in the density channel.

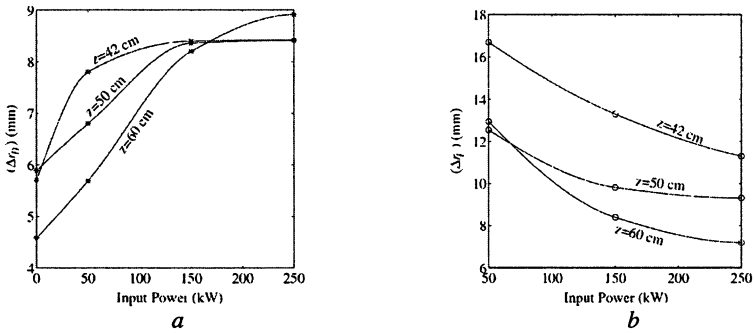


Fig. 4. Variation of radial half widths of electric field and preformed density channel with incident microwave power.

Similar behavior can be seen for the radial half width of microwave electric field.

Above mentioned results can be explained by analyzing the propagation characteristics of microwave in dielectric waveguide having step index profile of dielectric constant. Let us assume that a rectangular dielectric waveguide has dielectric constant ϵ_1 in a dimension $2a$ and ϵ_2 outside. We also assume that the variation is only in x direction, which is perpendicular to the microwave field polarization (in y direction). One can look for the TE mode solution due to symmetry of the problem in the present experimental conditions. The solution can be straight forwardly written as

$$E_y = \begin{cases} E_0 \cos(\beta x) \exp(-ikz) & (|x| \leq a) \\ E_0 \cos(\beta a) \exp[-\gamma(|x| - a)] \exp(-ikz) & (|x| > a) \end{cases}, \quad (1)$$

where β and η are connected by following two equations with k_0 is the vacuum wavenumber:

$$\begin{aligned}\gamma &= \beta \tan(\gamma a), \\ \gamma^2 + \beta^2 &= k_0^2 (\epsilon_1 - \epsilon_2).\end{aligned}\tag{2}$$

Approximately, the half width of the electric field is proportional to inverse of perpendicular wavenumber β and consequently Eq. (2) leads to

$$\beta / \cos(\beta a) = \sqrt{\epsilon_1} k_0.\tag{3}$$

Here, ϵ_2 is assumed to be zero out size the channel as the density is cut-off for the incident microwaves. Thus, one can approximately write that radial half width is inversely proportional to the refractive index

$$\Delta r \sim 1/\beta \sim 1/\sqrt{\epsilon_1} \sim 1/\eta_1.\tag{4}$$

Equation 4 explains the experimentally observed results very well. When high power microwaves enter the preformed density channel; density channel is expanded due to the radial ponderomotive force thereby increasing the refractive index there. From Eq. (4) then it is clear that radial extent of the electric field then shrinks to narrower region of higher refractive index. As higher incident power exhibits greater change in the refractive index, results shown in Fig. 4 are very well explained.

Conclusions

We have shown that high power microwaves expand the preformed channel by its ponderomotive force and propagate up to five Rayleigh lengths. Fractional change in radial width of electric field and density depends on the unmodified channel structure. Experimental results can be explained by propagation of electromagnetic waves in dielectric waveguide.

References

1. *Maine P., Strickland D., Bado P., Pessot M. and Mourou G.*, IEEE J. Quantum Electron, 1988, QE-24, 398.
2. *Tabak M., Hammer J., Glinsky M. E., Kruer W. L., Wilks S. C., Woodworth J., Campbell E. M., Perry M. D. and Mason R. J.*, Phys. Plasmas, 1994, 1, 1626.
3. *Tajima T. and Dawson J. M.*, Phys. Rev. Lett., 1979, 43, 267.
4. *Sprangle P., Esarey E., Ting A. and Joyce G.*, Appl. Phys. Lett., 1988, 53, 2146.
5. *Yugani N., Higashiguchi T., Gao H., Sakai S., Takahashi K., Ito H., Nishida Y., Katsouleas T.*, Phys. Rev. Lett. 2002, 89, 065003-1.
6. *Sprangle P. and Esarey E.*, Phys. Fluids B, 1992, 4, 2241.
7. *Max C., Arones J. and Langdon A.*, Phys. Rev. Lett., 1974, 33, 209.
8. *Mori W., Joshi C., Dawson J. M. and Kindle J. M.*, Phys. Rev. Lett., 1988, 60, 1298.
9. *Sprangle P., Esarey E. and Joyce G.*, Appl. Phys. Lett., 1988, 53, 2146.
10. *Durfee III C. G. and Milchberg H. M.*, Phys. Rev. Lett., 1997, 71, 4047.
11. *Esarey E., Sprangle P., Krall J. and Ting A.*, IEEE. Trans. Plasma Sci., 1996, 24, 252.

LOW FREQUENCY SHEATH INSTABILITY STIMULATED BY THE RESONANT ABSORPTION OF A SHORT MICROWAVE PULSE

M. Starodubtsev¹, Md. Kamal-Al-Hassan, H. Ito, N. Yugami, Y. Nishida

Energy and Environmental Science, Graduate School of Engineering,
Utsunomiya University, Utsunomiya, Japan

¹Institute of Applied Physics, Nizhny Novgorod, Russia

Low frequency sheath instability has been observed in the circuit of a positively biased electrode when the ambient nonuniform plasma is irradiated by a microwave pulse of short duration (τ is approximately equal to the ion-plasma period). The instability with its characteristic frequencies below the ion plasma frequency is stimulated by a flux of accelerated ions produced by the microwave resonant absorption process. A qualitative model of the instability is suggested.

Sheath-plasma instabilities are of the great interest for fundamental plasma physics as a basic plasma property and for different applications, such as plasma diagnostic techniques [1], plasma diodes [2] and discharges [3, 4], antennas in plasmas [5, 6] and current systems in space [7, 8]. The high-frequency sheath-plasma instability (at frequencies closed to the electron plasma frequency ω_p) is a well-known process [6], which occurs in the sheath of a positively biased electrode due to the finite electron transition time through the sheath. Low-frequency current instabilities have also been observed in large magnetoplasma with a positively biased electrode [8] and in hollow cathode discharges [3].

In this report we present a low-frequency sheath-plasma instability that occurs at the electron saturation current (i.e. when the electrode is biased positively with respect to the plasma) in presence of energetic ion flux.

In the present experiment, the high-energy ion component has been produced by the resonant absorption of a short microwave pulse (pulse duration is in the order of an ion plasma period). It is known that the resonant absorption process can cause the ion acceleration [9] due to different physical processes. We believe that in the present experiment the main mechanism of ion acceleration is provided by the ambipolar electric field due to the plasma density gradient. This ambipolar field produces ion acceleration in the direction down the density gradient, which confirms to our experimental observations. Nevertheless, the exact identification of the ion acceleration process is out of scope of this report.

The experiments (see Fig. 1) are performed in a large (60 cm diameter, 1 m length) laboratory plasma device with multipol magnetic confinement system. A nonuniform plasma column with maximal density $n_e \approx 2 \cdot 10^{11} \text{ cm}^{-3}$, electron temperature $T_e \approx 2 \text{ eV}$, ion temperature $T_i \approx T_e/10$, is produced at argon gas pressure $p \approx 4 \cdot 10^{-4} \text{ Torr}$ with a pulsed dc discharge (pulse duration $\tau_{dis} = 2.5 \text{ ms}$, repetition

rate $f_{dis} = 10$ Hz) using tungsten filaments as cathode. The typical density gradient scale lengths in the axial direction (z -direction) and in the radial (r -direction) are, respectively, $L_z = (\partial \ln n_e / \partial z)^{-1} \approx 100$ cm and $L_r = (\partial \ln n_e / \partial r)^{-1} \approx 50$ cm. A p -polarized microwave pulse with frequency $f_0 = \omega_0 / 2\pi = 2.86$ GHz and a maximum power of 10 kW is produced by a klystron and is irradiated into the plasma volume from a high gain horn antenna located at the lower-density side of the plasma chamber. The pulse width ranges from 60 ns to 10 μ s at a full width at half maximum. The critical density layer ($\omega_0 = \omega_p$, where ω_p is the plasma frequency) is located near the center of the chamber. Diagnostics used in the presented experiment include two oppositely directed disc probes measuring the ambient plasma density and its fluctuations, a short dipole antenna and an electrostatic energy analyzer oriented to the over-dense plasma to measure the particles accelerated toward the lower density side.

Figure 2 shows a set of typical oscillograms of the electron and the ion saturation currents for two oppositely directed probes (double probe). The double probe has been placed at the lower-density side of the resonant absorption region at a distance $\Delta z \approx 5$ cm from the resonance point. One can notice an ion-wave streamer (propagating down the density gradient), clearly in Fig. 2, $b-d$. However, Fig. 2, a displays not only the streamer, but also the high-frequency oscillations (with characteristic period $\tau_{osc} \approx 0.3$ μ s), which occur in the electron saturation current of a probe facing the resonance region. This paper is aimed towards uncovering the nature of these oscillations stimulated by the resonant absorption of a short microwave pulse. Comparing Fig. 2, a and Fig. 2, $b-d$, one can conclude that the oscillations do not correspond to the real plasma density perturbations as same are not detected when probe is biased in the ion saturation region (Fig. 2, c) as well as by the probe facing opposite to resonance region (Fig. 2, b, d). We believe that the oscillations in the electron saturation current are due to the sheath instability.

Nature of high frequency oscillations has also been examined with a microwave resonator probe [10]. The probe design is presented in Fig. 3, a and a typical oscillogram is presented in Fig. 3, b . A quarter-wavelength U-shaped high-quality ($Q \approx 170$) resonator exhibits a resonance at $f_{res} \approx 4.88$ GHz in vacuum and $f_{res}^* \approx 5.28$ GHz in plasma near the resonance region. Measurements have been performed when the signal frequency is tuned to the slope of the resonance curve ($f \approx 5.32$ GHz) such that small shifts of the resonant frequency due to plasma density perturbations produce approximately proportional variations of the

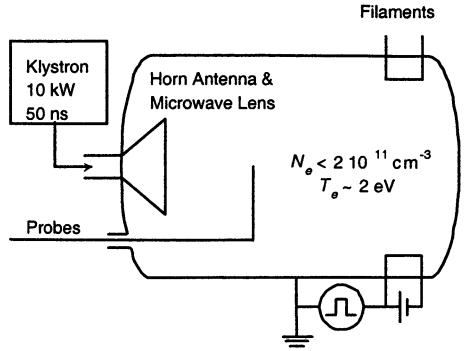


Fig. 1. Schematic view of the experimental setup

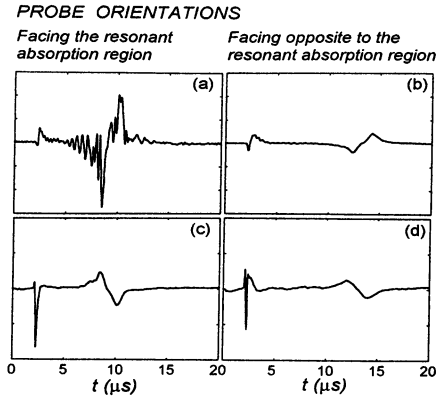


Fig. 2. Probe currents vs time at different probe orientations. *a, b* – the electron saturation current (at $V = 50$ V); *c, d* – the ion saturation current (at $V = -70$ V); *a, c* – probe facing the resonant absorption region; *b, d* – probe facing opposite to the resonant absorption region.

amplitude of the probe output signal. Measurements by the resonator probe presented in Fig. 3, *b* are similar to ones presented in Fig. 2, *b–d* and do not display the oscillations observed in Fig. 2, *a*, although the probe time response is approximately $t \approx Q/f_{res} \approx 30$ ns which is much shorter than the characteristic period of these oscillations.

The above results clearly demonstrate that the oscillations in the electron saturation current are not due to plasma density fluctuations but are related to the sheath instability. The instability occurs only when the probe is biased positively with respect to the plasma, as it is displayed in Fig. 4 where the ratio I_{osc}/I_{dc} is plotted as a function of the probe bias voltage. One can see that the relative amplitude of the observed oscillations does not remain constant (as it should be for the case of real density perturbations) but exhibits threshold, growth and saturation, which is a typical behavior for instabilities [6].

Figure 5 presents the temporal evolution of the electron saturation current at different distances Δz between the probe and the resonant region. One can see that the instability gets well separated in time from the microwave pulse when

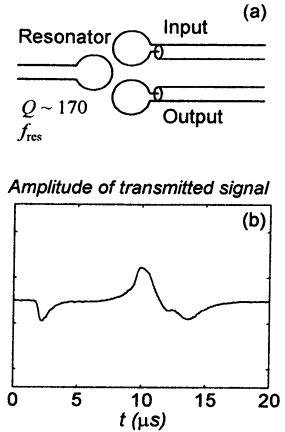


Fig. 3. Measurements of plasma density perturbations by using the microwave resonator probe. *a* – Schematic view of the probe. *b* – Temporal behavior of the probe output signal at $f = 5.32$ GHz.

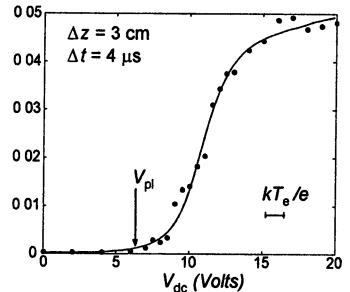


Fig. 4. Relative instability amplitude versus dc bias voltage.

Δz increases. At larger distances (Fig. 5, *d*, *e*) one can observe that the instability starts few microseconds before the ion-wave streamer reaches the probe. This result shows that the instability is stimulated by energetic ions produced by the resonant absorption process propagating toward the lower-density side with velocities $v_b \sim (3 \sim 7)c_s$, where c_s is the ion acoustic speed (note that the streamer propagates down the density gradient with approximately $2c_s$).

Typical energy spectrum of accelerated ions is displayed in Fig. 6 showing the presence of energetic ions with energies up to 17 V, which is approximately one order higher than background electron energy. These measurements were performed with an ion-energy analyzer which discriminates against ions below certain energy by a positive potential applied to the collector. Two grids are placed in front of the collector: the outer one is left at floating potential in order to reduce disturbances of analyzer on the ambient plasma and the inner one is biased negatively in order to reflect plasma electrons. The analyzer is located at approximately 3 cm down the density gradient from the resonant region. One can see that the resonant absorption of a short microwave pulse produces a bunch of accelerated ions with a wide range of ion velocities. As this ion structure travels down the density gradient, the peak disperses and fast ion components reach the probe significantly earlier than the ion wave streamer (compare with Fig. 5, *e*).

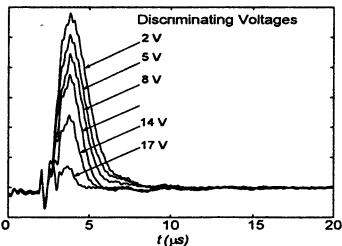


Fig. 6. Higher-energy ions observed with an ion energy analyzer.

If $U_0 > U_b$, the beam is reflected inside the electron-reach sheath. Near the reflection point its density increases manifolds and diminishes, consequently, the

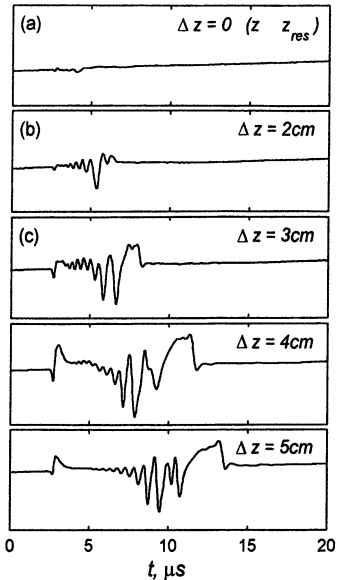


Fig. 5. Electron saturation current ($V = 50$ V) at different distances from the resonance absorption region showing that the instability is associated with the bunch of energetic ions produced by the resonant absorption process.

Summarizing the above measurements, the observed low-frequency oscillations of the electron saturation current do not represent the plasma density perturbations but are due to instability of positively-biased electrode driven by an energetic ion beam component.

We suggest a simple physical model of the observed instability. Consider a positively biased (at U_0) probe immersed into plasma with an ion beam (eU_b – beam energy). If $U_0 > U_b$, the beam is reflected inside the electron-reach sheath. Near the reflection point its density increases manifolds and diminishes, consequently, the

the observed instability. Consider a positively biased (at U_0) probe immersed into plasma with an ion beam (eU_b – beam energy). If $U_0 > U_b$, the beam is reflected inside the electron-reach sheath. Near the reflection point its density increases manifolds and diminishes, consequently, the

total negative space charge of the sheath. As a result, an overshoot of the electron saturation current occurs due to the fact that the plasma ions do not evacuate instantaneously (recall that $v_b \gg c_s$ from the present experimental data). The duration of the overshoot corresponds to the time ($\tau_s \approx r_s/c_s \approx 0.15 \mu\text{s}$) taken by plasma ions to move with the sound speed ($c_s \approx 2 \cdot 10^5 \text{ cm/s}$) across the sheath region ($r_s \approx 5\lambda_D \approx 0.3 \text{ mm}$). Before plasma ions can move, the positive probe potential strongly penetrates into the plasma and in turn influences the ion beam. While the beam front has propagated toward the probe through potential-free plasma, the subsequent part of the beam propagates into sheath through a decelerating potential. Hence, the ion beam disruption occurs due to the time-of-flight effect and beam density inside the sheath decreases leading the sheath back to its initial unperturbed state. The above mentioned process should continue for the subsequent part of the ion beam. It is necessary to notice that the detailed analysis of the observed instability implies rather complicated dynamics of plasma particles, which require further theoretical investigations.

In conclusion, a new kind of low frequency sheath instability has been observed when nonuniform laboratory plasma is irradiated by a short microwave pulse. The instability with its characteristic frequency lower than the ion plasma frequency is stimulated by a flux of accelerated ions, which is produced by the resonance microwave absorption process. The instability occurs in the sheath of a positively biased electrode due to the sheath collapse and consequent disruption of the ion flux. A simple physical model of the instability process has been suggested. The observed phenomena can occur in both space and laboratory plasmas with non-Maxwellian ion distribution and could contribute to the particle collection process in plasma discharges and active space plasma experiments (including beam injection from rockets and satellites, electrodynamic tethers or RF ionospheric heating).

References

1. *Chen F. F.* In: Plasma Diagnostic Techniques, R. H. Huddleston and S. Leonard, eds. (Academic, New York, 1965).
2. *Nezlin M. V.* Physics of Intense Beams in Plasmas (IOP Publishing, Bristol and Philadelphia, 1993).
3. *Arbel D., Bar-lev Z., Felsteiner J.* et al., Phys. Rev. Lett., 1993, **71**, 2919.
4. *Arbel D., Bar-lev Z., Felsteiner J.* et al., Phys. Rev. Lett., 1997, **78**, 66.
5. *Takayama K., Ikegami H., and Miyazaki S.*, Phys. Rev. Lett., 1960, **5**, 238.
6. *Stenzel R. L.*, Phys. Fluids B, 1989, **1**, 2273.
7. *Dobrowolny M. and Melchioni E.*, J. Geophys. Res., 1993, **98**, 13761; *Samir U., Stone N. H. and Wright K. H.*, J. Geophys. Res., 1986, **91**, 277; *Linson L.*, J. Geophys. Res., 1969, **74**, 2368.
8. *Stenzel R. L. and Urrutia J. M.*, J. Geophys. Res., 1990, **95**, 6209; *Stenzel R. L. and Urrutia J. M.*, Phys. Plasmas, 1997, **4**, 26.
9. *Wong A. Y. and Stenzel R. L.*, Phys. Rev. Lett., 1975, **34**, 727.
10. *Stenzel R. L.*, Rev. Sci. Instrum., 1976, **47**, 603.

**GAS DISCHARGES IN
ELECTROMAGNETIC
WAVE FIELDS
AND OTHER
APPLICATIONS
OF HIGH-POWER
MICROWAVES**

MICROWAVE PLASMA AND ITS APPLICATION

Yu. A. Lebedev

A. V. Topchiev Institute of Petrochemical Synthesis RAS, Moscow, Russia

Basic types of microwave plasma generators are briefly reviewed. The peculiarities of physical processes in microwave plasmas are analyzed (spatial structure of the discharge, electron energy distribution functions, plasma energy consumption, chemical activity of microwave plasma). Self-organization of microwave unbounded plasma is also presented. Different approaches to plasma application for different purposes are analyzed (active plasma zone, afterglow zone and plasma light emission) together with their advantages and disadvantages. Selected examples of microwave plasma application are presented. Potentialities of microwave discharges are formulated.

Achievements in development of microwave generation and techniques created preconditions for application of microwave energy in science and technique, e.g. for generation of gas discharge plasma. Frequencies permitted for industrial, medical and scientific applications: 460, 915, 2450, 5800, 22125 MHz ($\lambda[\text{cm}] = 30/f[\text{GHz}] < 30 \text{ cm}$). Frequency 2.45 GHz is the most spread frequency.

The term "microwave plasma" unites the plasma formations generated in different microwave devices. Such devices (microwave-to-plasma applicators) define relations of external and internal plasma parameters, structure of microwave field, bandwidth, homogeneity and size of plasmas, energy efficiency of plasma generator, values of minimal and maximal plasma consumption. Therefore it is more convenient to consider the "microwave discharges" (microwave plasma in a particular microwave-to plasma applicator) for analysis of application of microwave energy in plasma physics and application. Typical schema of microwave plasma arrangement is shown in Fig. 1.

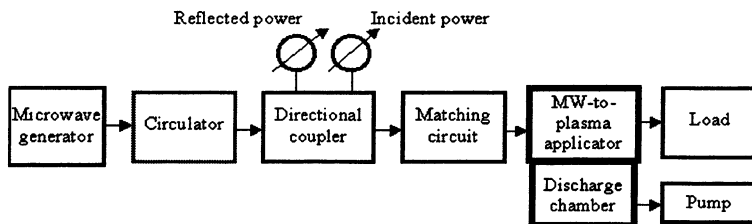


Fig. 1

Microwave discharges have now a strong position in the line of other plasma generators. They used in plasma chemistry, analytical chemistry, gas discharge light sources, etc [1–10]. Properties of microwave discharges and plasmas are considered in all scientific meetings related with plasma physics and plasma technologies. Interest to microwave plasma stimulated carrying out the special-

ized periodical scientific meetings devoted to the problems of microwave plasma. They are the International Workshops "Strong Microwaves in Plasmas" and "Microwave Discharges: Fundamentals and Applications". Proceedings of these Workshops contain a comprehensive information on all aspects of microwave discharges, plasma and application and were the basic of this review.

The review contains a brief consideration of microwave plasma generation, peculiarities of microwave plasma and selected aspects of application of microwave discharges.

Main types of microwave-to-plasma applicators

All designs of microwave-to-plasma applicators can be conditionally distributed into several groups:

- a) microwave cavity plasma generators;
- b) microwave waveguide plasma generators;
- c) surface wave sustained plasma;
- d) slow wave plasma generators;
- e) microwave plasma with distributed energy input;
- f) wave beam microwave plasma generators;
- g) electrode microwave plasma generators;
- h) initiated microwave discharges;
- i) plasma generators with combinations of microwave and other fields;
- j) microwave plasma generators with external magnetic fields.

First two groups can be attributed to so-called plasma "generators with localized discharge zone" where the plasma exists inside the microwave-to-plasma applicator and plasma dimensions are defined by dimensions of the applicator. As usual the characteristic plasma dimensions are less than wave length. To increase the plasma size it is possible increase the wave length or to place the discharge tube along the waveguide. Some examples of *cavity* and *waveguide* plasma generators are shown in Fig. 2, 3.

Microwave fields give the unique possibility to increase the plasma size by using the propagated waves Fig. 2, *c* and radiate structures Fig. 2, *d, e, f*.

Surface waves represent a family of propagating waves. Figure 4 shows two devices for *surface wave sustained plasma* with a discharge generated inside the discharge tube (surfatron) and outside it (duo-plasmaline). Numerous devices from this group produce the plasma in large volumes and over large treated substrates.

Radiate structures are presented by two families of constructions. *Slow wave plasma generators* realize the concept to place a discharge vessel to the field space near the slow wave structure of different configurations. To increase the plasma homogeneity the discharge tube can be places at the angle to the structure. Increase the plasma volume can be provided by use of two slow wave structures ("sandwich" system) as it is showed in Fig. 5.

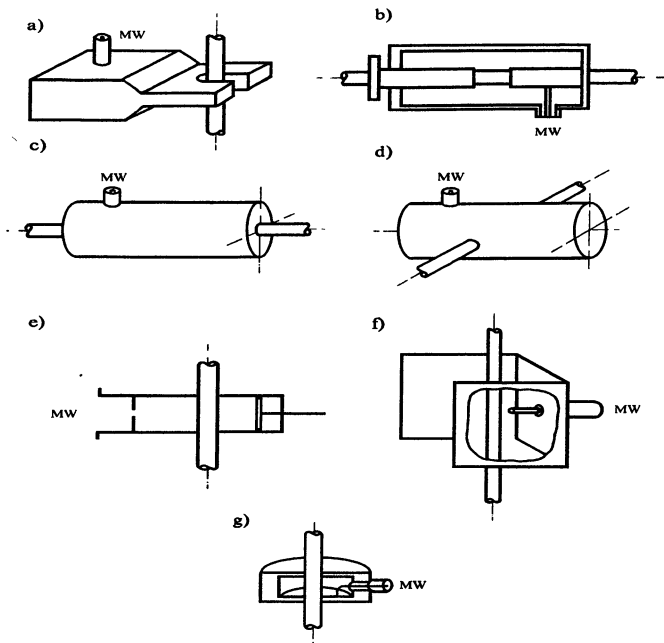


Fig. 2. Microwave cavity plasma generators

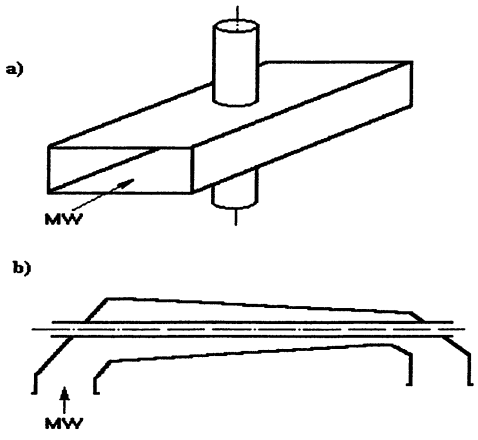


Fig. 3. Microwave waveguide plasma generators

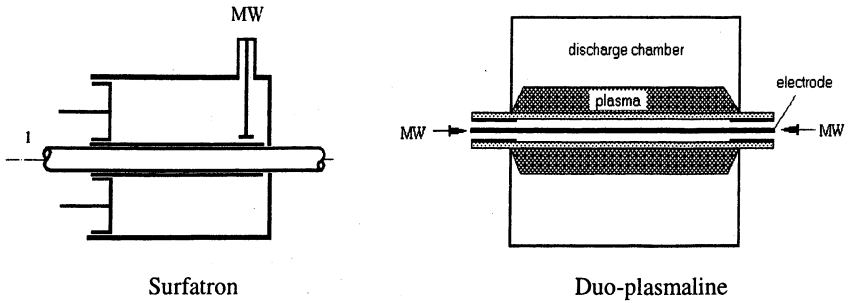


Fig. 4. Surface wave sustained plasma

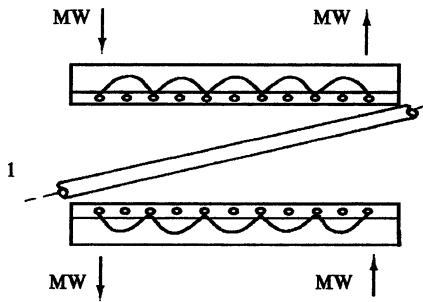


Fig. 5. Slow wave plasma generator

Systems with *distributed energy input* use different types of antennas (waveguide with slots, ring cavity with slots, rod antennas, etc) to introduce microwave energy into discharge vessel (Fig. 6). Coupling elements can be adjusted to produce homogeneous plasma. To provide necessary level of homogeneity the working pressure often should be decreased.

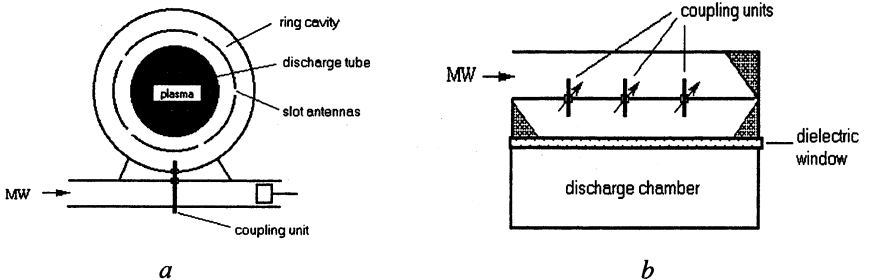


Fig. 6. Microwave plasma with distributed energy input *a* – slotted antennas system (SLAN-System), *b* – rod antennas system.

Microwave beams can produce the plasma in large discharge chambers including the free space (freely localized discharges). Application of quasi-optical systems and crossed beams gives the possibility to generate plasma in the chosen region of space. Displacement of plasma position provides the treatment of large volumes. Minimal role or even absence of walls of plasma container creates conditions for super pure plasma chemistry processes.

All plasma generators considered above realize one of obvious advantages of microwave discharges or the concept of design of discharges without electrodes. It is important because there are no the sources of plasma contamination in the discharge chamber.

But recent experiments with electrode microwave discharge showed that dangerous of contamination in microwave field was overestimated if the microwave power less than several kilowatts. In this condition the mechanism of electrode erosion is related with high energy ion bombardment and is negligible due to small DC accelerated field in the electrode plasma sheath. This is the reason why attention now is paid to *electrode* (Fig. 7) and *initiated microwave discharges*.

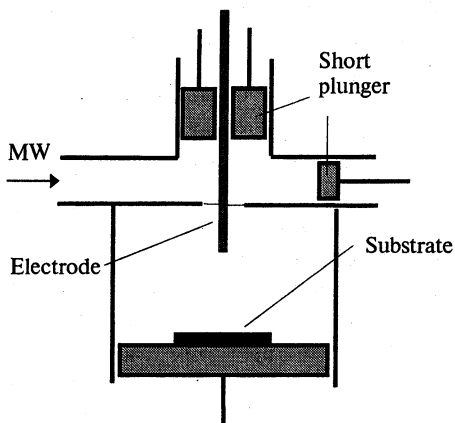


Fig. 7. Electrode microwave plasma generator

Initiated discharges are the discharges which can not exist without initiator at a particular level of microwave power. Additional electrodes, hard particles, ionizing radiation etc can be used as initiators.

Peculiarities of *electrode microwave discharges* are:

- localization of a plasma action region in the chosen position,
 - generation of a plasma active particles just near the treated surface,
 - low maintenance microwave power;
 - absence of a surface pollution by the products of electrode erosion,
 - the area of plasma region is controlled by the electrode shape.
- Initiated discharges* have additional advantages:
- nonequilibrium plasma can be generated at atmospheric pressure. This is important for increasing the plasma process capacity,
 - electric field strength can be adjusted for maximum efficiency of the process. This gives the additional channel of control of plasma chemical activity.

Combined discharges (one example is given in Fig. 8) are used if it is necessary to:

- use the positive properties of each of discharges;
- generate the plasma at power levels insufficient for existence of self-sustained discharge;

- produce plasma with desirable properties (additional possibility of control the plasma parameters, widening of range of variation of parameters, increase of active particle densities, homogeneity, etc);
- increase the stability of plasma system.

Any microwave plasma system can be placed in the *magnetic field* (Fig. 9) to provide:

- matching of plasma device with the microwave power transmitted line;
- realizing of ECR-regime ($f(\text{Hz}) = f_{ce} = 2.8 \cdot 10^{10} B_0(\text{T})$);
- limitation of plasma zone (protection of the walls, dielectric windows from the action of plasma, decrease of the charged particles losses which leads to decrease of microwave maintenance field strength);
- transport of plasma particles to the necessary direction;
- plasma anisotropy.

Figures 2–9 showed only small portion of designed devices. It is clear that special microwave-to-plasma applicator can be designed for any particular application.

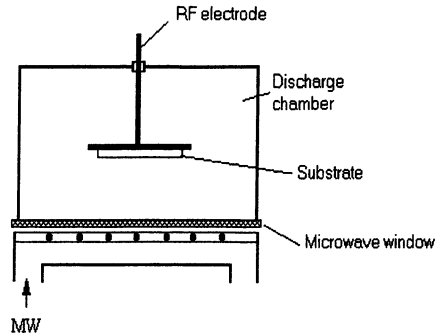


Fig. 8. Plasma generator with combinations of microwave and RF fields.

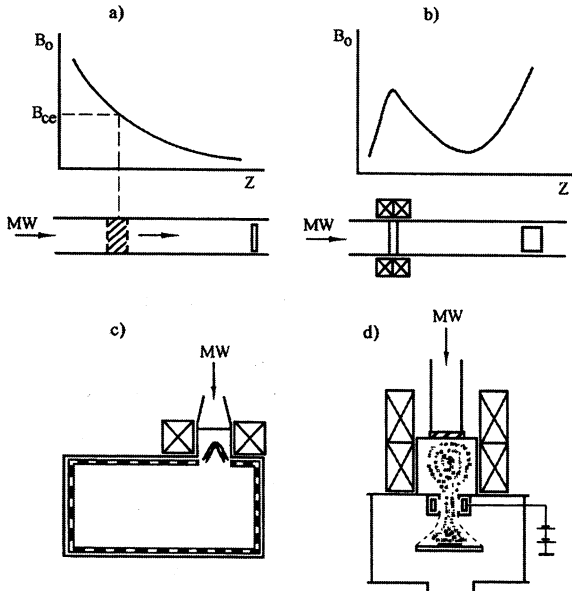


Fig. 9. Microwave plasma generators with external magnetic fields

Peculiarities of microwave plasma

Microwave plasma generators can produce plasma in any gas phase medium at pressures from 10^{-5} Torr to pressure higher than atmospheric one in impulse or continuous wave mode. Plasma densities are ranged between 10^{-9} cm^{-3} and over-critical values ($n_e > n_{ec}$ [cm^{-3}] $\approx 1,24 \cdot 10^{10} f^2$ [GHz]), the average powers are varied between units of Watts up to hundreds of kW. The plasma absorbed power is of 95% of the incident power.

Peculiarities of microwave discharges and plasma are related with peculiarities in the spatial structure of plasma caused by behavior of plasma in microwave field and by peculiarities in kinetics of plasma electrons. Both these factors can define the perspective directions of plasma application.

One of distinct features of microwave plasma is non-uniform electric field strength (e.g., skin-effect). This non-uniformity leads to non-uniform energy input, non-uniform density profiles of electrons and excited particles, non-uniform plasma emission (e.g. displacement of region of maximum plasma emission with increase of the frequency from the center of the discharge to the plasma walls). Non-uniformity of plasma depends on gas pressure, field frequency, plasma size, plasma power.

Both local and averaged over the volume plasma properties of compared discharges having different spatial structures can define the comparative efficiency of the different discharges. This factors should be taken into account when chose the type of discharge.

Light sources is an example of influence of local plasma parameters. E.g., although the intensity of light emission of DC plasma in maximum (axis of plasma) is higher than that of microwave plasma, displacement of region of maximum emission towards the wall in microwave plasma leads to increase output emission (over the walls of discharge vessel) in microwave plasma. This is caused by decrease of the role of self absorption of the emission in microwave plasma.

Plasma chemistry of volume processes is an example of the role of averaged over the volume values in the efficiency of discharges.

The important factor defined the structure of the discharge is the phenomenon of self-organization which was demonstrated in plasma in large plasma containers (plasma dimensions is less than dimensions of discharge vessel). These plasma structures are often ball-shaped at pressures from mTorr to 100 Torr. The physics of these formations is far from complete understanding.

One of advantages of microwave discharges is that they can produce high density plasma without contraction as it takes place e.g. in DC plasma.

Peculiarities of electron kinetics in microwave field can be illustrated by plasma chemical activity. Chemical activity of plasma is the ability of plasma to purposeful influence on chemical components of plasma or on the properties of objects immersed in plasma. Chemical activity of plasma depends on the internal plasma parameters.

Comparative study chemical activity of plasmas started 50 years ago. On the base of investigation of the process of dissociation of different molecules it was stated that microwave plasma have maximum efficiency for this process per unit of absorbed power (R. L. MacCarthy, 1954). This statement is often cited in the literature and for a long time it was a basement for chose of microwave plasma. But question "Why is it so?" was without answer.

To answer the question several problems should be solved. How to compare the discharge properties (or what is the most convenient invariants of comparison)? What plasma parameters define the chemical activity of plasma? How plasma parameters depend on the type of discharge (e.g., on the field frequency)?

These problems were the topics of special analysis and they were solved for energy capacious reactions in quasi-homogeneous plasma of non-equilibrium self-sustained discharges. Only basic results will be given here.

The following set of external discharge parameters seems to be the most convenient for the purposes of plasmas comparison:

- the absorbed powers per unit volume;
- the gas pressure and initial gas composition;
- the wall temperature;
- the dimensions of plasma container (e.g., tube radius).

Plasma chemical activity depends on the rate of processes initiated by electron impact. The rate of the process is defined by product of electron density and rate constant. The last one is defined by the electron energy distribution function (EEDF).

At present it is possible to formulate the general conformity to the natural laws describing the differences of EEDF's in different plasmas (e.g., in DC and microwave plasmas). Self-consistent modeling, the numerical and analytical solutions of the electron Boltzmann equation have shown that major parameter defining the characteristic feature of EEDF's in different plasmas is the shape (the energy dependence) of the electron-heavy particle momentum transfer cross-section $\sigma_{tr}(\epsilon)$.

Although EEDF in microwave plasma has some peculiarities and can be enriched or depleted in high energy region as compared with other discharges (rate constants have the same behavior), the rates of energy capacious processes are the same at the same power consumption in different plasmas. This is the consequence of self-consistency of plasma parameters: change of EEDF leads to corresponding change of plasma density to conserve the plasma absorbed power.

This means that plasma chemical activity of quasi-homogeneous non-equilibrium plasmas are the same at the same plasma absorbed power. But high energy consumption and high electron densities and active particles are provided in microwave plasma much easier than in other discharges.

As plasma power consumption is the parameter defining the internal properties of the plasma it is necessary to not the peculiarity in the nature of this power which appear at pressures less than 20–30 mTorr. Electron gains the energy in

quasi-homogeneous alternating field only in the presence of collisions with heavy particles (Joule heating). In low pressure plasma ($\omega > \nu$) local narrow regions of plasma resonance exist where electric field strength can be high. Additional non-collisional mechanism of heating (acceleration) is realized for electrons crossing this region with thermal energy. This process leads to enrichment of EEDF in high energy region. This effect was registered in experiments.

Application of microwave discharges

Number of publications devoted to different application of microwave plasma are counted by thousands papers. Only several examples will be given below to illustrate potentialities of microwave plasma. Principles of microwave plasma processing are the same as that for other discharges and are shown in Fig. 10. Main area of application of microwave plasma is plasma chemistry.

<p>Conventional method of organization of plasma processing</p> <p>Advantage: high concentrations of active particles</p> <p>Disadvantage: influence of chemical processes on parameters of plasma</p>	<p>ECR reactors with nonuniform magnetic field Discharges with gas dynamic transport of active particles</p> <p>Advantage: plasma parameters independent of chemical processes</p> <p>Disadvantage: active particles losses during their transport to reactor</p>	<p>High intensity light plasma sources (light stimulated chemical reactions, analytical chemistry)</p>

Fig. 10

Microwave plasma is used for decomposition and synthesis of inorganic compounds, e.g. for decomposition and synthesis of nitrogen oxides. Microwave discharges are effective atomizers. Decomposition of H_2O and CO_2 were considered in the frame of the problem of production of energy carriers (production of H_2 and CO).

Decomposition of SiCl_4 in different gas mixtures are used in the processes of forming of half-products for optical fibers with low losses. This process, especially realized at reduced pressures, illustrates advantages of microwaves, related with use of surface waves. The process is based on the deposition of SiO_2 -layers. The profile of refractive index is provided by addition of Ge, B, P, N. Addition of rare-Earth elements produces the active fibers (Fig. 11).

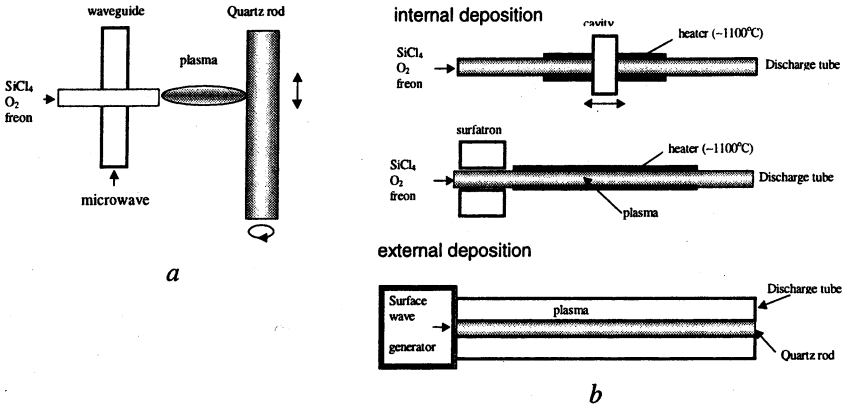


Fig. 11. Processes of manufacture of half-products for optical fibers: *a* – MIP at atmospheric pressure; *b* – MIP at reduced pressures (1–10 Torr).

Microwave discharges in mixtures, contained hydrocarbons are widely used for film deposition (plasma chemical polymerization). It is necessary to mention one direction where microwave plasma keeps a leading position. This direction is diamond growth and deposition of diamond and diamond-like films. The process is usually realized on substrates heated up to 1000°C in the mixture of hydrogen with small quantity of hydrocarbons. High power density and high concentrations of active particles (H-atoms) provides the success of microwave plasma.

Special possibilities inherent to microwaves give application of wave fields. Microwave plasma in wave fields is used for:

- Generation of artificial ionized regions in upper layers of the Earth's atmosphere (e.g., reflectors for broadcast system).
- Cleaning of upper layers of the Earth atmosphere from chlorine- and fluorine containing compounds.
- Recovering of the earth ozone layer.
- Decrease of frontal flow resistance of bodies moving in the air (experiments showed 10% decrease of flow resistance).
- Transmission of energy to the objects on the upper layers of the Earth's atmosphere (generation of plasmas in vacuum near dielectric surface with transformation of microwave energy in direct current – efficiency of transformation is of 20 %).

- Welding of metal and dielectric super fine powders (10–40 microns): microwaves initiate the gas breakdown near the contact points of powder particles at microwave power density higher than 10 kW/cm^2 . This discharge leads to the local heating and welding of particles.
- Design of chemical reactors for super pure processes (free space reactors with small role of the walls). The purity of products is defined by the purity of initial reagents.

New term "plasma catalysis" was introduced into the scientific literature during last decade to describe the phenomenon of increase of the rates of chemical reactions at low temperatures under the action of plasma active particles when plasma energy is a small portion of the total process energy consumption. This phenomenon was demonstrated with strongly non-uniform, non-stationary non-equilibrium plasma of impulse-periodical (0.1–1 μs , 1 kHz) microwave discharge (9 GHz, pulse power 100 kW) in hydrocarbons at atmospheric pressure. The process of hydrocarbon decomposition to soot and hydrogen was studied. Increase of the conversion degree and decrease of the energy cost of products (several times) were shown.

Microwave discharges are used in analytical chemistry. Plasma transforms the energy of external power source to the form which can be effectively transmitted to the compound which have to be analyzed. As usual spectra of emission are registered which gives the possibility to define the compound and its concentration. Good results gave the combination of microwave discharge with gas chromatographic column. This leads to increase of selectivity of analysis as it permits to separate compounds with the same retention time. Although microwave discharges have already used in analytical chemistry, perspectives of this type of discharge are not clear in comparison with widely used RF discharge.

Microwave discharges are used for design of plasma light sources. Investigation and design of powerful sources of UV radiation started in 1973 (Fusion Systems Inc. USA) (Fig. 12). These sources operate in gas medium (noble gases, mercury, halides, etc.) at pressures 1–10 atm, volume power density 100–300 W/cm^3 , surface power density 20–100 W/cm^2 , gas temperature 4000–6000 K, electron density 10^{15} – 10^{16} cm^{-3} , radiation efficiency 40–70%.

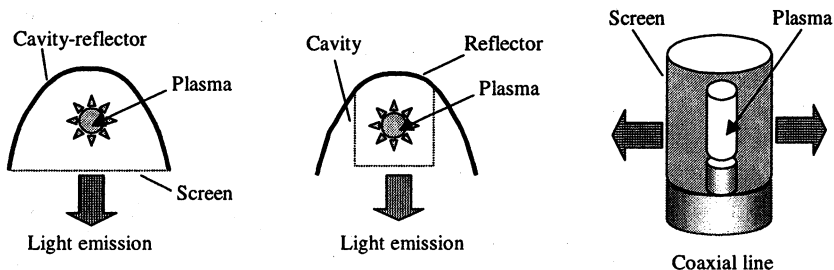


Fig. 12. Configurations of microwave discharges for light sources

Recently interest appeared to gas discharge sulfur-containing lamps. These lamps having the Sun-like spectrum of molecular sulfur (the color rendering index is of 80% – low level of UV and IR radiation in comparison with spectrum of the Sun) were designed in 1992 (Fusion Systems, Inc. USA) and illumination systems were demonstrated in 1994. Argon at pressure of 1 Torr is used as starting gas, microwave power is of 3–4 kW, light efficiency 65–100 lm/W.

Potentialities of microwave discharges

- Plasma can be generated both with high ($>1 \text{ W/cm}^3$) and low ($<1 \text{ W/cm}^3$) specific power consumption;
- Wide region of operating pressures (from 10^{-5} Torr up to pressures higher than atmospheric pressure);
- Generation both quasi-equilibrium and strongly nonequilibrium plasmas;
- Control the internal structure of plasma by change in the design of the microwave-to-plasma applicator;
- Generation of plasma both in discharges with and without electrodes. The erosion of the electrode is absent in the latter case in contrast to DC and RF discharges;
- Generation of plasmas of small and large dimensions, including the free space (e.g., the Earth's atmosphere);
- Possibilities of plasma treatment of large surfaces by scanning the small plasma region over the treated surface;
- Possibilities of combined influence of plasma and microwaves on the treated objects to increase the efficiency of the process.

Summary

Analysis of publications showed that any plasma conditions and any plasma based process can be realized with the help of representatives from the designed family of effective microwave-to-plasma applicators. The most pronounced advantages of microwave plasma can be obtained in the processes which should be carried out in the conditions of high energy consumption, in free space or which should realize the concept of propagate, radiate waves or electrode discharges.

This study was partly supported by RFBR (grant 02-02-16021).

References

1. *Batenin V. M., Klimovskii I. I., Lysov G. V., Troitskii V. N.* Generators of microwave plasma: Physics, Technics, Application. Moscow, Energoatomizdat, 1988 (in Russian).
2. *Dresvin S. V., Bobrov A. A., Lelevkin V. M., Lysov G. V., Paskalov G. Z., Sorokin L. M.* RF and UHF plasmatoms. Novosibirsk, Nauka, Siberian branch, 1992 (in Russian).

3. Microwave Excited Plasmas. Eds. M. Moisan, P. Pelletier. Amsterdam: Elsevier, 1992.
4. Microwave Discharges: Fundamentals and Applications. Eds. C. M. Ferreira and M. Moisan. Plenum Press, New York and London, 1993.
5. Microwave Plasma and its Applications. Ed. by Yu. A. Lebedev. Proc. Int. Workshop on Microwave Plasma and its Applications, 5–8 September 1994, Zvenigorod (Russia). The Moscow Physical Society, 1995.
6. J. Phys. IV France, 1998, 8, Pr7. Proc. III Int. Workshop on Microwave Discharges: Fundamentals and Applications, 20–25 April, 1997, Fontevraud (France), Eds. C. Boisse-Laporte and J. Marec.
7. Strong Microwaves in Plasmas. Ed. By A. G. Litvak. Institute of Applied Physics RAS, 2000. Proc. of the Int. Workshop (August 2–9, 1999). V. 1. P. 271–290.
8. Microwave Discharges: Fundamentals and Applications. Ed. by Yu. A. Lebedev. The United Phys. Soc. of the Russian Federation, Publ. Comp. "Yanus", 2001. Proc. IV Int. Workshop on Microwave Discharges: Fundamentals and Applications (September 18–22, 2000), Zvenigorod (Russia).
9. Plasma Chemistry. Eds. L. S. Polak and Yu. A. Lebedev. Cambridge International Science Publishing (1998).
10. *Brandt A. A., Tikhomirov Yu. V.* Plasma Multipliers of Frequency. Moscow, Nauka, 1974 (in Russian).

ECR ION SOURCES: RECENT DEVELOPMENTS

S. Golubev, D. Mansfeld, S. Razin, V. Skalyga, A. Vodopyanov, V. Zorin, V. Murugov¹, A. Senik¹, A. Kravchenko¹, D. Litvin¹, V. Misko¹, S. Petrov¹, R. Geller², T. Lamy², P. Sortais², T. Thuillier²

Institute of Applied Physics, RAS, Nizhny Novgorod, Russia

¹Russian Federal Nuclear Center – All-Russia Scientific-Research Institute of Experimental Physics, Sarov, Russia

²Institut des Sciences Nucléaires UJF-IN2P3-CNRS, Grenoble, France

The dynamically developing line in plasma physics is related with the perfection of ECR sources of multi-charged ions (MCI). Plasma in ECR sources of MCI is created and heated in mirror magnetic trap by microwave radiation at electron-cyclotron resonance frequency. Actually the reports on the new progress in this field appear every year. At present all modern accelerator centers all over the world are equipped with such ion sources, and significant progress in nuclear physics achieved during last years is bounded with this equipment. However modern requirements to the sources significantly exceed their potential. First of all it is necessary to increase the ion beam current. For this purpose higher frequency and more powerful microwave radiation is used for creation and heating of plasma. This allows to create more dense plasma and thus to increase ion current. The experiments performed in Italy, France and Russia have demonstrated the perspectives of millimeter range gyrotron application for plasma heating in ECR sources of multi-charged ions. The presented work includes the review of recent experimental and theoretical investigations in this field.

Introduction

Pulsed sources of multicharged ion (MCI) beams are widely used in science and technology at present [1]. More than 40 MCI sources of this kind are operating in leading scientific centers of nuclear physics research; new cyclotron accelerators planned to be put into operation are also oriented to utilizing electron cyclotron resonance (ECR) multi-charge ion sources [2]. For a number of applications it is necessary to increase significantly the current of MCI beams. For example for the modernized version of heavy ion accelerator in CERN the beams of multicharged lead ions with advanced parameters (charge 27, current up to 10 e mA, pulse duration 100 μ s, repetition rate 1 Hz) are required [3], which cannot be provided by using traditional sources of MCI. One of the most promising ideas to reach such parameters seems to be related with use of powerful pulsed gyrotron radiation for production of high-density plasma in the mirror trap under electron cyclotron resonance conditions. Indeed, ECR ion sources are most suitable for applications in accelerating facilities, they lead among all other types of sources in complex of parameters and the most important of them is ion current. Ion current is determined mainly by plasma density from which ions are extracted. As it is shown in [4], significant increase of plasma density in ECR

sources is possible only with increase of frequency of pumping microwaves and gyrotrons make it possible.

Using of powerful gyrotron radiation of millimeter wavelength range gives opportunity to perform investigations with high plasma density, high microwave radiation intensities (tens kW per cm²) and to provide high specific power deposition (tens kW per cm³), thus opening prospects to get plasmas with the extreme parameters useful for MCI production.

Classical ECR ion sources use rather complicated magnetic trap for plasma confinement. They are mirror traps with so-called minimum B configuration. The magnetic field in such traps is increased in all directions from its center. This allows to stabilize one of the most dangerous plasma instabilities – magnetohydrodynamic (MHD), causing the plasma ejection to trap walls and thus decreasing plasma confinement time.

The necessity to heat plasma at ECR resonance frequency imposes the value of magnetic field in a trap. The more is frequency of microwave radiation the more should be the magnetic field. Using frequencies above 30 GHz requires application of superconductive coils causing sharp growth of their cost. Thus it seems impossible to produce traps with min B field configuration for frequencies above 30 GHz in the nearest future.

An influence of MHD instabilities becomes lower at high plasma density. An increment of MHD instability is independent on plasma density value and is determined in general by magnetic field configuration. Increasing plasma density in trap leads to the reduction of longitudinal confinement time, that is determined (for classical ECR sources conditions) by electron-ion collisions keeping stable confinement parameter determining the efficiency of MCI generation in plasma. At rather high plasma density the lifetime related with collisions (let us call it useful lifetime) can be lower than time of plasma collapse due to MHD instability, even in the case of using axisymmetric magnetic trap. In other words the longitudinal plasma losses determining ion flow into extractor become higher than transversal ones. This method of MCI generation in the magnetic trap was for the first time demonstrated in IAP RAS where the opportunity of MCI generation in plasma with axisymmetric (without min B) mirror trap was shown at plasma heating on 37.5 GHz [5].

Present paper contains the review of the results obtained in IAP RAS on the investigation of dynamics of plasma creation and MCI generation in mirror magnetic trap at action of millimeter radiation.

The gyrotron was used for the first time to create and heat plasma in a simple mirror trap with aim of multicharged ion formation in 1988 at Osaka University [6]. 60 GHz/50 kW gyrotron radiation launched into plasma trapped in the simple mirror machine. Multicharged ions were registered by vacuum ultra violet emission. Unfortunately these experiments were not continued.

Plasma confinement in a simple mirror trap

Significant increasing of plasma density in the trap can change the mechanism of plasma confinement [7]. Distinction of various regimes of plasma confinement in a mirror trap was studied depending on plasma parameters. Regime of confinement for a plasma with hot electrons and cold ions depends crucially on the ordering of the characteristic timescales such as time $\tau_c = \ln R/v_{ei}$ of Coulomb electron scattering into the loss-cone, time $\tau_T = LR/V_T$ of thermal escape of ions from the trap, and gasdynamic confinement time $\tau_g = LR/V_s$. Here, R and L are the trap mirror ratio and length, respectively, v_{ei} is the electron-ion Coulomb collision frequency, $V_T = \sqrt{T_i/M}$ is the ion thermal velocity, $V_s = \sqrt{zT_e/M}$ is the ion sound velocity, T_i and T_e are the ion and electron temperatures, M is ion mass and z is the average ion charge state. At low plasma density, the slowest of all three processes is that of Coulomb scattering: $\tau_c \gg \tau_T \gg \tau_g$. Therefore, the loss-cone turns out to be essentially empty, and the electron confinement time $\tau_e \approx \tau_c \gg \tau_T$. Accordingly, to retain plasma quasineutrality, an ambipolar field in the trap should retard ion escape. That is achieved by means of ambipolar potential "humps" formed in the vicinities of the magnetic plugs. In this case the ion confinement time can be estimated roughly as:

$$\tau_i \approx \tau_T \cdot \exp\left(\frac{z_i \cdot e \cdot \Delta\phi}{T_i}\right),$$

where τ_i is the confinement time of an ion with charge state Z_i , e is the electron charge, and $\Delta\phi$ is the height of the potential "hump". As the plasma density is increased, the electron confinement time decreases and at some point drops below the time of ion thermal escapes from the trap. Thereafter, the potential "humps" have vanished, and ambipolar field starts contributing to ion expel from the trap ($\Delta\phi$ becomes negative). Due to the frequent ion-ion collisions, the confinement times for different sorts of ions appear to be almost the same, and, thus, equal to the electron confinement time, which is determined by Coulomb scattering:

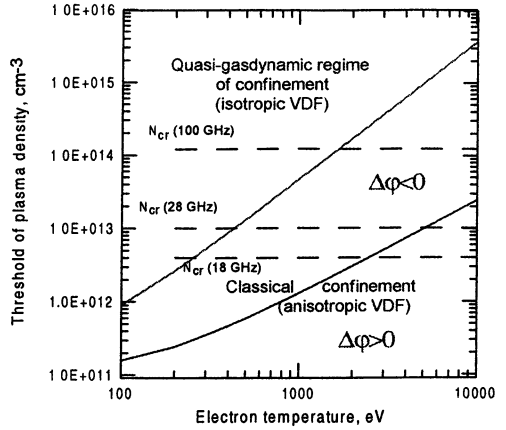
$$\tau_i \approx \tau_e \approx \tau_c,$$

when $\tau_c > \tau_g$, or by gasdynamic processes:

$$\tau_i \approx \tau_e \approx \tau_g,$$

when the plasma density is so high that $\tau_c < \tau_g$. In Fig. 1, according to the argument above, the plane of plasma parameters is split into characteristic regions for three regimes of plasma confinement.

Fig. 1. The borders between the three regimes of plasma confinement.



In order to simulate formation of the ion charge state distribution in plasma, we employ the set of ionization balance equations for ions with arbitrary charge i [8]:

$$\frac{\partial N_i}{\partial t} = (k_{i-1,i} N_{i-1} - k_{i,i+1} N_i) \cdot N_e - \frac{N_i}{\tau_i}.$$

Here, τ_i is the confinement time for an ion with charge state i , $k_{i,i+1}$ is a electron impact ionization rate calculated according to the Lotz formula [9]. Equations for the electron and neutral gas (argon) densities:

$$\frac{\partial N_e}{\partial t} = N_e \cdot \sum_{i=0}^{17} k_{i,i+1} N_i - \frac{N_e}{\tau_e},$$

$$\frac{dN_0}{dt} = I(t) - k_{0,1} N_0 N_e,$$

where $I(t)$ is the rate of gas influx to the trap. The set of equations is completed by the quasineutrality condition:

$$\frac{1}{\tau_e} = \frac{1}{N_e} \sum_{i=1}^{18} \frac{i \cdot N_i}{\tau_i}.$$

The dependence of average ion charge in plasma on the density of electrons at different temperatures was obtained as a result of the numerical simulation (see Fig. 2).

The horizontal area of these functions correspond to the classical confinement regime, rising zone – to quasi-gasdynamic one. This plot looks so because in classical regime the confinement parameter $p_i = N_e \cdot \tau_i$, determining ion charge state distributions, doesn't depend on plasma density, so average ion

charge doesn't vary with its growth. In quasi-gasdynamic regime plasma lifetime doesn't depend directly on N_e , thus p_i grows linearly with growing density and consequently average charge increases (see Fig. 2).

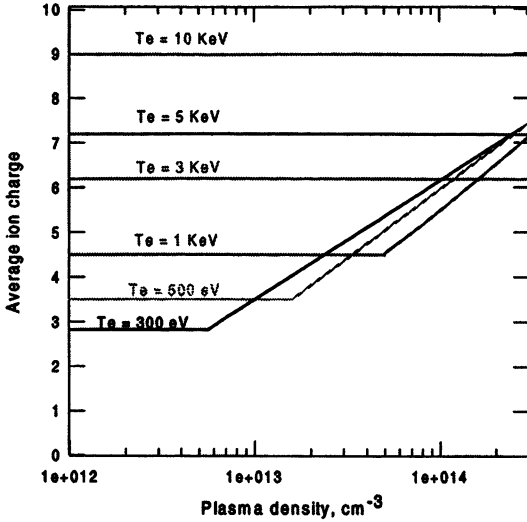


Fig. 2. Dependence of the average ion charge on the plasma density at different electron temperatures.

The total ion current density, carried by the plasma out of the trap along the magnetic field lines, is equal to:

$$J = \frac{N_e L e R}{2\pi_e} \tag{1}$$

The results of the corresponding calculation are shown in Fig. 3.

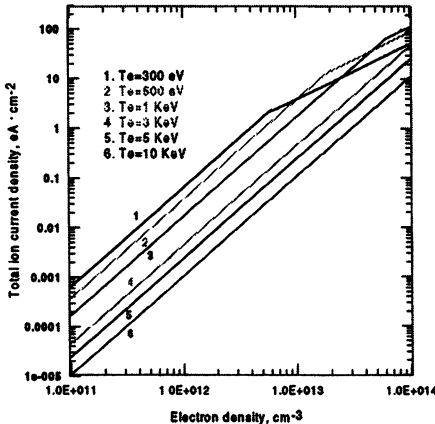


Fig. 3. Dependence of the total ion current density in the plug on the plasma density.

At plasma density of 10^{13} cm^{-3} the ion current density in the plug of the trap can vary from 10 mA/cm^2 to 1 A/cm^2 , depending on the electron temperature. Thus it was demonstrated during this study that in frame of unified approach it is possible to describe qualitatively both the traditional ECR sources pumped at frequencies up to 18 GHz and the sources with very high plasma density using microwave pumping with frequency 37.5 GHz and more.

Experimental setup

All the experiments were performed on the setup with name SMIS-37 schematically presented on Fig. 4. The source of microwaves was gyrotron. Maximum power level was 130 kW, pulse duration was 1.5 ms, and frequency was equal 37.5 GHz. Quasi-gaussian beam of microwaves was focused into the vacuum chamber placed in warm pulsed simple mirror trap. Length of the trap was 25 cm. Mirror ratio was 4. Maximum value of the magnetic field in the trap was

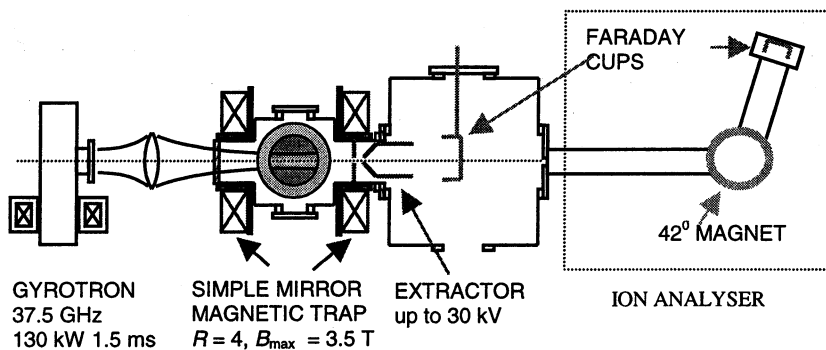


Fig. 4. Schematic presentation of the setup SMIS-37

more than 3.5 T. We used two-electrode quasi-Pierce extraction system for ion beam formation. The extractor was placed into the plug. The diameter of the hole in the plasma electrode was 1 mm. We could apply up to 30 kV of extracting voltage. Extracted beam was analyzed and collected by two Faraday cups. Removable Faraday cup was placed right after the puller electrode.

Experimental investigation of plasma instabilities

Investigation of plasma instabilities is the key point in the investigation of plasma confinement in the magnetic trap. In the result of experiments carried out on SMIS-37 the three types of plasma instabilities were selected.

Near-wall instability. The experimental investigations of the peculiarities of ECR discharge in various conditions allowed to select two different kinds of discharge: volumetric and axial ones. The discharge properties at these stages differ rather strongly. At the axial stage the current of ions extracted from plasma is relatively low (200 mA/cm^2 , see below), but average ion charge is high. At the volumetric stage current density reaches 1 A/cm^2 at average charge close to 1. This section is devoted to the description of reasons of the transition from axial to volumetric discharge.

One of the possible explanations of such behavior is related with the process of ionization in gas excreted from walls of discharge chamber under the action of plasma flow from the trap. Actually the significant increase of gas pressure measured by a vacuum lamp at the discharge evolution confirms the essential gas appearance in the discharge volume that may be connected only with gas entrance from vacuum chamber walls.

The optical image of the plasma in the trap was registered by the high-speed frame-mode CCD camera with shortest exposure duration about $5 \mu\text{s}$. Image corresponding axial stage of the discharge is shown on Fig. 5 (left image). The image remains its appearance during the first stage of the discharge. The typical image of the plasma in the volumetric stage of the discharge is shown on the same figure (right image). In this case plasma consists of several columns, they appear and disappear at different radiuses independently. Lifetime of columns is less than the lowest repetition period of the camera; which equals $10 \mu\text{s}$.

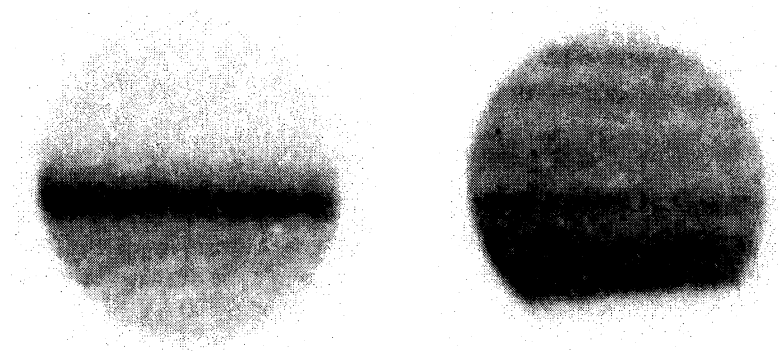


Fig. 5. Typical negative image of the discharge. Left image is in axial stage of the discharge; right image corresponds to volumetric stage.

Such a small rising time of a plasma column discharge requires very intense source of neutrals. Authors suppose process of desorption of the gas from the chamber walls can play an important role. Desorbed neutrals can be taken into account in a simple zero-d model:

$$\begin{cases} \frac{\partial N_e}{\partial t} = k \cdot N_e N_a - \frac{N_e}{\tau(N_e)}, \\ \frac{\partial N_a}{\partial t} = \alpha \cdot \frac{N_e}{\tau(N_e)} - k \cdot N_e N_a + F, \\ \tau(N_e) = 1.5 \cdot 10^4 \frac{T_e^{3/2}}{N_e}, \end{cases}$$

where N_e is plasma density, N_a is neutral density, $T_e = 300$ eV [10] is electron temperature, $k = 2 \cdot 10^{-7} \text{ cm}^3 \cdot \text{s}^{-1}$ is ionization rate coefficient, τ is confinement time, F is neutral gas inlet, α is ion-atom secondary emission factor (desorption). Free path of atoms excreted from the walls before ionization is much less than diameter of the axial discharge, so atoms and ions are trapped into a magnetic tube of certain diameter. Figure 6 shows the calculated densities of neutrals and plasma in time for different α . There are three parts in the curve. First part is ionization process, it lasts up to 100 μs for conditions corresponding to the experiment; there is a quasi-stable flat part of the curve and very drastic increase of the densities to the infinity at finite time – the explosive instability. The duration of the stable part of the curve depends on α (see Fig. 6) and F and this dependence character corresponds to the experiment.

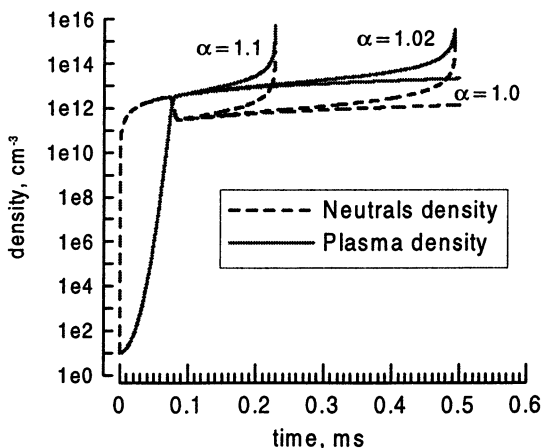


Fig. 6. Calculated neutrals and plasma densities for different desorption factor α

This simple model shows the importance of the desorption process which can lead to an explosive instability of the discharge. This instability can play the main role while "volumetric" stage of the discharge changes "axial".

Whistler instability. Another instability evolving in non-equilibrium anisotropic magnetoactive plasma of ECR discharge and influencing generation of multi-charged ions is related with excitation of Whistler wave modes. The cyclotron plasma instability in the mirror magnetic trap appears when electron distribution over velocities has strongly non-equilibrium group of electrons with high energy; and anisotropic velocity distribution must exist in plasma. The synchronism of fast electrons having high transversal energy relatively to the magnetic field with natural modes of the electromagnetic waves in plasma causes resonance interaction. In the result the energy of fast electrons is transmitted to the electromagnetic waves. This process is accompanied by transfer of high-energy electrons into the loss cone and emptying them out from the trap [11].

The electron energy distribution required for instability evolution is realized at gas ECR discharge in a mirror trap. It was demonstrated in experiments on SMIS-37 setup described in [10] that two components of electron energy distribution exist in such plasma. The first component is the cold electron fraction with isotropic velocity distribution ($T_e \sim 300\text{--}400$ eV, $N_e \sim 10^{14}$ cm⁻³); the second one is the hot fraction with anisotropic electron velocity distribution ($T_e \sim 7\text{--}10$ keV, $N^c \sim 10^{10}$ cm⁻³). The transversal energy of hot electrons is converted into the energy of electromagnetic waves and longitudinal energy of electrons during resonance interaction. In the result the high-frequency electromagnetic radiation comes from plasma and fast electrons pour from the plugs of magnetic trap. Registration of electromagnetic radiation was performed by several coaxial-waveguide-transitions placed outside vacuum chamber near the axis of trap magnetic field. Four registration channels with different frequency bands 2–4.5, 5.4–8.1, 8.2–12.4, and 11.8–17.8 GHz were used. The moveable pin-diode placed 60 cm off the trap center was used for registration of energetic electrons. Pin-diode detected electrons with energies exceeding 7 keV.

It was found that signal received by microwave detector in each registration channel has a form of series of short pulses, while pulsed generation regime exists only in some region of plasma parameters. Studies of fast electrons flowing from plasma have demonstrated that characteristic peculiarities of signals from pin-diodes recording the high-energy electrons are similar to those of microwave detectors.

The experimental investigations indicate the existence of correlation between evolution of plasma cyclotron instability with the efficiency of generation of multi-charged ions in the trap.

MHD instability. The evolution of various spatial plasma instabilities also prevents the effective generation of multi-charged ions in plasma. The pulsations of ion current to the Langmuir probe, current of the extracted ions and signal from photoelectron multiplier proportional to the discharge luminance are evidence of the evolution of these instabilities. The instability evolution is the most evidently seen on the streak camera images of the discharge. Ones of these images are shown on Fig. 7. It is clear from the images that plasma in the trap is

unstable in both cases of axial and volumetric discharge, but timescales differ. In first case it is about 150 μs , in the second case timescale of spatial instability is about 15 μs .

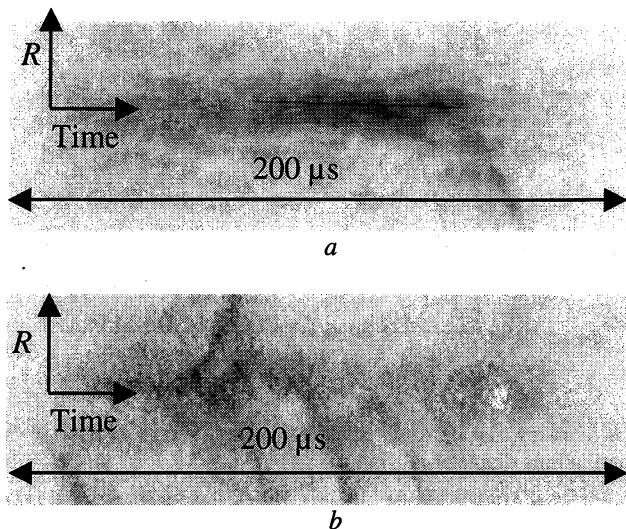


Fig. 7. Negative streak camera images

One can suppose that the ejection of luminescent plasma to the chamber walls is related with MHD instability which evolution violates the uniform discharge combustion. Spatial instability limits plasma lifetime because of transversal plasma losses. The experimental data allow to make rough estimation of transversal lifetime of plasma in the trap, i.e. lifetime related with plasma ejection to the wall across magnetic field. Suppose that the significant fraction of ions is lost at one plasma splash as it is shown on Fig. 7. Then the time interval between two splashes can be associated with the transversal lifetime approximately equal to $\tau_{\perp} = 100\text{--}150 \mu\text{s}$ in case *a* and about 15 μs in case *b*.

Ion extraction

Using gyrotron with frequency 37.5 GHz as a source of microwaves we can obtain plasma with rather high density $\sim 5 \cdot 10^{13} \text{ cm}^{-3}$ and with high flux of the plasma through the plugs. Such dense plasma requires quite high extracting voltage being applied to produce an ion beam with good characteristics. Due to some technical problems it is possible to apply only 30 kV now. It is not enough for a good beam formation. But fine-tuning of the extraction system and control of plasma parameters makes it possible to achieve the result than 80% of extracted

current with flux density of 200 mA/cm^2 (axial stage of the discharge) reaches Faraday cup placed right after the long (33 cm) puller (see Fig. 8).

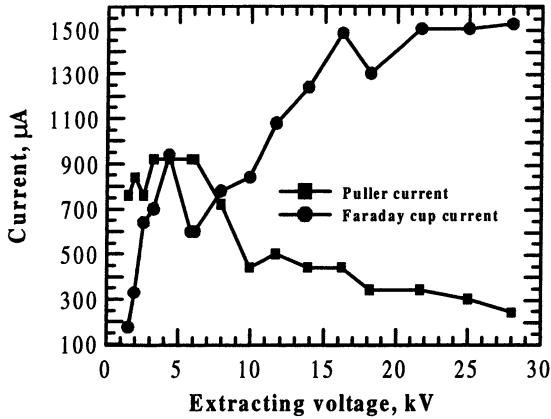


Fig. 8. Faraday cup current and puller current versus extracting voltage. Extracting hole diameter is 1 mm.

First of all such experiments allowed us to estimate the confinement parameter and plasma lifetime related with plasma escape along magnetic field. This flow can be estimated from the relation (1).

The plasma density was estimated by measurements of the transmission factor of diagnostic microwave passing through the discharge. An influence of plasma on the diagnostic microwave radiation is noticeable. This possibly means that plasma density is close to critical value (permittivity is noticeably different from 1). The critical plasma density for diagnostic microwave radiation is $N_e = 1,5 \cdot 10^{13} \text{ cm}^{-3}$. For further estimations we assume plasma density at this stage to be equal $5 \cdot 10^{12} \text{ cm}^{-3}$.

Plasma lifetime in trap and confinement parameter can be estimated from (1). For the axial discharge the ion current density is about $J = 200 \text{ mA/cm}^2$, $L = 25 \text{ cm}$, $R = 4$, $N_e = 5 \cdot 10^{12} \text{ cm}^{-3}$, thus lifetime is $\tau_{ax} \approx 2 \cdot 10^{-4} \text{ s}$. Estimation of plasma confinement parameter determining ion charge distribution gives a value $N_e \tau_{ax} \approx 10^9 \text{ cm}^{-3} \text{ s}$. According to the calculations which have analogy with ones adduced above at this value of the confinement parameter maximum value of ion charge state distribution should correspond to the nitrogen ions $N^{+4} - N^{+5}$, which has been observed in the experiments.

Ion charge state distribution

Figure 9 shows the typical temporal evolution of ion charge state distribution during the microwave pumping pulse measured by ion analyzer with extracting voltage of 15 kV. First 100 μs of the discharge ions of injected gas (nitrogen) with low charges dominate, average charge Z is less than 1.5. Z grows up with time. In a certain time average Z became quite high, maximum in ion charge state distribution corresponds to charge + 4.

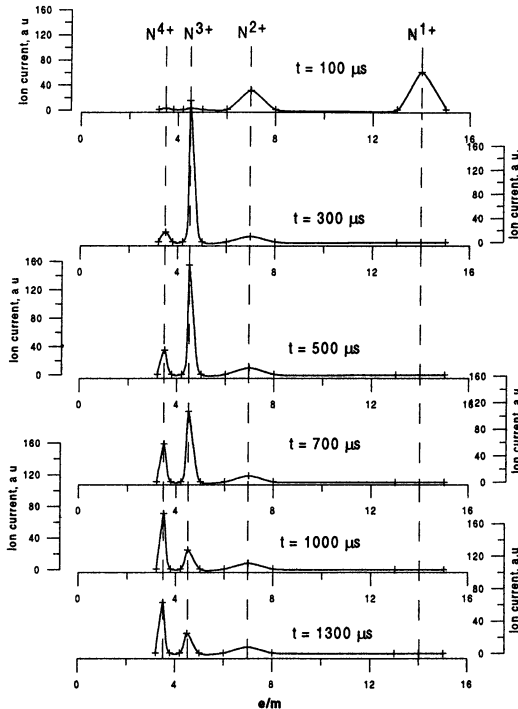


Fig. 9. Experimental distribution of nitrogen ions on the ionization multiplicities in various time moments after beginning of gyrotron pulse.

Conclusions

Thus we have demonstrated the perspectives of using of powerful millimeter-wave range gyrotron for production of multicharged ions with very high ion current densities in a simple mirror magnetic trap.

This work was supported by ISTC Grant 1496, INTAS Grant 01-0373, RFBR Grant 02-02-17092.

References

1. *Geller R.* Electron Cyclotron Resonance Sources: Historical Review and Future Prospects. Review of Scientific Instruments, **69**(3), 1302–1310 (1998).
2. *Sortais P.* General Review of Recent Development for Electron Cyclotron Resonance Ion Sources. Review of Scientific Instruments, **63**(3), 867–872 (1996). D. P. May, ECR ion Sources for Accelerators. Proceedings of International conference of Cyclotrons and their Applications (Caen, France, June 14–19, 1998).
3. *Schindl K.* Ions in LHC and the injector chain. Proceedings of the 14th International workshop on ECR Ion Sources (Geneva, 1999).
4. *Geller R., Jacquot B., and Sortais P.,* Nuclear Instruments and Methods in Phys. Res. A **243**, 244 (1986).
5. *Golubev S. V., Zorin V. G., Razin S. V.* Ion charge-state distribution in a high-power pulsed electron cyclotron resonance discharge sustained by millimeter-wavelength radiation. Technical Physics Letters, **23**(4), 319–320 (1997).
6. *Arata Y., Miyake S., Kishimoto H., Abe N., Kawai Y.* Production of ECR Mirror Plasma by High Power Millimeter-Wave Radiation, Japanese Journal of Applied Physics., **27**(7), 1281–1286 (1988).
7. *Golubev S. V., Razin S. V., Semenov V. E., Smirnov A. N., Vodopyanov A. V., Zorin V. G.* Review of Scientific Instruments, **71**(2), pt. 2, 669–671 (2000).
8. *Semenov V., Skalyga V., Smirnov A., Zorin V.* Scaling for ECR Sources of Multicharged Ions with Pumping at Frequencies from 10 to 100 GHz. Review of Scientific Instruments, **73**(2), Part II, 635–637, 2002.
9. *Lotz W.* Zeit. fur Phys., **216**, 241 (1968).
10. *Vodopyanov A. V., Golubev S. V., Razin S. V., Zorin V. G., Shilov M. A.* Parameters of a plasma of electron cyclotron resonance discharge in an open magnetic trap in a quasi-gasdynamic regime of confinement. Technical Physics Letters, **25**(7), 588–589 (1999).
11. *Bespalov P. A. and Trakhtengerts V. Yu.* The cyclotron instability in the Earth radiation belts, in: Reviews of Plasma Physics. (ed. M. A. Leontovich), Plenum Press, N. Y., **10**, 155–192 (1986).

INTERACTION OF HIGH-POWER MICROWAVE BEAMS WITH METAL-DIELECTRIC MEDIA (PHYSICS AND APPLICATION)

*G. M. Batanov, N. K. Berezhetskaya, I. A. Kossyi, A. N. Magunov,
and V. P. Silakov*

General Physics Institute, Russian Academy of Sciences, Moscow

Results of experimental investigation of powerful microwave beams action on the metal-dielectric compositions are presented. Dielectric surfaces with introduced metallic grains as well as dielectric powder containing small admixtures of a metallic one have been explored as an objects of irradiation. At a relatively small microwave power ($P \leq 1$ mW) all investigated targets were practically completely transparent for incident electromagnetic wave. At a relatively high power (microwave generators based on the gyratrons and powerful magnetrons) the irreversible changes in the electric and radiophysical properties of metal-dielectric composites exposed to microwave radiation whose intensity is below the threshold intensity for plasma production have been observed (sharp increase of conductivity and microwave absorption coefficient).

1. The formation of plasma by irradiating composite metal/semiconductor – dielectric structures with high-power is one of the problems extensively studied in the last years at the General Physics Institute of the Russian Academy Sciences. The compositions used in the experiments are shown in Fig. 1. These are either exposed dielectric surfaces with introduced metal grains of size no more than 1 mm (Fig. 1, *a*) or mixtures of metal (semiconductor) and dielectric powders with particle sizes about 1–40 μm (Fig. 1, *b*).

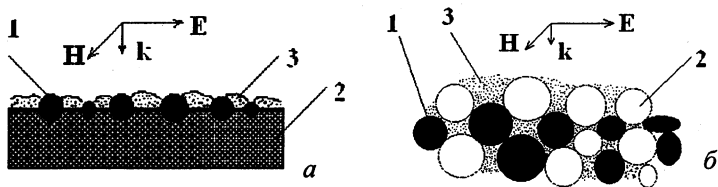


Fig. 1. Metal-dielectric compositions irradiated by powerful microwave pulses: *a* – metallic grains introduced in a surface of a dielectric; *b* – mixture of a fine metal (semiconductor) – dielectric powders. 1 – metallic (semiconductor) grains; 2 – dielectric; 3 – plasma arising in the presence of microwave breakdown of metal-dielectric compositions.

In the version shown in Fig. 1a, metal grains were chaotically distributed over the dielectric surface. Their surface density (the number of grains per 1 cm^2) was low enough, so that conducting paths over the surface did not exist and, when irradiated with low-power microwaves, such targets transmitted radiation

almost completely. However, the experiments [1, 2] showed that, if the beam power exceeded a certain, rather high level, a plasma was produced near the metal-dielectric surfaces. This plasma perturbed the irradiating microwave beam, and the absorption and reflection effects were observed in this case. The threshold intensity for the plasma production depended weakly on the gas pressure and rather well satisfied the relation:

$$\Psi_{thr} \tau_f \geq 0.1 \text{ J/cm}^2, \quad (1)$$

where Ψ_{thr} is the threshold intensity (in W/cm^2), and τ_f is the microwave-pulse duration in (s).

When the metal-dielectric surfaces are in rarified gases or high vacuum, the microwave discharge results in the generation of a high-density collisionless plasma expanding into the surrounding space and filling the chamber [3]. In high-pressure gases ($v_{eff} > \omega$, where ω is the microwave angular frequency, and v_{eff} is the effective frequency of electron – neutral collisions), we observed non-self-sustained microwave discharges excited near the target surfaces, in which case the ionization of surrounding gas was predominantly by ultraviolet radiation emitted from the surface discharge (see [2, 4]).

The microwave discharges on the targets with metal-dielectric surfaces were successfully used at the General Physics Institute in experiments on heating and melting of metal inclusions [2], and also for generating collisionless plasmas in the converters of microwave energy into the energy of dc or ac (at frequencies commonly used in industry) electric fields [3]. It should be noted, however, that the mechanism governing the excitation of a microwave slipping surface discharge and the breakdown on metal-dielectric surfaces is not completely understood now.

Recently, at the General Physics Institute, the experiments have been carried out with thin layers of metal-dielectric powder mixtures (Fig. 1, *b*). The possibility of the plasma production by irradiating such layers with microwave beams was conjectural. First of all, it was not clear whether the mechanisms providing the excitation of a microwave discharge on a free metal-dielectric surface would work in this case. Indeed, the small distance between neighboring powder grains ($\sim 10 \mu\text{m}$) (i.e., the sizes of the pores in the irradiated targets) should result in significant diffusion losses of charged particles and, accordingly, the low probability of the plasma formation in the pores. Nevertheless, the experiments with millisecond microwave beams generated by gyrotrons showed that, above certain threshold intensities, the irradiation of a thin (0.5 mm) layer of a metal-dielectric powder mixture is accompanied by the formation of a plasma, in which case the target, which was transparent to microwaves in its initial state, begins to absorb radiation (see [5, 6]). The breakdown intensity turns out to be much higher than in the case of metal-dielectric surfaces and is determined by the approximate relationship:

$$\Psi_{thr} \tau_f \geq 10 \text{ J/cm}^2. \quad (2)$$

As in the case of the plasma production on free metal-dielectric surfaces, the mechanisms of discharge generation in composite powder mixtures remain to be explored.

The experiments described in this paper are aimed, at the first place, at studying specific features of the processes involved in microwave discharges in metal-dielectric compositions.

2. The experiments were carried out in two testing devices shown schematically in Figs. 2 and 3.

In the Svecha testing device (Fig. 2), a quasioptical system forms a microwave beam acting on a thin layer of a powder mixture. The microwave radiation is generated by a gyrotron at a wavelength of $\lambda_0 = 4$ mm. The microwave power in the experiments was varied from 60 to 240 kW, and the pulse duration ranged from 1 to 10 ms.

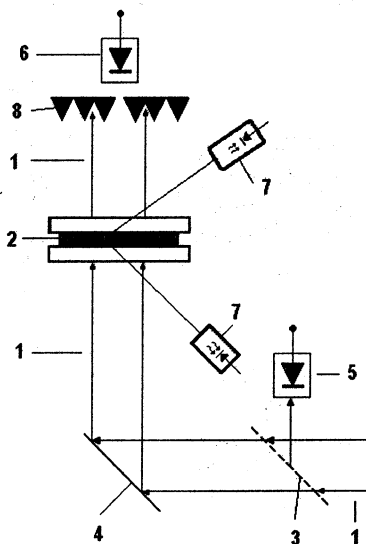


Fig. 2. Schematic of Svecha testing device. 1 - microwave beam; 2 - testing metal-dielectric composition; 3 - quasioptical microwave coupler; 4 - microwave reflector; 5, 6 - detectors of transmitted and reflected microwave radiation; 7 - photodiodes (photomultiplier); 8 - microwave radiation absorber.

A run of experiments on irradiation of metal-dielectric powder mixture layers was carried out also in the GREM testing device (Fig. 3), in which a horn-lens antenna formed a converging microwave beam ($\lambda_0 \cong 2.5$ cm) launched into the chamber. A target containing the layer of some metal-dielectric powder mixture was placed at the beam focus. The intensity of microwaves generated by a MI-389 magnetron [7] in the focal plane did not exceed 5 kW/cm^2 . The microwave-pulse duration was about $5 \mu\text{s}$ and, consequently, was considerably shorter than that in the Svecha device.

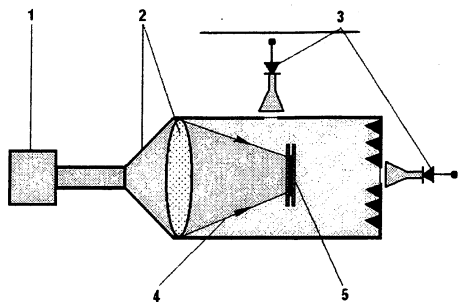


Fig. 3. Schematic of GREM testing device. 1 – magnetron; 2 – horn-lens antenna; 3 – detectors of microwave radiation; 4 – microwave beam; 5 – investigating of metal-dielectric composition.

The target (Fig. 4) consisted of three quartz components: two 1-mm-thick disks 80 mm in diameter and a 0.5-mm-thick ring whose outer diameter was 80 mm and the inner diameter was about 40 mm. The cavity inside the ring between the disks was filled with powder mixtures of different compositions.

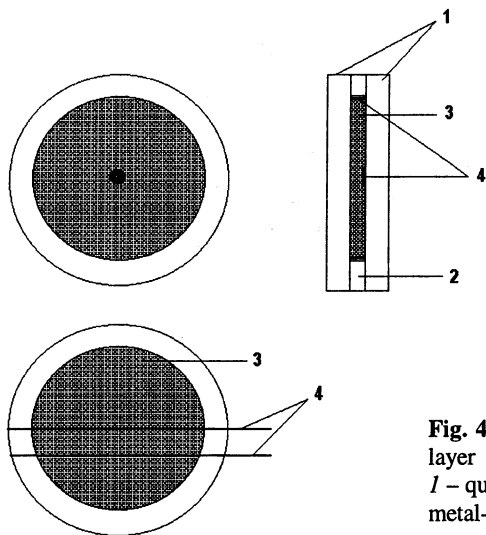


Fig. 4. Construction of target including thin layer of metal-dielectric powder mixture. 1 – quartz discs; 2 – quartz ring; 3 – layer of metal-dielectric powder; 4 – electrodes.

The signals of incident and reflected radiation as well as the total (integrated over the spectrum) glow of the target irradiated with the microwave beam were measured with the help of photomultipliers and photodiodes. The glow spectrum was measured with the help of an Ocean S 2000 spectrograph. The radiophysical properties of the powder layers were measured in a special testing device at a low (~ mW) microwave power.

In most of the experiments, fine-wire (~ 100 μm) electrodes were inserted into the powder layer as is shown in Fig. 4. With these electrodes, we measured the resistance of the interelectrode gap before, during, and after the irradiation.

The average size of powder grains was 1–40 μm). We studied semiconductor (SnO_2 , SnO , CrO_3) and dielectric (Al_2O_3 , PbO , glass) powders and also their mixtures with Al, Fe, Ti, and Si powders.

3. Figure 5 demonstrates typical oscillograms obtained in the Svecha device when irradiating the powder-mixture layer under the scheme shown in Fig. 2. Shown in the figure are the passed and reflected microwave signals, together with the signals from the photodiodes measuring the glow of the target on both sides (on its side exposed to the microwave beam and on the rear). In all of our experiments, the target was in air at atmospheric pressure.

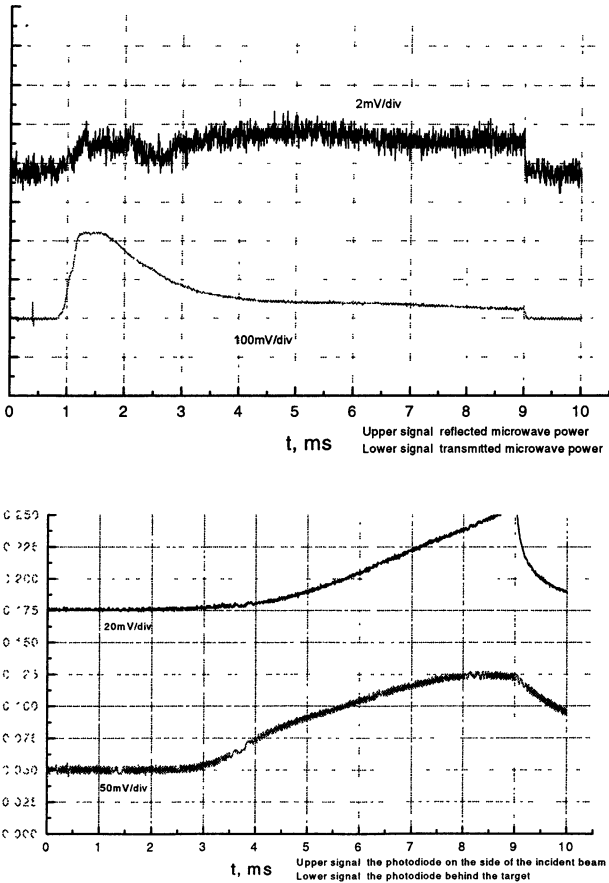


Fig. 5. Characteristic oscillograms. From top to bottom: reflected microwave radiation; transmitted microwave radiation; light detected on the source side of incident microwave beam; light detected on opposite side. Powder mixture Si + PbO (1 : 3).

The attenuation of the passed microwave signal and the appearance of a glow of the irradiated layer is evidence that a plasma is generated in the powder layer. The effect is similar to that observed in [5, 6]. The characteristic form of these oscillograms is identical to the form of oscillograms presented and discussed in [6]. However, we call attention to the peculiarity that has escaped consideration in the previous paper: the passed microwave signal begins to fall well before (about 1 ms early) reaching a noticeable glow of the target. This fact suggests the occurrence of processes setting the stage for the discharge breakdown in the irradiated powder mixture, accompanied by the production of a plasma in the metal-dielectric powder layer.

The results presented in Fig. 5 stimulated the performance of the experiments on studying the pre-breakdown stage in the Svecha and GREM devices. To do this, the duration of the gyrotron microwave pulse was reduced to $\tau_p \leq 2$ ms. As for the GREM device, the maximum pulse duration was always shorter than that required for the breakdown. Hence, all of the results obtained in these experiments refer to the stage preceding the plasma production.

The main experimental results are the following:

(i) On irradiating a metal-dielectric powder mixture by high-power microwave pulses such that the product ($\Psi\tau_p$) is below the threshold level prescribed by relationship (2), the initially nonconducting and microwave-transparent layer becomes conducting and strongly absorbing. The number of microwave pulses required for this transformation depends on the level of microwave power, on the relative content of metal inclusions (the smaller the content, the greater the number of pulses), and also on the material of the powder composition.

Typical results are listed in Table and in Fig. 6. As follows from Fig. 6, when a Ti + Al₂O₃ (1:1) mixture was irradiated in the Svecha device, the resistance of the powder layer between the electrodes inserted into the layer (as is shown in Fig. 4) falls from $R_\Omega \geq 1$ M Ω to $R_\Omega \cong 70$ Ω already in the first microwave pulse. The electric properties of the layer change irreversibly and remain the same after the irradiation ends. Figure 6 also shows how the microwave transmission coefficient of the target (T) depends on the number of pulses. The increase in the steady-state conductivity of the target is accompanied by a considerable decrease in the passed microwave signal. Thus, the experiments demonstrate that a practically nonconducting and nonabsorbing material transforms into the conducting and strongly absorbing state.

Given in Table are typical results of similar experiments conducted with short (≤ 5 μ s) microwave pulses in the GREM device. It is seen that, after irradiating with a sequence of microwave pulses, the remaining reflection coefficient of the target (R) varies only slightly, whereas the transmission coefficient (T) decreases sharply, indicating a substantial increase in the absorption coefficient from values lesser than 0.1 up to nearly 0.5.

Table

Material	R		T		A		R_{Ω}	
	1	2	1	2	1	2	1	2
Al + Al ₂ O ₃	0,1	0,12	0,9	0,39	< 0,1	0,49	> 2 M Ω	2 Ω

1 – before microwave action; 2 – after microwave action.

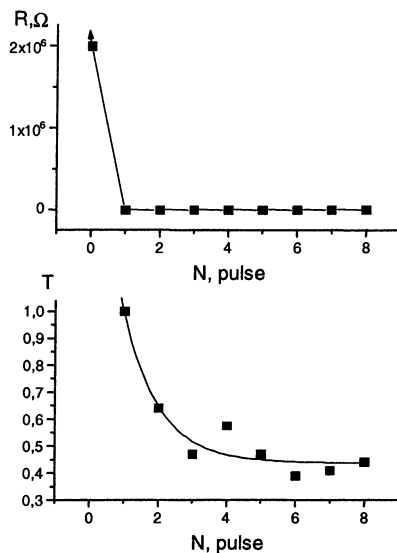


Fig. 6. Interelectrode resistance and microwave absorption coefficient as function of number of microwave pulses (SVECHA testing device).

The effect of irreversible changes in the electric properties of powder mixtures and the transformation of the nonconducting and nonabsorbing layers into the material capable of conducting and absorbing microwave radiation was observed in the Svecha device for the following powder compositions (with the given relative content of the components):

0.2 Al + 0.8 Al₂O₃;

0.3 Al + 0.7 Al₂O₃;

0.4 Al + 0.6 Al₂O₃;

0.5 Ti + 0.5 Al₂O₃;

0.3 Ti + 0.7 Al₂O₃;

0.4 Fe + 0.6 Al₂O₃.

(3)

(ii) In the same microwave pulse in which the steady-state resistance R_{Ω} of the layer dropped, we simultaneously observed an increase in the voltage between the electrodes inserted into the layer (U_p). The voltage reached its maximum during the microwave pulse and fell off in millisecond times. Figure 7 shows typical dependences of the interelectrode resistance and voltage on the pulse number which were obtained in the GREM device. As can be seen, the voltage amplitude U_p is maximum for the pulse involving the change in electric properties of the layer and decreases slowly in subsequent pulses.

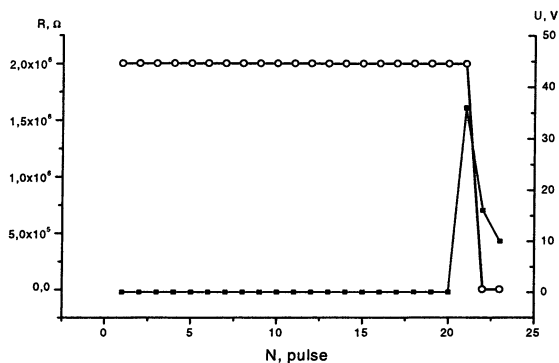


Fig. 7. Interelectrode resistance (\circ) and potential difference between electrodes (\blacksquare) as function of number of microwave pulses (GREM testing device).

(iii) The powder layers listed in (3), when irradiated with high-power microwave beams (even under conditions precluding the excitation of a discharge and the appearance of a plasma), are sources of the invisible, near UV radiation ($\lambda \sim 360$ nm), detected by photomultipliers in combination with filters cutting the visual spectrum. At the same time, the composite powder mixtures show a weak emissivity in the long-wave, visual spectral region. A typical oscillogram of the detected near UV radiation is shown in Fig. 8.

(iv) The increase in the steady-state conductivity of the layer and its microwave-absorption coefficient were independent of whether the electrodes were inserted or they were absent in the irradiated target.

(v) In most of the experiments, the transformation of the nonconducting microwave-transparent layer of a powder mixture into the conducting and absorbing state was not accompanied by any change in the structure of the mixture, which was thoroughly examined visually and under the microscope. However, an interesting effect was observed in the particular experiment in the Svecha device, when we operated with submicron iron grains admixed to a dielectric powder. In this case, we observed a complicated structure containing metal filaments in the powder. The characteristic thickness of filaments is $\sim 1 \mu\text{m}$, i. e., it is close to the size of metal grains in the original mixture.

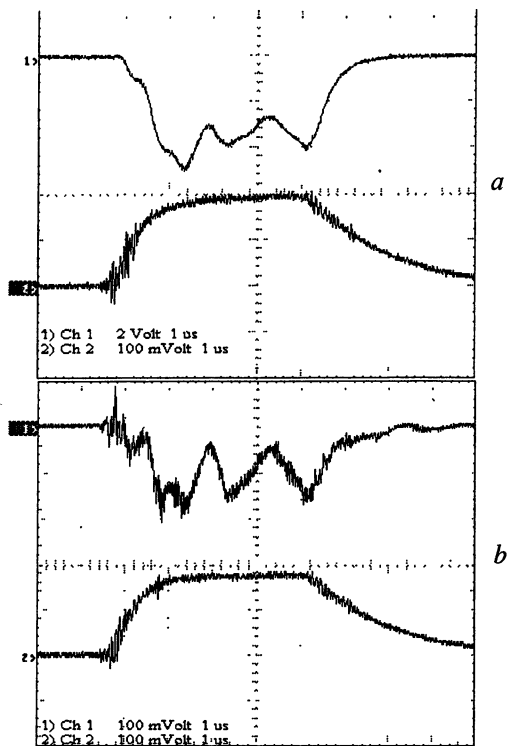


Fig. 8. Characteristic oscillog-ramms of signals from photomultiplier (upper traces in *a* and *b*) recording radiation with λ in range 320–380 nm (2 V/div) (*a*) and radiation with λ in range 450–500 nm (100 mV/div) (*b*). Lower traces in *a* and *b* – oscillogramms from microwave detector.

4. Analyzing possible mechanisms for plasma production on metal-dielectric surfaces and in layers of metal-dielectric powder mixtures, the authors of papers [2, 6] propose that of crucial importance in discharge phenomena may be the injection of electrons from the metal into the conduction band of the dielectric where it is in contact with metal inclusions. The electron emission at the metal-dielectric interface can significantly be enhanced due to two effects: a decrease in the electronic work function of metal and an enhancement of the electric field of the electromagnetic wave on metal grains. We call attention also to the possibility of resonance effects in metal-dielectric media irradiated with microwaves [8, 9]. Such a resonance also provides a significant enhancement of the electric field of the electromagnetic wave in metal-dielectric composites.

Electron injection into the dielectric increases the conductivity of the dielectric in a narrow layer adjacent to the metal; as a result the conductivity of the dielectric reaches a level typical of semiconductors (see [10]). The absorption of microwave power in the dielectric with an enhanced conductivity is accompanied by the heating of dielectric regions around the metal grains. Both the conductivity of the dielectric and the flux of electrons injected into the dielectric from the metal increase as the temperature of the metal-dielectric contact increases. This leads to the development of thermal instability [10] resulting in an explosive energy release in the contact region, which is accompanied by a solid-plasma phase transition.

The studies of pre-discharge stage in fine powder mixtures of metals (semiconductors) and dielectrics which are described in the preceding section, in principle, are consistent with the qualitative model of the phenomenon proposed in [2, 6]. However, as follows from our experiments, the processes occurring at the stage preceding the plasma production are very involved and call for closer and thorough analysis.

Among the effects observed which cannot be described by the relatively simple model considered in [2, 6], we should mention the following:

- The irreversible change in the electric and radiophysical properties of metal-dielectric composites exposed to microwave radiation whose intensity is below the threshold intensity for plasma production;
- The enhanced conductivity in the dielectric regions far from the metal-dielectric interface;
- Invisible, near UV radiation accompanying the action of high-power microwaves on composites;
- A rather high (up to 10–40 V) voltage arising between far regions in the metal-dielectric composite which comes to the conducting state under the action of the microwave pulse.

Apparently, it is necessary to construct a more complicated model than considered in [2, 6]. In constructing a comprehensive model, first of all, it is necessary to take into consideration the solid-state processes developing in metal-dielectric compositions under the action of a high-power electromagnetic wave.

5. The effects discovered in the experiments described in this paper can find application in technological and engineering areas. First and foremost, we should mention the problem of microwave soldering (welding) of dielectric components. This problem can be solved based on the two-stage technology. At the first stage, various layers of mixtures of fine metal and dielectric powders are irradiated with a sequence of short intense (but with the intensity below the breakdown intensity) microwave pulses to produce a "solder" capable of absorbing microwaves. At the second stage, the solder, placed at the interface of the samples to be joint, is heated by cw microwave radiation with a relatively low intensity. Once the melting temperature for the metal components is reached, the samples can be joint. This technological procedure does not include the stage of plasma production. The matter is that excitation of discharge in a surrounding gas is usually accom-

panied by an excess pressure which "pushes away" the processing samples and hampers their soldering (welding).

The effects discovered in this work may be useful in the technique of detecting high-power microwaves, in the problem of converting microwave energy into the energy of dc electric field, etc.

This work was supported in part by the Program "Investigations and Projects in Priority Directions of Science and Technology" for years 2002–2006 and Federal Program "Leading Scientific Schools" (Project 00-15-96676).

References

1. *Askar'yan G. A., Batanov G. M., Berezhetskaya N. K.* et al., JETP Lett., **29**, 648 (1979).
2. *Batanov G. M., Bol'shakov E. F., Dorofeyuk A. A.* et al., J. Phys. D, **29**, 1641 (1996).
3. Generation of Nonlinear Waves and Quasi-Steady Currents in Plasma, Ed. by L. M. Kovrizhnykh (Nauka, Moscow, 1988), Tr. Inst. Obshch. Fiz. Akad. Nauk SSSR, vol. 16.
4. *Batanov G. M., Gritsynin S. I., Kossyi I. A.* et al., Tr. Fiz. Inst. Akad. Nauk SSSR, **160**, 174 (1985).
5. *Batanov G. M., Berezhetskaya N. K., Kossyi I. A.* et al., Zh. Tekh. Fiz., **71**, 119 (2001).
6. *Batanov G. M., Berezhetskaya N. K., Kossyi I. A.* et al., Plasma Phys. Rep., **28**, 871 (2002).
7. MI-389 Magnetron, M., 107120, "Pluton".
8. *Oraevskii A. N., Protsenko I. E., Pis'ma Zh. Eksp. Teor. Fiz.*, **72**, 641 (2000).
9. *Novikov V. V., Wojciechowski K. W.*, Fiz. Tverd. Tela, **44**, 1963 (2002).
10. *Vershinin Yu. N.*, Electric Breakdown of Solid Dielectrics. (Nauka: Novosibirsk, 1968).

RAPID MILLIMETER WAVE ANNEALING OF SILICON WAFERS

*Yu. V. Bykov, A. G. Ereemeev, V. V. Holoptsev, I. V. Plotnikov,
N. A. Zharova*

Institute of Applied Physics, Nizhny Novgorod, Russia

The roadmap for advanced ultra large scale integrated (ULSI) device technology requires the ability to form extremely shallow junctions (< 30 nm) which also have a very low resistance ($< 300 \Omega$). Among the most challenging problems in producing shallow junctions that satisfy down to 0.10 micron technology are

- thermal processing of 300 mm wafers,
- dynamic temperature control that restricts the temperature variation to less than ± 2 °C across the whole surface of wafer,
- rapid thermal annealing (RTA) with ramp-up rates of more than 200 °C/s, so called "spike anneal".

The millimeter-wave heating has a potential to be an alternative RTA technique for the processing of large-size wafers. Results of experiments performed on a gyrotron system at a frequency of 30 GHz have demonstrated feasibility of the spike annealing of 76 mm diameter silicon wafers. The ramp-up rate of 110 °C/s and cooling rate of 165 °C/s have been achieved in the cold-wall cavity of the system at an input power of 4.5 kW. The results of annealing of silicon wafers shallow doped with low energy boron satisfied to the 0.13 micron technology node of the roadmap.

A crude model for microwave heating of wafers in an untuned supermultimode cavity has been developed. The model has been used to calculate the microwave power needed to spike anneal 200 mm and 300 mm silicon wafers and estimate the achievable temperature non-uniformity over the wafers.

Introduction

The development of integrated circuits (ICs) microelectronics within the past three decades gave rise to the ultra large scale integration (ULSI) era by the late 1980s. An increase in memory, operating speed, transistors density, and complexity have been the driving force for ICs miniaturization with major contribution arising due to reductions in such main parameters as gate dielectric thickness, physical gate length and extension junction depth. Today, the semiconductor industry is focused on fabrication of silicon based devices with feature sizes on the order of 100 nm which require junction depth of less than 70 nm, and a host of studies are in progress to identify an ultra shallow junction fabrication method adequate to the sub-100 nm technology generations. The International Technology Roadmap for semiconductors has projected device scaling to year 2014, by which time the minimum feature size are to be 35 nm and chips with more than 10^{11} components are expected to be fabricated [1].

Formation of ultra shallow junction is one of the most challenging problem of the further ULSI development. Despite a decrease in the energy of implanted ions needed to form ultra shallow conductive layer, an ion implantation unavoidably creates numerous defects in the silicon crystalline structure. What is more,

a pre-amorphization of the near surface silicon layer becomes commonly used to prevent ion channelling at implantation. An annealing, or heating of as-implanted Si-wafer to the temperature high enough to enable thermally activated motions of atoms, is used for restoration of crystallinity and electric activation of implanted atoms. It is clear that, even if one manages to implant dopants in a shallow surface layer with thickness of tens nanometers, then, at high annealing temperature, typically slightly over 1000 °C, diffusion will broaden the initial distribution of doped atoms. Due to these competing processes, the demands on the across-wafer temperature uniformity becomes more and more severe as the thickness of junction decreases; non-uniformity should be less than ± 2 °C ($\approx 0.2\%$) for junction depth of 100 nm. Since the processing of wafers with diameter of 300 mm, at least, is considered today as a mainstream manufacturing technology, this appears to be very stringent requirement. So, today much effort of the process designers are focused on the development of methods allowing to achieve a trade-off between putting the dopants in the proper place of the perfect crystalline structure while avoiding their undesirable diffusion.

A rapid isothermal anneal (RTA) using infra red (IR) incoherent radiation appears to be the most promising alternative to a rather slow conventional furnace heating. The use of arrays of IR lamps with the total electric power up to 200 kW allows to conduct the so-called "spike annealing" with the ramp-up rate of more than 200 °C/s and dwell time at the temperature over 950 °C less than 3 second. However, as the recent research showed the progress towards meeting the needs of future technology has come to a standstill, and the combination of implantation and annealing seems to have reached a barrier. The major limitation on the further reduction in thermal budget at IR RTA arises from a failure of increase in the cooling rate of a heated wafer.

The prospects of rapid thermal processing of semiconductors using microwave heating has been discussed by many authors [see, for example, 2, 3, 4]. Both doped and implanted silicon can be heated efficiently with microwaves provided that the sample under processing is properly positioned relative to the electromagnetic field structure of a particular microwave applicator. If a single mode resonator has a high enough quality factor and the resonance condition is maintained, then fairly high heating rates can be achieved. At the same time, the cooling rate can be also large enough, since the walls of microwave applicator normally remain cool and the resonator has no elements at elevated temperature. However, the question about the capability of rapid microwave heating of large size (300 mm diameter and more) wafers with particular emphasis on the required temperature uniformity was left open until recently.

It is well known that a closed-wall multimode cavity fed with millimeter wave radiation appears to be the most attractive in terms of achievable uniformity of the microwave energy distribution at a given level of applied power [5]. Rather uniform microwave energy distribution can be achieved in the microwave cavity if it is designed in a manner that provides simultaneous excitation of many

modes, and a "mode stirrer", which ordinarily is a movable reflector installed in the cavity, displaces the pattern resulting from interference of the electromagnetic fields of these modes. The degree of uniformity increases with the frequency of microwave power, since the number of modes that can be excited in a cavity with the dimension L increases with the ratio L/λ (λ is the wavelength of radiation). When the ratio L/λ is large enough, then the resonance curves of neighboring modes overlap each other. An excitation of modes in such "untuned" resonator depends only weakly on parameters of applied radiation and on the dielectric characteristics of a sample undergoing processing in the cavity. This factor favorably differs the radiation of the millimeter-wave (mm-wave) range ($f \geq 24$ GHz) from the microwaves traditionally used in industrial applications ($f \leq 2.45$ GHz).

This work presents the first results of the feasibility study of using the mm-wave power for RTA of large size silicon wafers.

Experimental

The experiments on anneals of 76 mm diameter Si wafers at a frequency of 30 GHz were performed on the specialized 10 kW gyrotron system for microwave processing of materials. The description of the system was given elsewhere [6, 7].

The output radiation of the gyrotron was converted into a gaussian wave beam in the transmission line and entered the cavity through a microwave transparent vacuum proof window, Fig. 1. The cavity had the ratio of $D/\lambda \approx 43$. The copper cylindrical insert was used to increase the Q -factor of the cavity.

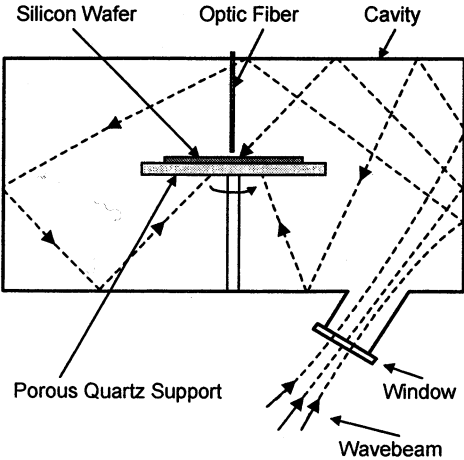


Fig. 1. Schematic diagram of the millimeter-wave heating of silicon wafer in the cavity fed by a wave beam.

A silicon wafer was fixed on a support made of porous fused quartz of very low microwave absorption. The support was rotated by electric motor at the regulated rate of up to 300 rpm. The cavity was evacuated down to a pressure of 10 Pa before microwave processing. The temperature of the top surface of wafer was measured by an Optical Fiber Thermometer (Model M10, Luxtron Corp.). A signal from the Thermometer entered the PC-based control system, which regulated the microwave power produced by the gyrotron. Resolving time of the temperature control, determined by the Thermometer response time, was equal to 0.1 s. Both spike anneals and anneals with a 30 sec holdup time were performed. At spike anneals, the gyrotron was tuned manually so that the mm-wave power applied to the chamber was about 5 kW, and turned-off automatically as soon as the Thermometer reading exceeded the pre-set annealing temperature. The holdup anneals were performed with automatic control of microwave power. In both spike and holdup anneals, the wafer cooled down freely by the radiation loss after the gyrotron was switched-off. The temperature uniformity during anneal was assessed by the results of a series of 4-point sheet resistance measurement in 32 points of the wafer.

Results and discussion

The series of experiments were undertaken to determine the ramp-up and cooling rates, and the uniformity of annealing achievable for the 76 mm diameter Si wafers using the available 30 GHz gyrotron system.

The typical temperature-time profiles for the spike anneal of (100) oriented single-side polished p-Czochralski wafer doped with B, resistivity 17.5–20.0 Ωcm , at two temperatures of annealing are shown in Fig. 2.

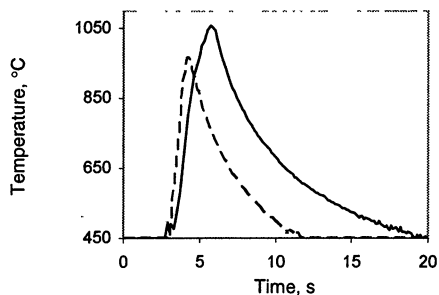


Fig. 2. Temperature-time profiles for spike anneal of 76 mm diameter wafer at the applied millimeter-wave power of 4.5 kW.

For wafer annealed at the temperature $T = 1050\text{ }^{\circ}\text{C}$, the time of heating up from $T = 500\text{ }^{\circ}\text{C}$ to $T = 1050\text{ }^{\circ}\text{C}$ was about 2.4 s, the average heating rate in the range of 950–1050 $^{\circ}\text{C}$ was 110 $^{\circ}\text{C/s}$, and the average cooling rate in the interval of 1050–950 $^{\circ}\text{C}$ was 165 $^{\circ}\text{C/s}$. The total dwell time of the wafer in the temperature interval over 950 $^{\circ}\text{C}$ was about 1.75 s.

The accuracy of maintaining the fixed temperature at the holdup annealing at $T = 900\text{ }^{\circ}\text{C}$ was no less than $\pm 3\text{ }^{\circ}\text{C}$. It should be noted that since a gyrotron processing system is the electronic device which has no appreciable inertia, and its cavity does not contain any microwave heated component, the temperature control could be made much more accurate and faster provided that an instrument with higher speed of response is used for temperature measurement.

An insight into the across-wafer temperature uniformity at annealing can be derived from the data on the sheet resistance in the as-annealed sample. The initial sheet resistance, averaged over the 32 points of measurement, was $478.2\text{ }\Omega/\text{sq}$, with $\sigma = 30.35\text{ }\Omega/\text{sq}$. After the spike anneal at the temperature of $1050\text{ }^{\circ}\text{C}$, the averaged sheet resistance reduced to $109.5\text{ }\Omega/\text{sq}$, with $\sigma = 4.49\text{ }\Omega/\text{sq}$. The sheet resistance averaged over the eight points along the periphery of wafer was $108.9\text{ }\Omega/\text{sq}$, with $\sigma = 3.07\text{ }\Omega/\text{sq}$.

To test the effectiveness of the millimeter-wave technique for ultra shallow junction formation, experiments were conducted on several Si-wafers, beam line implanted with BF_2 or B+ or Plasma Doped with a BF_3 source gas under varying conditions of dose and energy ranging within $0.5\text{--}4.0\text{ keV}$. The initial depths of implants were about $12\text{--}15\text{ nm}$. The samples were then spike annealed to temperatures ranging between $900\text{ }^{\circ}\text{C}$ and $1100\text{ }^{\circ}\text{C}$. All anneals were performed in an uncontrolled ambient at a pressure of residual air about 10 Pa . Then 4-point probe was used for the sheet resistance measurement, and secondary ion mass-spectrometry (SIMS) analysis provided the data on junction depth. The results of anneals are shown in Fig. 3 in terms of the achieved sheet resistance (R_s) – junction depth (X_j) relationship and the boron concentration profile. The junction depth and sheet resistance of a blanket-implanted layer are typically plotted to demonstrate the performance of a shallow junction. As is customary, the junction

depth is taken where the boron concentration determined by SIMS measurement equals 10^{18} cm^{-3} . For comparison, the standard technology benchmark is shown in Fig. 3 as the dashed line. Data points falling to the southwest of this curve indicate an improvement over the benchmark due to either a higher percentage of activated dopants or less dopant diffusion profile. The rectangles show the corresponding technology node requirements.

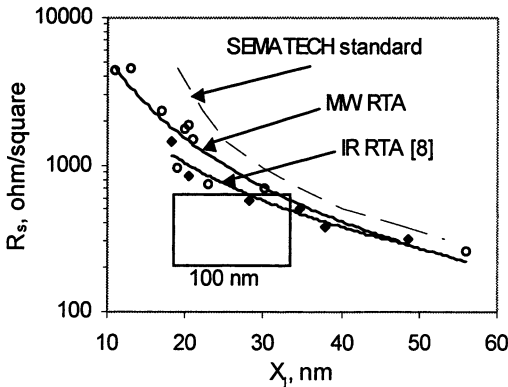


Fig. 3. Sheet resistance (R_s) – junction depth (X_j) curves for boron implanted and annealed silicon samples.

While the sheet resistance values were still rather high, it is important that a sizable fraction of the implanted boron was activated with minimal disturbance of the initial profile. The typical increase in the junction depth due to annealing was about 3–6 nm (Fig. 4).

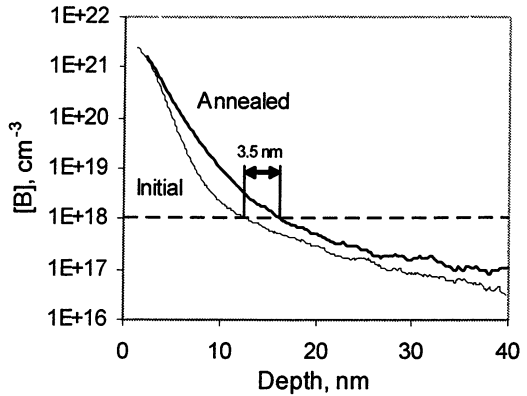


Fig. 4. Boron profiles in ultra shallow implanted silicon samples.

What can be the reason of a rather large sheet resistance, despite a short time of microwave anneal? It must be emphasized that all anneals in this experimental study were performed in uncontrolled ambient and since the implanted layer were very shallow (several tens of the atomic layers) then the significant loss of doped atoms must have occurred, and this loss of dopants should result in a rather high sheet resistance. Also plotted in Fig. 3 are the best known to the date results obtained using the IR lamp technique [8]. These results were obtained by annealing in an oxygen controlled nitrogen purge with optimized heating and cooling rates. It is seen that the results of the very first microwave anneals performed in an uncontrolled ambient and under non-optimized condition correlate well with the best IR results.

Modeling

Acquired experimental data allow developing of the model for numerical simulation of the heating of arbitrary size Si-wafer in a chamber of arbitrary dimension. The goal of modelling is to answer the following questions:

- how much microwave power is needed for spike annealing of silicon wafer of a given diameter,
- what across-wafer temperature uniformity can be achieved at this.

It should be noted that a rough answer to the first question can be easily derived from a simple energy balance approach applied to the heating of a sample in the multimode cavity. We follow below the approach described first by us in [9].

The microwave power applied to the cavity dissipates through three channels: absorption in the walls of cavity, loss through the coupling port, and absorption in the sample. Each channel can be characterized by its quality factor Q . The total Q -factor of the cavity is

$$\frac{1}{Q} = \frac{1}{Q_{ohm}} + \frac{1}{Q_c} + \frac{1}{Q_w}, \quad (1)$$

where Q_{ohm} , Q_c , and Q_w are the Q -factors for the ohmic loss in the cavity walls, the coupling loss, and microwave absorption in the wafer, respectively. Let us suggest that the millimetre-wave power is applied to the cavity as the wave beam entering through an opening in the wall of cavity, as it was in the experiment. For a large cavity with $L \gg \lambda$, assuming that the electromagnetic field fills its entire volume uniformly and neglecting diffraction effects on the coupling port and wafer, the Q -factors are determined as follows [10, 11]:

$$Q_{ohm} = \frac{3V}{2S\delta}, \quad (2)$$

$$Q_c = \frac{8\pi V}{\lambda A}, \quad (3)$$

$$Q_w = \frac{8\pi V}{\lambda(S_w)_{eff}}. \quad (4)$$

Here, V and S are the volume and surface area of cavity, respectively, A is the area of a coupling opening, $(S_w)_{eff}$ is the effective surface of wafer, which depends on the electric conductivity of wafer, and δ is the skin depth in the cavity wall

$$\delta = \frac{c}{2\pi\sqrt{f\sigma_{wall}}}, \quad (5)$$

where c is the velocity of light, σ_{wall} is the conductivity of the wall.

Then, the efficiency of wafer heating, η_w , is the ratio

$$\eta_w = \left(\frac{1}{Q_w}\right) / \left(\frac{1}{Q}\right) = \frac{(S_w)_{eff}}{(S_w)_{eff} + A + \frac{16\pi}{3}S\delta\frac{1}{\lambda}}. \quad (6)$$

Thus, one can roughly estimate the efficiency of microwave energy transfer heating of the wafer of a given size in the cavity of a given dimension, if the conductivity of wafer is known.

In a general case, the conductivity of silicon depends on temperature and doping concentration. However, in the high-temperature region which is of the particular interest for spike annealing (temperature over 500–600 °C), there is practically no difference in the electrical conductivity of intrinsic and doped silicon [4]. At high temperature, the conductivity is high enough ($\sigma \approx 5 \cdot 10^{13} \text{ s}^{-1}$

[3, 4]) to make the approximation of Hagen and Rubens [12] applicable. In this approximation, the reflection coefficient, R , for the normal incidence of a plane wave on the surface is

$$R = 1 - 2\sqrt{\frac{f}{\sigma}}, \quad (7)$$

and the effective surface of the wafer can be estimated as

$$(S_w)_{eff} = k_{abs} S_w = (1 - R) S_w = 2\sqrt{\frac{f}{\sigma}} S_w, \quad (8)$$

averaging over all incidence angles and both faces of the wafer absorbing the incident radiation.

From (6) and (8) we obtain, for the parameters of the experimental cavity, $V = 3 \cdot 10^4 \text{ cm}^3$, $S = 5 \cdot 10^3 \text{ cm}^2$, $A = 12.5 \text{ cm}^2$, $f = 30 \text{ GHz}$, the following partition of microwave energy at the heating of 76 mm diameter Si wafer at a temperature of about 1000 °C: $\eta_w = 0.11$, $\eta_{ohm} = 0.3$, $\eta_c = 0.59$. The portion of energy transferred into wafer heating increases with an increase in the diameter of wafer. At the heating of a 300 mm wafer for the same parameters and conditions, the respective values are the following: $\eta_w = 0.65$, $\eta_{ohm} = 0.12$, $\eta_c = 0.23$.

This approach can be considered valid only for the rough estimate of the efficiency of the microwave energy heating. To gain insight into the temperature distribution over the wafer it is necessary to solve the self-consistent problem that includes equations for the electromagnetic field in the cavity containing the sample and the thermal conductivity equation for the wafer with the heat sources generated by the absorption of microwave energy. It is practical to apply recently developed approximate methods for calculation of the electromagnetic fields inside the multimode cavity whose dimension-to-wavelength ratio is on the order of a hundred [13, 14]. The method developed in [14] has been exploited to calculate the microwave intensity distribution in the cavity with parameters close to the cavity used in experiments. An implicit finite difference scheme was used to simulate wafer heating. Because of the cylindrical symmetry and small thickness of the wafer, the thermal conductivity equation is solved in a one-dimensional approximation.

The experimental data acquired in the anneals of 76 mm wafers were used to provide temperature dependencies of the main specific parameters of the problem – thermal loss from wafer and microwave absorption. Despite the devised model does not go into many details pertinent to Si wafer heating, it is still useful in providing understanding of the dynamics of heating.

The temperature $T(r)$ is obtained from the heat conduction equation

$$hC_p \frac{\partial T}{\partial t} = ha \frac{1}{r} \frac{\partial}{\partial r} r \frac{\partial T}{\partial r} - \varepsilon^* \sigma_0 (T^4 - T_0^4) + P_{abs}(T, r) \quad (9)$$

with the boundary condition

$$\left. \frac{\partial T}{\partial r} \right|_{r=0, r=R_w} = 0. \quad (10)$$

Here, h is the thickness of wafer, R_w is its radius; $C(T)$, ρ , and $a(T)$ are the thermal capacity, density, and thermal conductivity of silicon, respectively; ε^* is its effective emissivity, σ_0 is the Stephan-Boltsman constant, $T_0 = 300$ K is the wall temperature, P_{abs} is the microwave power absorbed per unit square of wafer. In experiment, the wafer is cooled by the radiation from its top surface and by heat loss into and through the porous quartz support. An account of the latter heat loss is a considerable challenge. However, in this model it is circumvented by introducing the effective emissivity $\varepsilon^*(T) = m(T) \varepsilon_{Si}(T)$ ($1 < m < 2$), which is derived from the experimental dependence $\partial T_{exp} / \partial t$ at cooling of wafer, assuming that the emissivity is the same at the heating and cooling stages:

$$hC\rho \frac{\partial T_{exp}}{\partial t} = -\varepsilon^* \sigma_0 (T_{exp}^4 - T_0^4). \quad (11)$$

The wavebeam entering the cavity is represented as a set of rays with intensities specified by the wavebeam angular spectrum [14]. The trace of each ray is calculated with due regard to the attenuation of its intensity caused by absorption in the cavity walls and in the wafer. The rays falling on the cavity coupling port are assumed to be lost. The code calculates the angular spectrum of the radiation intensity incident on both top and back surfaces of wafer. The absorbed power distribution $P_{abs}(r)$ is obtained by summarizing intensities of the incident rays:

$$P_{abs}(r) = \int_{-\pi}^{\pi} P_{inc}(r, \Theta) \cdot k_{abs} \cdot \cos\Theta d\Theta = 2 \sqrt{\frac{f}{\sigma}} \int_{-\pi}^{\pi} P_{inc}(r, \Theta) \cdot \cos\Theta d\Theta, \quad (12)$$

where $P_{inc}(r, \Theta)$ is the incident radiation per a steradian, Θ is an angle of the incident ray with the wafer normal.

The temperature dependence of conductivity, $\sigma(T)$, is determined from the energy balance equation

$$P_{abs} = hC\rho \frac{\partial T_{exp}}{\partial t} + \varepsilon^* \sigma_0 (T_{exp}^4 - T_0^4), \quad (13)$$

in which the data on $T_{exp}(t)$, $\partial T_{exp} / \partial t(t)$ are taken from the experimental anneals carried out at a fixed power applied to the cavity. In these calculations, the dependence $\sigma(T)$, shown in Fig. 5, is obtained as a fitting parameter yielding the value of P_{abs} calculated by the ray tracing method, at each temperature of wafer, consistent with the power provided by the input wave beam. Being supplemented with dependencies $\varepsilon^*(T)$ and $k_{abs}(T)$ the model becomes complete.

It is interesting to note that, in contrast to the data on $\sigma(T)$, presented in [3, 4], the growth of silicon electric conductivity becomes slower at high tempera-

ture ($T > 900\text{ }^{\circ}\text{C}$) according to the experimental results obtained at microwave heating. It looks like the electric conductivity of silicon changes from semiconductor to metallic one at high temperature.

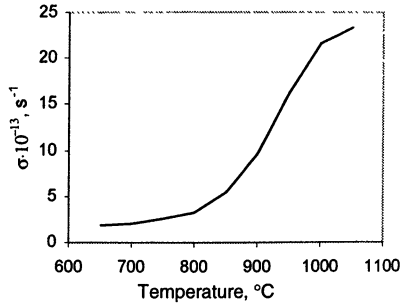


Fig. 5. Microwave electric conductivity of silicon via temperature.

The model was applied first to the simulation of the heating of a 76 mm Si wafer in the cavity used in the experiments for the parameter values close to the experimental ones: the mm-wave input power of 4.5 kW, the ramp-up rate of $100\text{ }^{\circ}\text{C/s}$ and the cooling rate of $150\text{ }^{\circ}\text{C/s}$ in the range of $950\text{--}1050\text{ }^{\circ}\text{C}$. The calculated across-wafer temperature non-uniformity was about $\pm 3.5\text{ }^{\circ}\text{C}$ in this case.

The heating of 200 mm and 300 mm diameter wafers was modelled with due account for the apparent emissivity ϵ_{app} of wafer, which arises from the exchanging of radiation between wafer and the cavity walls,

$$\epsilon_{app} \approx \frac{1}{\frac{1}{\epsilon^*} + \frac{S_w}{S} \cdot \left(\frac{1}{\epsilon_{wall}} - 1 \right)}. \quad (14)$$

Here $\epsilon_{wall} = 0.03$ is the emissivity of unpolished copper wall at the temperature $T_{wall} = 300\text{ K}$ [15].

The calculated temperature distributions over 200 and 300 mm diameter wafer at the maximal temperature of annealing $T = 1050\text{ }^{\circ}\text{C}$ are shown in Fig. 6. As compared with the requirement imposed by the International Technology Roadmap the temperature variation along the radius is less in the case of 200 mm wafer ($\leq 0.2\%$), and slightly higher for 300 mm wafer ($\approx 0.5\%$) even in the cavity of very simple geometry. It is clear that across-wafer temperature profile can be improved considerably in the cavity of optimised geometry. The estimated

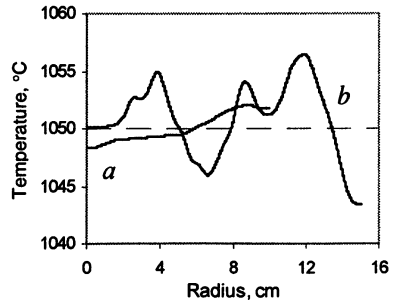


Fig. 6. Temperature profile across 200 mm wafer (a) and 300 mm wafer (b) at the maximal temperature of annealing, $T = 1050\text{ }^{\circ}\text{C}$.

mm-wave powers needed to provide the anneal with the summary ramp-up and cooling rates of 250 °C/s are about 13.5 kW and 50 kW for 200 mm wafer and 300 mm wafer with thickness of 0.8 mm, respectively. It is well known that the mm-wave power of several tens kilowatts is available with the gyrotrons developed to this date.

The partition of the microwave power entered the cavity is shown in Fig. 7 for the annealing of the 300 mm wafer. At the maximum annealing temperature, $T = 1050\text{ °C}$, the mm-wave power applied to the cavity is dissipated as follows: $\eta_c = 0.17$, $\eta_{ohm} = 0.11$, $\eta_w = 0.72$. It should be noted that the cited above rough estimates for the power breakdown are in a good agreement with the results obtained by numerical simulation.

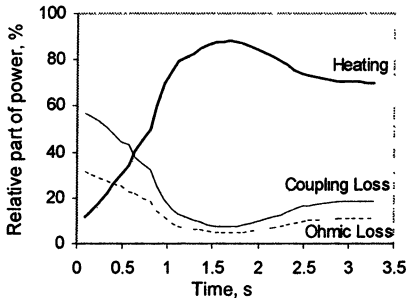


Fig. 7. Partition of microwave power between the heating, coupling loss and ohmic loss at annealing of 300 mm diameter wafer.

Conclusions

Results of experiments performed on a gyrotron system at a frequency of 30 GHz have demonstrated feasibility of the spike annealing of 76 mm diameter silicon wafers. The ramp-up rate of 110 °C/s and cooling rate of 165 °C/s have been achieved in the cold-wall cavity of the system at an input power of 4.5 kW. High across-wafer temperature uniformity was provided due to heating in the supermultimode microwave cavity. The results of annealing of silicon wafers shallow doped with low energy boron satisfied to the 0.13 micron technology node and compared well with the best results obtained with the infrared RTA. An improvement of the anneal results may probably come with better controlled and more rapid heating, optimized anneal temperatures, and with anneals in a controlled ambient.

Numerical simulation of microwave heating, based on experimental data on anneals, proves the high potential of the millimeter-wave RTA of 200 and 300 mm wafers using the gyrotrons available today.

Acknowledgements. The authors are grateful Keith Thompson of Madison-Wisconsin University, USA, for presenting the ultra shallow doped silicon sam-

ples and SIMS measurements, to Vladimir Skupov for sheet resistance measurements and Vladimir Semenov for useful discussions. This research was made possible in part by award № RE1-2065 of the U.S.A. Civilian Research and Development Foundation, and by grant № 00-02-17318 of the Russian Foundation for Basic Research.

References

1. International Technology Roadmap for Semiconductors, SIA (San Jose, CA , USA), 2001.
2. *Chenevier P.* et al., *J. Physique-Lettres*, 1982, **43**, L-291.
3. *Covas M.* et al., *J. Phys III France*, 1993, **3**, 973.
4. *Zhang S.-L.* et al., *Thin Solid Films*, 1994, **246**, 151.
5. *Janney M. A.* et al., *Mater. Res. Soc. Symp. Proc.*, Pittsburgh PA, 1991, **189**, 215.
6. *Bykov Yu.* et al., in *Microwaves: Theory and Applications in Material Processing III* (Am. Ceram. Soc., Westerville), 1995, 159.
7. *Bykov Yu.* et al., in *Proc. of 29th European Microwave Conference* (Munich, Germany), 1999, **1**, 123.
8. *Lerch W.* et al., in *Proc. of the Electrochemical Society* (2001).
9. *Bykov Yu.* et al., *Proc. of 9-th Int. Conference on Advanced Thermal Processing of Semiconductors – RTP 2001* (Alaska, USA, 2001), 190.
10. *Lamb W. E.*, *Phys. Rev.*, 1946, **70**, 308.
11. *Llewellyn-Jones D. N.* et al., *IEE Proc.*, 1980, **127(A)**, 535.
12. *Born M., Wolf E.*, *Principles of Optics*, Pergamon Press, 1968.
13. *Feher L.* et al., in *Mater. Res. Soc. Symp. Proc.* (Pittsburgh PA, 1996), **430**, 363.
14. *Semenov V. E.* et al., in *Proc. of 7-th Int. Conference on Microwave and High Frequency Heating* (Servicio de Publicaciones UPV, Valencia, 1999), 57.
15. *Izluchatel'nye svoistva tverdykh materialov*, Ed. A. E. Sheindlin, Moskva, Energia, 1974 (in Russian).

THIRD GENERATION ECR ION SOURCES

L. Celona, S. Gammino, G. Ciavola

INFN-LNS, Via S. Sofia 44, 95123 Catania, ITALY

The future accelerators need higher charge state and higher current beams from the ion sources. This demand will be met by the "third generation Electron Cyclotron Resonance Ion Sources" (ECRIS) which will make use of improved plasma confinement by means of higher magnetic field and of higher microwave frequency, thus boosting the performance of nowadays ECRIS operating at the frequency of 14 and 18 GHz. The possibility to obtain confining fields exceeding 4 Tesla, by means of special design of NbTi superconducting magnets, open the way to a new operational domain, at the typical frequencies of gyrotrons, above 28 GHz, with plasma densities never achieved before in ECRIS (10^{13} cm^{-3} and higher). The test of SERSE at 28 GHz, confirming the theoretical frame on which the third generation ECR sources design is based, will be presented, and a review of the new generation ECRIS will be presented, with a particular emphasis on the design of the GyroSERSE source.

At many large accelerator facilities there is a strong need of higher injection currents of highly charged ions, up to 1 mA for heavy ions with charge states above 25+ (both pulsed and cw mode). At INFN-LNS the ultimate goal for nuclear science is to produce between 0.5 and 2 μA of U^{60+} (cw mode) and other heavy ions to increase the energy of the beam extracted from the superconducting cyclotron (the advantage of coupling a 3rd generation ECRIS to an accelerator is clearly shown in Fig. 1). A similar advantage can be obtained by any other accelerator facility based on a linac or a cyclotron, and particularly relevant is the gain for the future accelerator facilities as LHC in Europe and RIA in US which needs currents of a few hundreds μA or even thousands (over a long term period the next project of GSI need 6 mA of highly charged heavy ions as Pb^{25+} [1]).

Another requirement of the future RNB facilities based on a linac or cyclotron post-accelerators is to have an efficient charge breeding process ($1^+/N^+$ transformation) in order to obtain high charge states ($Q > 20^+$) with a high ionisation efficiency ($> 20\%$) on a single charge state.

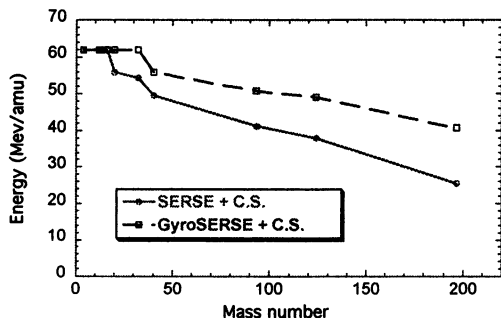


Fig. 1. Maximum energies achievable from the K-800 superconducting cyclotron of INFN-LNS with the best existing ECRIS and with the 3rd generation ECRIS, GyroSERSE.

In 1999 a research project funded by European Union and called "Innovative ECRIS" was established to meet all these requirements. Some tests were carried out with a high frequency-high power (28 GHz – 10 kW) microwave transmitter coupled to the superconducting source SERSE at INFN-LNS [2, 3].

The results were outstanding and beam intensities never obtained before were measured. Anyway we perceived that with an adequate source design more intense beams can be obtained. The successful exploitation of the SERSE source at 28 GHz opened the way to the GyroSERSE source, a high confinement superconducting source optimised for 28 GHz and designed following the scaling laws [4] and the high B mode concept [5].

Test of scaling laws from 2.45 GHZ to 18 GHZ

In 1987 from the results of the MINIMAFIOS source at 10 and 16.6 GHz, Geller inferred the scaling laws [4] which were for a few years the guiding line for ECRIS designers and users:

$$q_{\text{opt}} \propto \log B^{3/2}, \quad (1)$$

$$I^{q^+} \propto f^2 M_i^{-1}, \quad (2)$$

where q_{opt} is the optimal charge state, B is the peak field of the magnetic trap, f is the microwave frequency, I^{q^+} is the intensity of the charge state q and M_i is the ions mass.

During the following years different sources gave results which placed into crisis the statement that simple scaling laws exist and a more complicated framework was revealed.

A series of experiment carried out on the SC-ECRIS at MSU working at 6.4 GHz changed the ECRIS scenario, because this source was able to deliver ion currents exceeding the best 10 and 14 GHz sources and of the same order as the 18 GHz MINIMAFIOS. These results have been explained by the so-called High-B-mode concept [5] which state that by increasing the confining field the ECR sources work better because of higher electron densities and temperature. This concept does not conflict with frequency scaling, but it limits the benefits of frequency scaling to the sources with a very high confining field. This concept can be expressed in term of the mirror ratio:

$$B/B_{\text{ECR}} > 2, \quad (3)$$

where B_{ECR} is the magnetic field corresponding to the ECR frequency.

In 1998 and 1999 extensive tests to validate the scaling laws at 14 and 18 GHz have been performed on the SERSE ion source at INFN-LNS.

Figures 2 and 3 show confirmed the validity of formula (3) [6, 7] for frequencies between 2.45 and 18 GHz. Except for the lower frequency, the curves are quite similar and however all of them obey to the High B mode concept. The tests described in details in [6, 7] outlined the rules that an efficient ECRIS must

follow to produce intense beams of medium and high charge states and that have been recently defined as the ECRIS standard model [8]:

- a) the last closed iso- B surface must have $B_{last} \approx 2B_{ECR}$;
- b) optimum radial magnetic field value at plasma chamber wall is obtained for $B_{rad} \geq 2.2 B_{ECR}$ (Fig. 2);
- c) axial magnetic field value at injection must be $B_{inj} \approx 3B_{ECR}$ or more (Fig. 3);
- d) axial magnetic field value at extraction must be $B_{ext} \approx B_{rad}$ (Fig. 3);
- e) axial magnetic field value at minimum $0.30 < B_{min}/B_{rad} < 0.45$.

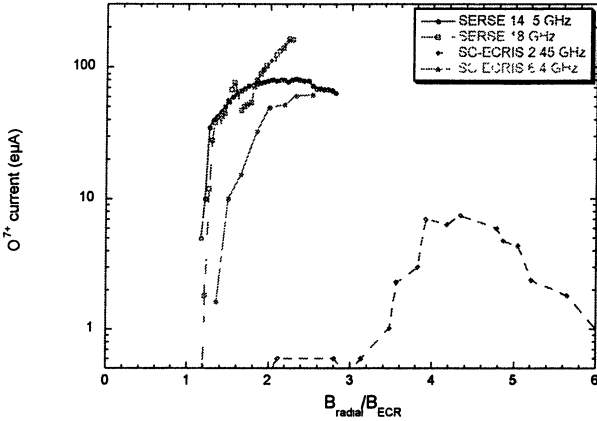


Fig. 2. Effect of radial magnetic field scaling on O^{7+} current [7]

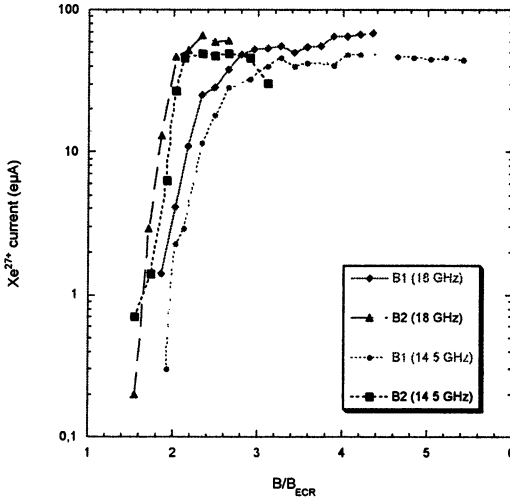


Fig. 3. Xe^{27+} currents for 14.5 and 18 GHz operations vs the axial field on the injection side (B_1) and on extraction side (B_2) [7].

Summary of the tests of SERSE with a 28 GHz gyrotron

In order to define the best parameters for future ECRIS, experiments have been performed with SERSE, the fully superconducting source installed at LNS Catania. It was the first time that this high frequency has been launched into a minimum- B structure and the first part of tests was devoted to the study of the RF coupling and RF power efficiency. This parameter has a paramount role on the high charge states buildup, as the electron temperature is dependant on the rf power and the injection of a few kW (about 1 kW/L) in the chamber is needed to boost the electron temperature to the keV order of magnitude.

On the other hand, the adequate strength and shape of the magnetic field in the B -minimum trap ensure a longer lifetime of the hot electrons that increases the possibility to remove the electron of the inner shells.

The electron confinement is strictly correlated to the magnetic structure of the source and the beam intensity I_{ext} to the magnetic confinement and to the ion density n_i^q

$$I_{ext} \approx k \frac{n_i^q q e}{\tau_i^q}. \quad (4)$$

An increase of n_i^q is needed to enhance the performance of any ECRIS. This increase can be obtained through the increase of the microwave frequency, as confirmed by many experiments [6, 7].

A rough picture can be the following: if we are looking for high current of medium charge states, a not so high confinement time is requested, because we want that the plasma density be high, but the electron confinement time be relatively low, to get a high flux of ions from the extraction hole; if we are looking for highly charged ions, a very good trap is needed, and high frequency and high magnetic field at the same time are needed, which is the basis of the High- B -mode concept.

In particular, the superconducting ECRIS of the INFN-LNS, SERSE, has been used at 14, 18 and 28 GHz with increasing performance, even if for the latter case the magnetic field was not the optimum one. The 28 GHz operation, indeed, permitted to get currents exceeding half mA of Xe ions with charge states up to 25+, as well as some μ A of charge states between 38+ and 42+, results which have been never obtained by any other source [2, 3]. For the tests of SERSE at 28 GHz, a 10 kW gyrotron has been used, but only 2 to 4 kW were used in cw mode. The maximum power launched into SERSE was limited by the plasma chamber cooling efficiency which was originally calculated for a maximum power of 2.5 kW at 18 GHz. In the afterglow mode, 6.5 kW has been launched at 10 Hz repetition rate. A more detailed presentation of the RF propagation and coupling is presented in [2].

Taking into account the RF power launched into an ECRIS per volume unit of the ion source, about 800 W/l are necessary for an optimised source running in

cw mode (Fig. 4) while 1.2 kW/L is needed in the afterglow mode [9]. Figure 4 shows that SERSE, the today best performing ECRIS, could deliver larger beam intensities at 18 GHz if more RF power would be used. On the other hand, the performances obtained at 28 GHz were not limited by the RF, but by the magnetic configuration and by the extraction limitations. In this case, the presence of space charge effects and emittance blow-out have reduced by a factor three, presumably, the extracted current.

This latter limitation deserves more investigations in future, whereas for the former one, the picture is quite clear.

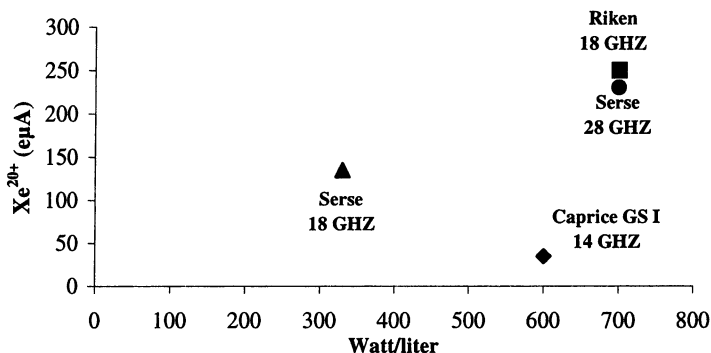


Fig. 4. Beam intensity as a function of the rf power per volume unit for different ECRIS in cw mode.

The role of the axial magnetic profile has extensively been described in literature [6, 7]. Whatever the frequency heating, the magnetic field value must be as high as possible on the injection side while the value at the extraction side is correlated to the radial magnetic field value.

The radial confinement has also a major influence in the beam production for medium and high charge states as well. Fig. 5 presents Xe^{20+} intensity variation with the radial mirror ratio (B_{rad} / B_{ECR}) at 18 GHz and 28 GHz. The 2nd Y-axis is proportional to the main Y-axis by the square of the frequency, then one can notice the remarkable superimposition of both curves in dc mode.

The technological limit for the SERSE radial magnetic field being 1.45 T, one can easily extrapolate the possible beam intensity at the optimum radial mirror ratio: between $R = 1.45$ and $R = 2$, a 75% gain is possible while keeping the other parameters constant.

Figure 6 shows a nice picture of the validity of the frequency scaling [9]. Furthermore, this figure also shows that the frequency scaling is valid whatever the confinement: beam intensity is related to n_e then to ω_{ce}^2 , so that the different curves are more or less superimposed.

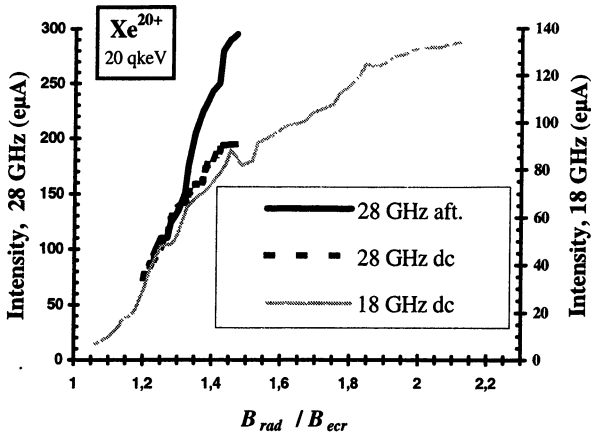


Fig. 5. Effect of radial magnetic field scaling on Xe^{20+} current [2]

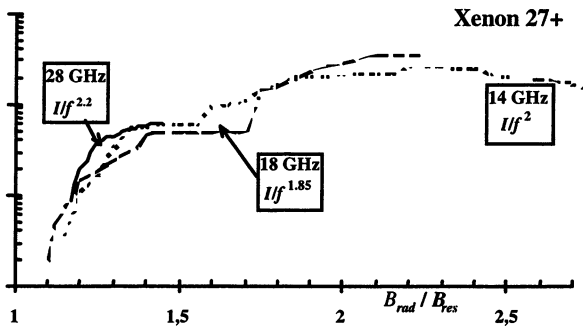


Fig. 6. Effect of radial magnetic field scaling on Xe^{27+} current, normalized to f^2

The state of the art

In 1994, at INFN-LNS a design study of an ECRIS operating at 28 GHz was carried out. This project was frozen because the technology needed to the construction of a 3 T hexapole was not available at that time. In 1995 a proposal of a similar source has been done from LBNL, but with a significantly lower magnetic field, because of technological limits. The VENUS project started in 1997 and after a long construction phase, it got its first plasma on May 2002 at 18 GHz only. In 1999 after the successful exploitation of the SERSE source at the frequency of 14 and 18 GHz the GyroSERSE project was reconsidered, because the possibility to obtain confining fields above 3 Tesla in the plasma chamber, by

means of special design of NbTi superconducting magnets, became realistic. In the meantime the "Innovative ECRIS" collaboration was established with the aim to enhance the performance of ion sources. In this framework the tests at 28 GHz with the sources SERSE and PHOENIX were carried out. The SERSE 28 GHz tests are described in the previous paragraph, while the PHOENIX tests [10] confirmed the validity of a different approach well suited for pulsed operations and for the production of high intensity of medium charge state ions, but not for the production of highly charged beams.

Some other innovative sources have been commissioned or built recently. The RIKEN 18 GHz source with hybrid magnets (superconducting solenoids and permanent magnet hexapole) have given good results (1.6 emA of Ar⁸⁺) [11] and even better results are expected from the VENUS source at the Berkeley National Laboratory [8]. This source can be considered to be the first third generation ECRIS which have been completed, being able to operate in High B mode at 28 GHz (this upgrading is scheduled for summer 2003). This source is deemed to get the leading role in the ECRIS field for the coming years, together with the Lanzhou source [12], at least for a few years, which are needed for the construction of the GyroSERSE source.

The conclusion that can be drawn is that the best solution to provide very high charge states ion beams is the design of a third generation ECRIS, with an appropriate magnetic trap for 28 GHz operation, according to the ECRIS standard model.

GyroSERSE: magnets and general design

The main features of the magnet design are given in Table 1. Figure 7 shows a model of the magnetic system, with the solenoids and the hexapole surrounded by an iron yoke and followed by the focusing solenoid which is the first element of the beamline.

Table 1. Comparison between the main parameters of SERSE and GyroSERSE

	SERSE	GyroSERSE
F	14 GHz +18 GHz	28–37 GHz
P_{\max}	2 kW + 2 kW	10 kW
B_{radial}	1.55 T	3 T
B_1	2.7 T	4.5 T
B_2	1.6 T	3.5 T
Φ_{chamber}	130 mm	180 mm
L_{chamber}	550 mm	700 mm
Φ_{cryostat}	1000 mm	1000 mm
L_{cryostat}	1310 mm	2150 mm
V_{extr}	20–25 kV	40–50 kV
LHe consumption	~4 L/h (100 L/day)	0

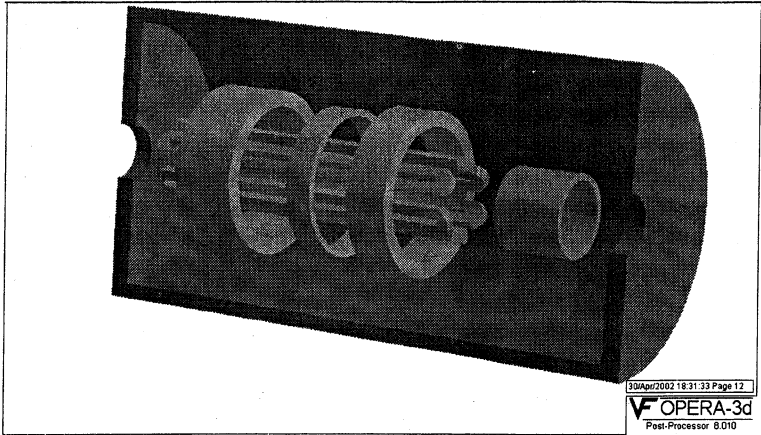


Fig. 7. The OPERA-3D model of the magnetic system

The mechanical constraints have obliged to choose a well larger inner bore than for SERSE, because of the boundary conditions for the hexapole (the stored energy exceeds 300 kJ). The plasma chamber inner diameter is 180 mm, 50 mm larger than the one of SERSE.

Figure 8 shows the B-mod lines in the plasma chamber, featuring a value of the last closed surface of about 3 T. Then the magnetic field will permit to operate in High B mode, with a mirror ratio greater than 2, at any frequency between 28 and 37 GHz.

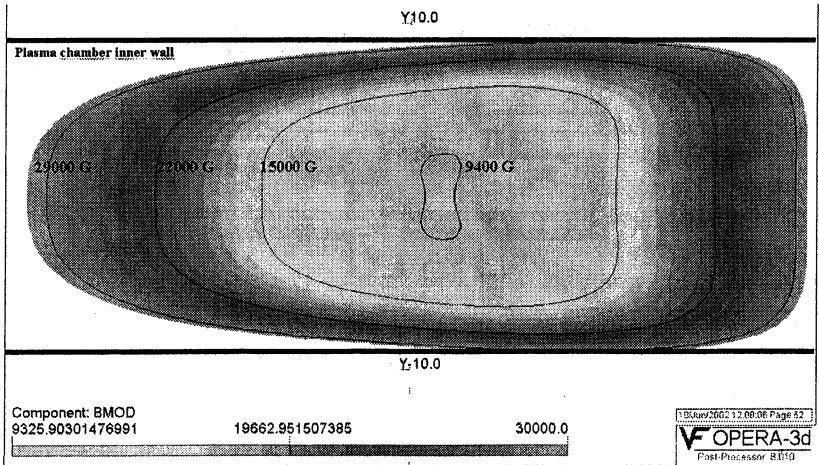


Fig. 8. The B-mod lines

The coils of the magnetic system will be wound from NbTi superconducting composites and cooled by immersion in a liquid helium bath. The electrical connection to the power supply at room temperature will be made by high critical temperature superconducting currents leads.

The use of cryocoolers will permit to operate the cryostat without external supply of liquid helium. Robust and reliable cryocoolers for the liquid helium temperature range are commercially available nowadays. Owing to their limited cooling capacity, however, more than one machine may be necessary for the present application.

The mechanical design

The large dimensions of the plasma chamber will allow to obtain a very good pumping speed, as it is for SERSE, which has a residual gas pressure of 10^{-8} mbar. As the radial pumping is not possible, the pumping will be performed only through 2 mm diameter holes drilled in the injection flange and in the outer part of the extraction electrode. A 5 mm double wall water-cooled stainless steel chamber will be able to dissipate a maximum power of 10 kW. High Voltage (50 kV) insulation will be provided by a 3 mm thick polyetherethercheton (PEEK) between the chamber and the cryostat. The length of the plasma chamber will be about 650 mm and the volume will be larger than 16 liters, well higher than any other existing source. In Fig. 9 the sketch of the GyroSERSE is presented.

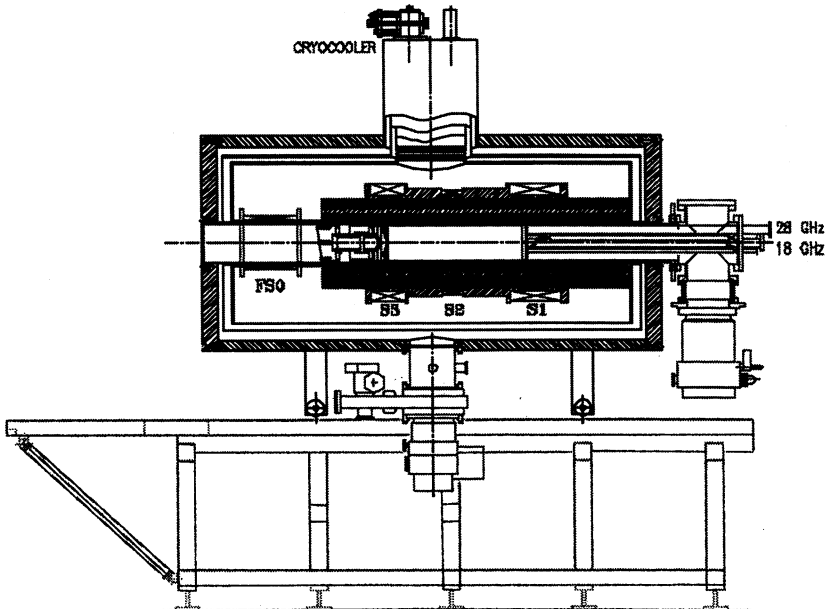


Fig. 9. The GyroSERSE source

The microwave injection

The behaviour of the 28 GHz rf coupling to the plasma was tested during the SERSE 28 GHz experiment and a new transmission line [2] based on the concepts used in the domain of magnetic fusion was designed for that purpose. The same design with minor modifications may be applied to GyroSERSE.

A 28 GHz 10 kW gyrotron (TE₀₂ output mode) will be used, with a transmission line similar to the one used for the SERSE 28 GHz experiment. It appears that the dc-break plays the role of an additional mode filter since only TE_{0n} modes are transmitted through this device. Higher-order reflected modes, if any, are dissipated in the line so that only a small fraction of the total reflected power returns to the gyrotron. The mode filter damps the residual reflected modes. During the experiment described in [2] about 2 to 6.5 kW (up to 4 kW in cw mode) were injected in the SERSE plasma; the maximum observed reverse power was less than 150 W, which enabled a safe operation of the gyrotron.

In the case of GyroSERSE the optimum power must be much higher. The optimum power for the ECRIS is given by the formula:

$$P_{\text{RF}} = \frac{n_e k T_e V}{\tau_e \eta_{\text{ECRH}}},$$

$$\text{where } \eta_{\text{ECRH}} = \frac{P_{\text{absorbed}}}{P_{\text{RF}}} = \eta_{\text{waveguide}} \eta_{\text{coupling}} \eta_{\text{plasma}}.$$

As the volume of the plasma will be higher than the SERSE one, but the confinement time and the density will be both higher, we believe that 6 kW or more will be sufficient to optimise the operation of the source.

The extraction optics and LEBT

By increasing the rf frequency heating from 18 GHz to 28 GHz, one then had to face with intense extracted beams, in the 10 mA range, so that space charge effects lead to larger emittances.

More than 0.5 mA has been obtained on a single charge state in afterglow mode operation with an extraction voltage of 25 kV only. It was demonstrated [2] that the currents scale as $V^{3/2}$ or higher. This is the combined effect of Child – Langmuir law and of the emittance decrease with the beam energy.

Simulations with KOBRA3D code have been carried out which confirmed that the large magnetic field (3.5 T) at the extraction may cause some emittance increase [13]. The triode topology was chosen for its simplicity and effectiveness. The distances and the shape of the electrodes have been optimized for high charge state extraction. Ray tracing of ion trajectories has been performed up to 10 cm downstream of the extraction aperture. The emittance values range between 120 and 200 π mm-mrad at 40 kV extraction voltage; a value of

150π mm-mrad has been used as starting condition for the preliminary beamline simulations here described. An extraction voltage higher than 40 kV may further decrease the emittance. We expect to operate at 50 kV, thus obtaining smaller emittance and high currents as well.

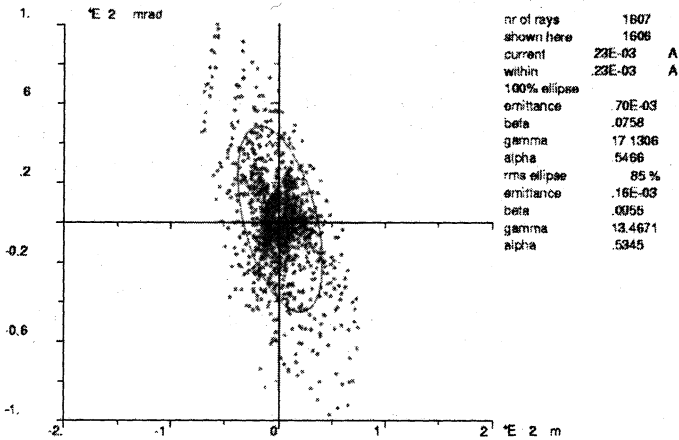


Fig. 10. A KOBRA3-INP simulation of the extraction system of GyroSERSE

The analysis section of the beamline has been also designed following the assumption that the focusing solenoid should be as close as possible to the extractor; moreover the solenoid should not be used to shrink the ion beam to a narrow focus; the analysis magnet should have a large curvature radius to have a good mass selection and a large gap to keep the beam losses small and the beam pipe should have a diameter of 160 mm to avoid beam losses and to provide a good vacuum conductance.

Some alternative designs have been considered, because GyroSERSE source may be built for different laboratories under different site constraints.

The simplest design is based on a single solenoid that matches the beam to the analyzing magnet. The solenoid is embedded in the cryostat 35 cm away from ion formation electrode and it is 300 mm long. The 90° dipole magnet (bending radius of 1200 mm, mass resolving power $M/\Delta M > 120$) has an air gap of ± 80 mm and field boundaries inclined by 26° in order to achieve x and y focussing; the distance between the solenoid and the entrance slit of the separator is 300 mm and the distance between the entrance slit and the dipole entrance is 1000 mm. The distance to the final focus is 2300 mm.

Other design options based on a combination of one solenoid and four quadrupoles are described in [12].

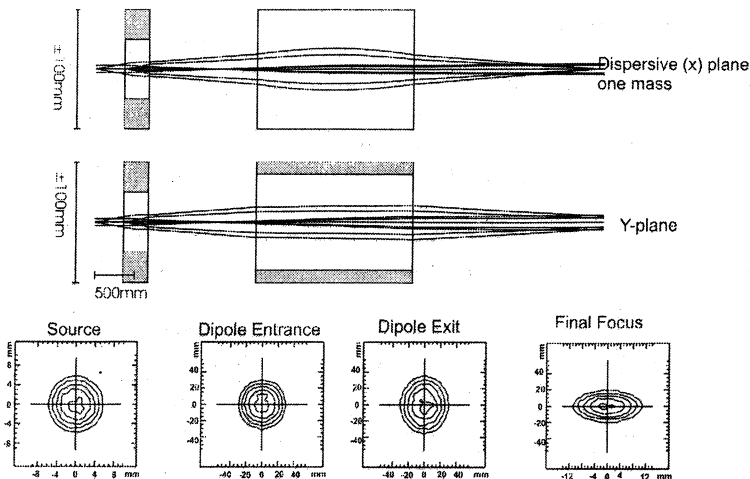


Fig. 11. A GIOSP simulation of the GyroSERSE beamline

Expected performances and conclusions

The GyroSERSE expected performances for Uranium and Xenon beams compared with the ones of other sources are shown in Fig. 12.

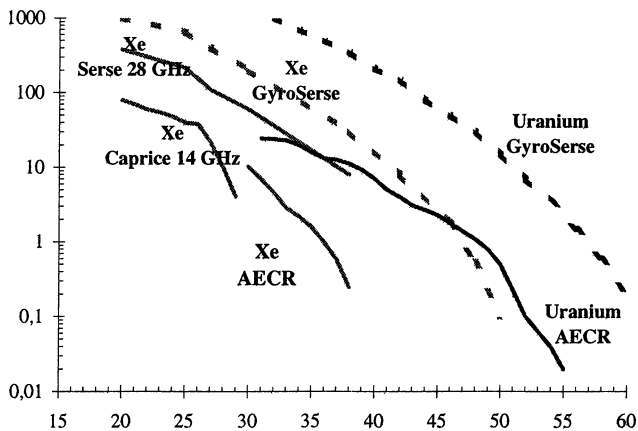


Fig. 12. The GyroSERSE expected performance compared with other sources for Uranium and Xenon beams and for cw operations.

Moreover Table 2 shows a comparison of the currents achievable from SERSE and GyroSERSE for different ion beams.

The evidence of a net increase of performance either in terms of higher charge states and of higher currents encouraged many laboratories to pursue the way of 3rd generation ECRIS in order to enhance the possibilities of their accelerator facilities. The continuous improvement of the technologies involved in the construction of ECR ion sources make possible to design in future even more performing equipment, getting benefit of each type of technological improvement.

Table 2. Comparison of different beam currents between SERSE and GyroSERSE

	SERSE	GyroSERSE
O ⁸⁺	~7 pμA	~50+100 pμA
Ar ¹⁸⁺	>20 pA	~1 pμA
Au ⁴⁵⁺	~1 pA	~0.1 pμA
Xe ⁴²⁺	–	~.02 pμA
Pb ⁵²⁺	–	~.01 pμA

Acknowledgements. The support of EU through the contract HPRI-1999-50014 "New technologies for next generation ECRIS" is gratefully acknowledged.

The support of L. Andò, F. Chines, S. Marletta, E. Messina and C. Percolla is acknowledged.

References

1. *Angert N.*, private communication.
2. *Gammino S., Ciavola G., Celona L., Hitz D., Girard A. and Melin G.*, Rev. Sci. Instrum. **72**(11), 2001, 4090 and refs. therein.
3. *Hitz D., Girard A., Melin G., Ciavola G., Gammino S., Celona L.*, Rev. Sci. Instrum. **73**(2), 2002, 509 and refs. therein.
4. *Geller R. et al.*, Proc. 8th Int. workshop on ECRIS / East Lansing, 1987, 1.
5. *Ciavola G., Gammino S.*, Rev. Sci. Instr. **63**(4), 1992, 2881.
6. *Gammino S. and Ciavola G.*, Plasma Sources Sci. Technol. **5**, 1996, 19.
7. *Gammino S. et al.*, Rev. Sci. Instr. 1998, **70**(9), 1999, 3577 and refs. therein.
8. *Lyneis C. et al.*, Proc. of RIA workshop (Argonne, 2002; unpublished).
9. *Gammino S., Ciavola G., Celona L., Andò L., Hitz D., Girard A., Melin G.*, Third generation ECR ion sources: news and perspectives, to be published on Nuclear Instr. & Meth. A.
10. *Thuiller T.*, New Xenon results of PHOENIX at 28 GHz, Proc. 15th ECRIS workshop (Jyväskylä, Finland, 2002, unpublished).
11. *Nakagawa T. et al.*, Recent progress of liquid He-free SC-ECRIS, Proc. 16th ECRIS workshop (Jyväskylä, Finland, 2002, unpublished).
12. *Zhao H.*, Status of IMP superconducting ECRIS SECRAL, Proc. 15th ECRIS workshop (Jyväskylä, Finland, 2002, unpublished).
13. *Ciavola G., Gammino S., Celona L., Andò L., Maggiore M., Spaedtke P., Winkler M., Wollnik H.*, Beamline transport for high intensity beams, to be published on Nuclear Instr. & Meth. A.

ION FLUX DIAGNOSTICS OF ECR DISCHARGE WITH DIFFERENT WAVE POLARIZATION

A. S. Smirnov, D. A. Malik, K. E. Orlov, T. V. Chernoziumskaya

Saint-Petersburg State Polytechnical University, Saint-Petersburg, Russia

Results of experimental study of ion flux from plasma of MW discharge in magnetic field are presented. The quarter-wave plate polarizer has been used to change an exciting wave polarization in the course of the experiment. Experiments have been carried out in argon at pressure range 0.1–1 mTorr. There was observed no essential wave polarization effect on the ion flux density at the pressures higher 0.4 mTorr. At the pressures below 0.4 mTorr there was no breakdown at left-hand polarized wave excitation; ion flux density in right-hand polarized wave excited plasma has strong maximum.

Introduction

Electron cyclotron resonance (ECR) plasma sources are widely used in microelectronics devices processing to obtain high density, low energy plasma at low gas pressure that provide high processing rate with improved process quality. A transverse MW electromagnetic wave is injected into the discharge volume along the magnetic field. As usual, in such type of sources magnetic field is inhomogeneous, so there is at least one surface in discharge volume, where the electron cyclotron resonance condition is fulfilled, i.e. the frequency of electron's rotation in magnetic field is equal to the electromagnetic wave frequency. Under this condition electrons are continuously accelerated in the resonance zone, if electromagnetic wave is circular polarized in the direction of electron rotation (RHP wave). For this reason, such type of sources called an "ECR" sources. ECR mechanism of a wave absorption is analyzed analytically and numerically in a number of works [1, 2]. However, in plasma in inhomogeneous field the wave always propagate on the angle to magnetic field. Thus the wave propagation and absorption mechanism is more complicated, it depends on magnetic field and plasma density distribution and position of the energy absorption does not coincide with the ECR zone [3, 4]. It can strongly affect on plasma parameters distribution near the substrate and process homogeneity.

The goal of presented work is to study experimentally the ion fluxes from plasma of ECR discharge in argon at pressure range 0.1–1 mTorr at the different exiting wave polarization. Results obtained would help us to understand the mechanism of the wave absorption and electron heating in ECR discharge and to derive a correlation between discharge parameters and characteristics of ion flux to the substrate (intensity, uniformity, ion energy).

Experimental setup

The sketch of the experimental setup is presented in Fig. 1.

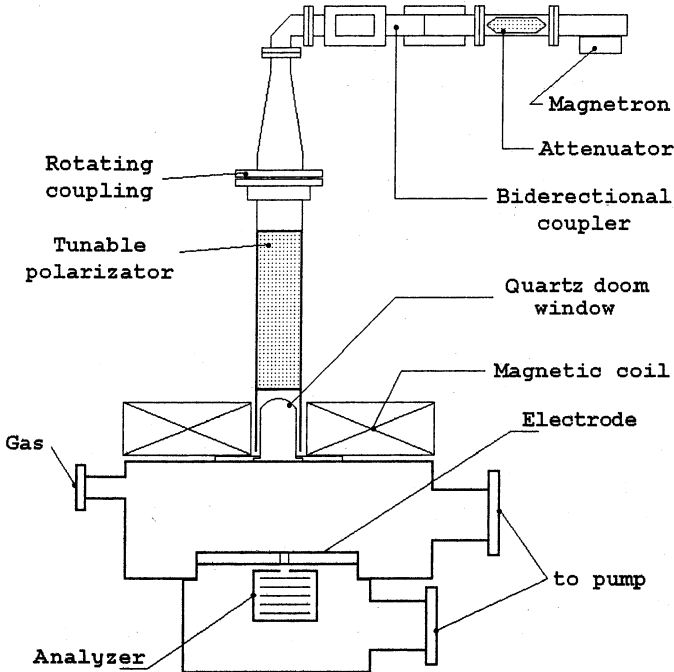


Fig. 1

A 2.45 MHz magnetron was used as a MW source. The magnetron operated in pulse mode with period 10 ms and pulse duration 4 ms. Averaged power was about 500 W. A bidirectional coupler was used for input and reflected power measurements. The wave polarization was varied continuously from right-hand (RHP) to left-hand (LHP) via linear by the quarter-wave plate polarizer. The polarizer is a section of the circular waveguide with a 3 mm thick dielectric plate inside. This plate provides 90° phase shift between the wave polarized in the plate plane and the perpendicular one. The wave polarization was changing by varying the angle between the plate and initial TE_{11} wave polarization plane. The microwave power coupled to the cylindrical 300 mm in diameter and 140 mm in height stainless steel discharge chamber through the quartz doom window. The 150 mm in height window was placed inside of the waveguide. External mag-

netic coil located on the top of the vacuum vessel induced the non-uniform magnetic field (up to 1200 Gs in the coil center). Position of the ECR resonance zone could be varied by the vertical movement of the coil and coil current variation. A disk-shaped, 200 mm in diameter aluminum electrode is placed in the chamber at 40 mm from the chamber bottom. This electrode was grounded. The electrode plane is perpendicular to the axis of magnetic field. The electrode isolates discharge volume from the separately evacuated high vacuum volume, where the four grid retarding field electrostatic energy analyzer [5] was mounted. Ions were extracted from plasma to the analyzer through the 1 mm diameter orifice in the electrode center. Residual gas pressure in the high vacuum chamber depended on gas pressure in the discharge volume but was better than $2 \cdot 10^{-6}$ Torr during the experiments.

Results and discussion

Ion retarding curves obtained at different exciting wave polarization presented at Fig. 2. Ions maximum energy corresponds to the potential drop at the electrode sheath. Flux intensity observed at left hand circular polarization of exciting wave only a 15% less when flux intensity observed at right hand circular and linear polarization. Flux intensity observed at right hand circular and linear polarizations are equal. So, there was observed no essential wave polarization dependence of the ion flux density at the pressures higher 0.4 mTorr. Pressure dependences of ion flux to the electrode, maximal and averaged ion energy are presented in Fig. 3. Ion flux and maximal energy are practically independent of pressure. It means that electron temperature and density did not vary in our experiments. Averaged energy slowly falls with the pressure. The broadening of the ion energy spectra may be due to ion scattering and to spreading of the particle generation region. Ion energy and current variations with the polarization are within the error range.

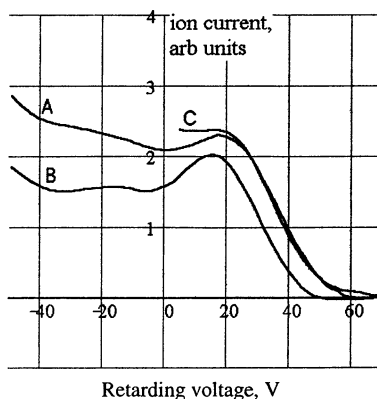


Fig. 2. Ar pressure $p = 0.4$ mTorr.
A – RHP wave, B – LHP wave,
C – linear polarized wave.

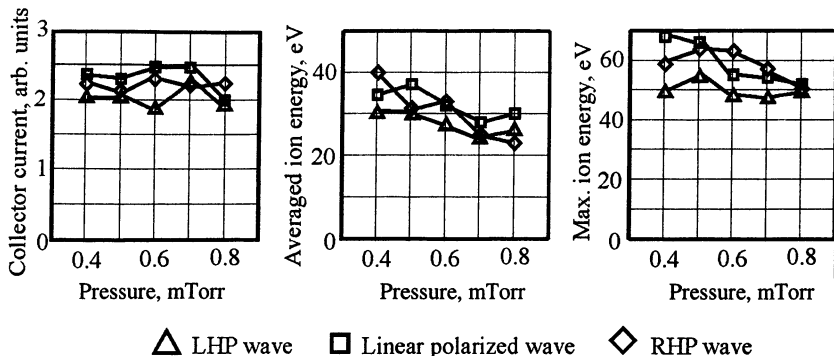


Fig. 3

Ion current dependences on polarizer angle at low pressures and constant MW power presented in Fig. 4. These curves display the strong maxima when the wave is RHP. At the pressures below 0.4 mTorr there was no breakdown at left-hand polarized (LHP) wave excitation, so ion current vanishes. Thus we can conclude that breakdown in low pressure ($p < 0.4$ mTorr) is determined by ECR power absorption.

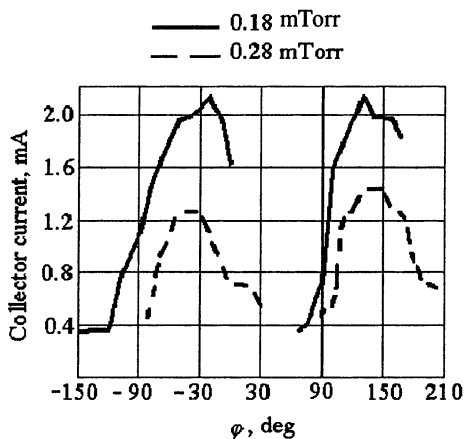


Fig. 4

$\phi = -30^\circ, 150^\circ$ correspond to RHP wave,
 $\phi = 60^\circ, -120^\circ$ correspond to LHP wave.

In the pressure range $0.4 \div 1$ mTorr breakdown does not depend on the wave polarization, so it can not be explained ECR power absorption. The alternative mechanism is nonresonance collisional electron heating. Amplitude of the microwave electric field in the waveguide estimated from the power is about $E_0 \cong 100$ V/cm. Corresponding electron oscillating energy is

$$W = \frac{e^2 E_0^2}{2m_e \omega^2} \cong 2.2 \text{ eV},$$

where $\omega = 2\pi \cdot 2.45$ GHz is electromagnetic wave frequency, e and m_e are electrons charge and mass correspondently. So, to reach ionization energy (15.8 eV), electron should collide more than 10 times. It is possible only if some electron confinement mechanism exists, because electron mean free path is about 25 cm and exceeds vessel dimension along the magnetic field. Additional experiments are necessary to study this mechanism.

Conclusions

The main results of the work are the followed:

Ion flux to the substrate in ECR discharge with various wave polarizations was measured.

Wave polarization affects only on discharge breakdown in low pressures ($p < 0.4$ mTorr).

Wave propagation and transformation in nonuniform plasma and magnetic field as well as collisional mechanism of power absorption should be taken into account in ECR discharge.

The ion flux generally concentrates in ring-shaped area. This area constitutes the projection of the wave absorption zone on a substrate plane. The ring-shaped area size and location are defined by magnetic field value and configuration.

References

1. *Williamson M. C., Lichtenberg A. J., Lieberman M. A.* J. Appl. Phys., 1992, **72**(9), 3924.
2. *Hemmers D., David M., Kempkens H., Uhlenbusch J.* J. Phys. D: Appl. Phys., 1998, **31**, 2155.
3. *Musil J., Zacek F.* Plasma Physics, 1970, **12**, 17.
4. *Musil J., Zacek F., Budnikov V. N.* Czech. J. Phys. B, 1973, **23**, 167.
5. *Smirnov A., Ustavshikov A., Frolov K.* Sov. Phys., Technical phys., 1995, **40**, 627.

MICROWAVE CONCEPT OF A LARGE VOLUME PLASMA SOURCE

*A. A. Litvak, S. V. Putvinski, V. E. Semenov¹, A. G. Shalashov¹,
O. B. Smolyakova¹, E. V. Suvorov¹*

Archimedes Technology Group Inc., San Diego, USA

¹Institute of Applied Physics, RAS, Nizhny Novgorod, Russia

The main aspects of plasma production and support of a steady-state plasma discharge using microwave radiation are discussed in application to a large volume plasma source. A number of scenarios are presented which allow to reach the nominated steady-state regime starting from break-down of a neutral gas, following plasma density ramp and establishing the required electron temperature and gas composition.

Introduction

Large volume plasma sources among other applications may be used for atom separation over their mass numbers basing on the idea of magnetron effect. The "Archimedes" facility designed for light and heavy fraction separation in the Hanford nuclear waste is based on a plasma source with axially symmetric magnetic configuration operating in a gas-dynamic regime of plasma confinement [1]. The separator may be treated as a steady-state plasma discharge with "working matter" injected into the installation in gaseous phase and escaping from it along magnetic field lines as ionized matter. From the point of view of such plasma source operation there are two evident and well separated problems:

- the break-down of a neutral gas and transition of a plasma discharge into a steady-state one;
- support of the steady-state operation regime.

The solution of the first problem may be achieved according to specific schemes, in which optimal variation in time is provided for a number of parameters such as the neutral gas pressure and its composition, the frequency and the full power of a microwave radiation, its distribution over the trap volume. In the steady-state stage such parameters as gas composition and gas-puff rate should be fixed. In the designed version of the "Archimedes" separator it is assumed that plasma discharge will be supported in a cylinder vacuum chamber (0.4 m diameter, 4 m length) with longitudinal magnetic field 1.5–2.0 kG. Electron density and temperature are restricted by the values $2 \cdot 10^{13} \text{ cm}^{-3}$ and 2 eV with the neutral gas-puff rate in the range 1–5 g/s. In the original design it is assumed that break-down and support of the steady-state discharge will be provided by a whistler wave system, operating at the frequency 5 MHz.

The alternative concept of power deposition into the plasma presented below is based on using the microwave radiation (frequency range 5100 GHz). Theoretical modeling is performed basing on the 0D approximation (uniform power deposition and gas-puff over the whole plasma volume).

Break-down conditions

Modeling of break-down and plasma density ramp stages is based on a usual set of particle and power balance equations

$$\dot{N}_0 = I_0 - k_i N_0 N_e - \tau_0^{-1} N_0, \quad (1)$$

$$\dot{N}_e = k_i N_0 N_e - \tau_e^{-1} N_e, \quad (2)$$

$$\frac{3}{2} \dot{T}_e = p_{abs} - q_V - q_C - \frac{3}{2} v_{ie}^e (T_e - T_i) - \frac{3}{2} v_{e0}^e (T_e - T_0), \quad (3)$$

$$\dot{T}_i = v_{ie}^e (T_e - T_i) + v_{i0}^e (T_0 - T_i) - T_e \tau_e^{-1}, \quad (4)$$

where I_0 is defined by gas-puff rate, τ_0 defines neutral particle losses from the trap, k_i is ionization cross-section, τ_e is electron life-time, p_{abs} is absorbed microwave power per an electron (proportional to a microwave field intensity), q_V and q_C are "volume" (ionization and radiative) and convective energy losses from electron component; other two terms in Eq. (3) describe the energy exchange between electron, ion and neutral components, the last term in Eq. (4) takes into account plasma potential. The temperature of neutral component is fixed (≈ 0.1 eV), only single ionization is taken into account. Electron life-time is defined as

$$\tau_e^{-1} = D_a \pi^2 / L^2 + \Theta D_e \pi^2 / L^2,$$

where $D_a = \frac{1}{\sqrt{8}} \sqrt{T_i / m_i} (1 + T_e / T_i) / (N_0 \sigma_{e0}) \pi$ and $D_e = \sqrt{T_e / m_e} / (N_0 \sigma_{e0})$ are coefficients of ambipolar and of free electron diffusion correspondingly and factor $\Theta = 1 / (1 + L^2 / r_{De}^2)$ is introduced to describe gradual transition from free electron diffusion to ambipolar one in the course of electron density increase. In the "volume" electron energy losses ionization of neutrals and excitation of neutrals and ions are included:

$$q_V = \left(E_i + \frac{3}{2} T_e \right) k_i N_0 + \left(\sum_m \xi_{0m} E_{exc,0,m} k_{exc,0,m} \right) N_0 + \left(\sum_l \xi_{1m} E_{exc,1,l} k_{exc,1,l} \right) N_e,$$

where factors ξ_{0m} and ξ_{1m} are introduced to take into account possible effect of trapping the line radiation by a plasma volume. For the set of parameters under consideration this effect may be of importance for the only line of neutral Na; in all other cases $\xi = 1$. For ionization and excitation constants data from [2] and [3] are used. Convective losses through the plugs are included in the case of high enough density (satisfying the quasi-neutrality condition):

$$q_C = \tau_e^{-1} T_e \cdot \left(\frac{1}{2} \ln \frac{T_e}{T_i} \frac{m_i}{m_e} - \frac{3}{2} \right).$$

Power deposition into electron component from the microwave radiation is calculated within the approximation of plane wave with the fixed amplitude propagating along the axis of installation in a uniform plasma with collisional absorption defined by dispersion relations:

- $n^2 = 1 - \omega_{pe}^2 / \omega(\omega - i\nu_{ei})$ for high frequency range ($\omega \gg \omega_{ce}$),
- $n^2 = 1 - \omega_{pe}^2 / \omega(\omega - \omega_{ce} - i\nu_{ei})$ for longitudinal propagation in the electron-cyclotron frequency range,

where ω_{ce} and ω_{pe} are electron gyro- and plasma frequencies and ν_{ei} is effective electron-ion collision frequency.

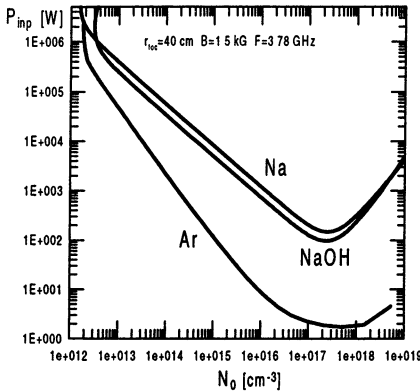


Fig. 1. Quasi-ECR break-down ($\omega = 0.9\omega_{ce}$): dependence of a threshold microwave power on a neutral gas density.

Break-down conditions for a number of pure gases (such as Na, O, H, Ar, Ne) and their mixtures has been investigated. Examples of some dependencies of a threshold microwave power on a neutral gas density are presented in Fig. 1 for a number of gases. The incident microwave power is assumed to be uniformly distributed over the whole cross-section of the trap. Because of negligibly small absorption at the break-down stage presented power values simply define the microwave field intensity in the vacuum chamber. Magnetic field $B_0 = 1.5$ kGs is uniform in the volume of the trap; to

increase the efficiency of microwave field – electron interaction the frequency of microwave radiation is chosen slightly below electron-cyclotron frequency. Fairly high values of the threshold power for the break-down of gases with Na content are related to high radiative losses, because at the break-down stage the radiation in the strongest neutral Na line is not trapped. Plots presented in Fig. 1 are obtained under assumption that electron losses are defined by ambipolar diffusion, which is realized when initial electron density exceeds the level about 10 cm^{-3} . Under these favorable conditions the microwave power required for the break-down of neutral gas with reasonable density (10^{13} – 10^{14} cm^{-3}) is not very high (10–300 kW). The break-down starting from free electron diffusion regime requires the microwave power at least by an order of magnitude higher.

Having in mind good prospect of using mm-wave radiation to support the steady-state discharge a possibility to use the same radiation for the break-down was also investigated. The threshold power for this frequency range is more than 3 orders of magnitude higher than in the case of "quasi-ECR" break-down presented above. Such strong requirement may be weakened by initiating the break-

down in the quasi-optical cavity. The other possibility is to stimulate initially the break-down in a neutral gas with high density and then to provide discharge evolution into a final stage by decreasing the neutral gas density.

Evolution of the discharge into a steady state

Evolution of the discharge beginning from the break-down into a steady-state stage was also investigated basing on the same set of balance equations (1)–(4) with slight modifications. Reflection of the microwave power from a plasma boundary is taken into account; in the electron life-time the possibility to change from ambipolar diffusion to gas-dynamic losses is foreseen. Characteristic example of the discharge evolution in pure Na with "quasi-ECR" break-down is presented in Fig. 2. The initial stage (break-down and density ramp) is governed by the microwave power with a relatively low frequency ($\omega = 0.9\omega_{ce}$). The electron density saturates at the level of $2 \cdot 10^{12} \text{ cm}^{-3}$, when significant part of the power is reflected from the plasma edge, and some low-temperature and low-ionized regime is established (ionization degree 13%, electron temperature 0.6 eV). At $t = 2 \text{ ms}$ an alternative power source (500 kW) is switched on; this radiation is supposed to be fully absorbed by a plasma, e. g., due to multi-pass absorption of mm quasi-optical beam. Applying of this power source results in a further gradual increase of electron density and temperature followed by a fast transition to the new steady state with gas-dynamic confinement regime (practically full ionization, $N_e \approx 3 \cdot 10^{13} \text{ cm}^{-3}$, $T_e \approx 4.4 \text{ eV}$). Parameters of this discharge are in the vicinity of required for the separator values. In the next section results of more detailed investigations of the steady-state discharge parameters are presented for various sets of governing parameters (gas-puff rate, gas composition, absorbed microwave power).

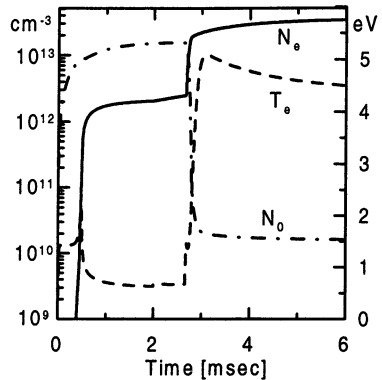


Fig. 2. Evolution of the discharge beginning from the break-down:

$B_0 = 1.5 \text{ kG}$, gas-puff: 2 g/s .
 0–2 ms: $P_{mw} = 0.8 \text{ MW}$ at 3.78 GHz ,
 2–6 ms: $P_{mw} = 0.5 \text{ MW}$ (all absorbed).

0D modeling of steady-state discharges

This modeling is also performed on the basis of Eqs. (1)–(4) with zero time derivatives with additional taking into account the possibility of higher ionization.

In Table below some examples of steady-state discharge parameters are presented for Na-O-H mixture, which may be considered as a good approach to the Hanford waste composition.

Table

Eletr. temp.	Gas-puff	Electron density	Total power losses and main loss channels	En.cost per ion
1.5 eV	5.0 g/s	$7.6 \cdot 10^{13} \text{ cm}^{-3}$	200 kW: 34% Na ⁰ ioniz., 35% Na ⁰ exc., 14% O ⁰ exc., 7% H ⁰ exc.	15 eV
1.5 eV	2.0 g/s	$3.0 \cdot 10^{13} \text{ cm}^{-3}$	83 kW: 32% Na ⁰ ioniz., 58% Na ⁰ exc., 5% O ⁰ exc., 3% H ⁰ exc.	16 eV
1.5 eV	1.0 g/s	$1.4 \cdot 10^{13} \text{ cm}^{-3}$	54 kW: 24% Na ⁰ ioniz., 74% Na ⁰ exc., 2% O ⁰ exc.	21 eV
2.0 eV	5.0 g/s	$9.2 \cdot 10^{13} \text{ cm}^{-3}$	720 kW: 13% Na ⁰ exc., 19% O ⁰ exc., 30% O ⁺ exc., 12% H ⁰ exc.	40 eV
2.0 eV	2.0 g/s	$2.9 \cdot 10^{13} \text{ cm}^{-3}$	170 kW: 16% Na ⁰ ioniz., 39% Na ⁰ exc., 14% O ⁰ exc., 8% O ⁺ exc.	30 eV
2.0 eV	1.0 g/s	$1.3 \cdot 10^{13} \text{ cm}^{-3}$	85 kW: 16% Na ⁰ ioniz., 63% Na ⁰ exc., 7% O ⁰ exc., 4% H ⁰ exc.	30 eV
5.0 eV	2.0 g/s	$3.2 \cdot 10^{13} \text{ cm}^{-3}$	5.5 MW: 2% Na ⁰ exc., 76% O ⁺ exc., 11% O ⁺⁺ exc., 2% H ⁰ exc.	460 eV
5.0 eV	1.0 g/s	$1.5 \cdot 10^{13} \text{ cm}^{-3}$	1.4 MW: 4% Na ⁰ exc., 74% O ⁺ exc., 5% O ⁺⁺ exc., 2.7% H ⁰ exc.	250 eV

It should be noted that important parameters of the steady-state discharge, such as optimal electron density and temperature, cannot be established for a given gas-puff rate by varying the total power deposition. All these parameters at

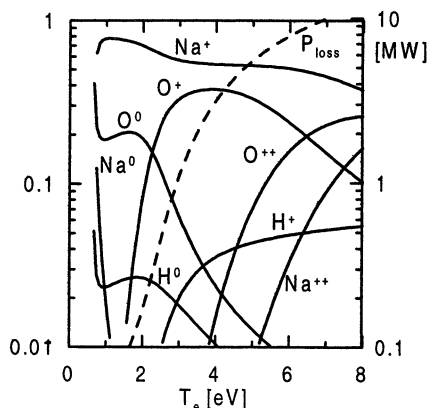


Fig. 3. Steady-state discharge parameters for NaOH puff rate 2 g/s.

the steady-state stage are related to each other in a complicated nonlinear manner. Fig. 3 presents an example of a discharge composition in relative densities and electron temperature for Na-O-H mixture with gas-puff rate 2 g/s depending on the total absorbed power. In the electron temperature range of interest the power required to support the discharge is quite moderate (less than 200 kW); as it follows from Table electron density is slightly above the optimal value what may be corrected by appropriate diminishing the gas-puff rate and the deposited power.

Conclusions

In numerical modeling based on the 0D approximation it has been demonstrated that the microwave radiation of moderate power level may be successfully used in the "Archimedes" separator facility both for the break-down of neutral gas and for the supporting of steady-state plasma discharge. Relatively low frequency radiation (below electron-cyclotron frequency) being very promising for the break-down with the plasma density increase undergoes strong reflection from the plasma boundary and becomes inefficient. At this stage high frequency radiation (up to 100 GHz) may be easily matched to the plasma with subsequent multi-passage collisional absorption. More details concerning ray trajectories and absorption along them for these two frequency ranges and various density profiles are presented in the paper H15.

This work was partially supported by Russian Foundation for Basic Research (grant № 00-02-17200).

References

1. See, e.g., <http://www.at-sd.com>, 2002.
2. *Voronov G. S.*, Atomic Data and Nuclear Data Tables, 1997, **65**, 1.
3. *Verner D. A., Verner E. M., and Ferland G. J.*, Atomic Data and Nucl. Data Tables, 1996, **64**, 1.

HYBRID RESONANCES IN MULTIPACTOR DISCHARGES

A. Kryazhev, M. Buyanova, V. Semenov, D. Anderson¹, M. Lisak¹,
J. Puech², L. Lapierre², J. Sombrin²

Institute of Applied Physics, Russian Academy of Science,
Nizhny Novgorod, Russia

¹Department of Electromagnetics, Chalmers University of Technology,
Gothenburg, Sweden

²Centre Nationale d'Etudes Spatiales, Toulouse, France

A plane parallel model of multipactor is studied in detail using both an analytical approach and numerical simulations. It is shown that the commonly accepted picture of the multipactor zones is not quite complete and should be modified by taking into account the existence of hybrid resonance modes and the important consequences of a secondary emission yield that significantly exceeds unity. Numerical simulations demonstrate that the chart of the multipactor zones is also very sensitive to the initial velocity spread.

Multipactor discharge is an avalanche-like increase of free electrons in vacuum systems when primary electrons hit the walls of vacuum device in resonance with RF electric field and knock out secondary electrons. Multipactor is an undesirable effect in powerful transmission lines and specifically in space communication systems. Therefore the problems of avoiding and suppressing multipactor have been studied extensively for more than 50 years. However still there is no common opinion concerning the multipactor even for a system with the simplest geometry.

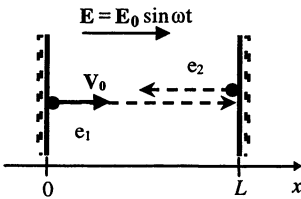


Fig. 1. One-dimensional two-sided multipactor.

The simplest system with two-sided multipactor is shown in Fig. 1. The primary electron leaves the first wall due to thermal emission and moves being driven by the RF field (see equation 1). When it arrives to another wall it may knock out secondary electrons if the impact energy belongs to some range that depends on the material. The electric field and initial velocities of electrons are supposed to have only one component directed perpendicularly to the planes.

$$\frac{d^2\xi}{d\varphi^2} = \sin \varphi, \tag{1}$$

$$\xi = x/a, \quad a = \frac{eE_0}{m\omega^2} = \frac{V_\omega}{\omega}, \quad \varphi = \omega t, \quad \text{distance } \lambda = \omega L/V_\omega, \quad \text{initial velocity } v_0 = \frac{V_0}{V_\omega},$$

$$\lambda = (\varphi^{impact} - \varphi^{start})(v_0 + \cos \varphi^{start}) + \sin \varphi^{start} - \sin \varphi^{impact}. \tag{2}$$

In the simplest case of multipactor we may neglect the initial velocity distribution: $\Delta v_0 \ll 1$. The resonant condition is that electron one-way transit time must be equal to the odd number of half-cycles of the field [1]:

$$\varphi^{impact} - \varphi^{start} = \pi k, \quad k = 2p - 1, \quad p \in \mathbb{N}. \quad (3)$$

Secondary electrons can be knocked out only if the secondary emission yield exceeds unity, that limits the range of allowed impact velocities [1]. In numerical calculations the analytical approximation of the secondary emission curve, suggested by J. R. M. Vaughan [2] may be used.

Each one of the well-known classical multipactor modes is described by equation on distance and resonance starting phase:

$$\lambda = \pi k \cos \varphi + 2 \sin \varphi + v_0 \pi k, \quad k = 2p - 1, \quad p \in \mathbb{N}. \quad (4)$$

The possible values of φ , k and λ in case of zero initial velocity are $0 \leq \varphi_R < \pi/2$, $\lambda > 2$, $k = 1, 3, 5, \dots$. In case of zero initial velocity they become

$$\varphi' \leq \varphi_R < \varphi'', \quad \varphi' < 0, \quad \varphi'' > \pi/2, \quad \lambda > 2, \quad k = 1, 3, 5, \dots, \quad k_{max}, \quad k_{max} = \frac{\omega L}{\pi v_0} \quad (\text{see Fig. 2}).$$

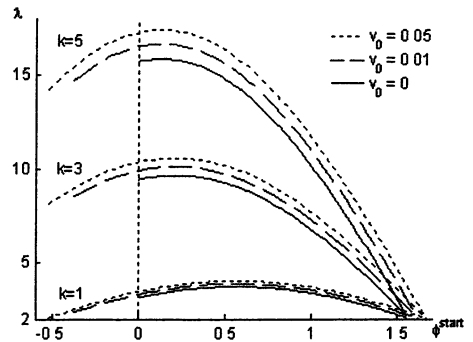


Fig. 2. The multipactor curves as dependence of dimensionless distance on the starting phase for various values of initial velocities.

The stability condition limits the range of possible starting phases for multipactor resonance. It means that the range of starting phases of secondary electrons is narrower than for primary ones:

$$\left| \frac{\pi k \sin \varphi_R + v_0}{2 \cos \varphi_R + v_0} \right| \leq 1. \quad (5)$$

The growing part of the resonant curve is stable. For the upper bound of starting phase the stability condition is more strict than the condition of non-returning to the wall of birth. But the lower bound depends much on the initial velocity and number of mode (Fig. 3a).

The problem of separation and overlapping of the resonant multipactor bands still is the question to discuss. There is no overlapping in case of not very high Δv_0 and if $\sigma \sim 1$ but greater values of σ may provide the multipactor development by compensating electron losses even if the starting phase is not stable. Thus the multipactor development condition (5) may be redefined:

$$\left| \frac{\pi k \sin \varphi_R + v_0}{2 \cos \varphi_R + v_0} \right| \leq \sigma. \quad (6)$$

Then for high values of secondary emission zones are expanded and the overlapping of adjacent resonant zones becomes possible (Fig. 3b).

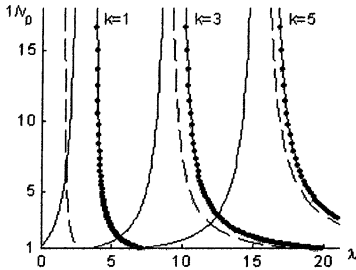


Fig. 3a. The bounds of stable values of λ in dependence on initial velocity for $\sigma = 1$. Lines marked with points correspond to upper bound, dashed lines – lower bound from the stability condition, solid ones – from "non-returning" condition.

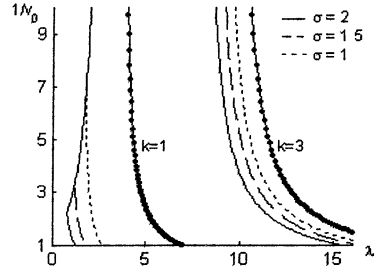


Fig. 3b. The bounds of stable values of λ in dependence on initial velocity for various σ . Lines marked with points correspond to upper bound, other ones – to effective lower bound defined as in (6).

The initial velocity spread leads to so called polyphase multipactor [3], since the velocity spread of primary electrons causes the spread of starting phases of secondary electrons. The development of multipactor becomes very sensitive to the secondary emission yield. If σ is low and velocity spread is rather high, some of secondary electrons may be lost for further multipactor development, and the multipactor will be suppressed. Otherwise if σ is high, the emission may compensate electron losses. Thus the initial velocity spread must be always taken into account.

Besides classical multipactor modes, new resonant modes were discovered. The resonance shows itself after every n transits of electrons. Every electron in a group has its own k and φ , not exactly equal to each other and to the certain odd number of half-cycles of the field. The resonance conditions are the following:

$$\varphi_1 = \varphi_{n+1}, \quad k_1 = k_{n+1}, \quad \sum_{i=1}^n \Delta t_i = \frac{2\pi}{\omega} p, \quad \sum_{i=1}^n k_i = 2p, \quad p \in N. \quad (7)$$

We suggest calling these modes hybrid, as opposed to the classical modes with one k for all electrons. Each hybrid mode is defined by its order n and the set of numbers k . Classical modes correspond to hybrid modes of the first order. The hybrid modes of the second order were described by Gilardini [4]. The motion equations for the simple case $v_0 = 0, \Delta v_0 = 0$ are as follows:

$$\begin{cases} \lambda = (\varphi_{i+1} - \varphi_i + \pi k_i) \cos \varphi_i + \sin \varphi_{i+1} + \sin \varphi_i, & i = 1, \dots, n-1, \\ \lambda = (\varphi_1 - \varphi_n + \pi k_n) \cos \varphi_n + \sin \varphi_n + \sin \varphi_1, \\ k_i = 1, 3, 5, \dots, \\ 0 \leq \varphi_i \leq \frac{\pi}{2}, & i = 1, \dots, n. \end{cases} \quad (8)$$

The curve of a hybrid mode lies in a limited region near the curve of the classical mode with $k^{classic} = k_{minimal}^{hybrid}$. The region of hybrid modes adjacent to the classic mode with certain k is well separated from the neighboring regions of hybrid modes (Fig. 4). Each region contains an infinite countable set of hybrid modes. Inside each region the curves are arranged in ascending order. The curves of modes with greater k are situated higher than other curves of the same order, and the curves of modes with more numbers k equal to minimal are situated closer to classical mode (Fig. 5).

Fig. 4. The first and second hybrid regions and some hybrid curves as dependence of λ on the starting phase of primary electrons. Hybrid modes are identified by set of numbers k .

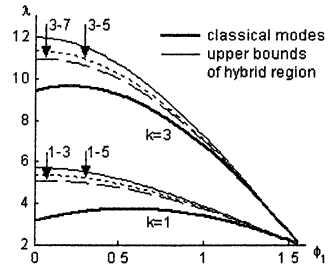
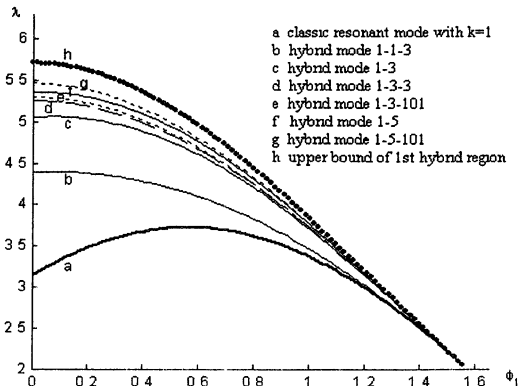


Fig. 5. The first hybrid region. Hybrid modes are identified by set of numbers k .



One of the differences between hybrid and classical modes is relatively narrow bands of stable resonance for hybrid modes. The stability condition is that at least one of the starting phases is quite small. Like in the classical case the growing part of λ dependence on φ_1 is stable [5].

The first hybrid mode is mode 1-3 and it has the widest range of stable parameters $\Delta\varphi \approx 0.08$, $\Delta\lambda \approx 0.008$. Stable parts of all other modes are even smaller and the hybrid modes are hard to find in numerical experiments. But they are very sensitive to other parameters such as σ , ν_0 , $\Delta\nu_0$. Some combinations of these parameters cause the widening of stable zones and even their overlapping.

Some of the hybrid modes may be found analytically, for example, mode 1-3, and some of them were demonstrated in numerical experiments. In these experiments hybrid modes may be identified by a specific diagram of impact phases (Figs. 6a, 6b).

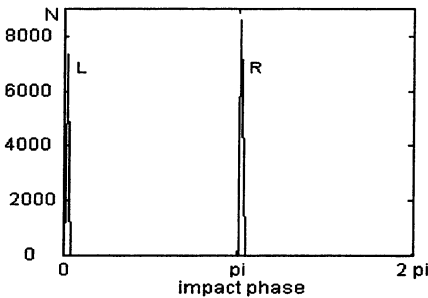


Fig. 6a. Hit phase distribution for classical mode $k = 1$, $\lambda = 3.3$, $\sigma = 1.2$, $\nu_0 = 0$, $\Delta\nu_0 = 0.018$: one peak for each wall (L-left, R-right).

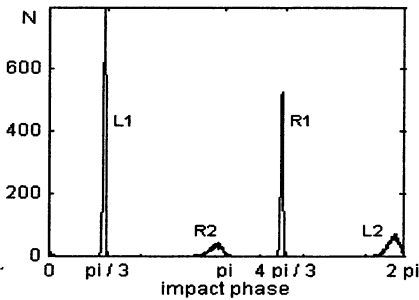
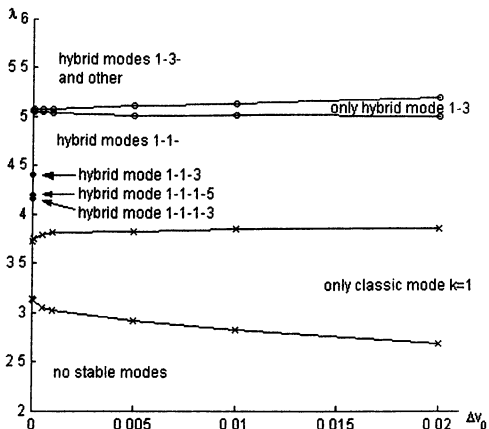


Fig. 6b. Hit phase distribution for hybrid mode $k = 1,3$, $\lambda = 5.04$, $\sigma = 2$, $\nu_0 = 0$, $\Delta\nu_0 = 0.01$: two peaks for each wall (L-left, R-right), because the primary and secondary electrons of each stream have different starting phases.

The influence of $\nu_0 \neq 0$ and $\Delta\nu_0 \neq 0$ is also very important. Like in the classical case, fixed $\nu_0 \neq 0$, the same for all electrons, leads to the displacing and widening of the ranges of possible φ and λ . The initial velocity spread also expands multipactor bands (Fig. 7) and leads to polyphase regime that may consist of some neighboring modes.

Fig. 7. Numerical experiments: expansion of resonant bands corresponding to increase of Δv_0 . $\sigma = 1.2$, $v_0 = 0$. All hybrid modes except 1-3 can be clearly identified only for $\Delta v_0 \ll 1$. At higher values of Δv_0 their bands become overlapped. All secondary electrons were assumed to have Maxwellian distribution of initial velocities with the zero mean and width Δv_0 .



The classical modes of multipactor, their dependence on initial velocity and secondary emission have been studied in detail using both an analytical approach and numerical simulations. Infinite number of new multipactor modes has been found. Their zones fill definite regions in the parameter space between the classical ones. The results of numerical simulations demonstrate the importance of initial velocity spread because multipactor becomes very sensitive to the secondary emission yield over unity. This means a detailed chart of the multipactor bands can not be given based on a classical theory which assumes fixed value of initial velocity for all electrons. The analysis requires extensive numerical simulations.

References

1. *Vaughan J. R. M.* Multipactor. *IEEE Trans. Electron Devices*, **35**(7), 1172–1180 (1988).
2. *Vaughan J. R. M.* A new formula for secondary emission yield. *IEEE Trans. Electron Devices*, **36**(9), 1963–1967 (1989).
3. *Luk'yanchikov G. S.* Uniform poliphase secondary emission RF discharge on solid surface. *Zh. Tekh. Fiz.*, **44**(9), 1922–1928 (1974; in Russian).
4. *Gillardini A. L.* Multipacting discharges: Constant-k theory and simulation results. *J. Appl. Phys.*, **78**(2), 783 (1995).
5. *Kryazhev A., Buyanova M., Semenov V., Anderson D., Lisak M., Puech J., Lapierre L., Sombrin J.* Hybrid Resonant Modes of Two-Sided Multipactor and Transition to the Polyphase Regime. *Phys. Plasmas* (to be published).

BREAKDOWNS AND DESTRUCTIONS OF DIELECTRICS IN STRONG MICROWAVE FIELDS

V. A. Ivanov and M. E. Konyzhev

General Physics Institute, Russian Academy of Sciences
Vavilov str. 38, 119991, Moscow, Russia
E-mail: ivanov@fpl.gpi.ru

In the experiments a pulsed (1–10 μ s) microwave radiation (frequency of oscillation ν was 2, 6 and 7 GHz, power was 0.4–10 MW, microwave electric field was 3–10 kV/cm) excited microwave discharges developing at the surface of some crystal and amorphous solid-state dielectrics (lithium fluoride LiF, sodium chloride NaCl, caesium iodide CsI, zirconium dioxide ZrO₂ crystals, Teflon, polyethylene, glass and other materials) in vacuum. The dense plasma of the discharges produced the electrodeless electric breakdowns and destructions on the surface and in the bulk of the dielectrics.

1. Introduction

The interest to studying electrodeless microwave discharges developing at the surface of solid-state dielectrics was appeared due to applied researches, oriented to increase the electric strength of the output windows of high-frequency vacuum devices and waveguides during the propagation of powerful pulsed microwave radiation along them [1, 2].

The empirically found methods of preventing the electrodeless breakdowns at the inner surfaces of vacuum systems, as a rule, were limited to reducing the level of the energy flux density of the incident microwave radiation at these surfaces. Special coatings and/or external electric and magnetic fields were applied also for suppression the microwave discharges at the surface of dielectrics, so in a number of cases it was possible to prevent the eventual development of the secondary electron emission microwave discharge to plasma stages of microwave discharges at the surface of dielectrics.

These procedures fruited some positive results. However, despite of these successes, the problem of increasing of an electric strength of dielectrics, semiconductors and composite metal-dielectric materials in strong microwave fields becomes more and more important due to the considerable advance in the development of powerful nonrelativistic and relativistic superhigh-frequency electronics engineering [3].

The necessity of solution of more common problems of powerful superhigh-frequency electronics engineering, concerning the generation, transporting and transformation of microwave radiation, initiated a development of both basic and applied studies of electrodeless microwave discharges developing at the surface of solid-state dielectrics in the vacuum. Investigations of nonlinear physical phenomena occurring in the plasma of the microwave discharges, interacting with dielectrics, were performed [4–6].

Of special interest are those physical processes in the near-surface layer of dielectric crystals which bring about the accumulation and relaxation of high concentrations of radiation-induced point defects, the arising of luminescence of induced color centers, the appearance of induced electrical conductivity, the stimulation of strong absorption of microwave power, the occurring of both contracted discharges and electrodeless breakdowns of crystals in a field of microwave radiation [7–12]. Due to our studies a classification of different types of electrodeless pulsed microwave discharges was developed.

In the experiments we study breakdowns and destructions on the surface and in the bulk of insulating materials strongly interacted with dense plasma of microwave discharges.

2. Experimental setup and measurement technique

Microwave discharges at the surface and in the bulk of dielectrics were investigated experimentally with pure crystal and amorphous solid-state dielectrics (lithium fluoride LiF, sodium chloride NaCl, caesium iodide CsI, zirconium dioxide ZrO_2 crystals, Teflon, polyethylene, glass and other materials) in vacuum (10^{-4} – 10^{-5} Pa). All used dielectrics have small absorption coefficients for microwave radiation at the frequency $\nu = 2$ – 7 GHz, the tangent of the dielectric loss angle was about $1 \cdot 10^{-4}$ – $3 \cdot 10^{-4}$.

The experiments were carried out in two configurations. In the first configuration some quasi-optical systems were used for focusing microwave radiation into big vacuum chamber [5, 6]. In the second one some waveguide systems were used for studying of interaction of electrodeless microwave discharges with dielectrics in vacuum [7–12].

High-speed photographs of microwave discharges were taken with a help of an electron-optical image converter (KADR-4) operating in the frame-by-frame mode (four frames with a frame exposure time of 50 ns, the time interval between the frames was 50 ns). The electron current from microwave discharges was measured by a multigrad electrostatic analyzer. X-ray emission with quantum energies from 3 to 20 keV was measured by scintillation detectors and a pinhole camera, with using the calibrated metal filters. The plasma density in microwave discharges was measured by a microwave interferometer, the wavelength of the probing radiation was 8 mm. The incident and reflected microwaves were recorded by directional waveguide couplers and semiconductor detectors. Destructions produced on the surface and in the bulk of the dielectrics due to electrodeless electric breakdowns were investigated with the help of a JEOLS scanning electron microscope and a BIOLAM optical microscope. The experiments were performed at room temperature.

3. Classification of different types of electrodeless microwave discharges developing at the surface of dielectrics

As well known pulsed microwave radiation excites electrodeless microwave discharges of different types developing at the surface of solid-state dielectrics in vacuum [5–12]. There are three types of electrodeless microwave discharges developing at the single surface of the dielectrics in vacuum:

- secondary electron emission microwave discharge (SEEMD),
- surface microwave breakdown (SMB) taking a form of a contracted discharge,
- plasma-flare microwave discharge (PFMD).

The SEEMD transforms to the PFMD passing through the stage of the microwave breakdown on the surface of the crystals in vacuum:

$$\text{SEEMD} \rightarrow \text{SMB} \rightarrow \text{PFMD}.$$

The mechanisms of these transformations have a great importance for the understanding of excitation and evolution of different types of microwave discharges at the surface of dielectrics. We study these mechanisms experimentally.

3.1. Secondary electron emission microwave discharge (SEEMD)

The SEEMD arises when $\varepsilon = e^2 E_0^2 / 2m\omega^2 > W_1$ and exists during the breakdown delay time $\Delta\tau < \tau$. Corresponding threshold electric field $(E_0)_{thr}$ is determined from the condition: $(E_0)_{thr} = [2m\omega^2 W_1 / e^2]^{1/2}$, where ε is the oscillation energy of electron, E_0 is the electric field amplitude of microwaves, e and m are the specific charge and mass of an electron, ω is the angular frequency of microwaves, W_1 is the first critical potential for the surface of solids, τ is the time duration of the microwave pulse, $\Delta\tau$ is the time duration of SEEMD, $(E_0)_{thr}$ is the threshold electric field for the onset both of the SEEMD and of the contracted discharge. Electrons of SEEMD have energies on the order of the oscillation energy ε . High pulsed electron current densities reach the value $j_e \leq (E_0 \omega) / 4\pi \sim \sim 1 \text{ A/cm}^2$. Microwave absorption coefficient (per unit area of the crystal) in the stage of the SEEMD is low:

$$\eta \sim eE_0 / m\omega c \sim 10^{-2}.$$

The high intensity luminescence of short-lived color centers, temporarily induced in the near-surface layer of pure dielectrics by pulsed electrodeless microwave discharges at the stage of SEEMD, were measured at room temperature. This luminescence was uniform over the surface of dielectrics.

It was found that the characteristic time of the luminescence growth/decay of LiF crystals, excited by pulsed microwave discharges at room temperature, was about 1 μs . These luminescence spectra of short-lived F_2^- и F_3^+ color centers were very close to the photo-luminescence spectra measured for LiF crystals previously colored by microwave discharges and containing stable F_2^- и F_3^+ centers.

The density of short-lived F , F_2 and F_3^+ color centers can reach the values of 10^{19} – 10^{20} cm^{-3} in the thin surface layer ($\sim 10^{-4}$ cm). The density of defects that are induced by the SEEMD electrons is much larger than the density of defects that are induced by X-rays, γ -rays, and relativistic electron beams [7, 9–12].

3.2. Microwave breakdown on the surface of dielectrics (SMB)

Surface microwave breakdown is initiated by the SEEMD. When the electrons of the SEEMD bombard the dielectric crystals, high density of electronic excitations (electron-hole pairs, excitons, plasmons) arises in the surface layer. Decay of the excitations leads to creation of "metastable" color centers with lifetime ~ 1 μs at room temperature. During the breakdown delay time $\Delta\tau$ an accumulation of these centers takes place. An increase in the length τ or the intensity S of the microwave pulse results in increase the concentrations of the centers up to 10^{19} cm^{-3} in the thin near-surface layer of the crystals. Recombination of the centers leads to the formation of an electron-hole plasma with such high carrier density, that a local electric field intensification arises near inhomogeneities in the plasma density. Absorption of microwave energy in these plasma regions produces phonons, so that a local heating of the crystal lattice stimulates the explosive recombination of short-lived centers and plasma production again. As a result of these processes the plasma channels intergrow in a near-surface layer of the crystals and stretch out along the electric field vector of the wave. The seed electron density in the conduction band of the crystals required to initiate this process is $n_e \sim 10^{15}$ cm^{-3} . The concentrations of "metastable" centers on the order of 10^{17} cm^{-3} are reached in our experiments, so that these values are sufficient here [8].

The breakdown delay time $\Delta\tau < \tau$ obeys the empirical law: $(S - S_{thr}) \cdot \Delta\tau = \text{const}$, where S_{thr} is the threshold intensity for the onset of the SEEMD. The value of the const is determined by the nature of the crystals: $\text{const} \approx (0.04\text{--}0.8)$ J/cm^2 , $\text{const} \sim \omega$. The breakdown is accompanied by the absorption of microwave energy up to 100 % with a time scale $\delta\tau \sim (0.05\text{--}0.1)$ μs , an intense flash of light, and a burst of electron and ion currents from the contracted discharge [6, 8].

3.3. Plasma-flare microwave discharge (PFMD)

PFMD is produced as a result of an evolution of the microwave breakdown on the surface of dielectrics and is accompanied by the formation of dense plasma with an electron concentration which is much more than the critical one $n_c = m\omega^2/4\pi e^2$. PFMD is characterized by a strong absorption of microwave power ($\approx 20\text{--}50$ %). The following phenomena take place in PFMD [4, 6]:

- excitation of strong Langmuir waves in a plasma resonance region (where an electron plasma concentration n_e is the same that the critical one $n_e = n_c$),

- acceleration of electrons up to maximal energies $\varepsilon_{e \max} \approx 2\pi e E_0 (L\lambda)^{1/2}$ due to a self-breaking of strong Langmuir waves (λ – the wavelength of microwave radiation, L – the characteristic length of the plasma in the resonance region),
- acceleration of ions up to maximal energies $\varepsilon_i \approx eZ\phi$ (Z – the charge number of the ions) due to a positive potential jump $\phi \sim 2\pi e_0 (L\lambda)^{1/2}$ in a plasma resonance region,
- transformation of microwave power to the power of quasistationary electric current in the plasma.

4. Destructions on the surface and in the bulk of dielectrics interacting with microwave discharges

At the stage of SEEMD there is a bombardment of the surface of dielectrics by electrons with characteristic energies of about 100–1000 eV. A depth of penetration of these electrons in dielectrics is 0.01–0.1 microns. A pulsed interaction of electrons with the surface of dielectrics during 1–10 microseconds results in pulsed heating of the surface of dielectrics up to the temperature of ~ 1 K. Thus, in the near-surface layer of dielectrics a depth of about 1–3 microns characterized by a high temperature gradient of about $(3 \cdot 10^3 - 1 \cdot 10^4)$ K/cm, which

causes strong thermo-mechanical tensions. In anisotropic Alkali-Halide LiF, NaCl, KCl crystals, which are characterized by high factors of temperature expansion ($\sim 1 \cdot 10^{-4} \text{ K}^{-1}$), a strong cracking is observed in the near-surface layer of the crystals along its cleavage planes (Fig. 1).

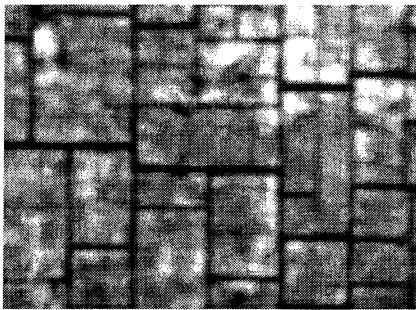


Fig. 1. Micro-cracks on the surface of LiF crystal.

At the stage of microwave breakdown of dielectrics (as a result of occurrence of the induced electrical conductivity and strong absorption of microwave radiation power in contracted plasma channels on the surface

of dielectrics) there are an intensive local interaction of dense plasma with dielectrics and formation of destruction tracks on the surface of dielectrics. The characteristic diameter of cross section of single destruction tracks on the surface of NaCl crystals is $\sim 10 \mu\text{m}$ (Fig. 2, 3).

As a result of repeated microwave breakdowns, new types of destructions of dielectrics are observed: (*) craters on the surface of dielectrics, (**) dendrites – a system of destruction branches in the bulk of dielectrics. The craters are formed on the destruction tracks on the surface of dielectrics, and the dendrites sprouts from the craters deep into the bulk of dielectrics.

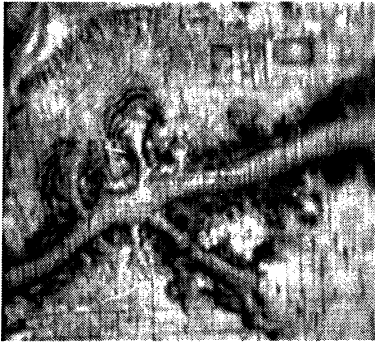


Fig. 2. Track on the surface of NaCl crystal



Fig. 3. Cross section of track in NaCl crystal

The characteristic diameter of craters on the surface of Alkali-Halide LiF, NaCl, KCl crystals is 150 microns, on the surface of ZrO_2 crystals – 50 microns, and on the surface of Teflon – 300 microns. The characteristic diameter of cross section of dendrites in the bulk of Alkali-Halide LiF, NaCl, KCl crystals is ~ 10–100 microns, and in the bulk of Teflon and polyethylene – 10–200 microns (Fig. 4–9).

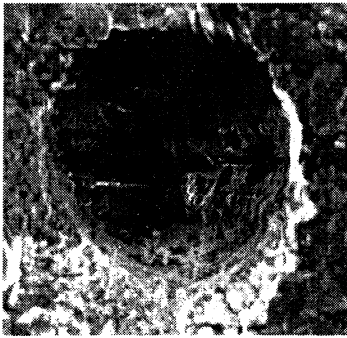


Fig. 4. Crater on the surface of LiF crystal

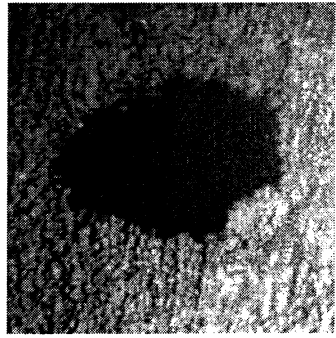


Fig. 5. Crater on the surface of Teflon

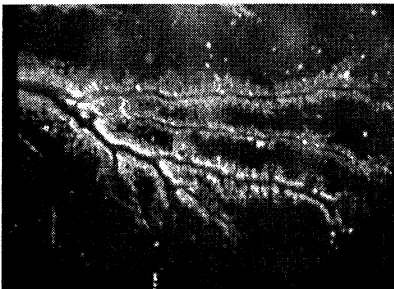


Fig. 6. Dendrite in the bulk of NaCl crystal

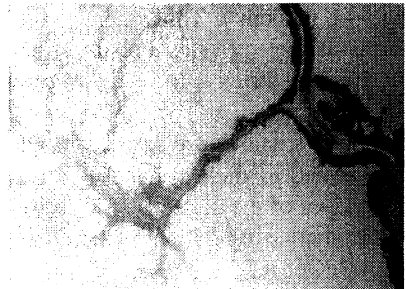


Fig. 7. Dendrite in the bulk of polyethylene

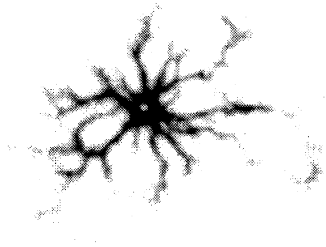


Fig. 8. Crater and dendrite in ZrO_2 crystal

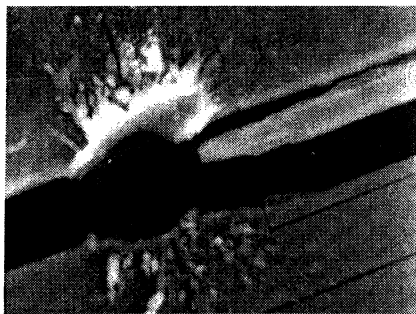


Fig. 9. Crater and macro-crack on the surface of NaCl crystal

At the stage of the plasma-flare microwave discharge there is a dense collisionless plasma with the maximal concentration of electrons near the surface of dielectrics $n_{\max} \sim 1 \cdot 10^{13} \text{ cm}^{-3}$, much exceeding the critical electron concentration in plasma $n_c = m\omega^2/4\pi e^2 \approx (5 \cdot 10^{10} - 6 \cdot 10^{11}) \text{ cm}^{-3}$ for microwave radiation with the frequency 2–7 GHz. The intensive absorption of microwave radiation power (20–50%) in a plasma-resonance region causes an excitation of strong Langmuir waves, which self-breaking results in generation of a flow of fast nonequilibrium electrons with characteristic energies of 15–20 keV. Due to an ejection of fast electrons from the plasma a jump of quasistationary positive potential inside plasma flare is formed. The value of this potential is comparable to characteristic energy of fast electrons and is 10–15 kV. Electrons with energies less than 10–15 keV bombard the surface of dielectrics. The depth of penetration of these electrons in the near-surface layer of dielectrics is 1–3 microns. A pulsed interaction of these fast electrons with dielectrics during 1–10 μs results in pulsed heating of the near-surface layer of dielectrics up to the temperature of $\sim 10^2$ – 10^3 K. Such high temperature exceeds the temperature of melting for many amorphous dielectrics and causes destructions in the near-surface layer of these dielectrics as a result of processes of melting and evaporation of substance. The average rate of evaporation of substance from the surface of amorphous dielectrics reaches the value $\sim 1 \text{ g}/(\text{s} \cdot \text{cm}^2)$. Thus, there is a strong erosion of the near-surface layer of amorphous dielectrics as a result of processes of melting and evaporation of substance of dielectrics at the stage of plasma-flare discharge. Besides, both the high temperature gradient of about $(3 \cdot 10^5 - 5 \cdot 10^6) \text{ K}/\text{cm}$ and the high thermo-mechanical tensions are formed in near-surface layers (with the depth of about 3–6 microns) of dielectrics. These tensions cause a strong cracking of the near-surface layer of the dielectric LiF, NaCl, KCl crystals along its cleavage planes.

The increasing of temperature in the bulk of dielectrics up to the value of 100–300 K occurs as a result of repeated pulsed interactions (number of pulses is $\sim 10^3$ – 10^4 , pulse repetition frequency is 1–10 Hz) of plasma-flare microwave dis-

charges with dielectrics. It results in essential change of mechanical and electrical properties of dielectrics. In particular, the mechanical fluidity is increased and the threshold of thermal electrical breakdown of dielectrics is decreased.

It can result in an essential decreasing of the threshold of the thermoelectrical breakdown in the bulk of dielectrics in a field of microwave radiation.

5. Classification of destructions in dielectrics excited by microwave discharges

Thus, during the studying of an interaction of electrodeless pulsed microwave discharges with dielectrics some types of destructions on the surface and in the bulk of crystal and amorphous dielectrics were discovered. The analysis of properties of these destructions allows us to develop the following classification of different types of destructions.

1. Micro-cracks, created in the near-surface layer of dielectric crystals along its cleavage planes (at the stages of secondary electron emission microwave discharge, microwave breakdown, plasma-flare microwave discharge).

2. Tracks, created on the surface of both crystal dielectrics and amorphous dielectrics (at the stage of microwave breakdown).

3. Craters, created on the surface of both crystal dielectrics and amorphous dielectrics (at the stage of microwave breakdown).

4. Dendrites, created in the bulk of both crystal dielectrics and amorphous dielectrics (at the stage of microwave breakdown).

5. Macro-cracks, created on the surface and in the bulk of Alkali-Halide dielectric crystals (at the stage of microwave breakdown).

6. Erosion, created in the near-surface layer of amorphous dielectrics (at the stage of plasma-flare microwave discharge).

6. Conclusions

It is established, that the destructions on the surface and in the bulk of dielectrics are formed at all stages of interaction of electrodeless pulsed microwave discharges with these dielectrics. It is shown, that the different types of the destructions depend strongly on the types of localization of the interaction of microwave discharge plasma with dielectrics. It is observed, that the strongest localization of the interaction of microwave-discharge plasma with dielectrics arises at the stage of microwave breakdown, thus there are strongest destructions not only on the surface, but also in the bulk of dielectrics.

Acknowledgements. This work was supported by Russian Fund for Basic Research (Project № 03-02-17140).

References

1. *Brown S. C.* Basic Data of Plasma Physics. Cambridge, Mass. – London (England): M. I. T. press, 1966, 312 p.
2. *Sazonov V. P.* Output Elements of Powerful Microwave Devices for Vacuum Electronics (Review) [in Russian], Electronic Technics, Series of Microwave Electronics, 1967, **11**, 47.
3. Strong Microwaves in Plasmas. Vols. 1, 2. Ed. A. G. Litvak. Nizhny Novgorod: Institute of Applied Physics, 2000.
4. *Batanov G. M., Ivanov V. A., Kossyi I. A., Sergeichev K. F.* Large-Amplitude Plasma Waves and Particle Acceleration in the Plasma Corona of a Microwave Discharge. Sov. Phys. – J. Plasma Physics, 1986, **12**, 317.
5. *Batanov G. M., Ivanov V. A., Konyzhev M. E.* et al. Generation of High Potentials in the Plasma by the Interaction with Intense Microwave Radiation. In book: Strong Microwaves in Plasmas. Vol. 2. Ed. A. G. Litvak. Nizhny Novgorod: Institute of Applied Physics, 1991, 553.
6. *Batanov G. M. and Ivanov V. A.* Plasma-Flare Conversion of the Energy of Microwaves in the Decimeter Band into the Energy of Quasi-Stationary Electric Current. In book: Generation of Nonlinear Waves and Quasistationary Currents in Plasma. Ed. L. M. Kovrizhnykh (New-York: Nova Science Publishers, Inc., 1992), 227 p. (Proc. of the Institute of General Physics, Academy of Sciences of the USSR. Moscow: Nauka, 1988, **16**, 46 [in Russian]).
7. *Batanov G. M., Ivanov V. A., Konyzhev M. E.* et al. Creation of an Optically Dense Layer on the Surface of a Lithium Fluoride Crystal During Coloring in a Microwave Discharge. Sov. Phys. – J. Tech. Phys. Lett., 1993, **19**, 653.
8. *Batanov G. M., Ivanov V. A., Konyzhev M. E.* Microwave Breakdown of Ionic Crystals Initiated by a Secondary-Emission Discharge. Sov. Phys. – J. Exper. Theor. Phys. Lett. (JETP Lett.), 1994, **59**, 690.
9. *Ter-Mikirtychev V. V., Tsuboi T., Konyzhev M. E.* et al. Spectroscopic Characteristics of Color Centers Produced in a LiF Crystal Surface Layer by Microwave Discharge. Phys. Stat. Solidi B, 1996, **196**, 269.
10. *Batanov G. M., Ivanov V. A., Konyzhev M. E., and Letunov A. A.* Luminescence of Short-Lived Color Centers Induced in LiF Crystals by a Pulsed Microwave Discharge. Sov. Phys. – J. Exper. Theor. Phys. Lett. (JETP Lett.), 1997, **66**, 170.
11. *Ivanov V. A., Konyzhev M. E.* Interaction of microwave discharges with dielectric LiF crystals. In book: Microwave Discharges: fundamentals and applications (Proceedings of IV International Workshop). Ed. Yu. A. Lebedev. Moscow: Yanus-K, 2001. P. 219–228.
12. *Ivanov V. A., Konyzhev M. E.* Strong Interaction of electrodeless microwave discharges with dielectric LiF crystals. In Book: Proceedings of the XX-th International Symposium on Discharges and Electrical Insulation in Vacuum. Tiurs (France) – July1–5, 2002. Ed. SFV 2002. P. 499–502. IEEE Catalog Number 02CH37331. ISBN 0-7803-7394-4. ISSN 1093-2941.

MICROWAVE PLASMA-ASSISTED CVD DIAMOND FILM DEPOSITION IN PULSED AND CW REGIMES

A. L. Vikharev, A. M. Gorbachev, V. A. Koldanov, D. B. Radishev

Institute of Applied Physics, Nizhny Novgorod, Russia

This work is a study of possible advantages of the pulsed regime of microwave plasma-assisted CVD (MPACVD) reactor operation for diamond film synthesis. It is shown that at a fixed mean specific microwave power and substrate temperature the deposition rate increases in the pulsed regime as the pressure increases.

A widely used type of the CVD reactor for deposition of diamond films is the microwave reactor, in which the gas mixture is activated with a microwave discharge (microwave plasma-assisted CVD (MPACVD) reactor). Some experiments demonstrated that there are differences in the process of film deposition in the pulse-periodic regime of discharge maintenance as compared with the continuous (CW) regime [1–5]. The results of modeling CVD reactors numerically also show that the pulsed regime has its interesting features as compared to the CW regime [6–8]. This work is a study of possible advantages of the pulsed regime of MPACVD reactor operation for diamond film synthesis. The results of experiments in reactor based on microwave plasma-assisted CVD reactor with a structure similar to that described in [9] are presented. It is made as a cylindrical resonator excited at the TM_{013} mode by means of a coaxial waveguide at the frequency of 2.45 GHz (Fig. 1).

The rate and quality of film growth depend on the composition of the working mixture, its pressure and the microwave power absorbed in the reactor. Specifically, as the pressure is increased with the composition of the working mixture held constant, the linear growth rate increases. However, two main parameters, pressure and power, determine the volume of the discharge region. For example, when the pressure increases, the dimensions of the discharge region become smaller, which results in the growth of mean specific power

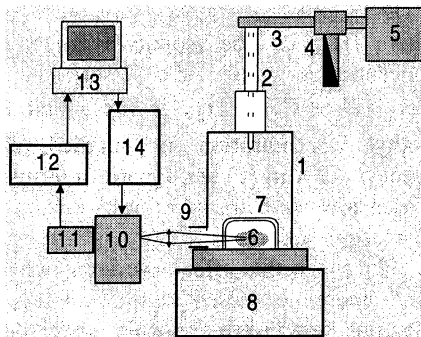


Fig. 1. The scheme of the experimental setup: 1 – cylindrical resonator; 2 – coaxial waveguide; 3 – rectangular waveguide; 4 – circulator; 5 – magnetron; 6 – discharge plasma; 7 – quartz dome; 8 – vacuum chamber; 9 – window in the resonator; 10 – monochromator; 11 – photomultiplier; 12 – digital oscilloscope; 13 – computer; 14 – monochromator controller.

(power per unit volume) absorbed in the plasma. Additionally, higher power leads to larger dimensions of the discharge region. Hence, when the dimensions of the substrate (the area of the deposited surface) are preset, in the continuous regime the gas pressure and microwave power prove to be interrelated. However, in the pulsed regime of discharge maintenance the dimensions of the discharge region are determined not by the mean, but by the peak pulse power, therefore in this regime there appears the possibility to vary mean power and pressure independently while maintaining a constant plasma volume.

The substrate temperature is one of the key parameters in determining the growth rate and depends on the mean specific power absorbed in the plasma. In our case the substrate is heated by the discharge plasma and is cooled due to thermal conductivity of the substrate holder.

A noticeable modulation of the density of chemically active particles is observed in the pulsed regime at relatively low pulse repetition rates [5, 7, 8]. While retaining a mean density of hydrogen atoms, this regime can become more advantageous for film growth [8]. Basically, the growth rate is essentially dependent on the density of atomic hydrogen at the substrate surface. According to results of D. G. Goodwin [10], the growth rate G and relative defect density (the defect fraction in the film) X_{def} may be estimated by the following formulas:

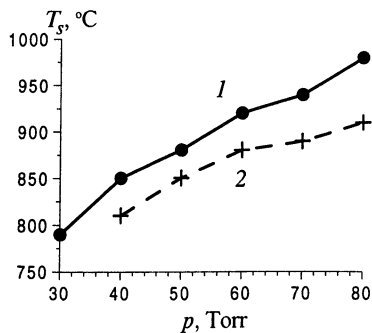
$$G \propto \frac{[\text{CH}_3]_{sur} [\text{H}]_{sur}}{3 \cdot 10^{15} \text{ cm}^{-3} + [\text{H}]_{sur}} \quad \text{and} \quad X_{def} \propto \frac{G}{[\text{H}]_{sur}^2}, \quad (1)$$

where $[\text{H}]_{sur}$ is the atomic hydrogen concentration and $[\text{CH}_3]_{sur}$ the methyl concentration at the surface. Often the gas-phase reaction, $\text{CH}_4 + \text{H} \leftrightarrow \text{CH}_3 + \text{H}_2$, is rapid and near partial equilibrium [10], therefore methyl concentration is coupled chemically to atomic hydrogen. The dependencies in (1) are square in terms of radical density, therefore modulation of densities with mean values retained should result in an increase in G and a decrease in X_{def} .

To check this effect, we compared the rate of diamond film growth in the continuous and pulsed regimes of reactor operation at the same mean power. Diamond films were deposited under the following conditions: mean microwave power 1500 kW, pulse duration $\tau = 5$ ms, pulse repetition rate $F = 100$ Hz, diameter of the silicon substrate 40 mm, hydrogen flow 200 sccm.

The substrate temperature T_s was monitored with an optical pyrometer. Figure 2 shows the pressure dependence of substrate temperature in the pulsed and CW regimes at the same average power. As it is seen from Fig. 2 T_s increases with pressure growth due to decrease of plasma volume and as result T_s increases due to growth of the mean specific power absorbed in the plasma. In the pulsed regime the substrate temperature is lower as the dimension of plasma is lager.

Fig. 2. Pressure dependence of substrate temperature in the CW (1) and pulsed (2) regimes at the same average power 1500 kW.



The pressure in the pulsed regime was higher than in the continuous one and was chosen so as to make the visually observed dimensions of the plasma equal in both regimes. In that case the mean specific power absorbed in the plasma and the substrate temperature were also equal (Fig. 2). In both cases the plasma fully covered the substrate and diamond film was deposited across the whole surface of substrate. The dependence of the film growth rate (determined as ratio of total film weight to deposition time) on the percentage of methane content is shown in Fig. 3. It is seen from the Figure that under equal pressure conditions (50 Torr) the pulsed regime has no advantages as compared with the continuous one; the pulsed regime is associated with a large plasma volume and, hence, lower mean specific power absorbed in the plasma. When the pressure is increased up to 70 Torr, the observed plasma volume in the pulsed regime becomes equal to that in the case of the CW regime at 50 Torr. In this case the pulsed regime leads to a higher film growth rate without any decrease of the film quality. In the pulsed regime the crystalline structure of the films is also more explicit as shown in Fig. 4. Raman spectra of the films produced in the continuous and the pulsed regimes are comparable as seen in Fig. 5.

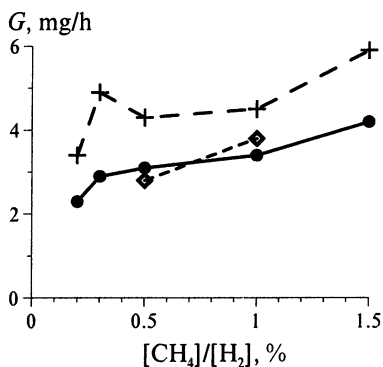


Fig. 3. Dependence of the diamond film growth rate on methane percentage content in the H_2+CH_4 mixture in the pulse (+, ♦) and continuous (•) regimes of reactor operation. The pressure of the gas mixture: • and ♦ - 50 Torr, + - 70 Torr; substrate temperature: + and • - $T_s = 880$ °C, ♦ - $T_s = 850$ °C.

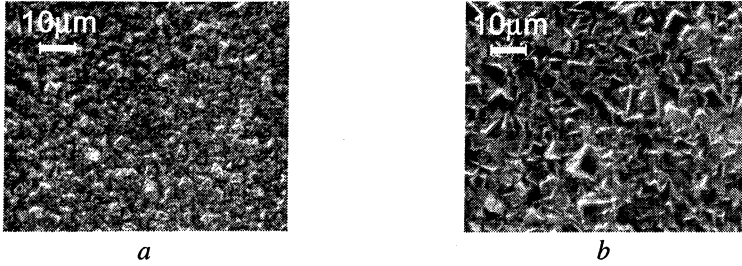


Fig. 4. Microphotos of the surface of diamond films produced under the pressure of 50 Torr in the continuous (*a*) and under 70 Torr in the pulsed (*b*) regimes. Methane content equals 0.3%.

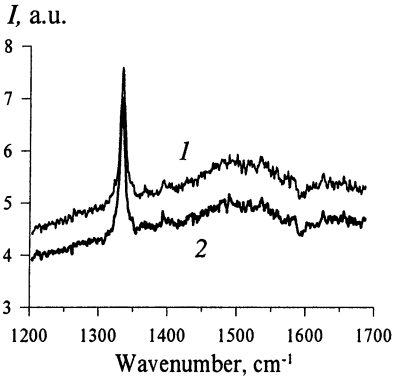


Fig. 5. Raman spectra of the films produced under the pressure of 50 Torr in the continuous (*1*) and under 70 Torr in the pulsed (*2*) regimes. The methane content equals 0.3%.

As seen from Eq. (1), an important role in film formation is played by hydrogen atoms. In order to measure the relative density of atomic hydrogen [H], we chose the well-known actinometry method, which is based on comparing intensities of radiation from atomic hydrogen and the actinometer, i.e. a chemically inert gas added in small amounts to the working mixture. We chose the pair of lines, hydrogen H_γ (wavelength 4340 Å) and argon (8115 Å), which is convenient for actinometric measurements under these conditions [11]. Figures 6 and 7 show the ratios of intensities of these lines, which the ratio of hydrogen atom density to the total density of neutral particles in the discharge is proportional to. In the pulsed regime a modulation of hydrogen atom density is observed. Along with that, under the conditions of film deposition the maximum hydrogen density in the pulsed regime under the pressure of 70 Torr exceeds noticeably the density in the continuous regime under the pressure of 50 Torr. On the contrary, in the pulsed regime under the pressure of 50 Torr the density of hydrogen atoms does not exceed the density in the continuous regime at the same pressure.

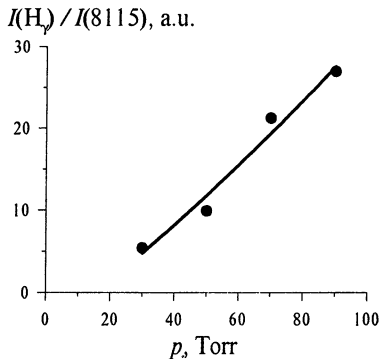


Fig. 6. Dependence of the ratio of intensities of lines H_γ (4340 Å) and Ar (8115 Å) on gas pressure in the continuous regime of reactor operation.

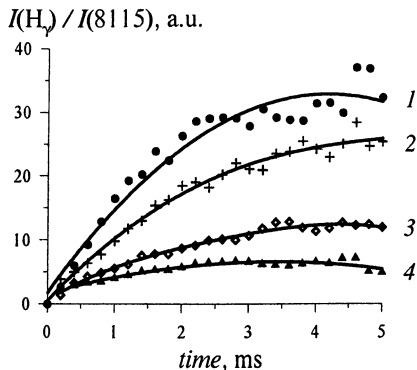
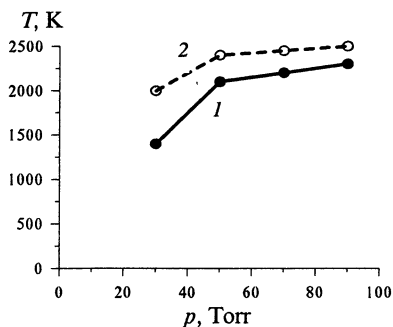


Fig. 7. Dynamics of the ratio of intensities of lines H_γ (4340 Å) and Ar (8115 Å) during a pulse under different gas pressures: 1 - 90, 2 - 70, 3 - 50 and 4 - 30 Torr.

The absolute density of hydrogen atoms depends on gas density, which is determined by pressure and temperature. The neutral gas temperature was measured by the distribution of the emission line intensities of the resolved rotational structure of the R-branch (0-0) in the $G_1\Sigma_g^+ \rightarrow B_1\Sigma_u^+$ band of hydrogen and the unresolved rotational structure 2+ of the nitrogen system (0-0 transition) added in small quantities for diagnostic¹ [12]. Both methods yield results close to each other [12], but the error of the hydrogen measurements is much greater. The results of temperature measurements are shown in Fig. 8. As seen from the plots presented, the gas temperature grows only slightly with the increase in pressure; correspondingly, gas density in the reactor grows as the pressure increases.

Fig. 8. Dependence of gas temperature on the pressure in the continuous regime (1) and of the maximum gas temperature achievable in the pulse regime (2) on the pressure.



¹ No films were grown in the presence of nitrogen. To measure temperature by this method, separate experiments were performed.

That is why the increase in absolute density of hydrogen atoms in Eq. (1) occurs faster as the pressure grows, than the observed growth of relative density, which is proportional to the ratio of line intensities shown in Figs. 6 and 7.

Thus, the modulation of density of chemically active particles that occurs in the pulsed regime benefits the growth of diamond films even when the mean value of the density is retained, which agrees with the results of numerical estimates [8]. It should be noted that the advantages of the pulsed regime manifest themselves only in the case when the plasma volume does not change and the mean specific power absorbed in the plasma is retained, i.e. when the pressure grows with the growth of the peak power.

One can explain it in other words in the following way. As follows from the results presented, the pressure increase is accompanied with a fast increase of hydrogen atom density, hence the increase of the pressure in the reactor is conducive to faster film growth. However, in the continuous regime, as the pressure grows, the dimensions of the discharge region become smaller, and the plasma does not cover the whole substrate area. The transition to the pulsed regime at the cost of greater peak power makes it possible to increase pressure while retaining plasma dimensions.

Thus, the experiments show that at a constant mean power and a fixed deposition area the pulsed regime allows using higher pressures of gas mixture. In this case a strong modulation of atomic hydrogen density $[H]$ may take place, but the mean value of $[H]$ remains the same. More specifically, experiments show that at the same specific power the growth rate of diamond film increases in the pulsed regime. This has implications that diamond deposition can be done in thermally floating substrate situations at higher pressures and hence with higher deposition rates in the pulsed regime as compared to CW without changing the substrate temperature. Examples of diamond deposition requiring a thermally floating substrate configuration include irregular-shaped, non-flat substrates and substrates with poor thermal conductivity.

Acknowledgements. This research was supported by the Russian Foundation for Basic Research under grant 00-02-16413. The authors are very grateful to J. Asmussen and T. A. Grotjohn from MSU (USA) with whom this work was started in the frame of CRDF grant RE1-352.

References

1. Laimer J., Shimokawa M., Matsumoto S., *Diam. Relat. Mater.*, **3**, 231 (1994).
2. Hatta A., Suzuki H., Kadota K. et al., *Plasma Sources Sci. Technol.*, **5**, 235 (1996).
3. Khachan J. and Gardner D., *J. Appl. Phys.*, **86**(11), 6576 (1999).
4. L. de Poucques, Bougdira J., Hugon R. et al., XXIV ICPIG (Warsaw, Poland), **1**, 203 (1999).
5. L. de Poucques, Bougdira J., Hugon R. et al., *J. Phys. D: Appl. Phys.*, **34**, 896 (2001).
6. Mankelevich Y. A., Rakhimov A. T., Suetin N. V. et al., *Diam. Relat. Mater.*, **5**, 964 (1996).

7. *Hassouni K., Duten X., Rousseau A. and Gicquel A.*, Plasma Sources Sci. Technol., **10**, 61 (2001).
8. *Gorbachev A. M., Koldanov V. A., Vikharev A. L.*, Diam. Relat. Mater., **10**, 61 (2001).
9. *Asmussen J.*, in High Density Plasma Sources, O. A. Popov, ed. (Noyes Publications, Park Ridge, 1995), 251.
10. *Goodwin D. G.*, J. Appl. Phys. **74**(11), 6888 (1993).
11. *Akhmedzhanov R. A., Vikharev A. L., Gorbachev A. M.* et al., Diam Relat. Mater., **11**, 579 (2002).
12. *Akhmedzhanov R. A., Vikharev A. L., Gorbachev A. M.* et al., XXIV ICPIG (Warsaw, Poland), **1**, 153 (1999).
13. *Grotjohn T. A. and Asmussen J.*, Microwave plasma-assisted diamond film deposition, in J. Asmussen and D. K. Reinhard, Diamond Films Handbook, Marcel Dekker, New York, 2001.

OPTICAL EMISSION DIAGNOSTICS OF MICROWAVE PLASMA IN A CVD REACTOR

*R. A. Akhmedzhanov, A. L. Vikharev, A. M. Gorbachev,
V. A. Koldanov, D. B. Radishev*

Institute of Applied Physics RAS, Nizhny Novgorod, Russia

This work is a study of different optical emission spectroscopy methods of gas temperature and atomic hydrogen density measurements in a microwave plasma-assisted CVD reactor for diamond film synthesis. Comparison of results obtained by different methods is presented. Optimal line pair for actinometric measurements is suggested.

The method of microwave plasma-assisted chemical vapour deposition (MPACVD) is widely used for synthesis of diamond films. Optimization of microwave reactor operation requires measurements of plasma parameters, such as gas temperature, atomic hydrogen and active radicals concentrations. Measurements in a running reactor require such methods that do not disturb plasma, are simple enough, and give reliable results. Optical emission spectroscopy has all of the required features. We tested different methods of gas temperature measurements by optical emission spectroscopy in a CVD-reactor, and measured atomic hydrogen concentration by the method of actinometry (by comparing the intensity of atomic hydrogen emission lines to lines of argon, used as an actinometer). The gas temperature was measured by observing spectral intensity distribution in R -branches of $d^3\Pi_u \rightarrow a^3\Sigma_g^+$ and $G^1\Sigma_g^+ \rightarrow B^1\Sigma_u^+$ transitions of hydrogen molecules. The gas temperature was also measured by adding small amount of nitrogen, and analyzing the rotational lines of $C^3\Pi_u$ of N_2 and $B^2\Sigma^+$ of CN emission spectra. Experimental setup for diamond deposition was described in details in the paper [1] submitted in this book.

Measurements of relative distribution of spectral lines intensities corresponding to transitions from rotational levels of excited molecular hydrogen are often used to determine the gas temperature in hydrogen plasmas. By measuring the intensity distribution, the rotational temperature T_{rot} of the upper level of hydrogen can be determined. At some condition it is possible to evaluate the gas kinetic temperature from rotational temperature of the upper level. Although there are many works devoted to determination of the gas temperature from the distribution of population of rotational levels, the results and evaluation methods are often contradicting. In [2], along with other methods, Q -branch of $d^3\Pi_u$ of molecular hydrogen was used, and it was supposed that the radiative lifetime of the upper level is long enough for the thermal equilibrium to establish. In [3] it was concluded that the thermal relaxation is not fast enough for the thermal equilibrium to establish, so T_{rot} differs from T_g . In [4] no direct relationship between rotational

temperature measured on $d^3\Pi_u$ state and on that of the ground state was found. In this paper the $G^1\Sigma_g^+$ state was used for determining the gas temperature, and the experimental results showed that the thermal relaxation was not complete. In [5] the experiments were performed in conditions close to typical CVD reactor, and it was found out that the emission from $d^3\Pi_u$ state was too weak, and the $G^1\Sigma_g^+$ level was completely thermalized. It seems reasonable to assume that the mechanism of formation of the distribution of population of rotational levels in molecular hydrogen strongly depends on experimental conditions, and for performing experiments in any specific conditions it is necessary to find a method that suits best for this particular conditions – gives precise enough results and is not overly complex.

In this paper we performed time-resolved temperature measurements by observing the relative spectral intensity distribution in R-branches of $d^3\Pi_u \rightarrow a^3\Sigma_g^+$ (0-0) and $G^1\Sigma_g^+ \rightarrow B^1\Sigma_u^+$ (0-0) transitions of hydrogen molecules. Unfortunately the intensity of Q-branch of $d^3\Pi_u \rightarrow a^3\Sigma_g^+$ transition recommended in [2, 3] was too weak in our experimental conditions to get reliable results.

In the case of Boltzmann distribution, the intensities of rotational lines are described by the formula

$$\frac{I_j}{S_j} = \exp\left(\frac{E_j}{kT_{rot}}\right),$$

where I_j – line intensity, S_j – line strength, E_j – upper level energy, T_{rot} – the rotational temperature. T_{rot} is then determined by the slope of plot of I_j/S_j dependence on E_j (Boltzmann plot). Example of the $G^1\Sigma_g^+$ spectrum and plot of dependence of I_j/S_j on E_j are shown in Fig. 1. Rotational temperature of the $d^3\Pi_u$ state was determined using R0–R5 lines. In the case of $G^1\Sigma_g^+$ lines, the temperature was determined by lines R0, R5, R7, R8 and R10. Lines R1–R4 are not resolved by our equipment, lines R6 and R9 were excluded because of their possible perturbation from the nearby levels. The plasma was considered optically thin on these wavelengths [6].

There are different approaches for evaluation of gas temperature T_g from rotational temperature T_{rot} depending on the time needed for V-T and V-R relaxation and on radiation lifetime of the upper level. If the radiation lifetime is long enough for the thermal equilibrium to establish, T_{rot} is equal to T_g . If the radiation lifetime is short and the distribution on the upper level "copies" that on the lower level $X^1\Sigma_g^+$, T_g corresponds to T_{rot} as the ratio of the rotational constants for these levels ($T_g/T_d = T_X/T_d = B_X/B_d$, where T_g – gas temperature, T_d and T_X – rotational temperatures of $d^3\Pi_u$ and $X^1\Sigma_g^+$ respectively, B_X and B_d – rotational constants for $d^3\Pi_u$ and $X^1\Sigma_g^+$ levels). Our estimations show that the collision rate ν_{coll} in our conditions is at least several times higher than the radiational rate ν , both for $d^3\Pi_u$ and $G^1\Sigma_g^+$, so we assume T_g to be in equilibrium with T_{rot} .

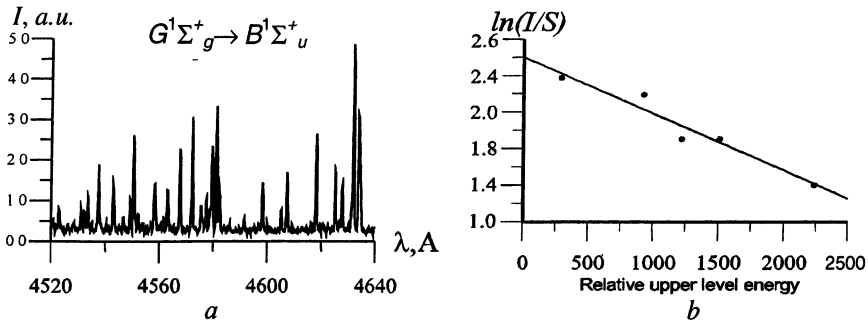


Fig. 1. Example of $G^1\Sigma_g^+ \rightarrow B^1\Sigma_u^+$ emission spectrum of molecular hydrogen; typical Boltzmann plot for this band.

The gas temperature was also measured by adding a small amount of nitrogen, and analyzing the spectrum of unresolved rotational structure of $N_2 C^3\Pi_u$ and $CN B^2\Sigma^+$. Small addition of nitrogen, although it changes the chemistry of the process, does not lead to a noticeable change in gas temperature. Nitrogen was not added in running CVD reactor during film deposition; it was used for temperature measurements in separate experiments. Temperature determination was done by fitting the theoretical curve to experimental points.

The results of temperature measurements by emission of $N_2 C^3\Pi_u$ (0-0) and (0-2) bands, $CN B^2\Sigma^+$ level, R-branches of $d^3\Pi_u \rightarrow a^3\Sigma_g^+$ (0-0) and $G^1\Sigma_g^+ \rightarrow B^1\Sigma_u^+$

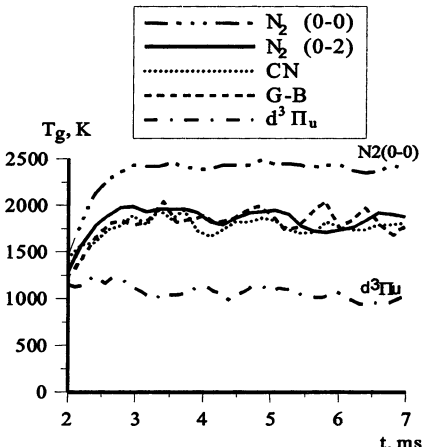


Fig. 2. Time dynamics of gas temperature, measured by emission of $C^3\Pi_u$ (0-0) and (0-2) bands; $CN B^2\Sigma^+$ level; R-branches of $d^3\Pi_u \rightarrow a^3\Sigma_g^+$ (0-0) and $G^1\Sigma_g^+ \rightarrow B^1\Sigma_u^+$ (0-0) bands of molecular hydrogen.

(0-0) bands of molecular hydrogen are shown in Fig. 2 for the following experimental conditions: gas pressure 50 Torr, average power 1500 W, pulse duration 5 ms and duty cycle 0.5. It is seen that the results obtained from (0-2) $C^3\Pi_u$ band of nitrogen, $B^2\Sigma^+$ band of CN and R-branch of $G^1\Sigma_g^+$ band of molecular hydrogen are in good coincidence with each other. Measurements using the (0-0) band of N_2 give higher temperatures, because of notable blending with other emission lines. The measurements by molecular hydrogen system $d^3\Pi_u$ give a constant temperature, independent both of the time and of the experimental conditions. Evaluating T_g as $T_g =$

$= T_{rot,d} \cdot B_X/B_d$ gives higher temperature values, but these values still does not depend on experimental conditions. That means that the R -branch of $d^3\Pi_u$ system cannot be used for determination of the gas temperature in our case. Since we can not add nitrogen during actual film deposition, measuring of gas temperature by emission from the R -branch of $G^1\Sigma_g^+$ of molecular hydrogen seems to be optimal choice for CVD reactor.

It should be noted that the minimal temperature measured in discharge was about 1000 K. Our previous experiments on other setup showed that the $G^1\Sigma_g^+$ state does not work well for the gas temperature below about 700–800 K [8]. That means that the $G^1\Sigma_g^+$ band should be used with caution for temperature measurements in a relatively cold gas.

Another important parameter that plays a significant role in diamond film deposition is the density of atomic hydrogen. In order to measure the density of atomic hydrogen [H], we chose the actinometry method, which is based on comparing intensities of radiation of atomic hydrogen and the actinometer, a chemically inert gas added in small amounts to the working mixture. For the results obtained by this method to be adequate, the following conditions should be met both for the atoms of hydrogen and the actinometer: (1) the radiating level should be excited by the electron impact from the ground state; (2) the threshold excitation energies should be possibly close to each other; (3) the levels should be quenched in a known way.

The question of applicability of different line pairs for actinometry was discussed in [9]. The first condition, as shown in [7], is usually fulfilled during the MPACVD reactor operation. Basing on the results of work [7] one can conclude that the following lines of hydrogen and argon, which are often used, are not quite good for that purpose: H_α ($\lambda = 6563 \text{ \AA}$, energy of the upper level $E = 12.09 \text{ eV}$) and Ar (8115 \AA , 13.08 eV), as well as H_α and Ar (7504 \AA , 13.48 eV). Though the difference between the excitation energies for these pairs is low as compared with the excitation energy, it is comparable with the average electron energy. This leads to a steep dependence of the ratio of excitation constants on the value of E/N . However, argon can be used for actinometry using the pair of lines of H_γ (4340 \AA , 13.06 eV) and Ar (8115 \AA , 13.08 eV) which have almost equal energies of the upper level, and the role of the dissociate excitation for the H_γ line is minimal.

Investigation of different argon lines dynamic [9] showed that the behaviour of the Ar ($2p_1$, 7504 \AA) line is significantly different from other argon lines. Apparently, this is associated with a considerably lower value of the constant of the $2p_1$ level quenching; that is why spontaneous radiation plays a noticeable part in de-excitation of this level [10]. As the result, the mechanism of Ar (7504 \AA) level quenching may change when the discharge condition change, and the use of this line may result in measurement errors. Dynamic of H_γ and Ar (8115 \AA) lines during microwave pulse is shown in Fig. 3.

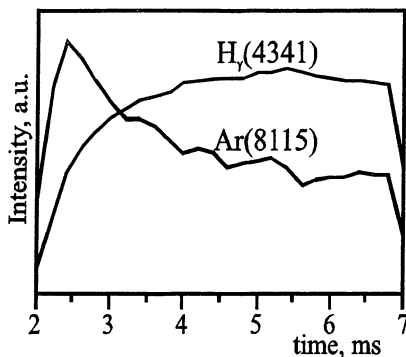


Fig. 3. Intensity of H_γ and Ar (8115 Å) lines during microwave pulse at pressure 70 Torr, peak power 1.5 kW. Line intensities are shown in different scales.

It is interesting to consider the intensity dynamics of the continuum spectrum of molecular hydrogen I_{cont} (measured near 4340 Å) as compared to the dynamics of argon and atomic hydrogen lines. The ratio of I_{cont} to intensity of Ar ($\lambda = 8115$ Å), as shown in Fig. 4, remains approximately the same (for a given width of a monochromator slit) during the pulse in a wide range of experimental conditions (pressure ranges from 30 to 90 Torr, microwave power from 1 to 3 kW). This fact may be understood if we consider that the value of E/N (the ratio of the electric field, E , to the gas density, N) is the same in various experimental conditions according to the results of numerical modeling [9], and that the ratio of the excitation rate for argon and for molecular hydrogen does not change significantly.

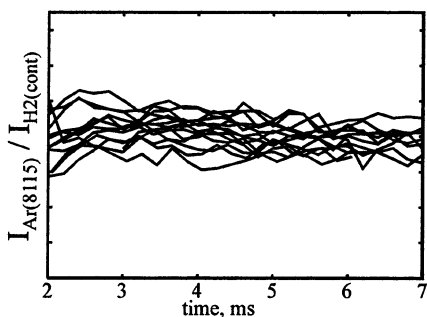


Fig. 4. The ratio of intensity of Ar ($\lambda = 8115$ Å) line to intensity of continuum spectrum of molecular hydrogen.

Although, this problem requires further studies, we may suggest using the emission of the continuum spectrum of molecular hydrogen (after "calibration" for a given optical registration system parameters) as a "substitute actinometer" during reactor operation. This allows to make measurements for estimation of atomic hydrogen concentration without adding actual actinometer, which is especially important during a real deposition process.

This research was supported by the Russian Foundation for Basic Research under grant 00-02-16413.

References

1. *Vikharev A. L., Gorbachev A. M. et al.*, in Proc. of 5th Int. Workshop "Strong Microwaves in Plasmas", 2002.
2. *Gritsinin S. I., Kossyi I. A., Malykh N. I. et al.*, J. Phys. D: Appl. Phys., 1998, **31**, 2942.
3. *Tomasini L., Rousseau A., Gousset G. et al.*, J. Phys. D: Appl. Phys., 1996, **29**, 1006.
4. *Gicquel A., Hassouni K., Breton Y. et al.*, Diam. Rel. Mat., 1996, **5**, 366.
5. *Duten X., Rousseau A., Gicquel A. et al.*, J. Phys. D: Appl. Phys., 2002, **35**, 1939.
6. *Chu H. N., Den Hartog E. A., Leskow A. R. et al.*, Phys. Rev. A, 1991, **44**, 3796.
7. *Diatko N. A., Kashko D. A., et al.*, Plasma Physics Reports, 1998, **24**, 1114.
8. *Akhmedzhanov R. A., Vikharev A. L., et al.*, XXIV ICPIG, 1999, **1**, 153.
9. *Akhmedzhanov R. A., Vikharev A. L., et al.*, Diam. Rel. Mater., 2002, **11**, 579.
10. *Francis A., Czarnetzki U., Dobele H. F. et al.*, XXIV ICPIG, 1999, **4**, 43.

MODELING OF ELECTRONEGATIVE PLASMAS FOR DESIGN OF MICROWAVE APPLICATORS

D. Korzec, J. Engemann

Forschungszentrum für Mikrostrukturtechnik - *fmt*, University of Wuppertal, Germany

The electrical properties of non-equilibrium electronegative plasma generated in pressure range of mbar can be modeled by real conductivity for microwave field simulation programs. The simulation example of a 2.45 GHz microwave plasma source for production of light guide preform shows the influence of the plasma density, electron temperature and O₂/SiCl₄ gas mixture on the field patterns.

Introduction

A substantial effort was focused recently on surface wave microwave plasma sources [1]. Most of this work deals with electropositive plasmas allowing the fulfillment of the over-dense plasma conditions [2]. But the most interesting from the point of view of technological applications are the electronegative plasmas. As examples the surface cleaning in oxygen plasma [3], etching in fluorine chemistry [4], deposition of silicon dioxide [5] or titanium dioxide [6] in chloride plasmas can be cited. Techniques for modeling plasma by use of a zone with complex dielectric constant for application in electromagnetic field simulators [7] have been developed. They are especially suitable for electropositive plasmas with high electrical conductivity. But the electronegative plasmas show high resistivity in the plasma bulk and much higher penetration depth of microwaves due to electron concentration on orders of magnitude lower, than in electropositive plasmas. In this work we are showing an approach based on modeling the electronegative plasma by a zone of finite conductivity for use with modern microwave field calculation tools [8]. The presented design strategy allowed the development of a novel microwave plasma source for plasma enhanced chemical vapor deposition (PECVD) of silicon dioxide films from the O₂/SiCl₄ gas mixture. Using the total electron collision cross sections for SiCl₄ [9], O₂ [10] and C₂F₆ [11] the determination of electrical properties of the plasma is possible. It allows the design optimization not only for ignition but also for operation conditions.

Calculation of plasma conductivity

The real and imaginary part of the plasma conductivity can be described by the couple of well known formulas:

$$\operatorname{Re}(\sigma) = \frac{e^2 N_e}{m_e} \frac{\nu_e}{\nu_e^2 + \omega^2} \quad (1)$$

and

$$\text{Im}(\sigma) = -\frac{e^2 N_e}{m_e} \frac{\omega}{v_e^2 + \omega^2}, \quad (2)$$

where N_e is the electron concentration, ω is the excitation frequency and v_e is the electron collision frequency. For a mixture of n different species the collision frequency is given as:

$$v_e = \sum_{i=1}^{i=n} N_i \int_0^\infty \sigma_i(W) \sqrt{\frac{2eW}{m_e}} f(W) dW, \quad (3)$$

where the Maxwell – Boltzmann electron energy distribution function (EEDF):

$$f(W) = \frac{2}{\sqrt{\pi}} \left(\frac{e}{kT_e} \right) \sqrt{\frac{eW}{kT_e}} \exp\left(-\frac{eW}{kT_e}\right) \quad (4)$$

is assumed.

The total electron collision cross sections for relevant gases are known and presented graphically in Fig. 1. For numerical integration of eq. (3) the tabulated main values and linearly interpolated values between the main values are used. The collision frequencies calculated as a function of electron temperature for different gas mixtures are shown in Fig. 2. The corresponding real and imaginary part of the conductivity for electron concentration of 10^{17} m^{-3} and temperature of 1323 K is shown in Fig. 3 and 4 respectively. Accordingly to the ratio of the eq. (1) and eq. (2), the imaginary part of the conductivity can be neglected if the collision frequency is much higher than the excitation frequency. This condition is fulfilled for the considered pressure range and this fulfillment improves with increasing pressure.

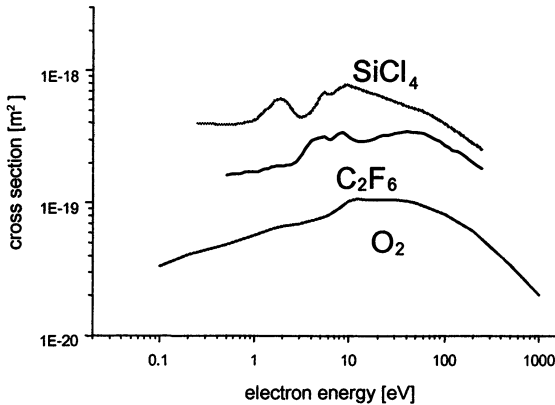


Fig. 1. The total cross sections for electron collisions with neutral particles in three main gases used for PECVD based production of light guide pre-forms.

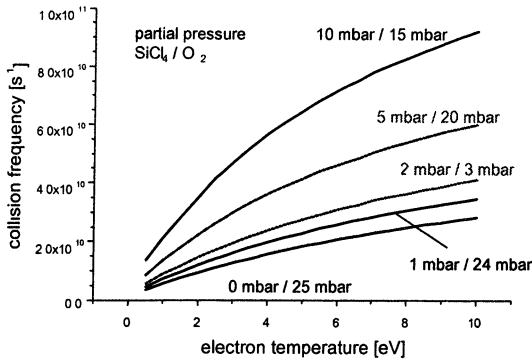


Fig. 2. Collision frequency of electrons in a silicon tetrachloride/oxygen gas mixture as a function of electron temperature for different partial pressure ratios.

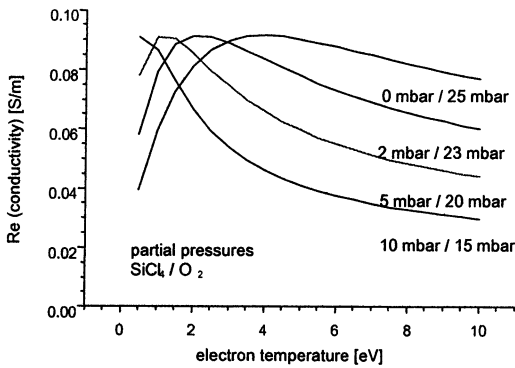


Fig. 3. Real part of plasma conductivity for electron concentration of 10^{17} m^{-3} and gas temperature of 1323 K.

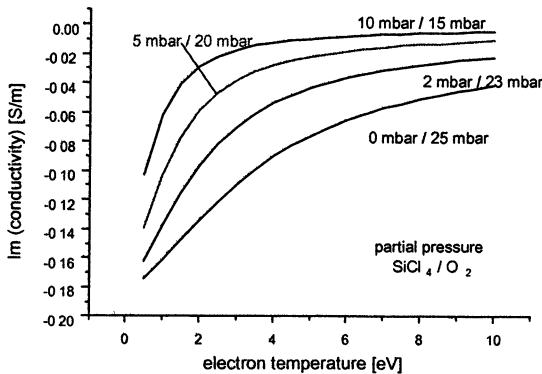


Fig. 4. Imaginary part of plasma conductivity for electron concentration of 10^{17} m^{-3} and gas temperature of 1323 K.

Modeling of the plasma source

For the calculation of the three-dimensional electromagnetic field distributions a commercial software package Microwave Studio of CST GmbH is used. In Figure 5 and 6 the field distributions in the symmetry plane perpendicular to the source axis and parallel to the source axis respectively are shown. The considered simulation example is plasma source based on the well known SLAN concept described in detail elsewhere [12]. The microwave power is coupled from a linear waveguide via movable coupling probe into the ring cavity and then via two slot antennas into the cylindrical cavity as shown in Figure 5. The geometry of the ring cavity is chosen for establishing a six field maxima. The position of the slot antennas in respect to the field pattern in the ring cavity allows the coupling of electromagnetic waves with equal phase but opposite direction, resulting in a very symmetric field pattern in the cylinder resonator. The field pattern established in the cylinder resonator before plasma ignition at operation frequency of 2.45 GHz corresponds to the eigenfrequency of a cylindrical cavity given as

$$f_{eigen} = c_0 \sqrt{\left(\frac{1.84}{2\pi r_{out}}\right)^2 + \left(\frac{5}{2l}\right)^2} \quad (5)$$

and has five maxima along the cylindrical resonator. Here r_{out} and l are the radius and length of the cylindrical resonator respectively.

After plasma ignition the field pattern is changing drastically. Assuming strongly conductive plasma, a coaxial mode with 7 maxima accordingly to formula

$$f_{eigen} = c_0 \sqrt{\left(\frac{2}{2\pi(r_{in} + r_{out})}\right)^2 + \left(\frac{7}{2l}\right)^2} \quad (6)$$

can be expected (see Fig. 10). Here r_{in} is the radius of the plasma column. The comparison of field patterns from Fig. 6 and Fig. 10 shows, that for both source conditions before plasma ignition and during plasma operation a clear resonant mode can be established. The conductivity model of plasma can help to design the source geometry for fulfillment of such source feature. It is especially attractive for pulsed operation of the source, which in other case must run with high mean value of reflected power.

An important output from the MICROWAVE STUDIO is the reflection factor calculated as a function of an excitation frequency. The electromagnetic waves are excited at predefined port. In our case the left edge of the waveguide (see Fig. 5) is defined as an excitation port.

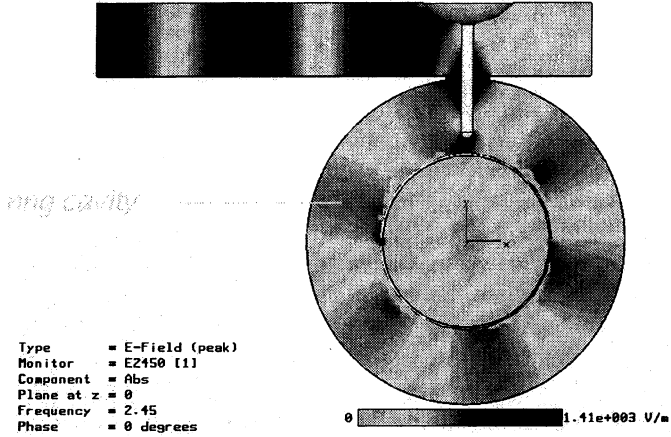


Fig. 5. Cross section of the plasma source perpendicular to the preform axis with E-field strengths calculated without plasma.

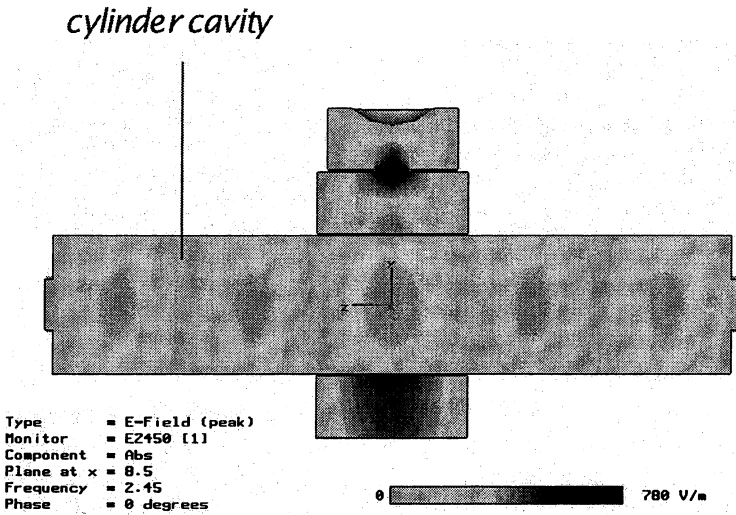


Fig. 6. Cross section of the plasma source parallel to the preform axis with E-field strengths calculated without plasma.

In Fig. 7 the influence of the plasma conductivity on the reflection factor curves is demonstrated. Strong influence of the plasma conductivity on the value of the eigenfrequency in the vicinity of 2.45 GHz can be observed. This part of

the curve is related to the cylindrical resonator resonance. Even though the entire plasma column is modeled as a uniform block with constant conductivity, disregarding the diffusion and field determined electron concentration variations, the influence of the plasma on the eigenfrequency of the resonator and its quality can be studied.

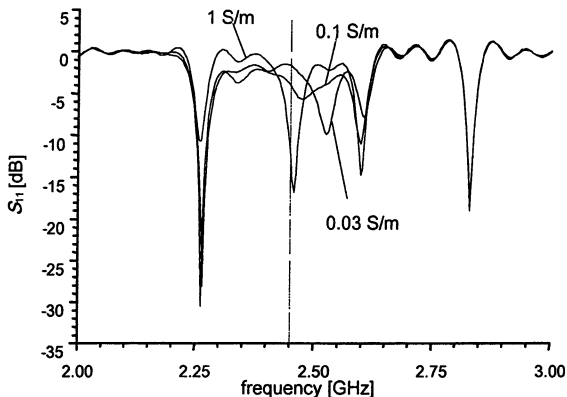


Fig. 7. Reflection factor vs frequency for three different plasma conductivities.

In Figs. 8, 9 and 10 the field distributions for plasma conductivity of 0.1 S/m, 1 S/m and 5 S/m respectively are displayed. They demonstrate the gradual transition from the cylindrical mode with five maxima establishing without or with very weak plasma to the coaxial mode with seven maxima along the plasma column for high conducting plasma.

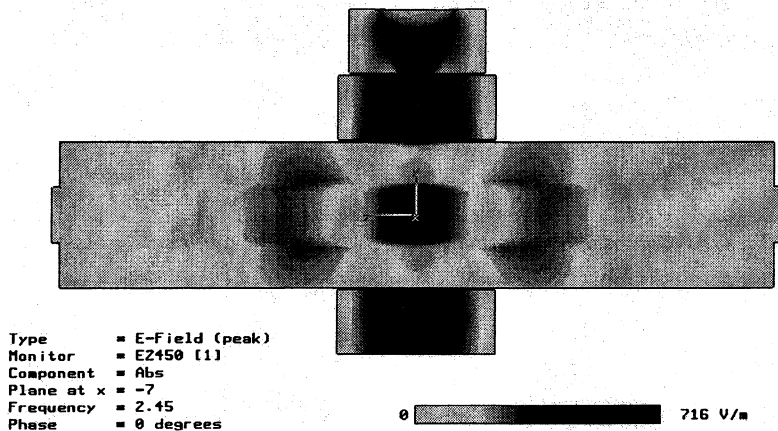


Fig. 8. Cross section of the plasma source parallel to the preform axis showing the electric field distribution for 0.1 S/m.

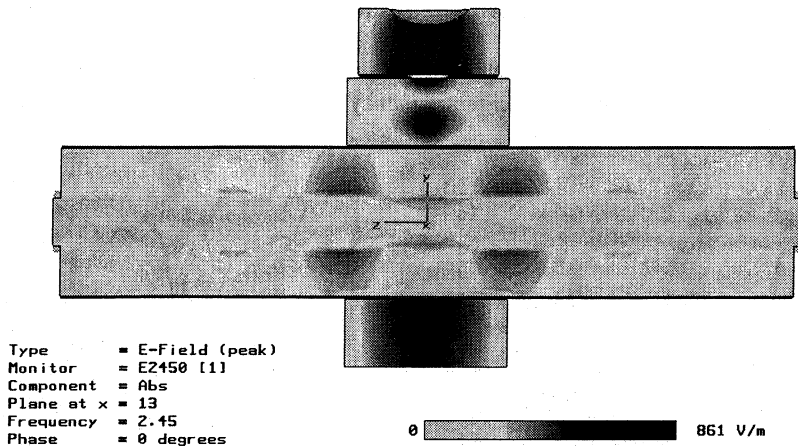


Fig. 9. Cross section of the plasma source parallel to the preform axis showing the electric field distribution for 1 S/m.

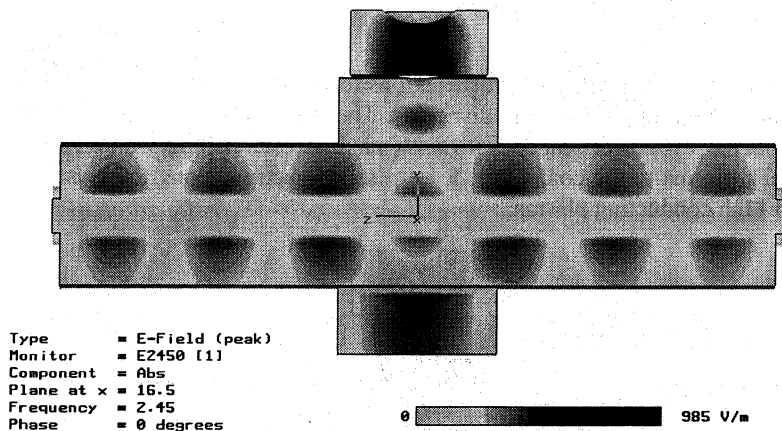


Fig. 10. Cross section of the plasma source parallel to the preform axis showing the electric field distribution for 5 S/m.

Conclusions

The electronegative plasma operated at pressure of more than 10 mbar can be modeled by real part of plasma conductivity. The model accuracy improves with increasing gas pressure and plasma electronegativity. Such model is useful for development of novel microwave applicators.

Acknowledgements. This work was performed in frame of a cooperation agreement of the first author with CST GmbH.

References

1. *Aliev Yu. M., Schlüter H., Shivarova A.* Guided-Wave-Produced Plasmas, Springer, 2000.
2. *Korzec D., Werner F., Winter R, Engemann J.* Plasma Sources Sci. Technol., **5**, 216 (1996).
3. *Winter R., Korzec D., Engemann J.* Surf. Coat. Technol., **93**, 134 (1997).
4. *Korzec D., Keßler T., Engemann J.* Appl. Surf. Sci., **46**, 299 (1990).
5. *Bauch H. et al.,* J. Opt. Comun., **8**, 130 (1987).
6. *Yeung K. S., Lam Y. W.* Thin Solid Films, **109**, 169 (1983).
7. *Walter M., Korzec D., Hütten H. M. and Engemann J.* Jpn. J. Appl. Phys., **36**, 4777 (1997).
8. Microwave Studio Reference Manual, CST GmbH.
9. *Możejko P. et al.,* Eur. Phys. J. D, **6**, 481 (1999).
10. *Itikawa Y. et al.,* J. Phys. Chem. Rev. Data, **18**, 23(1989).
11. *Szmytkowski C. et al.,* J. Phys. B, **33**, 15 (2000).
12. *Korzec D. et al.,* Plasma Sources Sci. Technol., **5**, 216 (1996).

ELECTRODE MICROWAVE DISCHARGES. STATE-OF-THE-ART

Yu. A. Lebedev, M. V. Mokeev, A. V. Tatarinov, I. L. Epstein

A. V. Topchiev Institute of Petrochemical Synthesis RAS, Moscow, Russia

Nonequilibrium nonuniform microwave discharges are briefly reviewed which can be generated at the top of an antenna introduced into a metal chamber at pressures 0.5–15 Torr in H₂, N₂, air, Ar and mixtures with CH₄, Ne. Discharge dimensions were less than chamber dimensions (chamber diameters were 8 and 14 cm). The structure and parameters of plasma (electron density and temperature, electric field strength, gas temperature) were studied by video camera, double probe method, plasma emission with spectral and spatial resolution, actinometry method. Results of quasi static modelling are briefly analyzed. General explanation of discharge structure is presented.

Microwave electrode discharges described below, are the discharges produced in the vicinity of powered electrode when characteristic dimension of plasma region is much less than dimensions of discharge vessel. This is the fundamental difference from conventional discharges where the plasma volume is controlled by the discharge vessel. This discharge property defines peculiarity both the electrodynamics of the discharge and plasma parameters and leads to self-organization of plasma.

During last years a lot of experimental results were obtained [1, 2, 5–10] but the physical processes occurred in the electrode microwave discharges are still far from a complete understanding. Some results of plasma chemical applications of such a discharge for diamond growth and CN_x-coatings deposition are presented in [3, 4].

One of important features of these discharges is the absence of electrode erosion in contrast to the electrode discharges at lower frequencies [2, 3]. This is related with absence of spraying of the electrode by ions accelerated in the near electrode sheath.

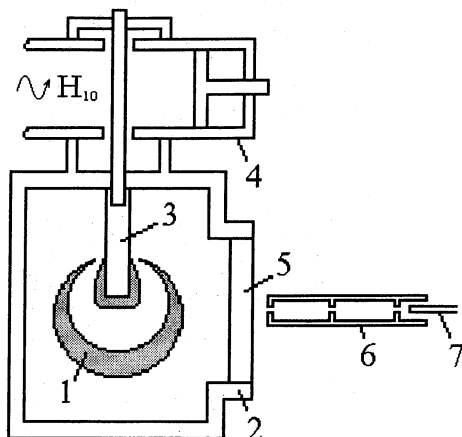
This paper briefly summarizes the known properties of the discharge and give some new results of experiments and modelling in the light of design of the picture of physical processes which can explain the observed discharge phenomena.

Experimental

Detail description of experimental set-up was presented in [1, 2]. Similar stainless steel cylindrical discharge cameras with diameters of discharge vessels $R_1 = 7$ cm and $R_2 = 4.2$ cm were used for experiments (Fig. 1). Plasmas in both arrangements revealed similar features, thus the properties of the described plasmas seems to be typical for the electrode microwave discharge systems. Plasma gases

Fig. 1. Experimental device.

1 - plasma, 2 - discharge chamber, 3 - antenna, 4 - waveguide-to coaxial converter, 5 - optical window, 6 - collimator, 7 - optical fiber.



were Ar, Ne, H₂, N₂, O₂, CH₄, C₂H₂, air, and their mixtures at pressures 0.5–15 Torr. Gas flow systems were used with total gas flow rate less than 1000 sccm.

A tubular and solid stainless steel and copper electrodes of different shapes (direct cylinder and bent electrodes, trident electrode, spiral electrode) with diameters of 0.5–6 mm have been used as the antennas.

Most of results has been obtained when the discharge was ignited at the end of cylindrical electrode (antenna). Microwave power (2.45 GHz) was transmitted from the magnetron generators with output powers of 2.5 kW or 150 W. The power absorbed in the system was measured by a directional coupler. The power absorbed in the discharge was obtained by subtracting of power losses in chamber without plasma from the power losses with plasma at the same incident power.

The set-up was equipped with the system of optical measurements. Discharge visualization was made with video camera (exposition times were ranged between 1/20 and 1/8000 s). Some results are shown in Fig. 2. Degree of hydrogen dissociation was defined by actinometry method [8]. Gas temperature of hydrogen plasma was defined in hydrogen plasma through the relative intensities of rotational lines of the electron excited molecules H₂(d²Π_u). Calculations were based on intensities of Q and R-branches emission for diagonal (v' = v'' = 0,1,2) bands of Fulcher α-system H₂(d²Π_u → a³Σ_g). Rotational temperature of the ground state of H₂ was calculated taking into account the ratio of rotational constants of the ground and excited states. The temperature had the flat radial distribution and does not exceed 700 K.

Parameters of electron component of the plasma and distributions of DC voltage in the plasma were measured with the help of a double electric probe [1, 2, 6, 7].

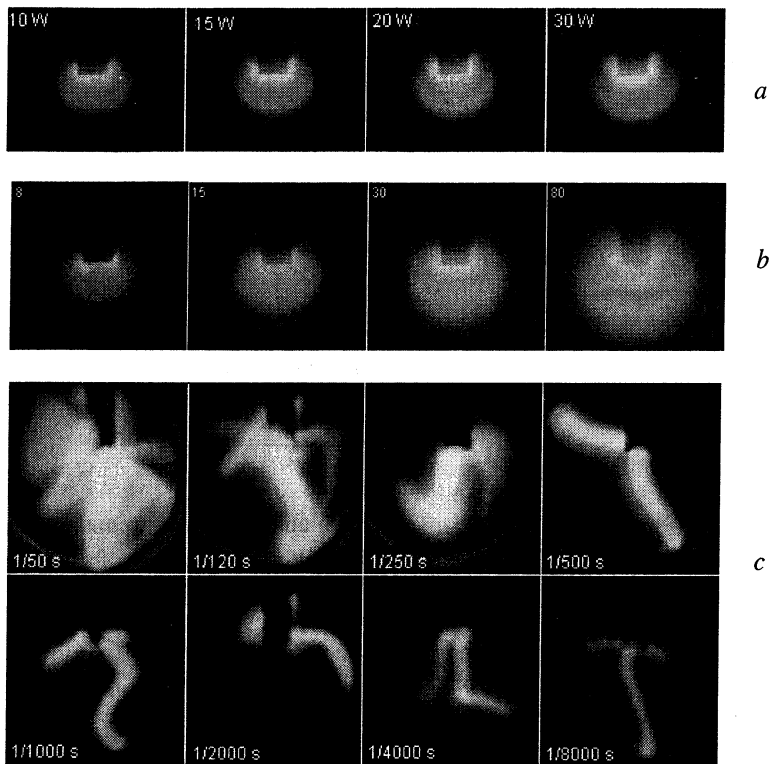


Fig. 2. Discharge in hydrogen (*a* – 1 Torr), nitrogen (*b* – 1 Torr), argon (*c* – 20 Torr)

Modelling

The radial distributions of plasma density and electric field inside coaxial and spherical system of electrodes in hydrogen has been calculated in quasi-static approximation [11]. Self-consistent solution of electron balance equation and the electric field distribution was numerically defined with the plasma absorbed power as the parameter.

The radial distribution of quasi-static electric field was given in accordance with chosen geometry of the system and the dielectric constant of plasma.

The processes of the direct ionization, ambipolar diffusion and volume dissociative electron-ion recombination were taken into account for solution of the electron balance equation with zero boundary conditions. The ionization frequency and the coefficients of diffusion and recombination were functions of the electric field. All the coefficients were calculated using the Boltzmann equation. The input parameters for calculations were the gas pressure, absorbed power and geometry of the system.

Phenomenology and basic properties

Discharge in molecular gases has nonuniform structure with pronounced ball shape periphery with sharp boundary and bright thin region surrounding the exciting electrode-antenna. Slight increase of the light intensity in plasma periphery is observed. The discharge in Ar has a thread-like form (Fig. 2).

The less the antenna diameter the less is the ignition and maintenance microwave field. The discharge could be ignited at incident powers of 2 W with 0.5 mm diameter antenna. Increase in the incident power leads to growth up of the discharge sheath along the antenna. As microwave power is increased up to certain threshold level, which is defined by the pressure and electrode diameter, the discharge runs away along the antenna towards the microwave generator. This gives natural limit of upper level of the incident power. These regimes were off our interest.

The plasma ball exhibits properties of medium with the elastic boundary: when the probes touch the boundary from outside and moves further, the boundary layer was bent inside. At certain moment the plasma covers the probes and the boundary returns to its initial position. In the reverse motion of the probes the boundary was bent outside moving together with the probes. Finally the plasma loses contact with the probes and several oscillations in shape and diameter of the plasma occur before it comes to the state of equilibrium with an initial diameter of the ball.

If the plasma gas is introduced through the channel in the electrode, the ball shape is distorted and plasma flux expands along the axis of the channel for the distance exceeding the ball dimensions. The length of the plasma flux depends on the flow rate of the plasma gas.

If plasma balls are generated with several electrodes (e.g. trident system) the diameters of plasma balls are increased with increase of the incident power but the balls never overlap and the dark region exists between plasma regions at any power.

Results of probe measurements showed the flat distribution of plasma density inside the ball, sharp decrease of it in the boundary layer and exponential decay of it in the plasma surrounding. It was showed the presence of direct potential inside the plasma ball which fell to zero level outside the ball.

Experiments showed the plasma density in the ball region less than critical one. In the electrode sheath the density can be overcritical.

Results of quasi-static modelling give good agreement of profiles of the specific absorbed power and experimental plasma emission and of calculated and measured electric field strengths (Fig. 3). Observed sharp plasma boundary was never calculated in diffusion controlled plasma. Additional physical phenomena should be taken into account which leads to plasma self-organization. Experimental results can be explained by existence of double plasma sheath at the ball boundary.

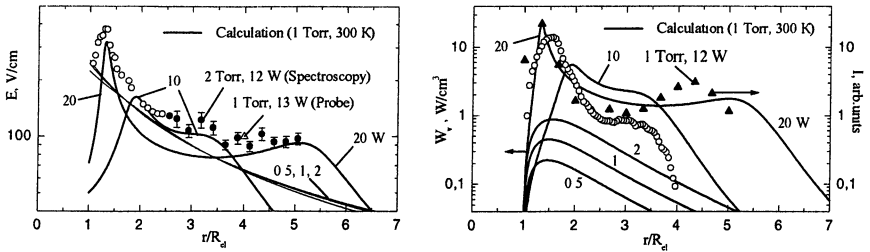


Fig. 3. Comparison of calculated and experimental dependencies of electric field strength (E) and calculated specific absorbed power (W) and experimental light intensity (I).

Conclusions

Summarizing all experimental and theoretical results, the structure of the discharge in molecular gases can be interpreted as follows.

The narrow plasma layer with high electric field gradient is generated close to the surface of an antenna. This part of discharge is self-sustained discharge and is characterized by high specific absorbed power, high electron (overcritical) density, and high intensity of plasma emission. This region is surrounded by ball-shape non-self-sustained region where the electron density can be less than critical one. All experimental data lead to the conclusion that sharp outer boundary of the discharge is caused by presence of the double electric sheath. The luminous discharge region is surrounded by dark afterglow where the electron density is ten time less as that in active discharge.

This study was partly supported by RFBR (grant 02-02-16021).

References

1. Bardos L., Lebedev Yu. A., Technical Physics, 1998, **43**, 1428.
2. Bardos L., Lebedev Yu. A., Plasma Phys. Reports, 1998, **24**, 956.
3. Bardos L., Barankova H., Lebedev Yu. A., Nyberg T., Berg S., Diamond and Related Materials, 1997, **6**, 224.
4. Bardos L., Barankova H., Lebedev Yu. A., 42-nd Ann. Conf. of Soc. of Vac. Coaters, Chicago, IL, April 17-22, Proc. SVC TC(1999), paper E-7.
5. Lebedev Yu. A., Mokeev M. V., Tatarinov A. V., Plasma Phys. Reports, 2000, **26**, 272.
6. Lebedev Yu. A., Mokeev M. V., High Temp. 2000, **38**, 338.
7. Bardos L., Lebedev Yu. A., High Temp. 2000, **38**, 528.
8. Lebedev Yu. A., Mokeev M. V., Plasma Phys Reports, 2001, **27**, 418.
9. Lebedev Yu. A., Mokeev M. V., Technical Physics, 2002, **47**, 135.
10. Lebedev Yu. A., Mokeev M. V., Technical Physics, 2002, **47**, 135.
11. Lebedev Yu. A., Tatarinov A. V., Epstein I. L., Plasma Sources Sci & Technol., 2002, **11**, 146.

DETAILED INVESTIGATIONS IN MICROWAVE SINTERING OF CERAMICS BY MEANS OF A DILATOMETER

*G. Link, M. Thumm*¹

Forschungszentrum Karlsruhe GmbH, Institut fuer Hochleistungsimpuls- und
Mikrowellentechnik, Germany

¹also University of Karlsruhe, IHE, Germany

Introduction

Dilatometry is a widely used technique in materials science and development, to measure thermal expansion coefficients, phase transformations or the linear shrinkage as a function of process temperature. The basic information such a dilatometer gives is the variation in sample length during heating or cooling through a programmed cycle. This information can be very effectively used to optimize the process parameters of a sintering process.

Although the accuracy of inductive displacement transducers used in such instruments is extremely high, one of the major obstacles for taking full advantage of this accuracy is the fact that one has to make sure that the sample is in thermal equilibrium with its environment. This gives strong restrictions to the programmed heating cycles with respect to the heating rates. With conventional heating, that means infrared heating, we can observe a sample surface with temperatures higher than in the volume. This results in heat flow from the sample surface into the volume until the sample is in thermal equilibrium. But this takes some time, depending on thermal conductivity, which for ceramic powder compacts is rather low. With pure microwave heating the problem appears the other way round. If the samples show low dielectric losses, resulting in volumetric heating, then there is permanent heat flow from the inside out where heat is lost from the sample surface by radiation and convection. But in contrast to conventional heating existing temperature gradients cannot be avoided by slow heating. Here a real thermal equilibrium can never be achieved.

There are different ways to overcome this problem. One is using a microwave transparent box of ceramic fiber boards for thermal insulation of the dilatometer sample holder, as it has been performed up to now [1]. Another solution is the combination of conventional and microwave heating technique, so called hybrid heating. This allows to control temperature gradients during the sintering process. At the same time it is a versatile tool to investigate the influence of different heating methods on the sintering process of ceramic compacts in a single system. So systematic errors due to different temperature measurement set-ups can be excluded. The compact 30 GHz, 15 kW gyrotron installation of the Forschungszentrum Karlsruhe, Germany has been equipped with such a dilatometer

system (see Figure 1) for detailed investigations in sintering of various functional and structural ceramics by means of millimeter wave (mm-wave) radiation.

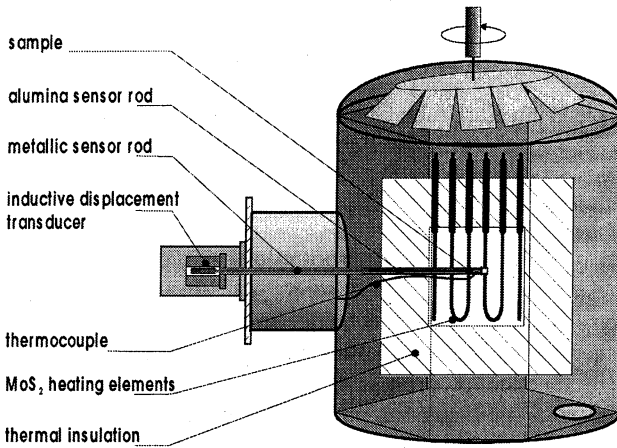


Fig. 1. Dilatometer system in the mm-wave applicator employing a combination of conventional and mm-wave heating.

Experimental results

Large efforts have been undertaken to study the intrinsic behavior of the dilatometer under various heating conditions for calibration purposes. This behavior is determined by the temperature evolution in the sensor head. If residual temperature gradients are present, the sensor rod may show a thermal expansion different to the sample holder. But this will result in a rather small intrinsic dilatometer signal superimposed to the large signal coming from the ceramic sample under test due to shrinkage during sintering. It was found that with pure mm-wave heating temperature profiles strongly depend on the heating rates and the dielectric loss behavior of sample itself, so that a calibration of the dilatometer system is unsatisfactory [1]. However with hybrid heating, where temperature profiles can be actively controlled, a proper calibration is feasible.

The sintering behavior of different types of functional and structural ceramics has been investigated in the prescribed dilatometer setup. Figures 2, *a* and 3, *a* show the relative linear shrinkage as a function of temperature with different heating rates for ceramic powder compacts made from nanocrystalline, yttria stabilized zirconia (YSZ) delivered from HITK, Germany and an ultra-fine alumina TM-DAR from Taimei Chemicals, Japan.

In case of zirconia samples (Fig. 2, *a*) the dilatometer curves indicate that sintering with mm-waves (MWS) starts at lower temperatures if heating rates are

increased. This might be interpreted as an increased non-thermal microwave effected, which has been reported from many authors for different ceramic materials [2]. If such an effect exists, caused form the interaction of the electromagnetic fields with the dielectric material, than one could expect, that with increased heating rates, which result from an increased field strength, sintering is even more enhanced and therefore starting at lower temperatures. Another indication for such an effect might be the fact that with conventional sintering (CS) shrinkage of the sample starts at a temperature more than 100 °C higher compared to mm-wave heating at an identical heating rate of 5 °C/min.

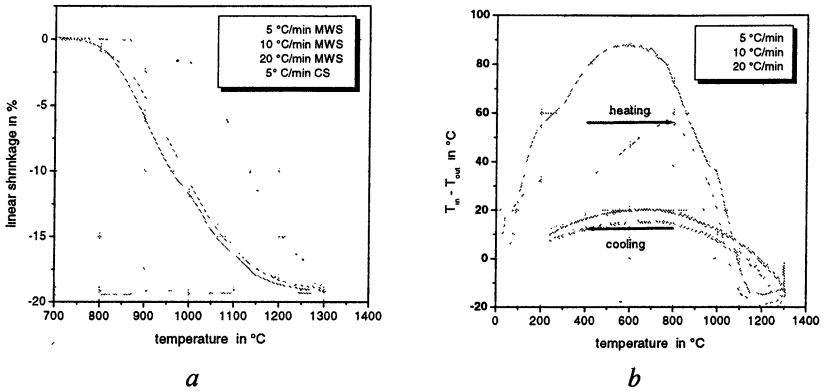


Fig. 2. Linear shrinkage (a) and temperature gradients (b) during mm-wave (MWS) and conventional sintering (CS) of nanocrystalline yttria stabilised zirconia.

But if we look at the results of identical experiments with low loss alumina samples, the effect is opposite (Fig. 3, a). With increased heating rates during mm-wave heating the onset of sintering, that means shrinkage is shifted to higher temperature values. This effect is similar but more pronounced with conventional heating. In the case of conventional heating such effects are explained by temperature gradients within the sample and by reduced annealing time at equal temperatures if heating rates are increased. If we are looking at temperature gradients within the sample holder during heating, that means at the temperature difference from the sample surface T_{in} to the outer surface of the sample holder T_{out} , we can see that temperature gradients in the sample holder are changing sign if we compare different materials (see Fig. 2, b and 3, b). Further more this gradients increase with increasing heating rates. Assuming that there are similar temperature gradients within the sample as well, these should be taken into account if one compares the temperatures measured with different heating methods. Unfortunately temperatures within the sample volume are not accessible.

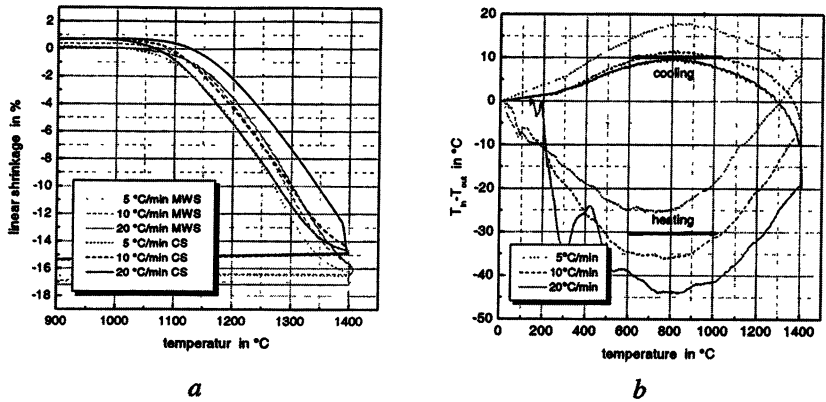


Fig. 3. Linear shrinkage (a) and temperature gradients (b) during mm-wave (MWS) and conventional sintering (CS) of submicron high purity alumina.

This clearly demonstrates that process parameters such as temperatures can hardly be used as the only argument for any microwave effects. Therefore further investigations have to be taken into account. For example investigations of grain size evolution as a functions of sintered density since this correlation is temperature independent. The results shown in Fig. 4 for both materials reveal a clear difference in densification kinetics for the nanocrystalline YSZ if we compare mm-wave and conventional heating but no remarkable difference for the alumina TM-DAR.

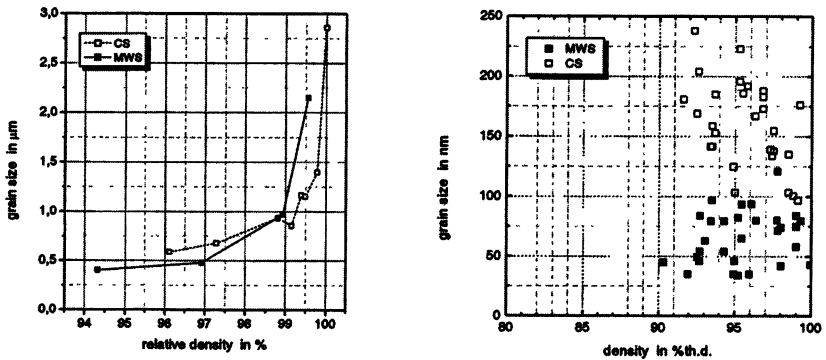


Fig. 4. Grain size as a function of relative sintered density for nanocrystalline YSZ (right) and TM-DAR (left).

The combination of mm-wave heating and conventional resistant heating, so called hybrid sintering (HS) is the only way to solve the problem of temperature gradients within bulk materials. But this solution is restricted to materials with dielectric losses sufficiently high, that means higher than losses of surrounding materials such as the dilatometer sample holder and the material for thermal insulation, respectively. Otherwise mm-wave power is predominantly absorbed in surrounding materials, which are acting than as an additional radiation source for infrared heating.

Investigations of hybrid heating with a submicron YSZ from Toso, Japan in comparison with conventional heating are shown in Fig. 5. The graphs show the linear shrinkage with different heating rates (5, 20 and 40 °C/min) as well as the temperature gradients from the sample surface T_{sample} to the inner wall of the thermal insulation box T_{wall} heated with MoS₂ heating elements. Conventional heating results in a shift of the onset of linear shrinkage to higher temperatures as well as in growing temperature gradients if the heating rate is increased as it has been observed with high purity alumina (Fig. 3, a). With hybrid heating where temperature gradients can be controlled to almost zero for all heating rates, the shift of the dilatometer curves is neglectable.

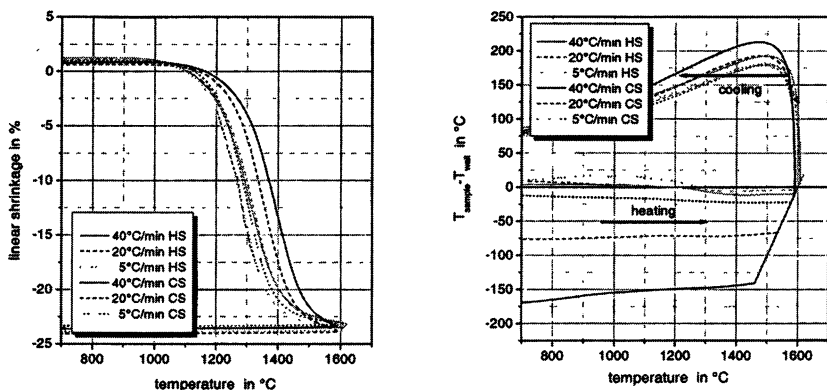


Fig. 5. Linear shrinkage (left) and temperature gradients (right) during hybrid (HS) and conventional sintering (CS) of Toso YSZ.

This dilatometer system can be used with changing heating conditions as well. That means one could start the sintering process with hybrid heating and then changing to conventional heating by switching of mm-wave power, as it has been reported by Wroe and Rowley with a comparable system at 2.45 GHz [3]. Equivalent experiments have been performed with nanocrystalline zirconia samples as shown in Fig. 6. If the shift of the dilatometer curves to lower temperature

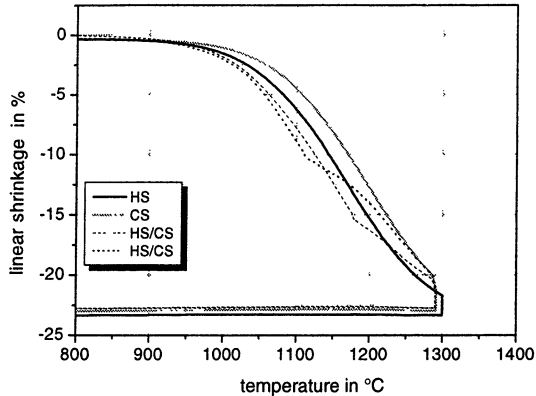


Fig. 6. Linear shrinkage of nanocrystalline YSZ under various heating conditions.

values with mm-wave power on would indicate an enhanced densification one would not expect the curves of linear shrinkage (dashed lines) going back to the conventional grey line as we found. The slope of the dilatometer curves after switching of mm-wave power is much smaller than the slope with conventional heating at the same temperature or density. But if the shrinkage rate is temperature driven or is a function of density, it would be expected to be similar. This is probably another clear indication for temperature gradients been responsible for such a behaviour which obviously changes if heating conditions are changing.

References

1. *Link G., Rhee S., Thumm M.*, Proc. of the 36th Annual Microwave Symposium of the IMPI (San Francisco, April 18–21, 2001), 23–26.
2. *Sutton W. H.*, Microwave Processing of Materials III, MRS Symp. Proc. V. 269, ed. Janney M. A. Pittsburgh, PA, 1992, 3–20.
3. *Wroe F. C. R. and Rowley A. T.*, Microwaves: Theory and Application in Materials Processing, Ceramic Transactions, v. 59, ed. Clarc D. E., ACerS (Westerville Ohio, 1995), 69–76.

TIME-RESOLVED IMAGING OF MILLIMETER-WAVES USING THE RECOMBINATION CONTINUUM OF CESIUM EMITTED BY A SLAB OF THE Cs-Xe DC DISCHARGE

I. E. Abubakirov, M. S. Gitlin, A. O. Perminov, and V. V. Zelenogorsky

Institute of Applied Physics, Russian Academy of Sciences, Nizhny Novgorod, Russia

A novel sensitive technique for time-resolved imaging of microwave patterns using the blue recombination continuum of cesium emitted by a slab of the positive column of the Cs-Xe DC discharge was developed. The millimeter-wave beams at frequency 35 GHz were imaged with temporal resolution of 0.1 ms and energy flux sensitivity of 10^{-4} J/cm².

For development of microwave sources and transmission lines, microwave nondestructive imaging in opaque material, as well as other scientific, industrial, and medical applications require convenient real-time techniques for recording spatial distribution of microwave intensity [1, 2]. Methods widely used now for microwave imaging are based on the thermal microwave action on various materials, such as liquid crystal films, paper screens, etc. Recording of the thermographic pattern enables to image the microwave patterns. The main disadvantages of the thermal methods of microwave imaging are slow response and low sensitivity. Because of these reasons the thermal methods of microwave imaging cannot be used to record the radiation patterns of low and moderate-power or short-pulse microwave generators (such as magnetrons, gyrokystrons, and relativistic microwave sources). Discharges produced by microwave beams in free space [3] or in gas-filled tubes (luminescent lamps, neon bulbs, etc.) [4] are used to image microwaves too. However, this technique makes it possible to obtain only a qualitative image of high-power microwaves.

In this paper we discuss a novel sensitive technique for time-resolved microwave beam imaging using the blue recombination continuum of cesium emitted by a slab of the positive column (PC) of a Cs-Xe DC discharge. The blue recombination continuum of cesium (optical wavelength shorter than 500 nm) originates from radiative recombination of electrons and cesium atomic ions into the $6P$ state of cesium [5, 6, 7].

The experimental setup for studying microwave beam imaging by use of the recombination continuum of cesium [8] is schematically shown in Fig. 1. The slab of PC of a Cs-Xe discharge was produced in a sealed discharge tube (DT). A rectangular parallelepiped placed in the middle of the discharge tube was made of plane-parallel quartz plates. Two square plane-parallel polished quartz windows (1) with their apertures 10×8 cm² were set at the distance of 2 cm between their internal surfaces. These windows allowed injecting the microwave beam into the tube with small reflection and without distortions. Two plane anodes (2) and two heated cathodes (3) were placed in glass cylinders (4 and 5) 10 cm

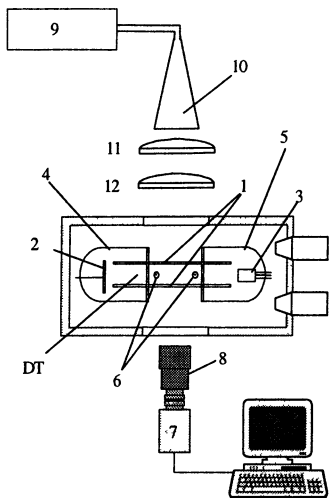


Fig. 1

in diameter, which were glued to the quartz cell. The distance between the anodes and the cathodes was 30 cm. Each pair of electrodes was connected to a separate current source. The discharge tube was filled with 45 Torr xenon. The discharge tube had sidearms, in which drops of cesium metal were placed. To obtain the required density of cesium vapor, the discharge tube was heated in an oven to the temperature of 80–110 °C. The oven had two plane-parallel polished quartz disk windows 20 cm in diameter. The temperature of the discharge tube wall was controlled by means of thermocouples. The longitudinal electric field in the positive column of the discharge was determined by the difference of potentials between two cylindrical probes (6). The electron temperature in the PC of the Cs-Xe discharge was deduced from the emission spectrum of the blue recombination continuum of cesium [5, 7, 9]. The discharge was imaged by a CV-450 monochrome CCD cameras (7) with a SE1212 lens. For imaging of the blue recombination continuum, a set of optical interference filters (8) was placed before the CCD camera lens. This filter set transmitted about $(40 \pm 10)\%$ of light in the region of 400–500 nm and less than 0.1%, beyond that range. It transmitted also less than 0.1% of light in the range of 450–460 nm, where the lines of the second resonance doublet of cesium ($7P \rightarrow 6S$) occur. The signal from the CCD camera was captured with a frame-grabber installed in a computer. A photomultiplier with the optical filters set also was used to record continuum intensity with microsecond temporal resolution. Millimeter waves were generated by a 35 GHz magnetron (9) with its maximum power of 20 W in the long-pulse mode (pulse duration is 0.1 s). The millimeter waves were fed to the pyramidal horn antenna (10), which was 50 cm long and had aperture dimensions of 8×6 cm. Plane-convex spherical

lenses (11 and 12) 20 cm in diameter and focal length 60 cm focused millimeter-waves to the center of the plasma slab.

Investigations of the microwave action on the positive column of the Cs–Xe discharge plasma were performed at the current of 1.5 A and a DT temperature of 368 K. Under these conditions, the positive column of the Cs–Xe discharge represents a flat homogeneous plasma layer occupying the whole aperture of the tube [8, 9]. In the absence of the microwave radiation, longitudinal electric field strength in PC E_0 is 0.9 V/cm, electron temperature T_{e0} is 0.4 eV, and electron density N_{e0} is equal to $4 \cdot 10^{12}$ cm³. We used the photomultiplier tube with the optical of interference filter set to measure the dependence intensity of the blue recombination continuum on the intensity of the microwaves. Figure 2 shows the plots of the relative variation of the continuum intensity ΔI as a function of the incident microwave intensity W .

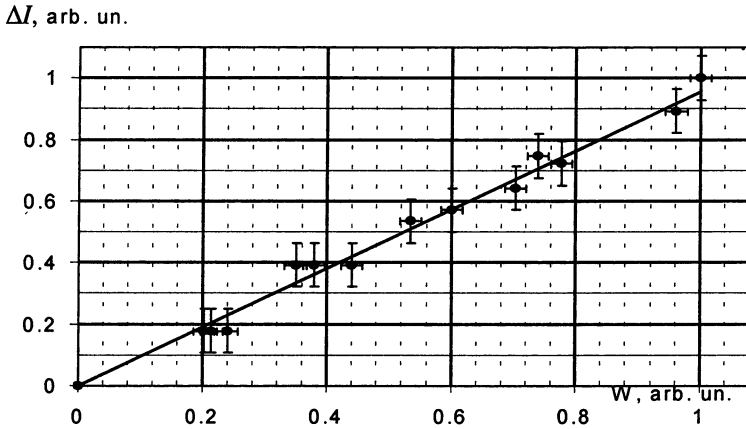


Fig. 2

It follows from this plot that the intensity of the blue recombination continuum is directly proportional to the intensity of the microwaves. When the intensity of the incident quasi CW microwaves was greater than 5 W/cm², a breakdown of the plasma slab occurred.

The spatial distribution of the blue recombination continuum intensity $I(x, y)$, where x and y are the longitudinal and transverse coordinates relative to the discharge current direction, was obtained by the CCD camera. The frames taken before the microwave pulse were used to determine the background emission of the recombination continuum $I_0(x, y)$. In order to find the spatial distribution of variation of the recombination continuum intensity $\Delta I(x, y)$ by the action of microwaves, background emission was subtracted from the image taken during the microwave pulse. In order to verify the proposed imaging technique, we have

compared the spatial distribution of the microwave intensity $W(x, y)$ in the focal plane of lenses, measured with a movable calibrated microwave diode, to the pattern of variations of the continuum intensity $\Delta I(x, y)$ measured using the CCD camera. The relative intensity $W/W(0, 0)$ of the microwaves (thick solid curve) and the relative variation of the continuum intensity $\Delta I/\Delta I(0, 0)$ (thin solid curve) measured along the coordinates x and y are presented in Figs. 3 (*a* and *b*), respectively. This profile was measured at the microwave intensity at the beam center $W(0,0) \approx 3 \text{ W/cm}^2$, for which the relative variation of the continuum intensity was $\Delta I(0,0)/I_0 \approx 1$. Exposure time was 0.2 ms.

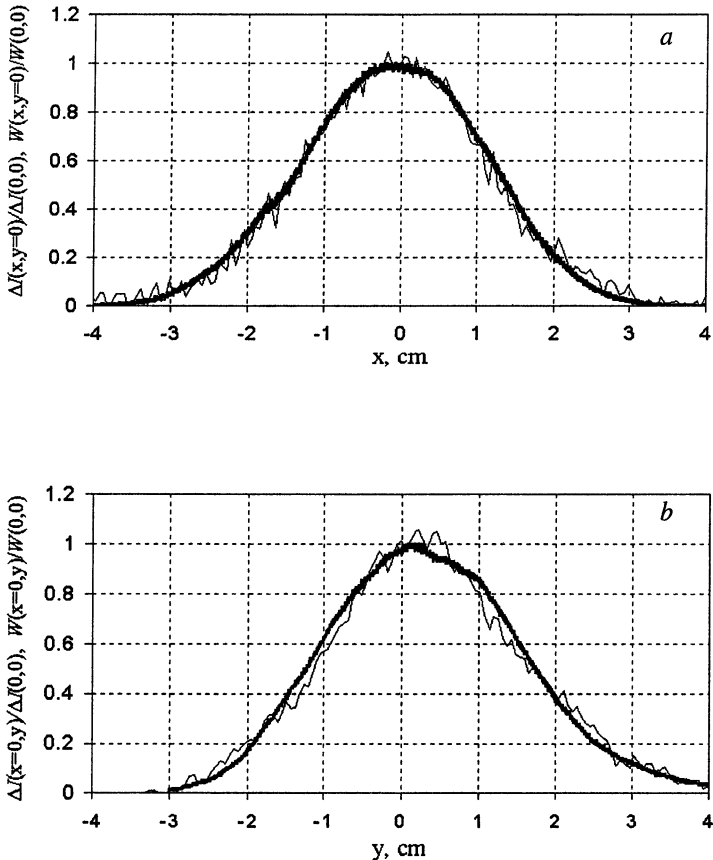


Fig. 3

Figure 3 shows that the patterns measured by the two techniques coincide within the experimental error.

We also performed experiments on imaging of the microwave radiation pattern in the region where two Gaussian beams cross. In this experiment two linear polarized microwave beams were directed onto the plasma slab at an angle to each other by means of two mirrors. The full width at half maximum of the beams was about 5 cm, and their power ratio was 4:1. Figure 4 shows the plot of the relative variation of the continuum intensity as a function of coordinate x for $y = 0$, measured when the angle between the crossing microwave beams was 20° . Exposure time was 2 ms.

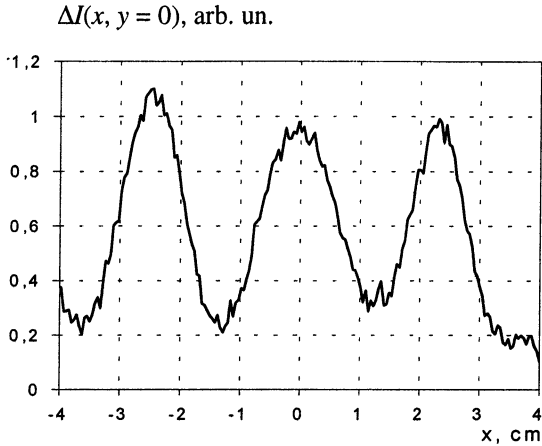


Fig. 4

The characteristic time of variation of the continuum intensity upon fast switch-on of the microwave source was measured with the photomultiplier. Continuum response time was equal to four microseconds. Thus, the temporal resolution of the proposed method can be of the order of microseconds, while the energy flux sensitivity can be as low as 10^{-5} J/cm². In our experiments, the temporal resolution was limited by sensitivity of the CV-450 CCD camera. At a fully opened lens diaphragm and maximum camera gain, the minimum exposure time that allowed the continuum emission to be recorded for one microwave pulse was 0.1 ms, while the energy flux sensitivity was about 10^{-4} J/cm².

Acknowledgement. The authors would like to gratefully acknowledge the support by Golubev S. V., Litvak A. G., Semenov V. E. This work is partly supported by the RFBR grant No. 00-02-17757.

References

1. Kuznetsov S. O., Malygin V. I., *Int. J. IR and MM Waves*, 1991, **12**, 1241.
2. Bolomey J.-C., *IEEE Trans. Microwave Theory Tech.*, 1989, **37**, 2109.

3. *Bugaev S. P. et al.*, Doklady Akademii Nauk, 1988, **298**, 92 (in Russian).
4. *Ginzburg N. S. et al.*, Phys. Rev. E, 1999, **60**, 3297.
5. *Wetzer J. M.*, Physica C, 1984, **123**, 247.
6. *Agnew L., Reichelt W. H.*, J. Appl. Phys., 1968, **39**, 3149.
7. *Huennekens J. et al.*, Phys. Rev. A, 1985, **31**, 196.
8. *Gitlin M. S. et al.*, Technical Physics Letters, 2002, **28**, 445.
9. *Bogatov N. A., Gitlin M. S. et al.*, Phys. Rev. Lett., 1997, **79**, 2819.

INTERACTION OF A SUPERSONIC AIRFLOW WITH THE COMBINED MICROWAVE DISCHARGE, CREATED ON THE EXTERNAL SURFACE OF A WEDGE DIELECTRIC BODY

*V. M. Shibkov, V. A. Chernikov, V. G. Gromov,
O. B. Larin, V. A. Levin, L. V. Shibkova*

Department of Physics, Moscow State University, 119899, Moscow, Russia

The interaction of supersonic airflow with the surface microwave discharge was examined. It was experimentally shown, that the inclination angle of a shock wave, arising on a leading edge of the antenna, increases at presence of a microwave discharge, accordingly, the airflow Mach number decreases. The numerical modeling of process of streamlining of different geometry bodies by supersonic airflow was fulfilled at various values of energy introduced into boundary layer. It was theoretically shown that the surface microwave discharge influences on the characteristics of a supersonic flow.

This paper deals with a surface microwave discharge outside a dielectric body in a low pressure chamber.

The surface microwave discharge on external surface of dielectric body was earlier created by us [1–7]. It was shown that the surface discharge represents uniformly luminous plasma coating all surface of a dielectric body and supersonic airflow does not destroy the surface discharge. Number of the results was obtained at investigation of the main properties of the surface microwave discharge. They confirmed to a feasibility of surface microwave discharges in aerodynamics, namely, for change of the characteristics of supersonic flow near a surface of flying vehicles and by that improvements of their aerodynamic properties. Thus it is possible to improve a manoeuvrability of a flying vehicle, to radically lower the model resistance at its flight in atmosphere at the expense of destruction of a head shock wave and reduction of turbulent friction force.

When a microwave power or pulse duration increase more than the values are necessary for creation of plasma on all surface of a wedge dielectric body, the new type of a microwave discharge, namely, combined microwave discharge was created by us. The discharge represents a combination of a surface discharge created in the area of a boundary layer on an external surface of a dielectric body, and a volumetric microwave discharge which is generated on a leading edge of a dielectric wedge body.

It is known, that an input of energy in area of a boundary layer or the local heating of a plate surface in the field of a turbulent boundary layer result in noticeable reduction of a local coefficient of turbulent friction at the expense of decreasing of a transverse gradient of longitudinal flow velocity and increase of a displacement thickness. In case of a surface microwave discharge the microwave field is localized in thin near-surface layer, that promotes the effective

contribution of energy to plasma and fast gas heating, that should result in change of supersonic flow near a body surface.

For check-up of the supposition that the surface microwave discharge in our conditions can render the noticeable influence on streamlining of model by supersonic airflow, the interaction of supersonic airflow with the microwave discharge, created on a external surface (in a boundary layer) of the wedge dielectric body, was examined. For this purpose the pulsed shadow graphics installation was produced. This set-up permits to record the shadow photos with a time resolution.

In experiments the antenna length was changed from 5 cm up to 20 cm. The direction of supersonic flow was opposite to the direction of the surface microwave discharge spreading. The surface microwave discharge represents a thin plasma layer covering, or partly, or all surface of a dielectric body, depending on an energy input and pulse duration.

It was shown, that the surface microwave discharge influences on the change of a head shock wave and both attenuation and disappearance of the jumps into area of a separated flow, and also degradation of the jumps in the field of turning-point of supersonic airflow.

It was experimentally shown, that in process of discharge evolution the boundary layer thickness starts to increase. It should result to decrease of a turbulent friction coefficient. The time evolution of the inclination angle of a head shock wave arising on a wedge dielectric body in supersonic airflow is submitted in Fig. 1. One can see, that in process of the surface discharge evolution the inclination angle of the head shock wave is increased. To the end of a microwave pulse $\tau = 70 \mu\text{s}$, when the plasma layer covers the whole antenna, the variation δ of the inclination angle reaches $\sim 20\%$, that corresponds to reduction of flow Mach number in this area of the antenna. Thus, if the microwave pulse should was the greater duration, the effect would prolong to be increased, as transition to a saturation does not take place in Fig. 1. After switch off of a microwave energy, the effect exists $\sim 100 \mu\text{s}$ continuously decreases in process of the heated gas drift by supersonic airflow.

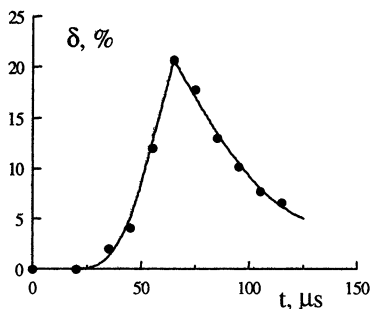


Fig. 1. The surface microwave discharge influence on the inclination angle of a head shock wave, arising on a leading edge of the wedge antenna at $\tau = 70 \mu\text{s}$, $p = 40 \text{ Torr}$, $M = 2$, and microwave power $W/W_{ow} = 2$. W_{ow} is microwave power necessary for creation of a surface microwave discharge on all surface of the wedge dielectric body.

Numerical model for studies of unsteady near wall discharge in supersonic flow have been developed too. The model bases on the Favre averaged Navier-Stokes equations for thermally equilibrium, chemically frozen air. For the description of turbulent transfer the algebraic Baldwin-Lomax model and two-parameter differential k-omega model are used. The pulse discharge influence on the gas flow is simulated by non-stationary near wall heat source with specified space and time distribution of intensity. The numerical modeling of process of streamlining of cylindrically blunted flat plate of finite thickness with length of 15 cm, width of 2 cm, and thickness of 0.2 mm by supersonic airflow is carried out at various values of energy introduced into boundary layer. In Fig. 2 and Fig. 3 the total power equals 2000 W.

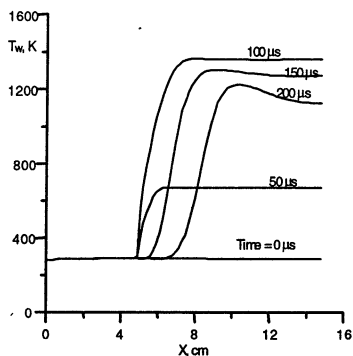


Fig. 2. The near wall heat deposition effect on the wall temperature distribution. $M = 2$; $T_e = 166,7 \text{ K}$; $L = 15 \text{ cm}$; $x_h = 5 \text{ cm}$; $y_h = 1 \text{ mm}$; $z = 2 \text{ cm}$; $\tau = 100 \mu\text{s}$; $P_{total} = 2000 \text{ W}$.

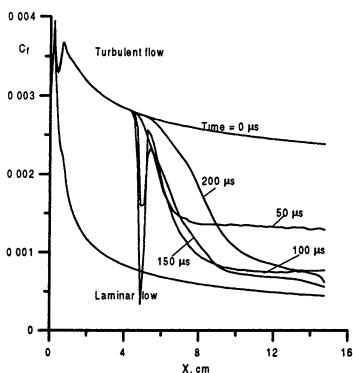


Fig. 3. The near wall heat deposition effect on the skin-friction coefficient distribution. $M = 2$; $T_e = 166,7 \text{ K}$; $L = 15 \text{ cm}$; $x_h = 5 \text{ cm}$; $y_h = 1 \text{ mm}$; $z = 2 \text{ cm}$; $\tau = 100 \mu\text{s}$; $P_{total} = 2000 \text{ W}$.

One can see that effect of heat deposition leads to significant decreasing of the local turbulent friction coefficient. Moreover the effect exists during long time after the heat deposition to gas is switched off. During some hundreds microseconds the flow parameters slowly return in initial state. It indicates prospects of pulsed-periodical discharge usage.

The influence of heat deposition to gas in area of the turbulent supersonic boundary layer have been also calculated in the presence of a rectangular thermal source in the turbulent boundary layer. The system of averaged equations of turbulent motion of a perfect gas in the absence of external mass forces has been used: Body geometry – flat plate with length of 15 cm; boundary conditions – heat-insulated surface. The same results was received also for the case when the heat deposition to the gas takes place only on part of plate. Portion of gas heating has 5 cm in length and calculations was also executed for a segment of a boundary layer of length 5 cm downstream from a heated portion.

In Fig. 4 the gas temperature longitudinal profile are given. In Fig. 5 the influence of heat deposition to gas in turbulent supersonic boundary layer on displacement thickness of turbulent boundary layer is represented. One can see that when heat deposition is increased the displacement thickness of turbulent boundary layer grows. It has to lead to decreasing of turbulent friction.

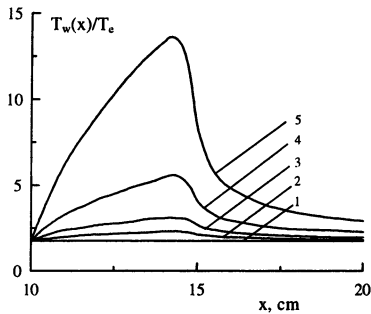


Fig. 4. Gas temperature longitudinal profile. $M = 2$; $T_e = 166,7$ K; $x_1 = 10$ cm; $x_2 = 15$ cm; $x_3 = 20$ cm; $y_2 = 0,5$ mm; A: 1-0; 2-1; 3-2; 4-4; 5-8.

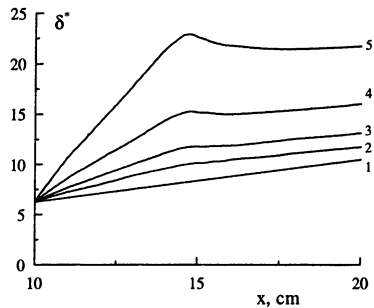


Fig. 5. Displacement thickness of boundary layer. $M = 2$; $T_e = 166,7$ K; $x_1 = 10$ cm, $x_2 = 15$ cm, $x_3 = 20$ cm, $y_2 = 0,5$ mm; $Y = 0.0917$ mm; A: 1-0; 2-1; 3-2; 4-4; 5-8.

Fig. 6 testifies this supposition. An input of energy in area of a turbulent boundary layer results in noticeable reduction of a local coefficient of turbulent friction at the expense of decreasing of a transverse gradient of longitudinal flow velocity and increasing of a displacement thickness. The reduction of coefficient of turbulent friction is spread to considerable distance downstream from a heated portion. Due to "long memory effect" of a turbulent boundary layer the considerable friction reduction is reached at local heat input in comparison with the uniform heating of all streamline surface. At presence of several following one after another the heating portion this "long memory effect" intensifies and more essential diminution of value of the turbulent friction can be obtained.

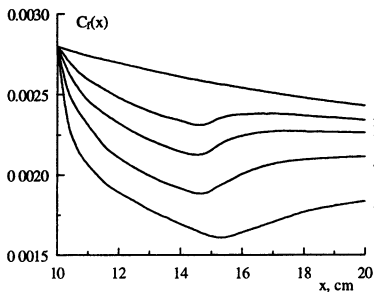


Fig. 6. Local friction coefficient. $M = 2$; $x_1 = 10$ cm, $x_2 = 15$ cm, $x_3 = 20$ cm, $y_2 = 0,5$ mm; A: 1-0; 2-1; 3-2; 4-4; 5-8.

At identical total energy consumption the reduction of an integrated friction coefficient more than in case of an uniformly distributed on all surface energy supplied to gas in a boundary layer. It testifies the results submitted in Fig. 7 and Fig. 8, where the comparison of thermal source effectiveness for the friction force decreasing for two cases considered by us were represented. In second case the effectiveness is higher then in first case.

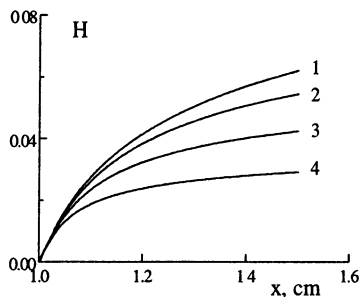


Fig. 7. Effectiveness of thermal source for decreasing the friction force. $M = 2$; $x_1 = 10$ cm; $x_2 = 15$ cm; $y_2 = 0,5$ mm; A: 1-1; 2-2; 3-4; 4-8.

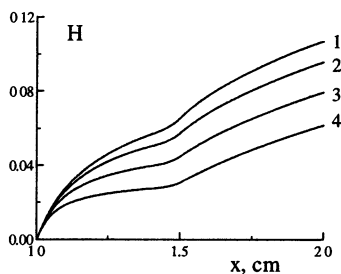


Fig. 8. Effectiveness of thermal source for decreasing the friction force. $M = 2$; $x_1 = 10$ cm; $x_2 = 15$ cm; $x_3 = 20$ cm; $y_2 = 0,5$ mm; A: 1-1; 2-2; 3-4; 4-8.

Acknowledgements. The work was partially supported under grants of the European Office of Aerospace Research and Development (grant № 2248p of International Science and Technology Center) and № 02-02-17116 of the Russian Foundation of Basic Research.

References

1. *Shibkov V. M. et al., Surface microwave discharge in supersonic airflow // Vestnik Moskovskogo Universiteta. Seriya 3. Fizika, astronomiya. 2000. V. 41, № 6. 64-66.*

2. *Shibkov V. M., Chernikov A. V., Chernikov V. A., Ershov A. P., Shibkova L. V., Timofeev I. B., Vinogradov D. A., Voskanyan A. V.* Surface microwave discharge on dielectric body in a supersonic flow of air, IV International workshop Microwave discharges: Fundamentals and applications (18–22 September 2000), Zvenigorod, Russia, Yanus-K, Moscow. 2001, 145–153.
3. *Shibkov V. M., Chernikov A. V., Chernikov V. A., Ershov A. P., Shibkova L. V., Timofeev I. B., Vinogradov D. A., Voskanyan A. V.* Surface microwave discharge in supersonic airflow, The 2nd Workshop on Magneto-plasma-aerodynamics in aerospace applications. 5–7 April 2000, Moscow (IHT of RAS, 2001), 163–168.
4. *Shibkov V. M., Chernikov V. A., Ershov A. P., Dvinin S. A., Raffoul Ch. N., Shibkova L. V., Timofeev I. B., VanWie D. M., Vinogradov D. A., Voskanyan A. V.* Surface microwave discharge in supersonic airflow, 32nd AIAA Plasmadynamics and Lasers Conference and 4th Weakly Ionized Gases Workshop (11–44 June, 2001). Anaheim, CA, USA, AIAA 2001–3087.
5. *Shibkov V. M., Chernikov V. A., Dvinin S. A., Ershov A. P., Shibkova L. V., Timofeev I. B., Vinogradov D. A., Voskanyan A. V.* Dense large-diameter uniform plasma of a surface microwave discharge, 15th International Symposium on Plasma Chemistry. Volume I. Oral Contributions (9–10 July, 2001), France, 179–184.
6. *Shibkov V. M., Alexandrov A. F., Chernikov V. A., Ershov A. P., Kuzovnikov A. A., Shibkova L. V., Timofeev I. B., Voskanyan A. V., Zlobin V. V.* Interaction of supersonic airflow with the combined microwave discharge, created on external surface of the wedge dielectric body, V International Workshop Strong Microwave in Plasma. Nizhny Novgorod, Russia, D26, 2002.
7. *Shibkov V. M., Dvinin S. A., Ershov A. P., Shibkova L. V., Timofeev I. B.* Surface microwave discharge in supersonic airflow, V International Workshop Strong Microwave in Plasma. Nizhny Novgorod, Russia, D27, 2002.

SURFACE MICROWAVE DISCHARGE IN A SUPERSONIC AIRFLOW

*V. M. Shibkov, V. A. Chernikov, A. P. Ershov,
L. V. Shibkova, I. B. Timofeev*

Department of Physics, Moscow State University, 119899, Moscow, Russia

The optimal way of creation of non-equilibrium plasma in supersonic airflow, namely, the surface microwave discharge on external surface of dielectrical body being flown of supersonic stream of air was proposed and investigated. The experimental approbation of a new method of creation of stable surface microwave discharge in boundary layer near a body streamlined of supersonic airflow was fulfilled. The breakdown characteristics, electric field strength, dynamics, space-temporary evolution of gas and vibrational temperatures in plasma of surface microwave discharge in air were measured. The degree of influence of supersonic airflow on common view and on gas heating in surface microwave discharge was considered.

Introduction

Recently a new direction of aerodynamics – so-called plasma supersonic aerodynamics was arisen. In this case it was supposed to use the various type of the gas discharges with the purpose of influence on the characteristics of gas flow near a surface of the flying bodies. The first laboratory experiments have shown an opportunity of a drag reduction at creation of the discharges of direct and alternative currents before a body streamlined supersonic airflow. However, the electrode discharges in flow are unstable and spatially non-uniform. Such discharges result in strong erosion of the electrodes and model surface and reliably are not reproduced in various realizations.

There was a task of search of optimum ways of creation of non-equilibrium plasma in supersonic flow. One of such ways offered in our laboratory is the new version of a surface microwave discharge, namely, a microwave discharge on an external surface of the dielectric bodies streamlined supersonic airflow [1–7].

It is known that at creation of the microwave discharges inside dielectrical tube filled by gas at a low pressure, the electromagnetic energy delivered to system is transformed to a surface wave. Thus, there is a self-sustaining system, when a plasma medium created by the surface wave is necessary for a surface wave existence, i.e. the presence of plasma is a necessary condition for distribution of a surface wave. The surface wave is travelled in space so long as its energy is sufficient for creation of plasma with an electron density no less then a critical value. In this case we have the plasma – dielectric – free space system, i. e. plasma, created by a surface wave, exists inside discharge tube, filled the gas with the lowered pressure. Plasma is limited to walls of dielectrical tube, which separate plasma from a free space.

This paper deals with a surface microwave discharge outside a dielectric body in a low pressure chamber. In this case plasma supported by a surface microwave is formed on an external surface of a dielectric.

Experimental set-up

The experimental set up consists of a vacuum chamber, magnetron generator, system for input of a microwave energy in a vacuum chamber, system for creation of supersonic airflow and diagnostic system. The magnetron generator had the following characteristics: a wavelength $\lambda = 2,4$ cm; a pulsed microwave power $W < 300$ kW; a pulse duration $\tau = 1-100$ μ s; a pulse period-to-pulse duration ratio $Q = 1000$. The direction of a supersonic flow with Mach number $M = 2$ was opposite to the direction of a surface microwave discharge spreading.

Experimental results

It was shown that the surface discharge represents uniformly luminous plasma coating all surface of a dielectric body and the supersonic flow of air at a Mach number $M = 2$ does not influence on common view of a surface discharge on a dielectric antenna of rectangular section and on values of a microwave power which are necessary for its creation. Fig. 1 represents the dependence on an air pressure of minimal microwave power which is necessary for a breakdown and beginning of a surface discharge formation on a dielectric body. One can see that the power of the used generator is sufficient for creation of the surface microwave discharge in a range of air pressures $p = 10^{-3}-10^3$ Torr. The minimum power, which is necessary for formation of a surface discharge, at first decreases at increasing of air pressure ($p = 10^{-3}-10^{-1}$ Torr) and then grows when pressure changes from 10 Torr up to 10^3 Torr. The obtained dependence is analogue of Pashen curve. Such behaviour of the breakdown power is explained by decreasing of diffusional losses of electrons at increasing of air pressure and growth of inelastic losses at it. For compensation of the electrons losses it is needed a large ionization frequency. The ionization frequency is growing function of electron temperature $\nu_i = f(T_e)$, i. e. reduced electrical field E/n . From here it is required to make a large power for creation of surface microwave discharge at small ($p < 10^{-1}$ Torr) and large ($p > 10$ Torr) pressure, as it is observed at experiment (Fig. 1).

The threshold characteristics of a surface discharge created at different pulse duration are submitted on Fig. 2. It is shown that at a fixed air pressure the power necessary for formation of a surface discharge sharply decreases with growth of a pulse duration from 1,5 up to 10 μ s, whereas for $\tau \geq 50$ μ s the threshold does not depend almost on pulse duration.

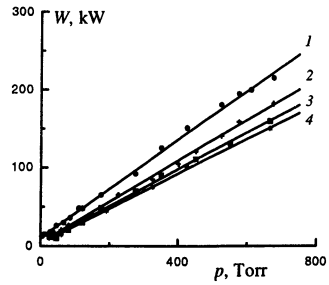
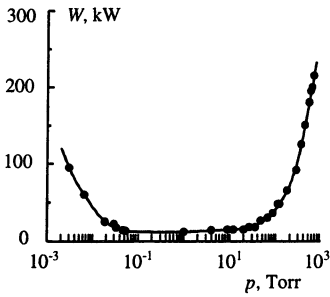


Fig. 1. Dependence of a minimum pulsed microwave power which is necessary for creation of a surface discharge on air pressure at $\tau = 50 \mu\text{s}$ and $f = 40 \text{ Hz}$.

Fig. 2. The threshold characteristics of a surface discharge created at different duration of microwave pulses τ , μs : 1 – 1,5; 2 – 5; 3 – 10; 4 – 50–100.

The longitudinal sizes of a surface discharge and its longitudinal velocities at $p = 10 \text{ Torr}$ as a function of a microwave pulse duration are submitted on Fig. 3 and Fig. 4. Parameter of this curves is the microwave power. It is shown that the longitudinal size of a surface discharge and its velocity at fixed pulse duration grow with an increasing of a microwave power. Thus, on initial stages of a surface discharge existence this velocity is large and reaches of value $v = 10^7 \text{ cm/s}$ at $W = 175 \text{ kW}$, whereas at late stages the velocity of the discharge propagation decreases up to $v = 10^4 \text{ cm/s}$ at $W = 25 \text{ kW}$. From Fig. 4 one can also see that all curves have the identical slope. The similar results are obtained also at other air pressures ($p = 40, 62$ and 100 Torr). The processing of the received data has shown,

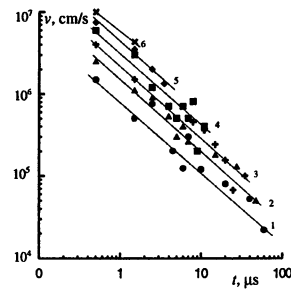
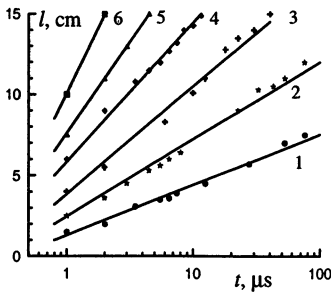


Fig. 3. Dependencies of the longitudinal sizes of a surface discharge on duration of a microwave pulse at $p = 10 \text{ Torr}$, $f = 20 \text{ Hz}$ and power W , kW: 1 – 25; 2 – 35; 3 – 55; 4 – 75; 5 – 100; 6 – 175.

Fig. 4. Longitudinal velocity of the surface microwave discharge on the antenna of rectangular section at $p = 10 \text{ Torr}$, $f = 20 \text{ Hz}$, and pulsed power W , kW: 1 – 25; 2 – 35; 3 – 55; 4 – 75; 5 – 100; 6 – 175.

that the time dependence of longitudinal velocity of the surface microwave discharges can be described by the law: $v = A \cdot t^{-(0.875 \pm 0.035)}$, where A is the coefficient which depends on microwave power, t is a time of microwave discharge existence. In various sections of a surface microwave discharge the dependencies of gas and vibrational temperatures on a pulsed microwave power were measured.

The gas temperatures in section $z = 2,5$ cm as a function of a microwave power is submitted in Fig. 5. The dependence of vibrational temperature on a microwave power measured by molecular bands of the second positive system of nitrogen (point) and on molecular bands of CN (daggers) is submitted in Fig. 6. One can see, that the gas temperature is growing function of a microwave power (the gas temperature increases from ~ 500 K at $W = 35$ kW up to ~ 1700 K at $W = 175$ kW) whereas the vibrational temperature remains practically constant under these conditions, insignificantly decreasing with increase of microwave power. At this the maximal gas heating is observed in a place of excitation of a surface microwave discharge and gas temperature decreases by the end of the discharge.

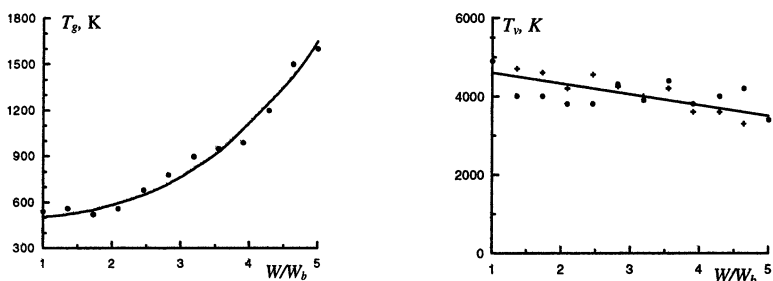


Fig. 5. The vibrational temperature of a surface discharge, measured by molecular bands of the second positive system of nitrogen (point) and on molecular bands of CN (daggers), as a function of a microwave power at $p = 40$ Torr, $\tau = 50 \mu s$ and $f = 40$ Hz in section $z = 2,5$ cm (W_b is breakdown power at air pressure $p = 40$ Torr).

Fig. 6. Time evolution of gas temperature under conditions of surface microwave discharge at $p = 10$ Torr, $\tau = 100 \mu s$, $f = 10$ Hz and $W = 100$ kW.

The electric field strength dependence's upon microwave power and longitudinal coordinate for air pressures $p = 10$ Torr and 40 Torr were determined. It was shown (Fig. 7), that the amplitude of an electric field in the surface microwave discharge plasma changes from $E = 5500$ V/cm on an initial stage of the discharge at microwave power $W = 175$ kW up to 250 V/cm at final stage at $W = 25$ kW. It is shown, that at the initial stages of a surface microwave dis-

charge at small air pressures $p < 40$ Torr the main mechanism of a surface microwave discharge propagation is the mechanism defined by an ambipolar diffusion, whereas at the end of a microwave pulse the slow combustion mechanism answers for discharge propagation. At large air pressures ($p = 60\text{--}100$ Torr) it is possible that the main mechanism of a surface microwave discharge propagation is photoionization.

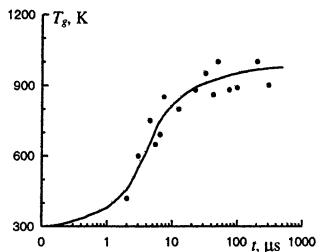
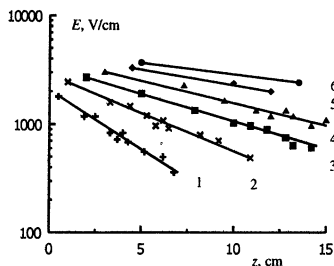


Fig. 7. Electric field strength as a function of a longitudinal coordinate z at air pressure $p = 10$ Torr and at different values of input microwave power W , kW: 1 – 25; 2 – 35; 3 – 55; 4 – 75; 5 – 100; 6 – 175.

Fig. 8. The gas temperature of a surface discharge as a function of a microwave power at $p = 40$ Torr, $\tau = 50 \mu\text{s}$ and $f = 40$ Hz in section $z = 2,5$ cm (W_b is breakdown power at air pressure $p = 40$ Torr).

The time evolution of gas temperature under conditions of surface microwave discharge is submitted on Fig. 8. It was shown that on initial stage of existence of the surface microwave discharge the fast gas heating with rate $dT_g/dt > 50 \text{ K}/\mu\text{s}$ is observed. The similar result was received by us at research of kinetics of gas heating in conditions of the freely localized microwave discharge in air in the focused beam of electromagnetic radiation. The various mechanisms are known which might lead to the heating of molecular gas. The contribution of these mechanisms to heating of molecular gas is detailed analysed in works [8–11], where was shown that the mechanism connected with effective excitation of electron-exited states of nitrogen molecules at large values of the reduced electrical field $E/n \geq 100 \text{ Td}$ and their subsequent quenching is responsible for the fast heating. At this the part of excitation energy of these states is transferred in the heat of air. Our estimations show that only the quenching of electron-exited long-living states of the nitrogen molecules which are effectively created in conditions of a surface microwave discharge in air provides the observed gas heating rate.

The work was supported by the EOARD (ISTC grant № 2248p) and the Russian Foundation of Basic Research (project № 02-02-17116).

References

1. *Shibkov V. M.* et al., Surface microwave discharge in supersonic airflow, *Vestnik Moskovskogo Universiteta. Seriya 3. Fizika, astronomiya*, 2000, **41**(6), 64–66.
2. *Shibkov V. M., Chernikov A. V., Ershov A. P.* et al., IV International workshop Microwave discharges: Fundamentals and applications (18–22 September 2000), Zvenigorod, Russia, Yanus-K, Moscow, 2001, 145–153.
3. *Shibkov V. M., Chernikov A. V., Ershov A. P., Shibkova L. V.* et al., The 2nd Workshop on Magneto-plasma-aerodynamics in aerospace applications. 5–7 April 2000, Moscow (IHT of RAS, 2001), 163–168.
4. *Shibkov V. M., Chernikov V. A., Ershov A. P.* et al., 32nd AIAA Plasmadynamics and Lasers Conference and 4th Weakly Ionized Gases Workshop, 11–44 June 2001. Anaheim, CA, USA. AIAA 2001-3087.
5. *Shibkov V. M., Chernikov V. A.* et al., 15th International Symposium on Plasma Chemistry. V. I. Oral Contributions (9–10 July, 2001, France), 179–184.
6. *Shibkov V. M., Alexandrov A. F., Chernikov V. A.* et al., V International Workshop Strong Microwave in Plasma. Nizhny Novgorod, Russia, D26, 2002.
7. *Shibkov V. M., Dvinin S. A., Ershov A. P., Shibkova L. V.* et al., V International Workshop Strong Microwave in Plasma. Nizhny Novgorod, Russia, D27, 2002.
8. *Zarin A. S., Kuzovnikov A. A., Shibkov V. M.*, Freely localized microwave discharge in air. Moscow: Oil and gas, 1996, 204 p. (Rus).
9. *Shibkov V. M.*, High Temperature. 1997, **35**(5), 681.
10. *Shibkov V. M.*, High Temperature. 1997, **35**(6), 858.
11. *Shibkov V. M.*, Kinetics of gas heating in plasma created in supersonic airflow, 9th Intern. Space Planes and Hypersonic Systems and Technologies Conf. Norfolk, Virginia, USA, 1999, AIAA-99-4965.

MICROWAVE TORCH. PHYSICS AND APPLICATION

*I. A. Kossyi, S. I. Gritsinin, M. A. Misakyan, N. I. Malykh, V. A. Kop'ev,
N. F. Larionova, and V. P. Silakov*

General Physics Institute, Russian Academy of Sciences, Moscow, Russia

The construction and performance of an original coaxial microwave torch is described. This torch can operate both in the pulsed and cw modes at atmospheric pressure with any gases – both noble and molecular ones. It is shown that the time evolution is different in noble and molecular gases. The characteristic feature of torches in noble gases is a dense core with plasma density no less than 10^{16} cm^{-3} . Plasma bunches with density of 10^{14} – 10^{15} cm^{-3} successively propagate downstream from this core, which are seen as glow bursts. In molecular gases, the core is absent and the torch is formed by propagating plasma bunches. Results are presented of measurements of the plasma and gas parameters measurements in the plasma stream. Peculiarities of the discharge development and maintenance are discussed, and possible application of the microwave torch is proposed.

1. Microwave discharges excited when microwave (MW) energy is fed to a gas medium through a coaxial line find wide application in modern physical laboratory as well as in various engineering and technological areas [1–4]. The variety of feasible versions of "coaxial microwave discharges" has recently been supplemented by a number of works made at the General Physics Institute (see, e. g., [5, 6]).

An original version of the torch and associated phenomena are described in this paper. The main distinction is that the inner electrode of the coaxial line is shorter than the outer electrode, but can be built up by a discharge plasma. The torch can be operated at low MW powers in various gases at high (up to atmospheric) pressures.

2. A schematic sketch of the MW plasma torch is shown in Fig. 1. The device is fed from a production magnetron (frequency $f \cong 2,45 \text{ GHz}$, half-period rectification power supply) through a rod antenna launching MW pulses into a rectangular cavity. The average input MW power in the cavity is $P \leq 1 \text{ kW}$.

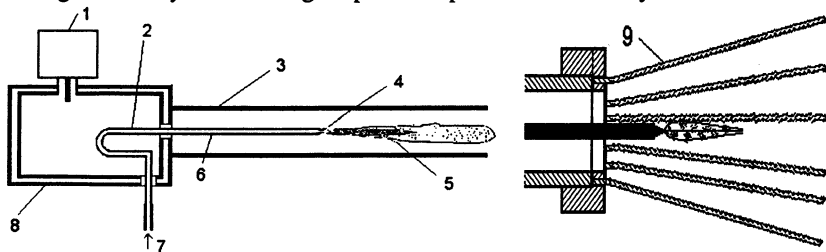


Fig. 1. Microwave coaxial plasma torch (on left) and the basket-type extension of the outer electrode (on right): 1 – magnetron, 2 – loop, 3 – outer electrode, 4 – nozzle, 5 – plasma stream, 6 – inner electrode, 7 – working gas, 8 – rectangular resonator, and 9 – copper wires.

From the rectangular cavity, the MW energy is transmitted into a coaxial line through an intermediate component – a current loop whose extension is the inner electrode, used as a pipeline for gas injection. The inner electrode is ended with a refractory metal nozzle, which has a sharp edge facilitating breakdown of the gas. The outer electrode is 2–3 cm in diameter, and its free end is a circular beyond-cutoff waveguide for electromagnetic waves $\lambda \approx 12$ cm.

To permit the wave propagation, we used an array of fine metal wires 2–3 mm in diameter spaced at intervals of 0.5–1 cm along the waveguide edge. Since the currents flow through the coaxial line in the longitudinal direction, this multi-wire array ("basket") fairly plays the role of a solid electrode. This design made it possible to achieve generation of a plasma jet extended for 10–20 cm along the axis (for distances much longer than sizes of torches produced by traditional generators). It is advantageous also that the plasma jet and the surrounding gas are accessible both to active and passive diagnostics.

The MW energy of waves reflected from the circular waveguide is accumulated in the system of cavities including the rectangular, the coaxial, and the proper magnetron cavity. The length of the inner electrode is chosen such that the nozzle edge is located in the maximum of the electric field of a standing wave generated when the travelling wave reflects at the inlet into the beyond-cutoff circular waveguide. As the energy is accumulated in the standing wave, the electric field at the sharpened edge of the nozzle increases and reaches the breakdown intensity. Thus, in spite of a relatively low level of MW power, it appears possible to achieve the gas breakdown in various gases (argon, nitrogen, air, carbon dioxide, hydrogen, methane, propane, freons, etc.) over a wide range of pressures, including the atmospheric pressure).

The plasma produced by the gas breakdown near the nozzle is entrained by the working-gas flow, and the arising plasma jet serves as an extension of the inner coaxial electrode. Microwaves can propagate through the newly formed coaxial structure toward the end of the torch, where again they fall into the circular beyond-cutoff waveguide and reflect backward, and ultimately are substantially absorbed in the torch plasma.

3. The time evolution of the torch was studied with the help of a streak camera, photomultipliers and photodiodes. The electron density was measured with laser and MW interferometers. The emission spectrum of the torch was recorded, and the radiant temperature was evaluated.

When operating with argon and other noble gases, we observed a bright cylindrical core 1–2 mm in diameter and 1–1.5 cm in length and, downstream, an extended, and less bright region (with curved boundaries) which was 2–3 orders of magnitude greater than the core volume. Such a core was absent when operating with molecular gases.

Measurements with a collimated photodiode showed that, at $0,5 \text{ ms} \leq t \leq 4 \text{ ms}$, the glow front moved at the almost constant velocity $v_z \cong 20 \text{ m/s}$ away from the nozzle for a distance $\approx 9.5 \text{ cm}$, the maximum length of the torch being $L_z^{\text{max}} \cong 11 \text{ cm}$.

Figure 2 demonstrates the streak photography of the torch propagation for argon and nitrogen. The camera slit was oriented along the axis of the coaxial line. With a slow time scanning (Fig. 2, *b*) in the case of argon, we see that, during the initial stage lasting ~ 0.5 ms from the beginning of the magnetron pulse, the torch exists structurally as a core 1–2 cm long. Then, a less bright glow wave tears away from the core and propagates along the axis of the system. It is interesting that, this primary glow wave is followed by a train of secondary waves arising synchronously with periodic bursts in the core. These secondary waves overtake the primary front and form the resulting glow wave.

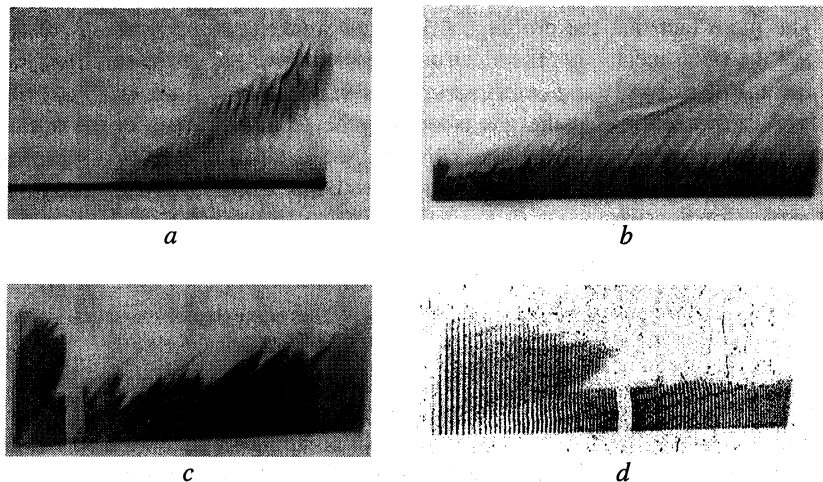


Fig. 2. Streak-camera photos of the microwave torch. The working gas is (a) N₂ or (b–d) Ar. The full scanning time is (a, b) 3 ms, (c) 750 μ s, and (d) 250 μ s; the full space scale is (a, b) 8 and (c, d) 2 cm.

A more rapid time scanning (Fig. 2, *c, d*) allows us to detect a high-frequency modulation of the core glow at times preceding the appearance of the glow wave. The characteristic modulation period 5–10 μ s correlates with the frequency of magnetron generation 100–200 kHz early in the magnetron operating pulse. After several hundreds of microseconds, a bright core appears, and bursts in the core occur synchronously with magnetron pulses. The pulse generation frequency increases gradually, and the generation becomes continuous.

The plasma density in the torch was measured with the use of a probing cw MW radiation (two horn-lens antennas) at a frequency about $\omega_d \cong 8 \cdot 10^{11} \text{ c}^{-1}$ ($\lambda_d \cong 2.3 \text{ mm}$). In the torch core, where the plasma density turned out to be higher, we used a submillimeter ($\lambda_d \cong 337 \text{ }\mu\text{m}$) radiation of an HCN laser. Most

of the experiments were carried out with argon and nitrogen at flow rates of 5–20 L/min.

We studied the propagation of the probing radiation through the torch at various distances Z from the nozzle. At distances $0 \leq Z \leq 20$ mm from the nozzle, a substantially (~80%) attenuated transmitted signal was observed during the entire operating pulse. This distance corresponds to the core length. At distances $20 \leq Z \leq 60$ mm, we observe a strong (20–100%) modulation of the transmitted signal at a frequency of ~1 kHz, which is interpreted as a generation of bunches of a dense and brightly radiating plasma moving in the direction of the gas flow in the torch.

The mere fact that the probing MW signal weakens strongly when passing through the torch means that the electron density in the bulk of the torch is close to the cutoff density n_{ecr} and even exceeds this value, and we have $n_e \geq n_{ecr}$. Taking into consideration that the gas is strongly heated, for plasma at the atmospheric pressure we come to the inequality $v_{en}^2 \ll \omega_d^2$, which defines our plasma as being collisionless. From this reasoning, we come to the following condition for the electron density:

$$n_e \geq n_{ecr} = m_e \omega_d^2 / 4\pi e^2 \cong 2 \cdot 10^{14} \text{ cm}^3.$$

With the submillimeter laser interferometer, the core density was estimated at $n_e \approx 10^{16} \text{ cm}^3$.

The spectrum of the microwave torch (Fig. 3) was studied over a wide range $2000 \leq \lambda \leq 8500 \text{ \AA}$ with the help of an S2000 (Ocean Optics) spectrometer. The spectrum contains both the continuous and line components identified as Ar, N, and O atomic lines and also N_2 molecular bands. The continuum of the spectrum was studied in pure argon and with tungsten grains of size 30–40 μm admixed to the gas. In both cases, the spectral intensity I_λ in the wavelength range $4500 \text{ \AA} \leq \lambda \leq 6500 \text{ \AA}$ appeared to be equilibrium. Taking into account that the inequality $\exp(hc/\lambda kT) \gg 1$ holds in this wavelength range, we can write

$$1.44 \cdot 10^8 / \lambda = \text{const} - T \ln(I_\lambda \lambda^4),$$

where λ is expressed in \AA , T in K, and I_λ in relative units.

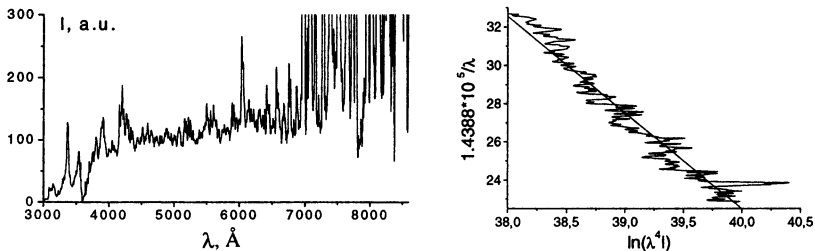


Fig. 3. Torch spectrum in the standard (on left) and the Planckian coordinates (on right)

The temperature value was deduced from the continuous spectrum transformed to the Planckian coordinates: $x \rightarrow \ln(I_\lambda \lambda^4)$, $y \rightarrow 1.44 \cdot 10^8 / \lambda$, in which case the radiator temperature T was determined from the slope of the function $y(x)$. Because of small sizes of the radiating tungsten grains, it was assumed that $T \approx T_g$. In this way, the temperature T_g was estimated at various distances from the nozzle.

The continuous spectrum of the torch plasma may be formed by both the bremsstrahlung and recombination mechanisms. In both cases, the spectral intensity is proportional to the Wien exponent $I_\lambda \sim \exp(-hc/\lambda kT_e)$. The continuous emission spectrum is explained by the fact that the gas is strongly heated and molecular lines are broadened so that they overlap.

Thus, based on the results these measurements, we can conclude that the gas temperature in the torch is maximum in the core and slowly decreases with distance away from the torch, and the gas in the core is heated to a rather high temperature: $T_g \cong 4000\text{--}5000$ K.

To verify this estimate for the gas temperature, we carried out experiments with a ceramic rod inserted into the flame. In this case too, the characteristic emission spectrum was close to the Planckian blackbody spectrum with a temperature of ~ 2300 K. This value may be reckoned as a conservative estimate for the gas temperature.

4. We emphasize that, structurally, the plasma of our torch operating on argon differ markedly from torches of the traditional devices, in which the inner and outer electrodes have nearly the same length. In our case, there is a bright core adjacent to the nozzle and extended for 1–1.5 cm along the Z-axis. The ionization in this region plays a dominant role and provides high released energies. In the traditional devices, the plasma density (and, consequently, the released energy) decreases sharply in this region because the intensity of ionization processes decreases. The reason is that energy of the pumping wave is absorbed only partially in the plasma, and the wave field additionally decreases owing to the geometric factor. In this case, the nonabsorbed wave is emitted into space by the torch acting as a rod antenna. In our case, downstream the core we observe a considerably greater region of less bright glow (with curved boundaries). The fraction of the wave energy that was not absorbed by the core can propagate through the formed plasma electrode, so that the size of the glow region increases considerably and the plasma density is sustained at a level high enough.

The mechanism causing the propagation of ionization waves and, thereby, the production of the plasma extended along the Z-axis is associated with the electromagnetic surface wave. The existence of this wave, in turn, suggests that the plasma electron density n_e at the torch axis exceeds the critical density n_{ecr} for microwaves propagating along the torch. The measurements of n_e by the microwave and laser interferometers confirm this conclusion.

5. The plasma sources of configurations described above can find wide application, including the following technologies:

- (i) treatment of industrial gas discharges to the atmosphere;
- (ii) plasmochemical deposition of thin films of different materials (silicon, diamond, diamond-like, metal);
- (iii) etching of sizable semiconductor components;
- (iv) welding of quartz pieces without using combustible gases, etc.

References

1. *Moisan M., Margot J. and Zakrewski Z.* In: Popov A., High Density Plasma Sources, Noyes Publ., New Jersey, (1995).
2. *Rauchle E. J.* Phys. IV France, 1998, **8**, Pr7–99.
3. *Moisan M., Sauve G., Zakrzewski Z. and Hubert J.* Plasma Sources Sci. Technol., 1994, **3**, 584.
4. *Mitsuda Y., Yoshida T., Akashi K.* Rev. Sci. Instr., 1989, **60**, 249.
5. *Gritsinin S. I., Kossyi I. A., Malykh N. I. et al.*, 14th ISPC, Prague, 1999, **II**, 675.
6. *Gritsinin S. I., Kossyi I. A., Malykh N. I. et al.*, Preprint N 1, General Physics Institute of RAS, 1999, Moscow, 24 p.

CONTENTS OF VOLUME 2

NONLINEAR PROCESSES IN PLASMAS (THEORY AND MICROWAVE EXPERIMENTS)

Collisional effects in ultra-high illuminated plasmas: from the theory to the experiment <i>A.A. Balakin, G.M. Fraiman</i>	437
Cyclotron masers in space <i>V.Yu. Trakhtengerts, A.G. Demekhov, M.J. Rycroft</i>	453
Classical plasma analogs of the electromagnetically induced transparency (EIT) and lasing without inversion (LWI) <i>M.D. Tokman, A.G. Litvak, M.A. Erukhimova, A.Yu. Kryachko</i>	474
Terahertz range sources from the ultra-short laser and plasma interaction <i>D. Dorrnian, M. Starodubtsev, N. Yugami, T. Higashiguchi, H. Kawakami, H. Ito, Y. Nishida</i>	487
Formation and evolution of dust ion-acoustic nonlinear structures in complex plasmas <i>S.I. Popel</i>	498
Self-consistent electromagnetically driven Langmuir turbulence in overdense plasma <i>A.V. Kochetov, V.A. Mironov, G.I. Terina, M.V. Shaleev</i>	505
Electroaerodynamic turbulence in the atmosphere and its laboratory modeling <i>E.A. Mareev, N.A. Bogatov, A.E. Sorokin, D.I. Iudin, V.Yu. Trakhtengerts</i>	511
Stochastic model of dust particle growth in plasmas <i>M.V. Shatalina</i>	517
Hot electrons at electron-ion collisions in strong laser fields <i>A.A. Balakin, G.M. Fraiman</i>	521
Optical-field-induced ionization of the gas by the axicon-focused laser pulses <i>V.B. Gildenburg, N.V. Vvedenskii</i>	526
Charged particle (CP) acceleration by an intense wake-field (WF) excited in plasmas by either laser pulse (LP) or a relativistic electron bunch (REB) <i>V.A. Balakirev, I.V. Karas', V.I. Karas', V.D. Levchenko, M. Bornatici</i>	531
Bohm criterion failure and periodic oscillations of the plasma sheath in nonstationary plasmas <i>Ya.Z. Slutsker, Yu.P. Bliokh, J. Felsteiner, P.M. Vaisberg</i>	537
The parametric instability of the cyclotron radiation in reactive electron medium <i>M.A. Erukhimova, M.D. Tokman</i>	544
Penetration of a microwave with a stochastic jumping phase (MSJP) into overdense plasmas and electron collisionless heating by it <i>V.I. Karas', V.D. Levchenko</i>	550
Dynamics of powerful plasma wave breaking and reflection phenomena <i>V.I. Arkhipenko, E.Z. Gusakov, V.A. Pisarev, L.V. Simonchik</i>	555
The upper hybrid resonance in the turbulent plasma <i>E.Z. Gusakov, A.V. Surkov</i>	561

The nonlinear regime of a resonance microwave probe based on a two-wire line section <i>I.G. Kondrat'ev, A.V. Kostrov, A.I. Smirnov, A.V. Strikovskiy</i>	566
Excitation of magnetic fields correlated with intense lower-hybrid waves in plasmas <i>S.I. Popel, K. Elsässer, Y. Takeda, H. Inuzuka</i>	570
Excitation of a wake field by a rectangular microwave pulse in a rectangular waveguide <i>H.K. Malik, H. Ito, N. Yugami, Y. Nishida</i>	576
Inhomogeneous plasma parametric decay instability driven by a frequency modulated pump <i>V.I. Arkhipenko, E.Z. Gusakov, V.A. Pisarev, L.V. Simonchik, B.O. Yakovlev</i>	582
The effect of the electromagnetically induced transparency in magnetoactive plasmas <i>A.Yu. Kryachko, M.D. Tokman</i>	587
Self-channeling of high power microwaves in a preformed plasma waveguide <i>C. Rajyaguru, T. Hosoya, H. Ito, N. Yugami, Y. Nishida</i>	593
Low frequency sheath instability stimulated by the resonant absorption of a short microwave pulse <i>M. Starodubtsev, Md. Kamal-Al-Hassan, H. Ito, N. Yugami, Y. Nishida</i>	598

GAS DISCHARGES IN ELECTROMAGNETIC WAVE FIELDS AND OTHER APPLICATIONS OF HIGH-POWER MICROWAVES

Microwave plasma and its application <i>Yu.A. Lebedev</i>	605
ECR ion sources: recent developments <i>S. Golubev, D. Mansfeld, S. Razin, V. Skalyga, A. Vodopyanov, V. Zorin, V. Murugov, A. Senik, A. Kravchenko, D. Litvin, V. Misko, S. Petrov, R. Geller, T. Lamy, P. Sortais, T. Thuillier</i>	618
Interaction of high-power microwave beams with metal-dielectric media (physics and applications) <i>G.M. Batanov, N.K. Berezhetskaya, I.A. Kossyi, A.N. Magunov, V.P. Silakov</i>	631
Rapid millimeter wave annealing of silicon wafers <i>Yu.V. Bykov, A.G. Ereemeev, I.V. Plotnikov, N.A. Zharova</i>	642
Third generation ECR ion sources <i>L. Celona, S. Gammino, G. Ciavola</i>	654
Ion flux diagnostics of ECR discharge with different wave polarization <i>A.S. Smirnov, D.A. Malik, K.E. Orlov, T.V. Chernoziumskaya</i>	667
Microwave concept of a large volume plasma source <i>A.A. Litvak, S.V. Putvinski, V.E. Semenov, A.G. Shalashov, O.B. Smolyakova, E.V. Suvorov</i>	672
Hybrid resonances in multipactor discharges <i>A. Kryazhev, M. Buyanova, V. Semenov, D. Anderson, M. Lisak, J. Puech, L. Lapierre, J. Sombrin</i>	678

Breakdowns and destructions of dielectrics in strong microwave fields	
<i>V.A. Ivanov, M.E. Konyzhev</i>	684
Microwave plasma-assisted CVD diamond film deposition in pulsed and CW regimes	
<i>A.L. Vikharev, A.M. Gorbachev, V.A. Koldanov, D.B. Radishev</i>	693
Optical emission diagnostics of microwave plasma in a CVD reactor	
<i>R.A. Akhmedzhanov, A.L. Vikharev, A.M. Gorbachev, V.A. Koldanov, D.B. Radishev</i>	700
Modeling of electronegative plasmas for design of microwave applicators	
<i>D. Korzec, J. Engemann</i>	706
Electrode microwave discharges. State-of-the-art	
<i>Yu.A. Lebedev, M.V. Mokeev, A.V. Tatarinov, I.L. Epstein</i>	714
Detailed investigations in microwave sintering of ceramics by means of a dilatometer	
<i>G. Link, M. Thumm</i>	719
Time-resolved imaging of millimeter-waves using the recombination continuum of cesium emitted by a slab of the Cs-Xe DC discharge	
<i>I.E. Abubakirov, M.S. Gitlin, A.O. Perminov, V.V. Zelenogorsky</i>	725
Interaction of a supersonic airflow with the combined microwave discharge, created on the external surface of a wedge dielectric body	
<i>V.M. Shibkov, V.A. Chernikov, V.G. Gromov, O.B. Larin, V.A. Levin, L.V. Shibkova</i>	731
Surface microwave discharge in a supersonic airflow	
<i>V.M. Shibkov, V.A. Chernikov, A.P. Ershov, L.V. Shibkova, I.B. Timofeev</i>	737
Microwave torch: physics and application	
<i>I.A. Kossyi, S.I. Gritsinin, M.A. Misakyan, N.I. Malykh, V.A. Kop'ev, N.F. Larionova, V.P. Silakov</i>	743

**STRONG
MICROWAVES
IN PLASMAS**

PROCEEDINGS
OF THE INTERNATIONAL WORKSHOP

In two volumes

Volume 2

Institute of Applied Physics,
Russian Academy of Sciences

46 Ul'yanov Street, 603950 Nizhny Novgorod, Russia

Printed by Printing House №2, "Nauka" Publishers,
6 Shubinsky Pereulok, 121099 Moscow